

**A study of melt-compounded
nanocomposites of polycarbonate and
carbon nanotubes in the melt and solid
states**

by

Gabriel Choong Yew Hong

BEng

Thesis submitted to the University of Nottingham
for the degree of Doctor of Philosophy

April 2014

Anybody who has been seriously engaged in scientific work of any kind realises that over the entrance to the gates of the temple of science are written the words: 'Ye must have faith'

Max Planck

Abstract

Polycarbonate-carbon nanotube nanocomposites are promising materials for electrostatic shielding and conductive packaging applications. The nanotubes impart electrical conductivity and increases thermal conductivity and stiffness of the matrix. However, the nanofiller also affects the rheology, and hence the evolution of a filler network during processing. This thesis examines the effects of matrix molar mass and of compounding temperature on the thermal, rheological, electrical and mechanical properties of these materials.

Thermal analysis demonstrated that the glass transition decreased as a consequence of the nanotubes. Degradation of the matrix was ruled out as a possible cause, and the decrease was attributed to a poor interface between matrix and filler. Thermal conductivity of the matrix increased with the addition of nanotubes, in line with model predictions. Furthermore, the nanofillers also marginally increased thermal stability of the matrix in atmospheric conditions.

Oscillatory shear rheology showed that the nanocomposites deviate from linearity earlier than the matrix polymers. A technique was developed to assemble mastercurves over an extended frequency range. The nanocomposites exhibit a low frequency plateau at $\sim 10^5$ Pa, identified as the stiffness of the nanotube network. Relaxation times estimated from the peak in loss tangent scale with matrix molar mass in the same way as terminal relaxation times in pure matrix materials, providing evidence that relaxation of the polymer network is the dominant relaxation mechanism in filled and unfilled polymers.

The effects of melt processing on electrical and mechanical properties were investigated using nanocomposites melt-compounded at a range of extrusion temperatures, but subsequently produced by either injection moulding or compression moulding. Electrical resistivity measurements obtained using a two-terminal method revealed that the resistivity of compression moulded specimens was an order of magnitude lower than that of injection moulded specimens. The compounding temperature had only a mild effect on resistivity. Compression moulded specimens also exhibited greater surface hardness and lower modulus than injection moulded specimens. The elastic modulus recorded is in line with expectation due to nanotube orientation, demonstrated using a modified Halpin-Tsai model. The model can explain much of the observed effects, but suggests that nanotubes may be considerably shortened by melt processing.

Acknowledgements

I would like to extend my heartfelt gratitude to the many people who have contributed to this project in the form of assistance, ideas and culinary skills.

Firstly, I would like to thank my supervisor, Dr. Davide De Focatiis for accepting me as a Ph.D. student. I am truly indebted to his insights during discussions, and for his patience to teach and to review my writings that are often riddled with grammatical errors. He was a source of inspiration with his gentle encouragement and unwavering support at times of technical failures and intellectually challenging findings.

I am immensely grateful to Prof. Nicholas Warrior who provided the opportunity and support to pursue my interest in research. I would like to thank Dr. David Hassell for a year of his guidance and his sense of humour. I wish to acknowledge Dr. Andy Lew of Nanocyl S.A. who made this project possible by kindly providing the materials.

This work would not be completed without the support of staff and researchers of the Faculty of Engineering and the School of Chemistry. I am grateful to Dr. Natasha Birkin and Dr. Jaouad El Harfi for the GPC measurements and the Soxhlet extraction. Special thanks go to the technical staff of L3, L4 and ITRC laboratories: Phil Bennett, Michael Fletcher, Jim Oswin, Frederick Anderson, Mel Hemsley, Reginald Briggs, Marion Bryce, and Roger Smith for efforts in manufacturing and maintaining test equipment, and for not hiding at the sight of me. My gratitude is extended to Dr. Michael Fay for the time on the FIB-SEM, Dr. Sven Pegel for assistance in the digital image analysis, Martin Roe for the SEM training, and Nicola Weston and Denise Christie for the efforts on the microtome. Sincerest thanks to Keith Dinsdale and Tom Buss for the guidance on the thermal and mechanical tests.

On a more personal note, I sincerely thank my friends in the Polymer Composite Group, Wolfson building and Cathsoc who made adversity a source of laughter. Special mention to the Matveevs, Maggie, Amanda and Mary for the dinners that were a source of respite, and Frank, Mikhail and Chris for proofreading. I particularly thank my girlfriend, Katherine, for her unfailing support, patience and care that never ceases to lift my spirits.

And most of all, I wish to thank my family for their tremendous support. No words can describe the gratitude I have for your love, sacrifice and constant encouragement that has helped me at every step of this journey. You are my pillars of hope, strength and faith. This thesis is dedicated to you.

Per Scientia Ad Dei Gloriam

Contents

Abstract	ii
Acknowledgements	iii
List of Figures	ix
List of Tables	xv
Abbreviations	xvii
Symbols	xix
1 Introduction	1
1.1 Background	1
1.1.1 Applications of CNT nanocomposites	2
1.1.2 Processing of CNT nanocomposites	3
1.1.3 Commercial outlook	4
1.2 Aims and objectives	5
1.3 Outline	6
2 Literature review	8
2.1 Polycarbonate and carbon nanotubes: an introduction	8
2.1.1 Polycarbonate	9
2.1.2 Carbon nanotubes	9
2.2 Processing of CNT nanocomposites	11
2.2.1 Melt compounding	12
2.2.1.1 CNT dispersion mechanisms	12
2.2.1.2 Small batch mixing	13
2.2.2 Forming processes in the melt state	14
2.2.2.1 Injection moulding	14
2.2.2.2 Compression moulding	17
2.3 Quantifying CNT dispersion	18
2.3.1 Optical microscopy	19
2.3.2 Electron microscopy	20
2.4 Thermal properties	21

2.4.1	Thermal conductivity of CNTs	22
2.4.2	Thermal conductivity of thermoplastic-CNT nanocomposites	22
2.4.3	Thermal degradation PC and CNTs	24
2.4.4	Thermal degradation of thermoplastic-CNT nanocomposites	25
2.5	Mechanical properties	27
2.5.1	Mechanical properties of CNTs	27
2.5.2	Fundamentals for mechanical reinforcement of nanocomposite	29
2.5.3	Thermoplastic-CNT nanocomposites	30
2.5.3.1	Influence of constituent material characteristics	30
2.5.3.2	Processing effects on orientation and dispersion of CNTs	32
2.5.3.3	Predictions of tensile modulus of CNT nanocomposites	33
2.6	Electrical properties	36
2.6.1	Carbon nanotubes	36
2.6.2	Thermoplastic-CNT nanocomposites	36
2.6.2.1	Influence of CNT network morphology	37
2.6.2.2	Influence of processing parameters	39
2.6.2.3	CNT network formation mechanism	40
2.7	Rheology	44
2.7.1	Linear rheology of thermoplastic-CNT nanocomposites	45
2.7.1.1	Effect of CNT loading content	46
2.7.1.2	Oscillatory shear studies	47
2.7.1.3	Influence of temperature	48
2.7.1.4	Influence of matrix molar mass	49
2.7.1.5	Influence of orientation and dispersion of CNTs	52
2.7.2	Non-linear rheology of thermoplastic-CNT nanocomposite	53
2.7.2.1	Transient, steady state and elongational shear	53
2.7.2.2	Non-linear oscillatory shear	55
2.8	Summary	56
3	Materials and preparation	59
3.1	Materials	59
3.1.1	Polymer matrix materials	59
3.1.2	Filler material	60
3.2	Melt compounding	61
3.3	Preparation methods	61
3.3.1	Compression moulding	62
3.3.2	Injection moulding	65
3.4	Molar mass distribution	65
3.4.1	Influence of melt compounding on molar mass	66
3.4.2	Influence of CNT presence on polymer degradation	66
3.5	Independent filler content determination	68
3.5.1	Soxhlet extraction	68
3.5.2	Density measurement	68
3.6	Conclusions	70
4	Thermal properties	72
4.1	Introduction	72

4.2	Influence of CNTs on the glass transition temperature	72
4.2.1	Method	73
4.2.2	Results and discussion	75
4.3	Thermal transport properties	78
4.3.1	Method	79
4.3.2	Results and discussion	80
4.3.3	Predicting thermal conductivity of PC-MWCNT	81
4.4	Thermal degradation and stability	83
4.4.1	Method	83
4.4.2	Results and discussion	84
4.4.2.1	TGA under nitrogen atmosphere	84
4.4.2.2	TGA under air atmosphere	86
4.5	Conclusions	89
5	Melt rheology	91
5.1	Introduction	92
5.2	Experimental	93
5.2.1	Materials	93
5.2.2	Amplitude sweep procedure	94
5.2.3	Frequency sweep procedure	94
5.3	Amplitude sweeps	95
5.3.1	Determination of the linear viscoelastic range	95
5.4	Preparatory experiments for isothermal frequency sweeps	97
5.4.1	Time dependence of structural build up	97
5.4.2	Effect of temperature step direction	98
5.4.3	Role of melt processing on rheology	99
5.5	Time-temperature superposition and construction of mastercurves	100
5.5.1	Vertical shifting	100
5.5.2	Horizontal shifting	103
5.6	Frequency sweeps	106
5.6.1	Application of a two-phase model to the viscoelastic data	108
5.6.2	Relaxation times	112
5.6.3	Large amplitude response	115
5.6.4	Roles of strain and temperature history	117
5.7	Conclusions	119
6	Microscopic investigation	121
6.1	Introduction	121
6.1.1	Optical microscopy sample preparation and techniques	122
6.1.2	SEM sample preparation and techniques	124
6.2	Optical microscopy	125
6.2.1	Characterisation of CNT dispersion	125
6.2.1.1	Section preparation methods	125
6.2.1.2	OM investigation	126
6.2.1.3	OM micrographs of thin sections	126
6.2.1.4	Attempts to produce an improved specimen surface	127
6.2.1.5	Image analysis	128

6.2.1.6	Image processing procedure	129
6.2.1.7	Quantification of CNT dispersion	130
6.2.2	Void determination	132
6.2.2.1	Grinding and polishing procedure	132
6.2.2.2	OM investigation	133
6.2.2.3	OM micrographs of polished sections	133
6.3	Scanning electron microscopy	133
6.3.1	Method	134
6.3.2	SEM micrographs	135
6.4	Focused ion beam-SEM	136
6.4.1	Method	137
6.4.2	FIB-SEM images	137
6.5	Conclusions	139
7	Electrical resistivity	140
7.1	Introduction	140
7.2	Resistivity measurements methods	141
7.2.1	Two-terminal method	141
7.2.2	Four-terminal method	142
7.2.3	Van der Pauw method	143
7.3	In-house two-terminal resistivity fixture	145
7.3.1	Technical description of a two-terminal fixture	149
7.4	Errors in electrical measurements using custom test fixtures	150
7.4.1	Considerations for current measurements	150
7.4.2	Temperature effects	152
7.5	Exploratory experiments	153
7.5.1	Two-terminal method	153
7.5.1.1	Thermoelectric effect	153
7.5.1.2	Heating of specimen	154
7.5.1.3	Non-ideal contacts and resistance sources in the fixture	156
7.5.1.4	Contact resistance and contact resistivity determination	159
7.5.1.5	Effects of contact location at the terminal and the external applied force	162
7.6	Experimental method	163
7.6.1	Detecting outliers	164
7.7	Results	165
7.8	Discussion	166
7.9	Conclusions	170
8	Mechanical properties	172
8.1	Introduction	172
8.2	Specimen preparation for mechanical testing	174
8.3	Vickers hardness	175
8.3.1	Method	176
8.3.2	Results and discussion	176
8.4	Tensile testing	178
8.4.1	Method	179

8.4.2	Results and discussion	180
8.4.2.1	Young's modulus	180
8.4.2.2	Ultimate tensile strength	181
8.4.2.3	Orientating the nanocomposites	183
8.4.3	Models for the prediction of Young's modulus of PC-MWCNT	183
8.4.3.1	Uniaxially oriented CNT nanocomposite	184
8.4.3.2	Randomly oriented CNT nanocomposite	187
8.5	Correlation between mechanical and electrical properties	188
8.6	Conclusions	190
9	Conclusions	193
9.1	Major conclusions	193
9.2	Summary of relevant findings	195
9.3	Recommendations for future work	198
A	Procedure for determining outliers in samples	200
A.1	Normality test	200
A.2	Tietjen-Moore test	201
A.2.1	Introduction	201
A.2.2	Procedure	201
	Bibliography	203

List of Figures

1.1	Illustration of manufacturing a final product made from CNT nanocomposite. An extruder compounds the raw materials for the polymer nanocomposite that is pelletised. These pellets are then re-melted and formed to shape using secondary processes such as injection moulding and compression moulding . . .	3
2.1	Chemical structure of polycarbonate (adapted from King (2000))	9
2.2	SEM micrographs of agglomerated Nanocyl NC7000 multi-wall carbon nanotubes as supplied by the manufacturer and used in this study, at different magnifications (Krause et al., 2010)	10
2.3	TEM micrographs of PC-MWCNT (2 wt%) injection moulded at (a) $V_{inj} = 150 \text{ mm s}^{-1}$ and $T_{melt} = 280 \text{ }^\circ\text{C}$, and at (b) $V_{inj} = 10 \text{ mm s}^{-1}$ and $T_{melt} = 320 \text{ }^\circ\text{C}$ (adapted from Villmow et al. (2008a))	17
2.4	An SEM image of a fracture surface of PA6-MWCNT (0.5 wt%) after tensile testing. The first arrow indicates a broken CNT whereas the second arrow shows a CNT embedded in the matrix that bridge across a crack (adapted from Liu et al. (2004))	21
2.5	A reconstructed 3D representation of poly[(butylene succinate)-co-adipate] filled with nanoclay using 2D images of the cross-sectional surfaces that were milled using focused ion beam in the Z direction (adapted from Ray (2010)) .	21
2.6	A MWCNT under tensile loading experiences failure through sword-in-sheath method. (a) AFM tips used to hold the nanotube in position. (b) An inner tube is removed from MWCNT. (c) The outer tube remains with the opposite AFM tip (reproduced from Ding et al. (2007))	28
2.7	In-situ observation TEM of a crack growing in PS-MWCNT showing (a) crack propagation and (b) bridging of crack faces (adapted from Qian et al. (2000))	30
2.8	Structure of interaction zones of a polymer-nanotube nanocomposite (adapted from Eitan et al. (2006))	32
2.9	Volume resistivity dependence on MWCNT loading content for PC-MWCNT (adapted from Pötschke et al. (2002))	38
2.10	TEM images of (a) PC-MWCNT (5 wt%) injection moulded sheets of surface resistivity = $10 \text{ } \Omega \text{ m}$ (b) after annealing for 1 hour at $300 \text{ }^\circ\text{C}$ giving surface resistivity = $10^{-1} \text{ } \Omega \text{ m}$ (adapted from Alig et al. (2008c))	41
2.11	Electrical conductivity recovery measurements of PC-MWCNT (0.875 wt%) at $260 \text{ }^\circ\text{C}$ (square symbols). The electrical conductivity below the percolation threshold was calculated with percolation theory (dashed line) and a cluster aggregation model (solid line) was used for filler concentrations above the percolation threshold. The initial increase in conductivity was calculated using an empirical relaxation function for shear flow oriented CNTs (dash-dot-dot line) (adapted from Alig et al. (2008))	42

2.12	Schematic of PC-MWCNT with CNT agglomerates (within circles) that cluster to form a pathway for electrical conductivity (reproduced from Zeiler et al. (2010))	43
2.13	Electrical conductivity time dependence measured for 2 hours of annealing followed by a steady shear rate of 0.02 rad s^{-1} for 600 s and a quiescent recovery. The solid lines represents partial MWCNT agglomeration whereas dashed lines represent well dispersed MWCNTs (adapted from Skipa et al. (2010))	43
2.14	Electrical conductivity of initially dispersed (solid circles) and agglomerated CNT (hollow circles) under steady shear rate of 0.02 rad s^{-1} for 1 hour (adapted from Skipa et al. (2010))	44
2.15	(a) Storage modulus, G' , (b) loss modulus, G'' and (c) complex viscosity, η^* as a function of frequency and increasing MWCNT (0.5-15 wt%) loading in PC, at $T = 260 \text{ }^\circ\text{C}$ (adapted from Pötschke et al. (2002))	48
2.16	Frequency dependence of storage modulus with increasing temperature at (a) $170 \text{ }^\circ\text{C}$, (b) $220 \text{ }^\circ\text{C}$ and (c) $280 \text{ }^\circ\text{C}$ (adapted from Pötschke et al. (2004)) . . .	49
2.17	Complex viscosity as a function of frequency for increasing molar mass: (a) low molar mass ($M_n=16400 \text{ g mol}^{-1}$), (b) medium molar mass ($M_n = 22000 \text{ g mol}^{-1}$), and (c) high molar mass ($M_n = 29300 \text{ g mol}^{-1}$). (d) Storage modulus as a function of frequency for increasing molar mass (adapted from Fornes et al. (2001))	51
2.18	Viscoelastic response of PMMA-SWCNT with 0.5 wt% for two different polymer molar mass. PMMA25K = 25000 g mol^{-1} ; 0.5NT25K (filled) = 25000 g mol^{-1} ; PMMA100K = $100000 \text{ g mol}^{-1}$; 0.5NT100K (filled) = $100000 \text{ g mol}^{-1}$ at $T = 200 \text{ }^\circ\text{C}$ (adapted from Du et al. (2004))	52
2.19	Storage modulus, G' and loss modulus, G'' of initially dispersed (solid squares) and agglomerated CNT (hollow triangles) under steady shear rate of 0.02 rad s^{-1} for 1 hour (adapted from Skipa et al. (2010)). The corresponding electrical conductivity measurement is presented in Fig. 2.14	55
2.20	(a) Storage modulus, G' of PBT-MWCNT (3 wt%) at different levels of strain. (b) Comparison of SAOS and LAOS measurements of G' , and (c) $\tan \delta$. (d) Cole-Cole plot of complex viscosity, η^* (the imaginary part η'' of as a function of the real part η') at different levels of strain (reproduced from Wu et al. (2007))	56
3.1	A TEM image of NC7000 MWCNTs obtained by merging two images for the measurement of the length and diameter of CNTs. A typical measurement of a CNT length is identified in red (Krause et al., 2011)	60
3.2	Multiple specimens mould capable of producing (a) circular specimen of 25 mm in diameter and 0.5 mm in thickness; (b) dog-bones with gauge length of 25 mm and 2 mm in thickness exhibited with sample prior to flash removal; (c) rectangular bars with dimensions of $60 \text{ mm} \times 5 \text{ mm} \times 2 \text{ mm}$ shown with samples without flash. The specimens illustrated are PC-MWCNT 2205 and PC 2205	63
3.3	A schematic diagram of the moulding process: (a) the mould arrangement with the mould cavity filled with polymer granules; (b) the mould is transferred to the heated press and the pressure cycle is applied; (c) the mould is then cooled and removed from the press to release the moulded specimens from the cavity.	64
3.4	The moulding procedure and the moulding temperature as a function of time	65

4.1	An illustration of the derivative heat flow as a function of temperature of the baseline; the specimen of grade PC 2205; and the subtraction of the baseline from the specimen measurement	74
4.2	Example of the determination of T_g using the peak of derivative heat flow and the inflection step change of heat flow as a function of temperature	74
4.3	Relationship between glass transition temperatures determined from signal peak in derivation of heat flow as a function of $\frac{1}{M_n}$ for MWCNT-filled (3 wt%) and unfilled PC	76
4.4	Change in heat capacity, ΔC_p of MWCNT-filled (3 wt%) and unfilled PC as a function of the weight-average molar mass. Error bars represent two standard errors	77
4.5	A schematic illustration of the (a) parallel and the (b) series two-phase models to estimate thermal conductivity of PC-MWCNT 2205 (adapted from Kochetov (2012))	81
4.6	Typical TGA curves for a specimen of PC 2205 and PC-MWCNT 2205 heated at $10\text{ }^\circ\text{C min}^{-1}$ under nitrogen atmosphere	85
4.7	Typical TGA curves for a specimen of PC 2205 and PC-MWCNT 2205 heated at $10\text{ }^\circ\text{C min}^{-1}$ under air atmosphere	87
5.1	Amplitude sweeps of normalised storage modulus G' and loss modulus G'' measured at $2\pi\text{ rad s}^{-1}$ of (a) unfilled PC 2205 at temperatures 160 - 260 $^\circ\text{C}$ and of (b) PC-MWCNT 2205 (3 wt%) at temperatures 160 - 300 $^\circ\text{C}$. The vertical dashed line indicates the linear viscoelastic limit	95
5.2	Storage modulus, G' and loss modulus, G'' of PC-MWCNT 2205 annealed at 280 $^\circ\text{C}$ at a single frequency (1 Hz) and 0.5% strain	97
5.3	Storage modulus, G' against frequency of PC-MWCNT 2205 at different temperature step directions. Arrows indicate temperature direction, initially decreasing followed by an increase. Lines are guide to the eye following increasing and decreasing step	98
5.4	Storage modulus, G' against frequency of PC 2205, as received from the supplier, and of PC 2205 1-pass, material that had experienced identical melt mixing conditions as PC-MWCNT without the addition of the filler, for $T = 160 - 260\text{ }^\circ\text{C}$. Lines are guide to the eye	99
5.5	(a) The van Gorp-Palmen plot of phase angle against complex modulus over a temperature range of 160 - 260 $^\circ\text{C}$ for PC 2205 and of 160 - 300 $^\circ\text{C}$ for PC-MWCNT 2205 (3 wt%). (b) Same plot with the reduced complex modulus at $T_{\text{ref}} = 200\text{ }^\circ\text{C}$	101
5.6	Vertical shift factors at reference temperature $T_{\text{ref}} = 200\text{ }^\circ\text{C}$ determined for unfilled PC based on a density correction using Eqs. 5.1 and 5.2 (thick solid line), and for PC-MWCNT using Eqs. 5.1 and 3.5 in Chapter 3 (green dashed line)	102
5.7	Vertical shift factors obtained by manual shifting using the van Gorp-Palmen plots for all PC-MWCNT grades. The thin lines are guides to the eye	102
5.8	Shifted van Gorp-Palmen plot for PC-MWCNT 2205 (3 wt%) at a reference temperature of $T_{\text{ref}} = 200\text{ }^\circ\text{C}$ used to determine the vertical shift factor. The lines are guides to the eye	103
5.9	Illustration of the construction of the area (shaded) minimised to determine the optimum shift factor. Solid lines are polynomial functions. Dashed lines represent the upper and lower boundaries of the overlapping area	105

5.10	Shift factors determined using an automated technique at $T_{\text{ref}} = 200$ °C for unfilled PC. The dashed line represents the WLF fit as defined in Eq. 5.5 . . .	106
5.11	Shift factors determined using an automated technique at $T_{\text{ref}} = 200$ °C PC-MWCNT (3 wt%). The dashed line represents the WLF fit as defined in Eq. 5.5 for unfilled PC	106
5.12	Reduced frequency mastercurves of (a) storage modulus and (b) loss modulus of unfilled PC of varying molar mass ($M_w = 33600 - 50500$ g mol ⁻¹) at a strain amplitude of 0.5%	107
5.13	Reduced frequency mastercurves of (a) storage modulus and (b) loss modulus of PC-MWCNT (3 wt%) of varying molar mass ($M_w = 33600 - 50500$ g mol ⁻¹) at a strain amplitude of 0.5%	109
5.14	The polynomial fit of PC-MWCNT (red solid line) and unfilled PC (blue solid line) of grades (a) 2205 (circle), (b) 2405 (up triangle), (c) 2805 (down triangle) and (d) 3105 (square) employed in the two-phase model (Song and Zheng, 2010). Only unfilled PC data that followed the relationship $G' \propto \omega^2$, and the corresponding PC-MWCNT of the selected unfilled PC reduced frequency range were considered in the model. The cross-over frequency is used to determine the characteristic relaxation time	111
5.15	Ratios of storage modulus (solid line) and loss modulus (dashed line) of filled PC-MWCNT (3 wt%) to unfilled PC of matching matrix molar mass ($M_w = 33600 - 50500$ g mol ⁻¹) as a function of reduced frequency, determined at a strain amplitude of 0.5%	112
5.16	Characteristic relaxation times obtained from the cross-over frequency in unfilled PC (hollow symbols) and from the peak in $\tan \delta$ in the PC-MWCNT (3 wt%) (dotted, grey symbols), as a function of molar mass. Dashed lines (black: unfilled PC; green: filled PC) represent linear regressions through the data sets	113
5.17	A typical example of fitting a Weibull (4 parameter) peak fitting algorithm (solid line) to the $\tan \delta$ data. The data shown here is of PC-MWCNT 2205 .	114
5.18	Vertical shift factors obtained from isothermal frequency sweeps at strain amplitudes of 0.05%, 0.5%, 5%, and 50% at $T_{\text{ref}} = 200$ °C. Lines are a guide to the eye	115
5.19	Horizontal shift factors obtained from isothermal frequency sweeps at strain amplitudes of 0.05%, 0.5%, 5%, and 50% at $T_{\text{ref}} = 200$ °C. The dashed line is the WLF fit using unfilled PC parameters	115
5.20	Mastercurves for filled PC-MWCNT 2205 (3 wt%) (G' : large dotted grey circles; G'' : small dotted grey circles) for strain amplitudes of (a) 0.05%, (b) 0.5%, (c) 5% and (d) 50%, at $T_{\text{ref}} = 200$ °C. Corresponding measurements obtained from amplitude sweeps (G' : up triangles; G'' : down triangles) measured at 2π rad s ⁻¹ . Solid and dashed lines are a guide to the eye	117
6.1	Optical micrographs of PC-MWCNT 2205 sections of thickness $2 \mu\text{m}$, obtained with a tungsten carbide knife	127
6.2	Optical micrographs of PC-MWCNT 2205 sections of thickness (a) $2 \mu\text{m}$ and (b) $4 \mu\text{m}$, obtained with a glass knife	127

6.3	Optical micrographs showing the heat treatment of a 2 μm section of PC-MWCNT 2205 at 10x magnification. At 170 $^{\circ}\text{C}$, a weight of 5 g was placed on the section and the images were obtained at several intervals showing (a) the specimen just after application of the load ($t = 0$). The formation of striations appearing at (b) $t = 3$ minutes, and remaining after (c) $t = 6$ minutes and (d) $t = 10$ minutes	128
6.4	The background correction procedure applied on the (a) original image of PC-MWCNT (3 wt%) with thickness of 2 μm to obtain the (b) new filtered image with minimised illumination gradient. A feature based algorithm (Pegel et al., 2011) is applied to (b) to yield the (c) binarised image with artifacts still visible as indicated by the red <i>ellipses</i>	131
6.5	An illustration of the triangle algorithm, described in Section 6.2.1.6, to determine the threshold value for Fig.6.4(c)	132
6.6	Optical micrographs showing the polished surfaces of (a) compression moulded PC 2805, (b) compression moulded PC-MWCNT 2205, (c) and (d) injection moulded PC-MWCNT 2205 at 4x magnification; (d) exhibits the identical location as (c) but the focus was adjusted to emphasize the bright features	134
6.7	SEM micrographs of cryofractured PC-MWCNT 2205 at different magnifications showing the (a) fracture surface, (b) MWCNTs protruding from the cryofractured surface and platinum deposits, (c) and (d) MWCNT strands	135
6.8	Schematic side view of the ion beam and electron beam with respect to the PC-MWCNT specimen (adapted from Bushby et al. (2011))	137
6.9	(a) The site window with a layer of tungsten on the surface of PC-MWCNT 2205, with a landmark (X) to identify the specific site on the specimen. (b) SEM image of PC-MWCNT 2205 cross-section obtained with ion beam milling. (c) Backscattered electrons image of PC-MWCNT 2205 cross-section	138
7.1	Two-terminal method for volume resistivity measurement (adapted from Blythe (1984))	142
7.2	Four-terminal method for volume resistivity measurement (adapted from Blythe (1984))	143
7.3	Clover-leaf and square geometry specimen for van der Pauw resistivity measurement	144
7.4	Eight measurement positions for the van der Pauw method to determine volume resistivity (adapted from Keithley Instruments (2004))	144
7.5	Two-terminal fixture setup with specimen positioned for resistivity measurement	146
7.6	Specimen with practical contact locations A_p and B_p and the corresponding ideal contact locations A_i and B_i	146
7.7	A cross section of the terminal showing the electrode components and the contact interface with the specimen; and schematic of the current distribution from the contacts to the specimen. The transfer length, L_t , the length over which current transfers between the contact and the specimen. L_t was determined as 67.6 mm using the extrapolation method, presented in Section 7.5.1.4	147
7.8	The circuit diagram of two-terminal method for the in-house fixture for resistivity measurements. Symbols are defined in Table 7.1	148
7.9	A typical experiment configuration to determine electrical resistivity of the specimen using the two-terminal method	149
7.10	Side view of the two-terminal fixture. The inset shows the cross-sectional view of one entire terminal in the inset. Dimensions are in mm	150

7.11	Top view of the two-terminal fixture. Dimensions are in mm	151
7.12	Current flow as a function of time for voltage supply between 0.25 V and 1 V, applied to the fixture in decreasing order of 0.25 V steps, at different polarities	154
7.13	Electrometer internal ammeter resistance as a function of current flow. The solid line represents the third order polynomial function	157
7.14	Total terminal resistance of the circuit as a function of current flow. The solid line represents the second order polynomial function	158
7.15	The comparison between the known resistance load, R_{actual} and the calculated resistance load, R_{estimate} for voltages of 5 V and 10 V. R_{estimate} is determined from the measured resistance, using the fixture, and accounting for the meter and terminal resistances	158
7.16	(a) Extrapolation method with surface contacts used to determine contact resistivity between the terminal and the PC-MWCNT specimen. (b) Total resistance of the circuit as a function of contact spacing. The solid line represents the linear regression through data of increasing and decreasing order of contact spacing	160
7.17	Electrical volume resistivity of PC-MWCNT 2205 (3 wt%) compounded at temperatures between 230 °C and 290 °C, and formed to shape by compression moulding and injection moulding	165
8.1	The location of hardness measurement of a CM dog-bone specimen with an inset of an optical micrograph at 10x magnification in reflection mode, exhibiting an indentation for PC-MWCNT 2205 obtained with 5 kgf (49.03 N). The diagonal lengths, d_1 and d_2 are used to calculate Vickers hardness	175
8.2	Vickers hardness of compression moulded and injection moulded PC-MWCNTs 2205 compounded at temperatures between 230 °C and 290 °C, the error bars represent two standard errors. The dashed lines represents the Vickers hardness of compression moulded unfilled PC 2205	177
8.3	Young's moduli of compression moulded and injection moulded PC-MWCNTs 2205 compounded between 230 °C and 290 °C. The dashed lines represent the unfilled compression moulded PC 2205. The dashed-dot line represents the modified Halpin-Tsai equation for randomly oriented CNTs whereas the dashed-dot-dot line represents the modified Halpin-Tsai equation for highly oriented CNTs	180
8.4	Ultimate tensile strength of compression moulded and injection moulded PC-MWCNT 2205 compounded between 230 °C and 290 °C. The dashed lines represent the unfilled compression moulded PC 2205	182
8.5	Uniaxial melt drawn CM PC-MWCNT 2205 (from left to right) at 150 °C, 156 °C, 160 °C and 165 °C with a nominal strain rate of 0.02 s ⁻¹ and a $\lambda = 2$	184
8.6	Relationship between hardness as a function of electrical resistivity for compression moulded specimens with linear regression, giving correlation coefficient, $R = -0.40$	189
8.7	Relationship between Young's modulus as a function of hardness for injection moulded specimens with linear regression, giving correlation coefficient, $R = 0.52$	190

List of Tables

1.1	Examples of current commercial applications for polymer-carbon nanotube nanocomposites (Giant Manufacturing Ltd. (2013); Nanocyl S.A. (2013); TBA Electro Conductive Products Ltd. (2013); Yonex (2013))	2
2.1	Electrical properties of selected MWCNT-polymer nanocomposites	37
3.1	Melt flow rate, melt volume rate and melt density of PC matrix at 300 °C (Bayer MaterialScience AG, 2012)	60
3.2	Melt compounded materials of different PC grades	61
3.3	Molar mass averages obtained via GPC for the PC materials	66
3.4	Molar mass measurements of extracted PC 2205 (PC _{extc}) and virgin PC 2205	67
3.5	Measurement of filler loading content in PC-MWCNT 2205	68
3.6	Average density measurements of PC 2205 and PC-MWCNT 2205	69
4.1	Glass transition temperatures, T_g , determined from the peak of derivative heat flow with respect to temperature for all materials (\pm two standard errors)	75
4.2	Thermal effusivity, e , thermal conductivity, κ , thermal diffusivity, d , and heat capacity C_p of PC 2205 and PC-MWCNT 2205 (\pm two standard errors). Δ MWCNT is the difference obtained by subtracting PC from PC-MWCNT	80
4.3	Thermal analysis of unfilled and MWCNT-filled (3 wt%) PC under nitrogen atmosphere obtained at 10 °C min ⁻¹	86
4.4	Thermal analysis of unfilled and MWCNT-filled (3 wt%) PC under air atmosphere obtained at 10 °C min ⁻¹	87
5.1	Parameters obtained from Song and Zheng's two-phase model, with $n = 5$, applied to the data of all PC grades	110
7.1	Symbols and its definitions to describe the equivalent circuit of the two-terminal fixture	147
7.2	Contact resistance of compression moulded (CM) and injection moulded (IM) PC-MWCNT 2205 dog-bone specimens determined using Eq. 7.18 with the contact resistivity of bar geometry	161
7.3	Electrical resistivity of compression moulded PC-MWCNT (3 wt%)	168
7.4	Electrical resistivity of injection moulded PC-MWCNT (3 wt%) determined with two-terminal method	168
8.1	Typical shear rates for polymeric processes (Mezger, 2011)	173
8.2	Correlation coefficients of the relationship between the final properties (electrical resistivity, ρ , hardness, HV, Young's modulus, E and ultimate tensile strength, UTS) for compression moulding	188

8.3	Correlation coefficients of the relationship between the final properties (electrical resistivity, ρ , hardness, HV, Young's modulus, E and tensile strength, UTS) for injection moulding	190
A.1	Resistance measurements of five CM PC-MWCNT 2205 specimens compounded at 230 °C and the absolute residuals calculated from Eq. A.1	202

Abbreviations

AFM	Atomic force microscope
BE	Backscattered electrons
CB	Carbon black
CM	Compression moulding
CNF	Carbon nanofiber
CNT	Carbon nanotube
CVD	Chemical vapour deposition
DMA	Dynamic mechanical analyser
DSC	Differential scanning calorimetry
DWCNT	Double-wall carbon nanotube
EDP	Electrostatic discharge protection
EM	Extrapolation method
EMF	Electromagnetic fields
EMS	Electromagnetic shielding
FEG	Field emission gun
FIB	Focused ion beam
GN	Graphene nanoplatelet
GPC	Gel permeation chromatography
HDM	hexamethylenediamine
HDPE	High density polypropylene
HMW	High molar mass
HV	Hardness Vickers
IM	Injection moulding
LAOS	Long amplitude oscillation shear
LDH	Layered double hydroxides
LDPE	Low density polypropylene
LMW	Low molar mass
LVE	Linear viscoelastic
MFR	Melt flow rate
MMW	Medium molar mass

MVR	Melt volume rate
MWCNT	Multi-wall carbon nanotube
OM	Optical microscopy
OMMT	Organo-montmorillonite clay
PA	Polyamide
PA12	Polyamide-12
PA6	Polyamide-6
PA66	Polyamide-66
PBT	Polybutylene terephthalate
PC	Polycarbonate
PDI	Polydispersity index
PE	Polyethylene
PEO	Polyethylene oxide
PMMA	Polymethyl methacrylate
PP	Polypropylene
PP-g-MA	PP grafted maleic anhydride
PS	Polystyrene
Pt	Platinum
PTFE	Polytetrafluoroethylene
PVA	Polyvinyl alcohol
PVC	Polyvinyl chloride
PVK	Poly(9-vinyl carbazole)
ROM	Rule of mixtures
SAOS	Short amplitude oscillations shear
SEM	Scanning electron microscopy
SWCNT	Single-wall carbon nanotube
TEM	Transmission electron microscopy
TGA	Thermogravimetric analysis
THF	Tetrahydrofuran
TLM	Transfer length method
TTS	Time-temperature superposition
UTS	Ultimate tensile strength
UV	Ultraviolet
VDP	Van der Pauw
VGCF	Vapour grown carbon nanofibers
VGP	Van Gorp-Palmen
WLF	Williams-Landel-Ferry

Symbols

a_T	Horizontal shift factor
b_T	Vertical shift factor
d	Thermal diffusivity (Chapter 4)
d	Distance between electrical terminals (Chapter 7)
d	Diagonal lengths (Chapter 8)
d_{CNT}	CNT diameter (Chapter 8)
e	Thermal effusivity
f	Packing density
m	Mass loading content
m_c	Critical m (percolation threshold)
t	Time
t	Thickness (Chapter 7, 8)
A	Area
A_{af}	Area fraction of CNT agglomerates
A_{CNT}	Total agglomerate area
A_f	Strain amplification factor parameter
A_o	Total observed area
C_p	Specific heat capacity
D	Degree of dispersion
D_{OM}	Degree of dispersion (determined using optical microscopy)
D_p	Depth of penetration
E	Young's modulus
E_{PC}	Young's modulus of PC
E_{MWCNT}	Young's modulus of MWCNT
E	Electrical energy (Chapter 7)
F_i	Indentation force
G'	Storage modulus
G''	Loss modulus

I	Electrical current
I_{meas}	The measured electrical current
L	Length of electrical contacts
L_t	Transfer length of electrical contacts
M	Mass of nanocomposite
M_{CNT}	Mass of CNT
M_n	Number average molecular mass
M_{PC}	Mass of PC
M_w	Weight average molecular mass
P	Pressure
P	Electrical power (Chapter 7)
P_{back}	Back pressure
P_{hold}	Hold pressure
Q	Thermal energy
R	Electrical resistance
S	Standard deviation
S_p	Pooled standard deviation
S^2	Variance
T	Temperature
T_g	Glass transition temperature
T_{max}	Temperature at maximum weight loss
$T_{\text{max}2}$	T_{max} at second step of decomposition
T_{melt}	Melt temperature
T_{mould}	Mould temperature
T_{onset}	Onset of degradation temperature
T_{ref}	Reference temperature
$T_{5\%}$	Temperature at 5% weight loss
$T_{10\%}$	Temperature at 10% weight loss
V	Electrical voltage (Chapter 7)
V	Velocity
V_{CNT}	Volume fraction of CNT
V_{inj}	Injection velocity
V_{meas}	The measured electrical voltage
V_{PC}	Volume fraction of PC
V_s	Voltage source
V_{sc}	Screw speed
W	Weight
\bar{X}	Mean

α	Frequency exponent factor
β_c	Critical exponent
δ	Phase angle
η	Steady shear viscosity
η (Halpin-Tsai model)	Filler geometry parameter
η_L	η for the longitudinal direction
η_T	η parameter for the transverse direction
η_o	Orientation factor
η_1	Length efficiency factor
η^*	Complex viscosity
$\dot{\gamma}$	Shear rate
γ_o	Strain amplitude (oscillatory shear)
κ	Thermal conductivity
κ_{MWCNT}	Thermal conductivity of MWCNT
κ_{PC}	Thermal conductivity of PC
$\kappa_{\text{PC-MWCNT}}$	Thermal conductivity of PC-MWCNT
l_p	Parallel length
l_{sp}	Static bending persistent length
λ	Stretch ratio
ω	Angular frequency
ρ	Bulk electrical resistivity
ρ	Density (Chapter 3)
ρ_{MWCNT}	Electrical resistivity of MWCNT
$\rho_{\text{PC-MWCNT}}$	Electrical resistivity of PC-MWCNT
σ	Electrical conductivity
τ	Characteristic relaxation time of PC
τ'	Characteristic relaxation time of PC-MWCNT
τ_o	Stress amplitude (oscillatory shear)
ζ	Filler geometry parameter (Chapter 8)

To my family

Chapter 1

Introduction

1.1 Background

In recent years in the field of material science, carbon nanotube (CNT) composites have emerged from the development of methods to control and characterise structures at the nanoscale. This process began in earnest in 1991, when Iijima used arc discharge production and atomic scale research to investigate fullerenes, eventually leading to the discovery of CNTs with wall thickness as small as two atomic layers (Iijima, 1991). These nanoscale structures offered incredible promise, largely due to their outstanding potential for increased mechanical stiffness, high electrical conductivity and high thermal conductivity (Dresselhaus et al., 2004).

The addition of particles or fibers to a polymer matrix forms a composite. In this work, the term fillers refers to the high value particles that are incorporated into the matrix. The addition aims to improve the properties of the matrix by harnessing the properties of the fillers, such as electrical conductivity and mechanical strength. In the past, the role of fillers was fulfilled by micron-sized and larger particles or fibers, such as carbon fiber, glass fiber, metallic particles, and carbon black. In contrast to nanoscale fillers such as CNTs, a high amount of traditional filler content is required to improve polymer properties by a sufficient amount, leading to loss of desirable polymeric attributes, for instance, ease of processability.

Therefore, polymer nanocomposites are a potential substitute for traditional filled composites. A nanocomposite is defined as a material in which at least one of its filler constituents is of the order of a few nanometers (Gupta et al., 2010). CNT diameters typically range

from 5 to 20 nm (depending on CNT type or synthesis), while CNT lengths may reach millimeters. CNTs produce substantial improvements of the nanocomposite properties with relatively limited filler content, owing to the large surface area available for matrix adhesion, and interactions between the matrix and filler. This provides an opportunity to avoid compromising the desirable aspects of the matrix.

1.1.1 Applications of CNT nanocomposites

The inclusion of CNTs into polymers has the potential to extend the applications of polymer materials. The antistatic properties of CNT nanocomposites make them ideal for electromagnetic shielding (EMS) and for electrostatic discharge protection (EDP) in packaging and manufacturing sensitive electronic devices. The addition of CNTs also increases the mechanical stiffness of the nanocomposite. Current applications of nanocomposites includes automotive, electronics and sporting goods, as summarised in Table 1.1.

TABLE 1.1: Examples of current commercial applications for polymer-carbon nanotube nanocomposites (Giant Manufacturing Ltd. (2013); Nanocyl S.A. (2013); TBA Electro Conductive Products Ltd. (2013); Yonex (2013))

Polymer matrix	Nanofiller	Applications	Manufacturers
Resin	CNTs and graphite	Badminton racquet	Yonex Co. Ltd.
Resin	CNTs	Bicycle frames	Giant Manufacturing Ltd.
Various	MWCNT	EDP (electronics)	Nanocyl S.A.
Polypropylene and polyaniline	CNTs	EMS (automotive)	TBA Electro Conductive Products Ltd.
Polycarbonate and polybutylene terephthalate	CNTs	EMS (communications equipment)	TBA Electro Conductive Products Ltd.
Polycarbonate	CNTs	Grounding plug earth pin	TBA Electro Conductive Products Ltd.

Advances in processing and manufacturing have indicated future potential for applications in transparent conductive films, in field emission displays, in structural components in aircraft and land vehicles, in flexible electronics, and in bio-sensors and drug delivery systems (Endo et al., 2008). Further progress in extending the functionality of nanocomposites is expected to increase with the manipulation and control of the composite structure at the nanolevel scale (Paul and Robeson, 2008). Morphology control involves dispersion and alignment of

CNTs, and is crucial in providing the step change in the properties of nanocomposites relative to the base matrix.

1.1.2 Processing of CNT nanocomposites

Currently, the most practical method to incorporate CNTs into a polymer matrix is melt compounding. This method is well developed and widely used for processing polymers. Fig. 1.1 illustrates a typical process of obtaining a nanocomposite product. An extruder compounds the matrix and CNTs, producing nanocomposite pellets that are then moulded into the desired shapes using other secondary processing methods such as injection or compression moulding. Extrusion and injection moulding are processes that are economic, capable of continuous production, has fast processing times and has versatile processing parameters. The ability to produce CNT nanocomposites using established processes is a requirement step for acceptance by the polymer industry.

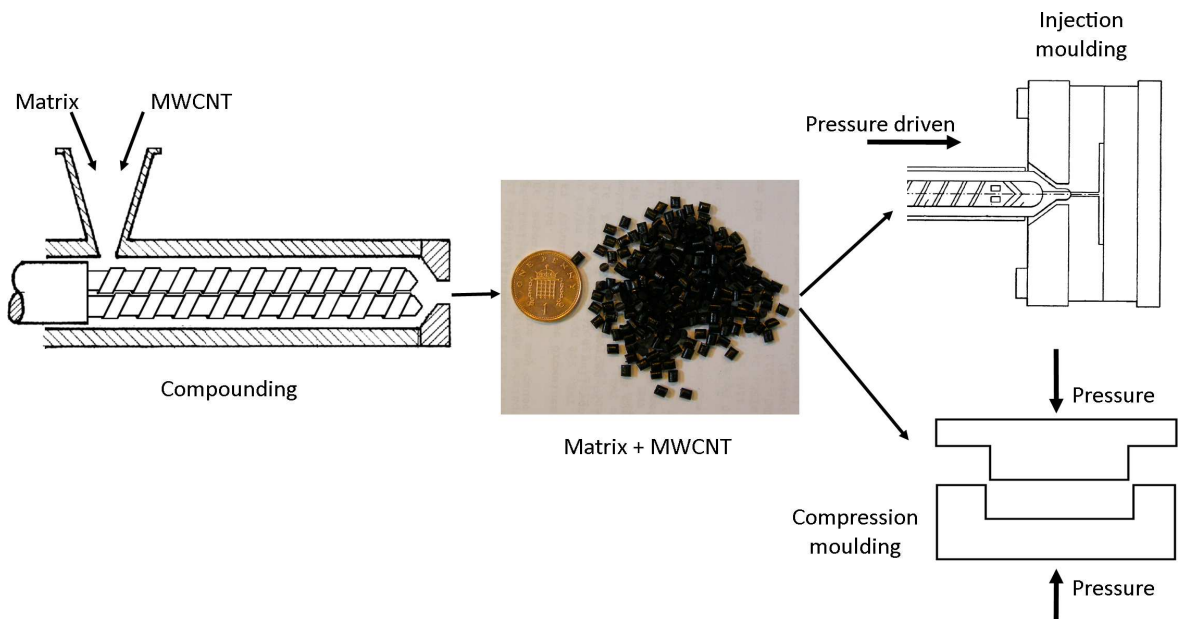


FIGURE 1.1: Illustration of manufacturing a final product made from CNT nanocomposite. An extruder compounds the raw materials for the polymer nanocomposite that is pelletised. These pellets are then re-melted and formed to shape using secondary processes such as injection moulding and compression moulding

The end properties of nanocomposites are ultimately dictated by the processing rate. The scientific literature provides an insight and appreciation into the vast number of experimental variables that can influence properties of nanocomposite systems. These variables range from processing parameters and polymer type to CNT characteristics and synthesis methods.

Many studies have observed that dispersion of CNTs is challenging, particularly in melt processes due to the van der Waals forces between the nanotubes and their high surface to volume ratio. However, CNT agglomeration is not necessarily undesirable. Although a well dispersed CNT system is ideal for mechanical stiffness, electrical conductivity reduces with increased dispersion due to a decrease in contact between the nanotubes.

Polycarbonate (PC) was selected as the base matrix for the nanocomposites in this study for its unique properties that distinguishes it from other thermoplastics. PC has high impact strength coupled with high thermal resistance, and is easy to compound with additives such as reinforcement fillers (DeRudder, 2000). There has been much focus on laboratory compounded PC-CNT systems that has provided insights into the influence of melt processing on these materials. In an effort to commercialise such materials, there is a need to understand the effects of industrial melt processing on these nanocomposites' behaviour in order to determine its applications.

Much of the work to date on melt processing of PC-CNT nanocomposites has been performed at laboratory scale. Although it provides insights into the influence of the processing parameters, it cannot capture the effects of complex flows that occur in industrial compounders and moulding machines. The raw materials and the melt processes used to produce PC-MWCNT in this work are of a commercial nature, rendering this study of particular industrial value for PC-MWCNT applications.

Currently, there is a lack of systematic assessment on the influence of matrix morphology on CNT nanocomposite behaviour. There is also a need for predictive models to consider the effects of processing conditions on the nanocomposite properties. A unified and coherent view on processing such materials has not yet been achieved.

1.1.3 Commercial outlook

Efforts to exploit the outstanding properties of carbon nanotubes have been of significant interest in research and industry alike. Contributing to this factor is the expansion of CNT manufacturers as demand for CNTs is rising from various markets. Most of the commercially available CNTs are produced via catalytic chemical vapour deposition process (CVD). Although the cost of production has been high relative to traditional fillers in the past, the increase in CNT production volume is reducing there costs. In 2009, CNano Technology

Ltd. achieved the capability to produce 500 tonnes of multi-wall CNTs (MWCNT) annually, while Arkema Inc. developed an industrial pilot plant to produce 400 tonnes per annum in 2011 (Bradley, 2009). Such commitment from manufacturers provides the platform for commercial growth of CNT nanocomposites.

1.2 Aims and objectives

This study has two fundamental aims (1) to understand the role of the matrix in the nanocomposite melt and (2) to comprehend the role of the primary and secondary processing conditions on the solid state properties of CNT polymer nanocomposite. The experimental evidence of this work is intended to facilitate the development of theoretical and numerical tools for the predictions of processing and properties of PC-MWCNT nanocomposites, and to aid with application-specific design. This study focuses on PC filled with a constant MWCNT loading content of 3% by weight fraction. The nanocomposites were compounded by industrial extrusion.

There are two objectives in this thesis: (1) to investigate the behaviour of PC-MWCNT in the solid and melt states, and (2) to determine the influence of the compounding temperatures and the forming process on the electrical and mechanical properties of these materials.

It is crucial to investigate the breath of the states of these materials because the melt state is concerned with the formation of the CNT network, that in turn determines the solid state behaviour of the nanocomposite. Since the CNT network affects the thermal, rheological, electrical and mechanical properties of PC, experimental studies were performed to characterise these properties, with emphasis on the role of the matrix. The nanocomposites response is compared to the corresponding virgin materials and to predictive models, where possible, to shed light on the structure-property relationships of the PC-MWCNT systems.

In order to develop an understanding of CNT filled systems in the melt state, the base matrix molar mass was varied to elucidate the role of the CNTs and of the matrix on the different aspects of the materials' rheological response such as relaxation processes, and the effects of strain and temperature history. Furthermore, it is of commercial interest to understand the effects of melt processing on the behaviour of PC-MWCNT as nanocomposite suppliers typically deliver the compounded feedstock to manufacturers, who subsequently re-melt the

pellets to form their products. Currently the effects of melt processing on PC-MWCNT is not fully understood.

1.3 Outline

This thesis contains nine chapters and an appendix. The second chapter presents a review of the literature relating to the thesis. Previous experimental characterisation of thermal, mechanical, electrical, and rheological properties of PC-MWCNT and of similar systems are reported, with attention to processing conditions. An overview of different processing methods for CNT nanocomposites is also provided, with an emphasis on melt processes like those used in this work.

Chapter 3 reports on the materials and the specimen preparation techniques for this work. Molar mass distributions of PC, before and after processing are reported. A method of separating the CNTs from the nanocomposite is presented, and the molar mass of the extracted PC is compared to the unfilled of the similar grade to identify evidence for matrix degradation. The density of specimens and the weight of CNTs extracted from the nanocomposite are used as a verification of the filler volume fraction.

Chapter 4 is concerned with the effects of the addition of CNTs to the matrix on thermal properties. The glass transition temperatures of the filled and unfilled PC are compared and discussed. The thermal transport properties are measured to highlight the role of CNT in thermal applications and in processing. Thermal stability and degradation due to the presence of CNTs in air and inert atmospheres are discussed.

Chapter 5 reports a rheological investigation into PC-MWCNT in the melt state. First, the experimental conditions for short amplitude oscillations shear (SAOS) and long amplitude oscillation shear (LAOS) are detailed. A new method for applying time-temperature superposition on the experimental data is described. The resulting master curves are then analysed, and the relaxation mechanisms associated with the interactions within the nanocomposite system are discussed. A simple model to account for the presence of the MWCNT network in PC matrix is also presented.

Chapter 6 describes various microscopy techniques for the characterisation of the morphology of PC-MWCNT nanocomposite, focusing on optical microscopy and scanning electron

microscopy. The challenges of obtaining suitable microtome sections for quantitative evaluation of the CNT dispersion in the matrix are discussed. Micrographs of polished specimens are presented in an effort to identify the presence of voids in the specimens.

Chapter 7 focuses on an investigation into electrical resistivity of PC-MWCNT, using a resistivity fixture especially developed for this purpose. The development and validation of the fixture for electrical resistivity measurement method is discussed. The test method is then used to investigate the effects of processing history on the electrical resistivity of percolated PC-MWCNT systems.

Chapter 8 presents the effect of compounding temperature and secondary processing, on hardness and tensile mechanical properties of the materials. Estimation of the Young's modulus of percolated PC-MWCNT, via a micromechanical model, is compared to the experimental data, to indicate the effect of interfacial interaction and to estimate CNT length after processing. These findings are combined with those of Chapter 7 to seek correlations between the properties.

Chapter 9 presents the conclusions of this work and proposes recommendations for future work.

Appendix A provides the statistical tests that were used to determine the specific distribution and the outliers in electrical resistivity measurements.

Chapter 2

Literature review

This chapter presents a review of the literature on thermoplastic nanocomposites that is relevant to this thesis. Section 2.1 outlines the limited literature specific to the materials investigated in this work. Melt processing of thermoplastics filled with carbon nanotubes (CNTs) is reviewed in Section 2.2, with particular attention devoted to the influence of processing parameters, and to how the different processing methods affect the morphology of CNTs in matrix. Section 2.3 is concerned with the morphological study of CNT nanocomposites using optical and scanning electron microscopy. Sections 2.4 - 2.7 reviews the behaviour of the constituent materials, comparisons to nanocomposite highlight the change in material response arising from the presence of nanofillers. Responses of certain thermoplastic and CNT based nanocomposite systems characterised in the solid and melt states are reported, with considerations on processing conditions. This review of several authors' work on nanocomposite systems is intended to facilitate the understanding of the mechanisms of CNT network formation in the melt and of how network structure and interactions dictate thermal stability, mechanical reinforcement, electrical conductivity and rheological response.

2.1 Polycarbonate and carbon nanotubes: an introduction

Both the intrinsic properties of the nanocomposite constituent materials and the nanocomposite production processes, consisting of mixing and forming procedures, are crucial to the improvements in the matrix properties. Before reviewing works that have probed into the

material and the processing related factors that influence nanocomposite behaviour, a brief introduction to the constituent materials used in this work is given in this section.

2.1.1 Polycarbonate

PC is a linear amorphous thermoplastic polymer made from aromatic polyesters and phenols such as 2, 2-bis (4-hydroxyphenyl) propane, known as bisphenol A. The chemical structure is shown in Fig. 2.1.

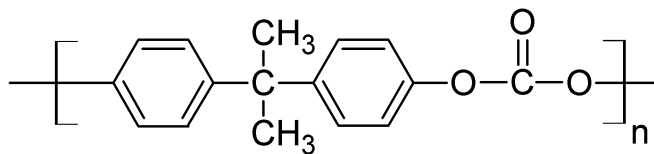


FIGURE 2.1: Chemical structure of polycarbonate (adapted from King (2000))

Generally, PC requires additives or coatings to improve weatherability, for ultraviolet (UV) stabilization, and to increase flame and chemical resistance (DeRudder, 2000). The properties such as mechanical and electrical can be influenced by processing conditions as well as by the introduction of fillers, to produce products that can be employed as commodity plastics and engineering plastics (McCrum et al., 1997).

Commercial applications of PC and its blends are found in a broad range of markets, such as automotive (headlamps, interior parts), medical apparatus (luer fittings, syringes), sports (impact resistant helmets), safety equipment (face shields, masks) and aircraft components (windows, wall panels) (Baccaro and Keenan, 2000; DeRudder, 2000). The addition of CNTs to PC is intended to extend the application of the thermoplastic into further markets, such as electronics (packaging and components), particularly with the current development of miniaturized electronic devices.

2.1.2 Carbon nanotubes

Carbon nanotubes can be thought of as sheets of graphene rolled into cylinders, and consist of hexagonal lattices of covalent carbon-carbon bonds. This rolling can be achieved at different angles, providing the symmetry (orientation of lattice structure) which determines the properties of the individual CNTs (Ajayan, 1999). There are three types of CNTs: (1) single-wall

(2) double-wall and (3) multi-wall. Fig. 2.2 presents scanning electron microscopy (SEM) images of multi-wall carbon nanotubes (MWCNTs) as used in this work. MWCNTs consists of several concentric cylinders with a small interlayer spacing, wrapped around a common hollow central tube. The spacing between each cylinder is approximately 0.34 nm, which is similar to the interlayer distance in graphite (Ajayan, 1999). The typical diameter of MWCNTs ranges between 5 and 50 nm.

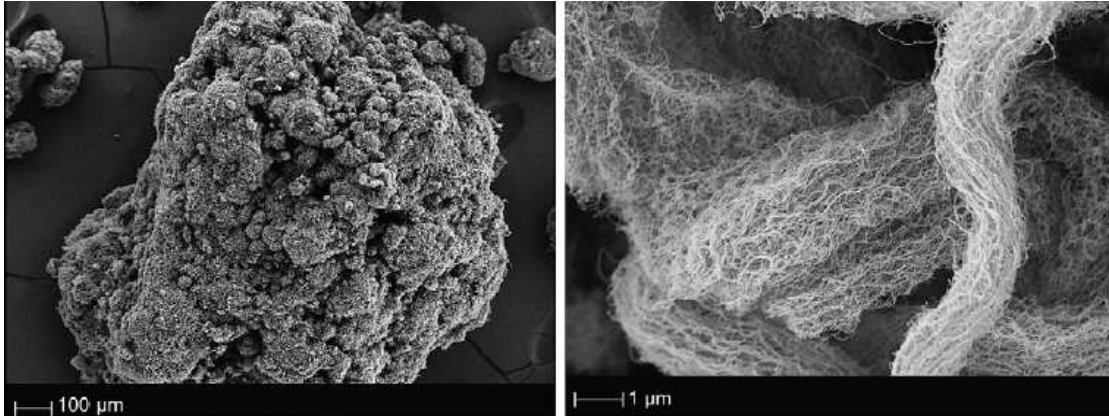


FIGURE 2.2: SEM micrographs of agglomerated Nanocyl NC7000 multi-wall carbon nanotubes as supplied by the manufacturer and used in this study, at different magnifications (Krause et al., 2010)

CNT properties are strongly influenced by fabrication methods. The synthesis methods and specific growth conditions determine both the quality and the quantity of CNTs produced. There is a balance that needs to be struck between the economics, resulting properties and production efficiency of synthesizing CNTs, depending on the application. The more commonly used synthesis methods to produce CNTs are arc discharge, laser ablation and various catalytical CVD techniques.

CVD involves decomposition of a hydrocarbon gas mixture with metallic nanoparticles acting as catalysts, and is the favoured option for the scale-up synthesis of larger quantities of CNTs (Colomer et al., 2000). The drawbacks of this method are: (1) the long processing times to produce nanotubes, attributed to the lower operating process temperatures; and (2) the presence of impurities such as catalyst residue that can be found in the tubes. More recently, efforts have been focused on improving the CVD method, for instance, by purification of CNTs to remove impurities after synthesis (Meyer-Plath et al., 2012). The reader is referred to Ebbesen and Ajayan (1992), Colomer et al. (2000), and Jiang et al. (2005) for further details on the other synthesis methods.

For commercial purposes, MWCNTs are the material of choice owing to their capability for large scale production leading to relatively low cost. Compared with other CNT varieties, MWCNTs have inferior and unpredictable properties because of defects in MWCNT walls and variations in structure.

2.2 Processing of CNT nanocomposites

There is a wide range of processing techniques to mix and form polymeric materials, with the dominant processes being extrusion and injection moulding (McCrum et al., 1997). It is thus desirable to retain the ease, flexibility and speed of these processes to form CNT nanocomposites. Ultimately, it is processing that will determine the characteristics of the final product. Therefore, processing parameters are important to filler dispersion, filler orientation, and filler-matrix interfacial interactions (Harris, 2004). Much attention has been directed at controlling parameters to manipulate CNTs structure and morphology in order to improve nanocomposite performance.

Realising the full potential of CNTs in nanocomposites has been a challenge, particularly due to the difficulties in achieving appropriate levels of filler dispersion. Other challenges consist of controlling CNT orientation, and achieving good interfacial bonding of CNTs with the matrix. These difficulties arise because CNTs are nanoparticles with very high surface to volume ratio. The van der Waals forces between the CNTs make it difficult to separate them and achieve homogenous dispersion within a polymer matrix. Thus, CNTs have a tendency to entangle and agglomerate. These agglomerates act as stress concentrators and reduces the mechanical properties of the nanocomposites.

Many different processing methods such as solution mixing, melt compounding, chemical functionalisation and in-situ polymerisation have been employed in research in order to achieve specific and reproducible dispersion, but there is *no single* processing technique recommended for all types of polymers and nanofillers. This is attributed to the interdependence of many factors, such as polymer chemistry, and durability of nanofillers in the processing environment (which in turn affect polymer-filler interactions). Additionally, the complexity involved in bridging the length scales between atomistic simulations and continuum mechanics means that few modelling techniques have thus far been able to support

nanocomposite processing. Currently, melt mixing has been the most efficient method to produce nanocomposites commercially (Gupta et al., 2010) and will be discussed in the following sub-section. There is a large volume of literature dedicated to other methods of processing nanocomposite, and the reader is referred to Spitalsky et al. (2010) for a concise review.

2.2.1 Melt compounding

Melt compounding or melt mixing is an industrial technique that relies on the use of traditional polymer processing equipment such as an extruder to generate high shear to mix and disperse CNTs in a polymer matrix. It has been widely used in processing thermoplastics.

The most common equipment employed for mixing nanoparticles with polymer is a twin screw extruder. Twin screw extruders have two screws that rotate beside each other at constant speed to perform a range of application such as mixing, blending and compounding, depending on the screw configuration. There are two configurations: co-rotating or counter-rotating screws, and the latter can be intermeshing or non-intermeshing, determined by the shearing intensity required. Krause et al. (2011) found melt mixing results in CNT shortening that reduces the surface to volume ratio of the CNTs, and hence, decreases the potential mechanical and electrical properties of the nanocomposite.

Rios et al. (2011) reported that the addition of MWCNTs loadings of up to 5 wt% into six different thermoplastic matrices PC, high-density polyethylene (HDPE), polyamide-6 (PA6), polyamide-66 (PA66) and polybutylene terephthalate (PBT) did not affect melt-compounding. More encouragingly, the presence of MWCNTs (<5 wt%), in a PC matrix were found to *improve* processability of PC due to shear thinning of the matrix under industrial processing conditions (Lew et al., 2011).

2.2.1.1 CNT dispersion mechanisms

The melt mixing process to disperse CNTs in a polymer matrix consists of several stages that occur alongside one another; the polymer melt initially wets the filler surface, then infiltrates the filler agglomerates (Kasaliwal et al., 2010). The shear stress generated during the mixing process disperses the filler through two mechanisms identified as (1) rupture and (2) erosion that decreases the size of the primary agglomerates to smaller MWCNT aggregates (Kasaliwal et al., 2010). Primary agglomerates represent the initial agglomerates

prior to addition into the melt. This process is similar to that seen in carbon black (CB)-filled materials. The smaller agglomerates then repeatedly experience the earlier process of wetting and infiltration as new CNT surfaces are exposed to the polymer melt. The difference between the two mechanisms is that rupturing of agglomerates is a rapid bulk phenomenon, whilst erosion is a surface phenomena that wears away the primary agglomerates over the mixing period, giving rise to smaller CNT agglomerates or individual CNTs (Kasaliwal et al., 2010).

Pegel et al. (2008) observed through sedimentation experiments that CNT dispersion and distribution is strongly dependent on the initial dispersion levels of raw MWCNTs. The strength of the primary agglomerates was suggested to come from physical entanglement and van der Waals forces between the CNTs, both dependent on the characteristics of the CNTs, for example, defects and purity levels.

2.2.1.2 Small batch mixing

In the laboratory, small batch mixing is commonly employed as a first approach to compare the different mixing parameters on the dispersion of CNTs in matrices, particularly beneficial when only small amounts of material are available (Alig et al., 2012). Although small batch mixing is not a representation of industrial conditions, it is a simpler method to investigate melt mixing with more precise control of variables such as temperature and torque (Alig et al., 2012).

Pegel et al. (2008) and Kasaliwal et al. (2009) performed studies on the influence of small batch mixing conditions on CNT dispersion and distribution in PC. They evaluated CNT dispersion via transmission electron microscopy (TEM) and electrical measurements. Pegel et al. (2008) probed into the formation of secondary agglomerates (i.e agglomeration after dispersion efforts of the primary agglomerates during melt mixing) and found that increasing the screw speed (V_{sc}) decreased agglomerate size, but extending mixing periods had no effect on dispersion of secondary agglomerates. They explained their finding through simultaneous formation and destruction of CNT agglomerates whereby shear could facilitate the CNT motion, or migration, between agglomerates but also break up agglomerates at increased shear rates. They also found that lower temperature improves CNT dispersion due to higher melt viscosity. This implies that rupture of agglomerates is primarily controlled by the matrix viscosity.

Whilst Pegel et al. (2008) observed clusters of agglomerates to increase electrical conductivity, Kasaliwal and co-workers (2009) found similar electrical resistivity for different CNT dispersion states, with a certain level of CNT dispersion being favourable to yield low resistivity. They also found a balance of good dispersion and low resistivity can be achieved by mixing at high speed, regardless of the melt temperature. This indicated that the formation of a conductive CNT network and the CNT agglomerate dispersion mechanism are different processes. In order to reduce damage of CNTs due to high shear stresses, they suggested mixing at high temperature and high mixing speed; which is postulated to form network structures of dispersed CNTs or nanoscale secondary agglomeration.

2.2.2 Forming processes in the melt state

2.2.2.1 Injection moulding

In industry, a common method to produce polymer articles is injection moulding (IM). This manufacturing process transfers a melt using pressure driven flow into a forming unit (i.e. a mould), where the melt cools rapidly and solidifies into the required shape.

Several studies have been performed in order to understand the effects of IM parameters such as injection velocity (V_{inj}) and mould temperature (T_{mould}), on the properties of nanocomposites (Lew et al., 2011; Mahmoodi et al., 2012; Rios et al., 2011; Villmow et al., 2008a). These investigations use a combination of investigative techniques such as electrical resistivity and microscopy to associate processing parameters with the state of CNT dispersion. Typical electrical properties measured are volume and surface resistivity. When the addition of filler to the matrix reaches a certain loading content, a continuous conductive path is formed resulting in an abrupt change in the material behaviour. This loading content is identified as the percolation threshold.

Villmow et al. (2008a) and Mahmoodi et al. (2012) performed a two-level and four factorial design study on the influence of IM parameters on CNT dispersion and alignment (or orientation) by measuring the electrical properties of PC-MWCNT and polystyrene (PS)-MWCNT respectively. Villmow et al. (2008a) identified four parameters that significantly influence of polymer nanocomposite behaviour due its effect on CNT dispersion: T_{mould} , V_{inj} , holding pressure (P_{hold}), and melt temperature (T_{melt}). They reported that the through-plane volume and surface resistivity of the IM nanocomposites were strongly dependent on V_{inj}

and T_{melt} , but only weakly dependent on P_{hold} and T_{mould} . The strong dependence of T_{melt} on volume resistivity was also reported by Rios et al. (2011) for PC-MWCNT and PBT-MWCNT systems. Although Mahmoodi et al. (2012) observed similar findings to both Villmow et al. (2008a) and Rios et al. (2011) for micro-injection moulded specimens, they observed the additional effect of holding pressure on the in-plane volume resistivity, depending on mould design. In summary, all three studies attributed lower electrical resistivity to the *decrease* in CNT alignment which promoted the build-up of a CNT network structure. Lellinger et al. (2008) suggested that V_{inj} facilitates the break-up of the CNT network in the polymer matrix whereas high temperatures promote the build-up of the CNT network structure. This supports the findings of increased electrical conductivity with low V_{inj} and high T_{melt} (Lellinger et al., 2008; Lew et al., 2011; Mahmoodi et al., 2012; Villmow et al., 2008a).

Lew et al. (2011) extended Villmow's work by including three more parameters: back pressure (P_{back}), hold time, and plasticising speed. In Lew's work, T_{melt} was identified as injection temperature, T_{inj} . They measured the volume and surface resistivity using in-plane measurements of a PC-MWCNT bar. The two most significant parameters that affected volume resistivity were reported to be T_{inj} and P_{back} whereas surface resistivity was influenced by V_{inj} and T_{inj} . The observation suggests that T_{inj} is crucial to both volume and surface resistivities. Lew et al. (2011) postulated that this is because increasing T_{inj} reduces the matrix viscosity which decreases CNT orientation, and in turn, enhances CNT-CNT interactions. Furthermore, the higher T_{inj} promotes polymer relaxation leading to reformation of CNT network structure (Lew et al., 2011). Volume resistivity was inversely related to V_{inj} whereas surface resistivity increased with V_{inj} , up to a plateau. The behaviour observed was attributed to the migration of CNTs towards the core of the sample and the alignment of CNTs on the sample surface. Lew et al. (2011) attributed the contradictory findings of surface resistivity as a function of V_{inj} to the difference in electrical measurement methods used by Villmow et al. (2008a). Factorial design studies of the references above have limitations due to (1) the assumption that there is a linear relationship between the variable and the electrical measurements and (2) the limited range for each variable. In the studies of Villmow, Lellinger, and Mahmoodi, they overlooked other IM parameters such as P_{back} , which was identified by Lew's group to have significant effect on electrical properties. At constant screw speed, P_{back} affects screw torque, hence, work done on the melt and consequently T_{melt} (McCrum et al., 1997).

Villmow et al. (2008a) performed resistivity measurements at nine positions on a single surface of an IM PC-MWCNT plate, using a custom plate rig fitted with ring electrodes, to evaluate the effect of IM on electrical properties of the material. They found that volume and surface resistivity along the plate specimen (in the injection flow direction) changed by up to 5 orders of magnitude between the gate and the opposite end of the specimen. For both surface and volume resistivity, measurements closest to the gate were the lowest, and resistivity increased with the distance from the gate. Lower values were recorded at the core of the specimen than of the sides. The trend of resistivity values followed a semicircular shape associated with injection flow lines. They attributed the variation of resistivity to the changes in CNT network formation during injection.

Figs. 2.3(a) and (b) reproduce the TEM micrographs obtained by Villmow et al. (2008a) for increasing depths towards the core of specimens processed at melt temperatures of 280 °C and 320 °C respectively. Significant orientation of CNTs in the flow direction are visible from the specimen surface to a depth of 10 μm towards the core of the specimen of 2 mm thickness. Lew et al. (2011) reported increases of surface resistivity as V_{inj} increased. In both studies, the skin of the specimen was insulating not because of migration of CNTs but due to CNT orientation that led a reduction in CNT-CNT interactions. Villmow et al. (2008a) investigated further by slicing specimens at distances of 17 - 23 μm from the surface towards the core of the specimen to reveal that the CNTs were less oriented and network structure was more established. Hence, the IM PC-MWCNT had a skin-core structure with orientation of CNTs decreasing towards to core region. The high temperatures, thus lower melt viscosity and greater CNT mobility promoted the formation of such a structure.

Other factors were found to affect the behaviour of nanocomposites but have received less thorough attention by researchers. Abbasi et al. (2009) found that sample geometry played a role as disc-shaped micro-injected samples were more conductive than dog-bone shaped samples. This was attributed to the more limited orientation of CNTs due to the radial flow which reduced shear rate and CNT alignment. Mahmoodi et al. (2012) reported an enhancement in electrical conductivity when using a fan gate compared to an edge gate for mould cavities with identical runners and filling period.

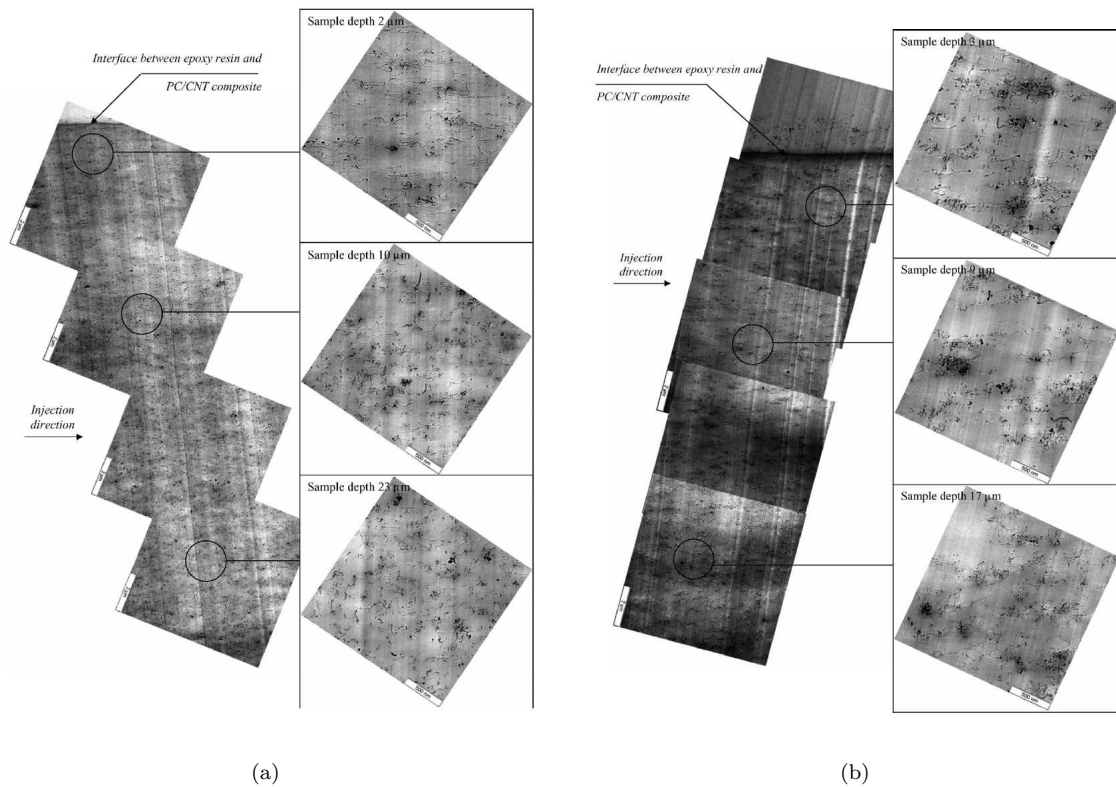


FIGURE 2.3: TEM micrographs of PC-MWCNT (2 wt%) injection moulded at (a) $V_{inj} = 150 \text{ mm s}^{-1}$ and $T_{melt} = 280 \text{ }^\circ\text{C}$, and at (b) $V_{inj} = 10 \text{ mm s}^{-1}$ and $T_{melt} = 320 \text{ }^\circ\text{C}$ (adapted from Villmow et al. (2008a))

2.2.2.2 Compression moulding

Compression moulding is a method employed to form products by filling polymer melt into a mould that consists of a matched pair of male and female dies. The advantages are short distance flows, no gate formation (weak points in moulding), low running cost and no sprue or runner required, whereas the disadvantage is the long cooling period that slows production (McCrum et al., 1997).

Compression moulding is used to obtain specimens with relatively random CNT orientation. Recently, Abbasi et al. (2009) performed morphology studies on compression moulded PC-MWCNT (5 wt%). A qualitative investigation into SEM images from compression moulded specimens verified random CNT orientation. This is expected, as compression moulding provides low shear rates and long relaxation times (Tiusanen et al., 2012). The cooling rate in compression moulding has been shown to affect surface resistivity. Lim et al. (2010) postulated that an increase in volume shrinkage caused a decrease in the spacing between CNTs during slow cooling, leading to lower resistivity.

Kasaliwal et al. (2009) investigated the effects of pressing temperature, pressing speed and pressing (holding) time of MWCNT filled PC at 1 wt% (near the percolation threshold) and 2 wt% on volume resistivity. Similar to melt mixing, significant effects were observed near the percolation threshold. The volume resistivity was not significantly affected by pressing speed regardless of the filler content loadings. The electrical measurements were dependent on the melt viscosity (temperature dependent) and the time for MWCNT diffusion or rearrangement in the melt. Similar findings were reported by Pegel et al. (2008) for PC-MWCNT (0.875 wt%). The decrease in resistivity with increasing moulding temperature was attributed to the rearrangement of CNTs at the nanoscale level. Optical light micrographs also showed similar dispersion levels (Kasaliwal et al., 2009).

Abbasi et al. (2009) conducted a comparative study between compression, micro-injection and conventional injection moulding. They found that CNT alignment significantly affects the rheological response as well as the electrical properties. Both the rheological and electrical percolation thresholds were lower for compression moulded specimens relative to injection moulded specimens.

2.3 Quantifying CNT dispersion

Literature has shown that dispersion of fillers is an important factor affecting the properties of the nanocomposite. However, there is a shortage of quantitative techniques for analysis of the dispersion of CNTs in the literature. More often than not, the physical properties are characterised and reported with only a qualifying statement provided on filler dispersion (e.g. Sennett et al. (2003)). This non-coherent approach makes it difficult to perform comparisons studies on different nanocomposites systems. In order to understand the structure-property relationships of nanocomposite materials, it is essential to quantify CNT dispersion. Hence, researchers have concentrated on gaining information of the state of CNT dispersion using both direct and indirect characterisation methods such as microscopy, electrical resistivity and rheological measurements (Kasaliwal et al., 2011a; Pötschke et al., 2002).

Dispersion of CNTs relates to the distribution of individual nanotubes, or aggregates of nanotubes in the matrix. Any method of quantifying dispersion will depend on the size of the region of interest. If the state of macro dispersion above the micron range is pursued, optical

light microscopy (OM) is an appropriate method, whereas scanning electron microscopy (SEM) and TEM are methods suitable for studying the nanometer range (Pegel et al., 2011).

2.3.1 Optical microscopy

OM has been used to characterise dispersion in PA-MWCNT (Krause et al., 2009), polylactic acid-MWCNT (Villmow et al., 2008b) and PC-MWCNT (Kasaliwal et al., 2009). All three studies employed the degree of dispersion, D , which is defined by the ratio of the volume fraction of filler dispersed to the volume fraction of filler added to the matrix. This is similar to the macroscopic dispersion index used to quantify filler dispersion in CB-filled rubber compounds (Kasaliwal et al., 2009). However, this only reflects volume fraction indirectly as the amount of agglomerates seen depends on the thickness of the sample slices. In order to minimise the error, the slice thickness should be smaller than the agglomerates appearing in the micrographs. The area fraction of CNT agglomerates, A_{af} , in an OM micrograph is the ratio of the total agglomerate area, A_{CNT} , to the total observed area, A_o (Pegel et al., 2011). The product of this ratio and a packing density, f , that was estimated as 0.25, leads to the volume fraction of CNT that has aggregated into visible agglomerates (typically $>1 \mu\text{m}$ in diameter due to wavelength of light)(Krause et al., 2009). Hence, D determined with OM, D_{OM} is

$$D_{OM} = 1 - \frac{f \left(\frac{A_{CNT}}{A_o} \right)}{V_{CNT}} \quad (2.1)$$

where V_{CNT} is the volume fraction of CNTs in the nanocomposite.

A D_{OM} value of 1 implies no visible CNT agglomerates (size of $>1 \mu\text{m}^{-2}$) are present, suggesting very good dispersion levels (Kasaliwal et al., 2010). The OM method can further be used for analysing agglomerate density and size distribution that are useful for correlating experimental variables with material response. Background correction has been attempted by Kasaliwal et al. in order to improve agglomerate contrast from the matrix and to achieve balanced background illumination. They devised a procedure using the commercial image processing system ImageJ (Rasband, 1997). This provides a consistent and repeatable method to evaluate several micrographs. The evaluation of different slice thicknesses from a specimen with this technique can yield an estimate of the unbiased agglomerate volume fraction (Kasaliwal et al., 2011b).

There are disadvantages with the OM method. Firstly, bulk information derived from two-dimensional (2D) slices may present an incomplete analysis of the material as the distribution content and size of the filler is dependent on the thickness of the imaged sample slice (Pegel et al., 2011). It must be noted that there are limitations to 2D micrographs, as they cannot provide information on the distribution of the distance of a nanotube to the nearest neighbour. Hence, the absolute dispersion of CNTs, a 3D structure, cannot be attained (Pegel et al., 2011).

2.3.2 Electron microscopy

One method of quantifying CNT dispersion and distribution is through statistical analysis of TEM images, identical to that of Fig. 2.3. The investigation of CNT dispersion with nanometer resolution allows for the study of the spatial relationship between the individual nanotubes and the distributed CNT agglomerates (Pegel et al., 2011). By assuming that the TEM images were a planar projection of a 3D fiber system, Pegel and co-workers determined the CNT packing density of the agglomerates, and estimated of the volume fraction of CNTs in the nanocomposite. This in turn yields a degree of CNT dispersion with lower uncertainty in comparison to the OM method (Pegel et al., 2011). A significant number of TEM sections would be required for such a study in order to obtain statistically confident data that is representative of the bulk nanocomposite.

On the other hand, SEM images as shown in Fig. 2.4 were typically used to qualitatively describe the CNT dispersion in CNT nanocomposites (Lew et al., 2009; Liu et al., 2004). The bright circles and lines in these images were associated to the CNTs. In an effort to understand the reinforcement mechanisms CNT nanocomposites, SEM images were also used to study the morphology of fractured surfaces (Liu et al., 2004; Satapathy et al., 2007).

A step towards 3D visualisation has been pursued by Ray (2010) who used many SEM images of clay filled poly[(butylene succinate)-co-adipate] nanocomposite slices taken on different planes using focused ion beam tomography, as shown in Fig. 2.5. They employed a software to reconstruct a 3D representation of the material, and was able to show the degree of dispersion and orientation of nanoparticles in the matrix.

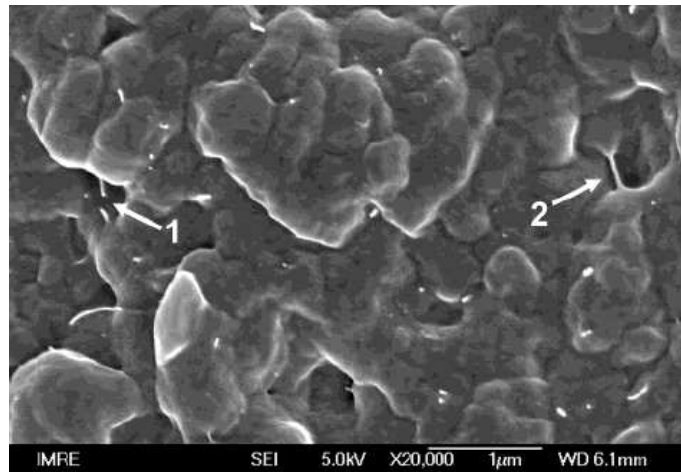


FIGURE 2.4: An SEM image of a fracture surface of PA6-MWCNT (0.5 wt%) after tensile testing. The first arrow indicates a broken CNT whereas the second arrow shows a CNT embedded in the matrix that bridge across a crack (adapted from Liu et al. (2004))

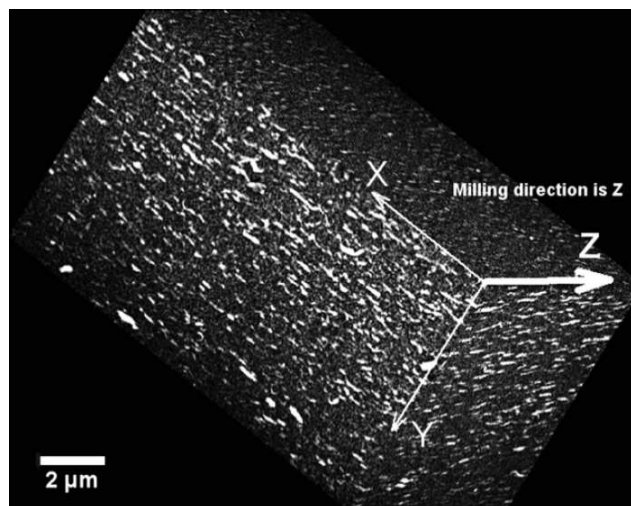


FIGURE 2.5: A reconstructed 3D representation of poly[(butylene succinate)-co-adipate] filled with nanoclay using 2D images of the cross-sectional surfaces that were milled using focused ion beam in the Z direction (adapted from Ray (2010))

2.4 Thermal properties

The low density, ease of fabrication of complex geometries and large production volumes make thermoplastics attractive options to replace metal and ceramic parts for applications such as consumer electronics. However, thermoplastics are thermally insulating materials that require fillers to enhance their thermal properties. Commonly used fillers include metal (e.g. copper, silver, gold) particles or flakes, carbon powder, carbon fibers and ceramic (boron nitride and silicon carbide) additives (Gupta et al., 2010). The disadvantage of using traditional fillers is that a high loading content is required. For example, 10 vol% boron nitride was required to increase the thermal conductivity of HDPE by $\sim 50\%$ (Zhou

et al., 2007). This often deteriorates other properties of the materials such as mechanical strength and density. The incorporation of nanoparticles such as MWCNTs, can improve thermal conductivity of base polymers at much lower filler content because of the CNT's high intrinsic thermal conductivity.

2.4.1 Thermal conductivity of CNTs

Widely differing values of thermal conductivity of CNTs have been reported. Yi et al. (1999) found the thermal conductivity of CVD-manufactured MWCNTs to be $20 \text{ W m}^{-1}\text{K}^{-1}$ at ambient temperature. Yang et al. (2002) measured the thermal conductivity of MWCNT films as $200 \text{ W m}^{-1}\text{K}^{-1}$ and showed that thermal conductivity is independent of CNT length. The following year, the thermal conductivity of individual MWCNT was measured by Small et al. (2003) as $3000 \text{ W m}^{-1}\text{K}^{-1}$ at ambient temperature using a customised mesoscopic device. More recently, Chiu et al. (2005) reported measurements of $600 \text{ W m}^{-1}\text{K}^{-1}$ for individual MWCNTs. Hone et al. (1999) reported that measurements of thermal conductivity of mats of SWCNT bundles were in the range of $1750 - 5800 \text{ W m}^{-1}\text{K}^{-1}$. Predictions employing molecular dynamics performed by Berber et al. (2000) suggested that the thermal conductivity of CNTs may reach up to $6600 \text{ W m}^{-1}\text{K}^{-1}$.

The variations in results is a reminder of the technical difficulties in conducting thermal conductivity measurements on individual nanotubes. MWCNTs are expected to have lower values of thermal conductivity compared with perfect SWCNTs, due to the structural defects present in MWCNTs, and to considerations of the inter-tube interactions needed for thermal conduction. Although the conductivities reported by different authors vary widely, the evidence shows that CNTs have very high thermal conductivity, similar to that of metals ($10 - 10^3 \text{ W m}^{-1}\text{K}^{-1}$) and diamond ($>10^3 \text{ W m}^{-1}\text{K}^{-1}$).

2.4.2 Thermal conductivity of thermoplastic-CNT nanocomposites

Factors that play a role in thermal conductivity, κ of nanocomposites include CNT variety, CNT-matrix interfacial interaction, CNT loading content, CNT dispersion, and CNT orientation relative to the direction of heat flow.

The influence of CNT variety on κ of epoxy was studied by Gojny et al. (2006). The study compared the contributions of MWCNTs, SWCNTs, DWCNTs, and CB. At constant

0.3 wt% loading content, κ of the nanocomposites was found to decrease following the order: MWCNTs>DWCNTs>CB>SWCNTs. The relatively higher efficiency of MWCNT as a thermal conductor was attributed to the enhancement of phonon transport of thermal energy (Gojny et al., 2006). They postulated the reduction of the specific surface area of MWCNTs led to a decrease in phonon scattering effects caused by the presence of defects in MWCNTs.

King et al. (2012) reported a marginal increase in through-plane κ of PC from $0.21 \text{ W m}^{-1}\text{K}^{-1}$ to $0.22 \text{ W m}^{-1}\text{K}^{-1}$ and $0.27 \text{ W m}^{-1}\text{K}^{-1}$ for 1 and 5 wt% MWCNT respectively. At 5 wt% (or 3.5 vol%) the presence of MWCNTs increased thermal conductivity of PC by 29%. In the same study, κ for PC filled with highly branched CB and exfoliated graphite nanoplatelets (GN) with identical filler loading content was also measured. It was found that CB (5 wt%) increased κ of PC up to $0.25 \text{ W m}^{-1}\text{K}^{-1}$ and PC-GN (5 wt%) recorded the highest κ at $0.31 \text{ W m}^{-1}\text{K}^{-1}$. It should be noted that King and co-workers used injection moulded disc specimens in their study, but no evaluation of CNT orientation was performed.

Kuriger et al. (2002) found that orientation of carbon nanofibers (CNFs) in polypropylene (PP) affected κ of the nanocomposite: CNFs parallel to the direction of heat flow recorded consistently higher conductivity than CNFs perpendicular to heat flow, at identical levels of filler loading. In an effort to verify the contribution of MWCNTs to κ of PP matrix, Kashiwagi et al. (2004) performed measurements with increasing filler loading content and test temperature. The technique confirmed that the presence of CNTs enhanced thermal conductivity of PP. At 2 wt% ($\sim 1 \text{ vol}\%$) loading, the thermal conductivity of pure PP improved by $\sim 30\%$ relative to pure PC for the temperature range of 50 - 140 °C.

Gojny et al. (2006) used experimental data to compare to theoretical models in an effort to understand the mechanisms for thermal transport in nanocomposites. They proposed two simple models to calculate the upper and lower boundary of κ for randomly oriented CNT nanocomposite. The first model uses the rule of mixtures (ROM) is expressed as

$$\kappa = \kappa_{\text{matrix}} \left(V_{\text{matrix}} + \frac{\kappa_{\text{CNT}} V_{\text{CNT}}}{\kappa_{\text{matrix}}} \right) \quad (2.2)$$

The second model is based on the parallel electric circuit model (or the inverse of ROM), expressed as

$$\kappa = \frac{\kappa_{\text{matrix}} \kappa_{\text{CNT}}}{V_{\text{matrix}} \kappa_{\text{CNT}} + V_{\text{CNT}} \kappa_{\text{matrix}}} \quad (2.3)$$

Eq. 2.3 overestimates κ because it considers the volume fraction of each phase separately, not accounting for interfacial interactions, and maximises the contribution of the CNTs (Gojny et al., 2006). They suggested that the formation of a percolated network affected heat transport, most likely decreasing distances between neighbouring CNTs, and thus, enhancing phonon conduction.

2.4.3 Thermal degradation PC and CNTs

It is crucial to study thermal degradation of a material for processing and applications. The most common method to study thermal stability and thermal degradation is thermogravimetric analysis (TGA). This consists of monitoring the change of mass of a specimen through a prescribed temperature history, at atmospheric pressure with a selected purge gas flowing through the furnace (Brown, 2001). To date, there are no standard criteria to identify features on a TGA curve for analysis, for example, the start of degradation (Su et al., 2011). Typical values used are (1) the onset of degradation temperature, T_{onset} , that is related to the temperature at 5% and 10% weight loss, $T_{5\%}$ and $T_{10\%}$ respectively; (2) the temperature at maximum rate of weight loss, T_{max} ; and (3) the amount of char or residue (Su et al., 2011).

In PC resin, T_{onset} has been reported at 450 °C and 500 °C in air and nitrogen atmospheres respectively, whereas T_{max} occurs at ~ 560 °C for both atmospheres (Jang and Wilkie, 2004, 2005).

Since thermal properties of the nanocomposite are dependent on the thermal properties of both network and filler, CNT structure and purity will influence its thermal stability of the CNT, and hence of the nanocomposite. MWCNT have been shown to have structured defects on the surfaces of the tubes. Bom et al. (2002) postulated that these defects resulted in oxidative instability as each layer of the MWCNT is peeled away, revealing edges and bonds as well as new defect sites. These defects promote degradation allowing it to initiate at a lower temperature compared to graphite or diamond.

The effects of atmosphere on the thermal stability of CNTs have also been investigated. Pang et al. (1993) demonstrated that CNTs produced by arc discharge method have very high thermal stability under an inert atmosphere (argon gas), up to 1000 °C. However, when the atmosphere was switched to oxygen-rich air, the CNTs degraded at a lower temperature; T_{max} was measured as 695 °C. For oxidative degradation, Marosfői et al. (2006) reported

T_{onset} and T_{max} for MWCNTs as 604 °C and 730 °C respectively. On the other hand, they found T_{onset} for MWCNTs to be 550 °C under nitrogen atmosphere. Similarly, Li et al. (2006) observed that CVD MWCNTs started to degrade at 600 °C under an inert atmosphere.

The presence of catalyst residue in the CNTs was suggested by Schartel et al. (2008) to be a likely cause of the decrease in thermal stability of PC-MWCNT relative to the base matrix. In contrast to this, Kashiwagi et al. (2004) found that the presence of iron particles did not have a significant effect on flammability of PP-MWCNT, which is closely associated to thermal stability. They postulated that since the iron residue is within or at the ends of the MWCNT, contact between the residue and PP chains which could enhance degradation of the matrix, would not take place until the MWCNT walls were thermally degraded; hence, the effect of the iron residue may not be critical in the study of thermal stability of nanocomposite. Bom et al. (2002) employed TGA to study the influence of the presence of iron residue on oxidative stability of CVD synthesized MWCNTs. The effects of the residue, if any, would be visible only at the later stages of TGA combustion as an abrupt acceleration in thermal degradation. They found negligible effects of iron residue on CNT oxidative stability.

2.4.4 Thermal degradation of thermoplastic-CNT nanocomposites

The literature has reported varying levels of improvements in thermal stability, no change and even a reduction in thermal stability of thermoplastic polymer nanocomposites relative to the respective unfilled matrices (Costache et al., 2007; Gedler et al., 2012; Kashiwagi et al., 2002; Li et al., 2006; Marosfői et al., 2006; Schartel et al., 2008, 2005).

Costache et al. (2007) reported an increase in thermal stability for PS-MWCNT and polyethylene (PE)-MWCNT in nitrogen atmosphere owing to a barrier formation that is dependent on the dispersion of nanofillers. The barrier formation is a temporary CNT network structure that inhibits the transport of degraded products to the gas phase. This is known as the barrier effect. Kashiwagi et al. (2002) found that the presence of MWCNTs improves thermal stability of PP in nitrogen but increasing filler loading above 1 vol% made a negligible increase. In an oxidative atmosphere, the thermal stability of PP-MWCNT showed an initial mass loss onset earlier than the base matrix but T_{max} of PP-MWCNT was enhanced with increasing CNT loading.

Marosfői et al. (2006) investigated the influence of CNT variety in the thermal degradation of PP and found that MWCNTs and DWCNTs increased T_{onset} and T_{max} of PP in *both* air and nitrogen atmospheres, in contrast to Kashiwagi's findings. This was attributed to the barrier effect. The CNT network deteriorated as temperature increased to a critical value. Raman microscopy verified that the residue of PP-MWCNT contained mainly MWCNTs, highlighting its high thermal stability (Marosfői et al., 2006). They suggested that good interfacial interaction between the filler and polymer, or otherwise good dispersion of CNTs, increases the activation energy for degradation leading to an improvement of thermal stability of nanocomposites.

Schartel et al. (2005) found comparable T_{onset} and identical T_{max} between PA6-MWCNT (5 wt%) and pure PA6 under air atmosphere. They found the residue to be consistent with the filler loading content. However, Li et al. (2006) reported delayed thermo-oxidation (increase in T_{onset}) of PA6 with the addition of both purified and hexamethylenediamine (HDM)-functionalised MWCNTs for filler loadings 0.1 - 2 wt%, whereas T_{max} was found to be similar to that of pure PA6 (± 5 °C). No significant change was reported in nitrogen atmosphere regardless of CNT variety. Improvements of CNT dispersion through functionalisation yielded lower thermal stability enhancements compared to purified CNTs, due to HDM degrading below 300 °C which promoted the nanocomposite degradation.

Su et al. (2011) summarised the mechanisms of thermal degradation of polymer nanocomposites as: (1) CNT thermal conductivity, (2) barrier effect, (3) polymer-CNT interaction, (4) physical or chemical adsorption of degraded products, and (5) radical scavenging action (i.e. radical trapping). Mechanisms (1) to (3) were observed through the findings of the references mentioned above. Evidence for mechanisms (4) and (5) have been associated with other nanofillers such as organically modified OMMTs (Feng et al., 2010) and layered double hydroxides (LDH) (Costache et al., 2007). The latter study performed gas chromatography-mass spectrometry that indicated such fillers could have altered the degradation products during TGA. Crucially, they found that both SWCNT and MWCNT fillers resulted in no change to the degradation products.

The difference between the findings of Kashiwagi et al. (2002) and Marosfői et al. (2006) for PP-MWCNT and between Schartel et al. (2005) and Li et al. (2006) for PA6-MWCNT could have arisen from the different nanocomposite processing methods, different CNT filler content and CNT synthetic route, all contributing to the dispersion state of CNTs in the

matrix. The variation in findings for similar nanocomposites systems shows that although CNTs have the potential to improve thermal properties, there is still a need for a more coherent and unified approach in determining the influence of CNT presence on thermal stability of thermoplastics.

2.5 Mechanical properties

In polymer composites, the enhancement of mechanical properties of the base matrix is dependent on the mechanical properties of the fillers. Conventional fillers for polymers have been primarily fibers such as carbon, glass, aramid and boron. Diameters of these fibers are generally in the micron scale whilst their lengths are in the order of millimeters. The Young's modulus, E and ultimate tensile strength, UTS in the ranges of 70 - 400 GPa and 2.5 - 3.4 GPa respectively (Gay et al., 2002).

On the other hand, MWCNTs have diameters in the order of nanometers and lengths that can approach those of conventional fibers, providing a very high surface to volume ratio that is desirable in increasing the mechanical properties of the polymer. The small size and high aspect ratio of the nanotubes promotes the formation of a CNT network. This CNT network structure, combined with the high stiffness of the nanotubes, has the potential to reinforce the base matrix at much lower filler concentrations than conventional fibers and produce nanocomposites with much improved mechanical properties.

2.5.1 Mechanical properties of CNTs

Numerous experimental studies have been attempted in the last two decades to measure the mechanical properties of individual CNTs. Early measurements of E_{MWCNT} made by arc-discharge were performed through recording intrinsic thermal vibrations in TEM, giving an incredibly high average value of 1.8 TPa (Treacy et al., 1996). Salvetat et al. (1999) used a different technique, an atomic force microscope (AFM) with custom clamps for CNT ends, to measure the E_{MWCNT} for arc-grown and CVD MWCNTs; they obtained an average E_{MWCNT} of 810 GPa (arc-discharge) and 27 GPa (CVD). When a different type of CNT was measured, SWCNTs (ropes), the same group reported higher values for E and shear modulus of the order of 1 TPa and 1 GPa respectively. For individual SWCNTs, (Krishnan et al., 1998) used amplitude of vibrations in TEM and found the average E_{MWCNT} as 1.25 TPa.

In an effort to understand MWCNT failure mechanism, Yu et al. (2000) developed a nanostressing stage with an AFM tip to grip the CNT, operated within a SEM. They measured E (outer wall) and UTS ranging 270 - 950 GPa and 11 - 63 GPa accordingly; while failure strain was 12%. They observed failure occurring by a pull out mechanism, where the inner tubes were separated from the outer tube. The authors called this fracture mechanism a sheath-in-sword failure, illustrated in the SEM micrographs in Fig. 2.6. They suggest that the outer wall of the CNT carried most of the load, as the interlayer interaction is made up of relatively weak van der Waals bonds. Shaffer and Sandler (2007) argued that there has been some ambiguity about the failure cross-section of the CNT that should be considered for analysis purposes. MWCNTs have generally been considered to be thick-walled cylinders, discounting the hollow core. A more recent study by Peng and co-workers (2008) addressed this ambiguity by using direct imaging to identify the number of fractured shells, providing direct measurements of tensile strength and obtained a fracture strength of ~ 100 GPa with failure strains between 6 and 12% and E of 1105 GPa for arc-discharge MWCNTs.

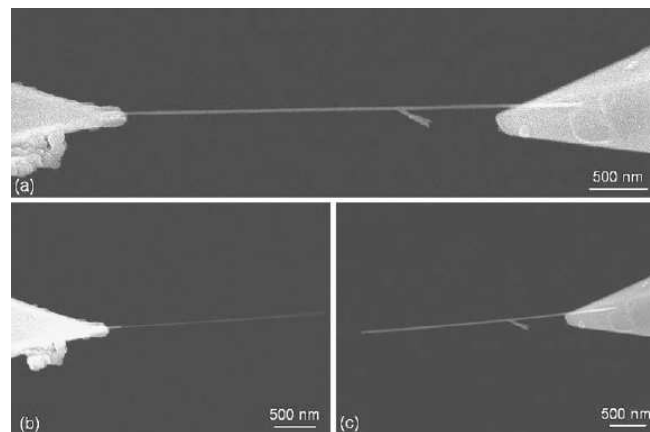


FIGURE 2.6: A MWCNT under tensile loading experiences failure through sword-in-sheath method. (a) AFM tips used to hold the nanotube in position. (b) An inner tube is removed from MWCNT. (c) The outer tube remains with the opposite AFM tip (reproduced from Ding et al. (2007))

The references above indicate that CNT mechanical properties vary depending on CNT variety and synthesis method, and the presence and density of structural defects. It should be noted that the CNTs in the all studies reviewed here were manufactured in research laboratories, and hence it is possible that commercial grade CNTs have lower mechanical properties because of increased likelihood of structural defects expected with large volume CNT synthesis.

2.5.2 Fundamentals for mechanical reinforcement of nanocomposite

Colomer et al. (2006b) highlighted four fundamental factors to achieve improvements in mechanical properties of the base matrix with the addition of CNTs. The factors are (1) CNT dispersion, (2) CNT alignment (or orientation), (3) CNT aspect ratio, and (4) matrix-filler interfacial strength. The first three factors are typically influenced by the nanocomposite processing methods. Factors (1) and (4) can be improved through the chemistry of the matrix and the CNT surface. Modification of the CNTs to improve its affinity to the matrix can be achieved via two methods: (1) physical adsorption or wrapping polymer to the CNT (non-covalent bonds) and (2) formation of chemical (covalent) bonds between the matrix and the CNT surface (Spitalsky et al., 2010).

Well dispersed CNTs increase the CNT surface area available for polymer wetting. Therefore, it is desirable to maximise the CNT aspect ratio in order to maximise the surface to volume ratio of the filler. This promotes efficient stress transfer of loads from the polymer to the individual CNTs. Agglomerations of CNTs create CNT clusters and matrix-rich regions, giving rise to stress-concentrations. Alignment of CNTs is crucial when considering applications of the nanocomposite. The bulk material will benefit most from the increased strength and stiffness if the service load is acting parallel to the oriented CNTs.

The strength of adhesion between the matrix and the CNTs is perhaps the most important factor in improving mechanical properties of the matrix. Strong adhesion of the matrix-filler enables effective stress transfer. However, measurement of the matrix-filler interaction is not trivial. Interfacial strength may be qualitatively studied using methods such as TEM observations of CNT surfaces (Cadek et al., 2002) and Raman spectroscopy (Wagner, 2011). Direct measurement of matrix-filler interfacial strength was first reported by Barber and co-workers (2003). They used AFM to performed nanopullout experiments, a technique to pull out single CNTs from a nanocomposite film. They found that matrix surrounding the CNTs supported higher stress levels relative to the bulk matrix. Other researchers have observed CNTs in nanocomposites to fail under loading by buckling, collapsing or fragmentation (Lourie et al., 1998; Lourie and Wagner, 1999).

2.5.3 Thermoplastic-CNT nanocomposites

2.5.3.1 Influence of constituent material characteristics

One of the earliest studies on thermoplastic nanocomposites was performed by Qian et al. (2000) on PS-MWCNT (1 wt%). They reported an increase of 36 - 42% in E , and $\sim 25\%$ increase in strain at break. Although the materials in their study were solution mixed, the in-situ TEM observation performed to understand the tensile fracture mechanism induced by thermal stresses is of particular interest. They observed a tendency for crack nucleation at regions of low MWCNT density, followed by crack propagation along weak PS-MWCNT boundaries, or in areas of low MWCNT density, as can be seen in Fig. 2.7. Furthermore, the MWCNTs aligned perpendicular to the crack direction and bridged the crack faces in the wake. The MWCNTs started to break and or pull out after the crack opening exceed a length of ~ 800 nm.

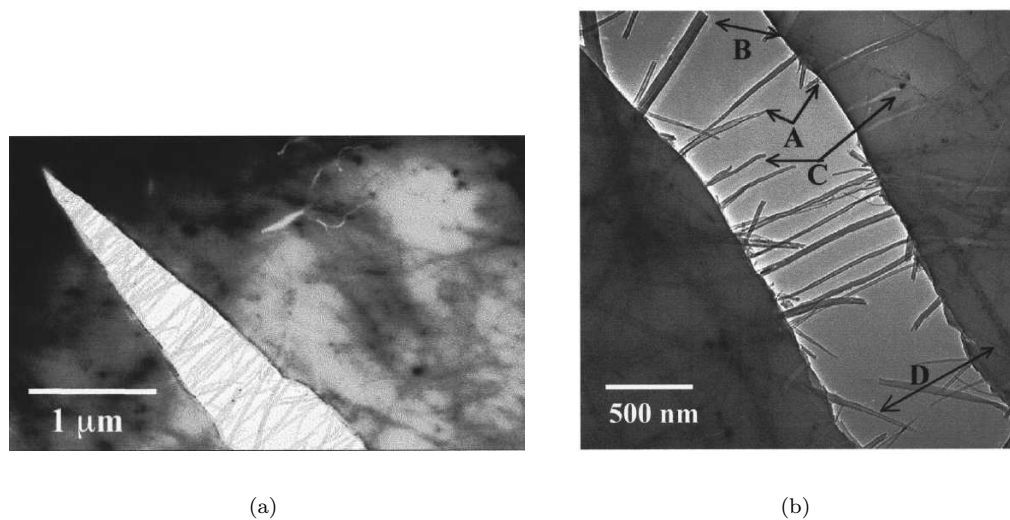


FIGURE 2.7: In-situ observation TEM of a crack growing in PS-MWCNT showing (a) crack propagation and (b) bridging of crack faces (adapted from Qian et al. (2000))

Probing the influence of matrix morphology, Cadek and co-workers (2002) compared mechanical properties of poly (9-vinyl carbazole) (PVK), an amorphous polymer, against polyvinyl alcohol (PVA), a crystalline material. Both were filled with MWCNTs processed into films. They reported E and hardness of PVA-MWCNT (1 wt%) increased by factors of 1.8 and 1.6 whereas PVK-MWCNT (8 wt%) increased by 2.8 and 2.0, relative to their respective base matrices. The comparable improvements in properties of both materials with significantly

different MWCNT content suggested that the ordered structure in PVA provided strong interfacial adhesion between matrix and CNT. This was evident from DSC data showing an increase in crystallinity for PVA with CNT content. The same was not found in PVK, leading the authors to suggest that stress transfer at CNT-amorphous polymers interface is relatively poor.

The role of CNT type is highlighted by Cadek et al. (2004) with the evaluation of SWCNTs, DWCNTs, and MWCNTs from various manufactures and produced by different synthesis methods, on the reinforcement of PVA. They found an inverse relationship between the CNT diameter (associated to CNT surface area) and E , indicating matrix-filler interfacial interaction is crucial. MWCNTs exhibited a higher increase in E relative to SWCNTs and DWCNTs (> 0.1 wt%). This is because SWCNTs and DWCNTs (> 0.1 wt%) tend to form bundles, which result in ineffective stress transfer between the matrix and filler due to slippage of individual tubes within the bundles (Cadek et al., 2004). Commercially produced CNTs, believed to have higher defect density relative to laboratory produced CNT, led to significant increases in nanocomposite E . This indicates the possibility that defect levels of CNTs do not influence stress transfer. More importantly, their work showed that CVD manufactured MWCNTs precede other CNT types for reinforcement.

Extending on Cadek and co-workers' work, Castillo et al. (2011) compared the influence of different MWCNT characteristics (e.g. diameter and length) and MWCNT loadings up to 1.25 wt% on mechanical response of PC-MWCNT using five different commercial MWCNTs. All were CVD synthesized MWCNTs and were used as received from the manufacturers. Comparing to unfilled PC, they found that E and UTS increased by up to 14% and 7% respectively, whereas strain to failure decreased by 165%. The variation in MWCNT manufacturer and loading content on E was reported to be *insignificant* while the opposite was true for failure strain. It was observed that the three highest aspect ratio MWCNTs did not influence UTS, whereas the other nanotube types exhibited an effect.

Eitan et al. (2006) studied the effects of MWCNT surface modification on the reinforcement of PC. Evidence from viscoelastic measurements and SEM microscopy suggested that the presence of regions of immobilized polymer chains surrounding the nanotubes improves mechanical properties. They proposed a structure of interaction zones, as shown in Fig. 2.8. The adsorbed polymer layer, corresponding to the polymer chains nearest to the CNT surface, is small and localised, and has different mechanical properties from the bulk polymer

due to the restricted chain mobility.

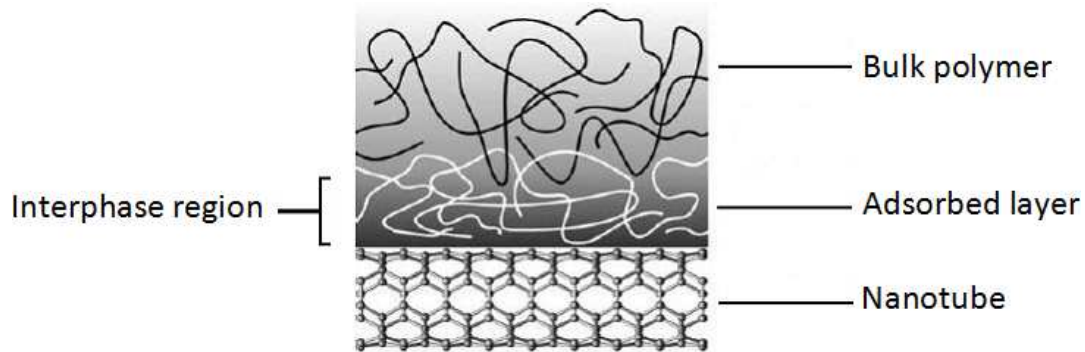


FIGURE 2.8: Structure of interaction zones of a polymer-nanotube nanocomposite (adapted from Eitan et al. (2006))

The need for CNT dispersion for mechanical reinforcement is highlighted by Prashantha and co-workers (2008). They used PP grafted maleic anhydride (PP-g-MA) to encourage dispersion of MWCNTs within PP. PP-MWCNT were melt mixed with PP-g-MA (2 wt%) and diluted to obtain CNT loadings from 1 to 5 wt%. They found that the addition of PP-g-MA increased E and UTS of PP-MWCNT by an average of 10% and 35% respectively. The increase in mechanical response was attributed to the adsorption of PP-g-MA onto the CNT surface, supported with SEM micrographs. They suggested the adsorbed layer enhanced PP-CNTs interfacial interaction and CNT dispersion.

2.5.3.2 Processing effects on orientation and dispersion of CNTs

The influence of CNT orientation on the reinforcement of PS-MWCNT (5 wt%) was investigated by Thostenson and Chou (2002). MWCNT-filled and unfilled PS were drawn to films with consistent draw ratios and were compared to the corresponding compressed moulded specimens. Using dynamic mechanical analysis (DMA) with axial fittings, they found that yield strength and UTS increased in the following order: PS (moulded) < PS (drawn) < PS-MWCNT (drawn). The findings show that the increase in tensile properties of aligned nanocomposites is not due only to polymer chain orientation, and suggested that the load was transferred from the polymer to the oriented CNTs.

Abbasi et al. (2009) measured the mechanical response of micro-injection moulded PC-MWCNT as a function of CNT content and injection speed. The effect of CNT loading content on E was incremental until 3 wt% loading, increasing by 30% from unfilled PC. Further addition of MWCNTs to 10 wt% increased E by only $\sim 9\%$ more. They attributed the lack of

reinforcement to the weak matrix-filler interactions. Elongation to break was significantly influenced by MWCNT content: ductility decreased until the material became brittle at high loading contents (7 - 10 wt%). Increasing the injection speed resulted in higher E due to polymer chain orientation and/or CNT alignment.

Rios et al. (2011) studied the relationship between conventional IM parameters on mechanical response of PC-MWCNT (3 wt%). They concentrated on five parameters that affect mixing and orientation: T_{melt} , V_{sc} , P_{back} , V_{inj} , and P_{hold} , and found that E was only dependent on P_{back} . They associated this parameter to better mixing, thus enhancement of CNT dispersion. Elongation to failure was inversely dependent on T_{melt} and V_{sc} , and both are linked to mixing and orientation. This study highlights the complexity of mechanical behaviour dependence on several IM parameters.

Effects of orientation of CNTs were also investigated on melt-spun PC-MWCNT fibers by Fornes et al. (2006). Using tensile testing with modified clamps for fibers, they reported a rise in E and yield strength with increasing CNT loadings. PC-MWCNT fibers recorded a *decrease* in strain to failure. The study with 3 wt% loading of MWCNTs reported an increase of 40% for both E and yield strength, and a 60% decrease in elongation to break. Defects were directly observed on TEM images showing twist-like features in individual MWCNTs. These observations suggest that mechanical properties are influenced by the morphology of MWCNTs. In comparison to melt processed bulk PC-MWCNT (Abbasi et al., 2009; Castillo et al., 2011), melt-spun fibers yield higher reinforcement.

2.5.3.3 Predictions of tensile modulus of CNT nanocomposites

This section gives a brief overview on models for the prediction of modulus of CNT nanocomposites. It is intended to enable comparison of experimental findings to theoretical values, and to shed light on factors that play a role in reinforcement but are difficult to verify experimentally.

Characterisation of nanocomposite fracture behaviour have been similar to that of fiber-composites, such as fiber failure and interfacial bonding between fiber and matrix (Lourie and Wagner, 1999). Thus, theoretical studies have been conducted to predict mechanical properties of CNT-composites using micromechanical models such as ROM and Halpin-Tsai equations. E of nanocomposites can be calculated using a modified ROM to include an

orientation factor, η_o and length efficiency factor, η_l , expressed as (Colomer et al., 2006a)

$$E = (\eta_l \eta_o E_{\text{CNT}} - E_{\text{matrix}}) V_{\text{CNT}} + E_{\text{matrix}} \quad (2.4)$$

where V_{CNT} is the volume fraction of the CNTs. Eq. 2.4 assumes uniform dispersion of CNTs in the matrix, good CNT-matrix bonding and equal straining of the CNT and the matrix under loading.

The Halpin-Tsai equation for aligned CNTs is expressed as (Colomer et al., 2006a)

$$E = E_{\text{matrix}} \frac{1 + \frac{2l}{D} \eta V_{\text{CNT}}}{1 - \eta V_{\text{CNT}}} \quad (2.5)$$

where

$$\eta = \frac{\frac{E_{\text{CNT}}}{E_{\text{matrix}}} - 1}{\frac{E_{\text{CNT}}}{E_{\text{matrix}}} + 1} \quad (2.6)$$

is a filler geometry parameter. l and D is the CNT length and CNT diameter respectively.

In the case of randomly oriented CNTs, the Halpin-Tsai equation is given as (Colomer et al., 2006a)

$$E = E_{\text{matrix}} \left(\frac{3}{8} \frac{1 + \frac{2l}{D} \eta_L V_{\text{CNT}}}{1 - \eta_L V_{\text{CNT}}} + \frac{5}{8} \frac{1 + 2\eta_T V_{\text{CNT}}}{1 - \eta_T V_{\text{CNT}}} \right) \quad (2.7)$$

where the filler geometry parameter for the longitudinal direction, η_L is

$$\eta_L = \frac{\frac{E_{\text{CNT}}}{E_{\text{matrix}}} - 1}{\frac{E_{\text{CNT}}}{E_{\text{matrix}}} + \frac{2l}{D}} \quad (2.8)$$

and the filler geometry parameter for the transverse direction, η_T is

$$\eta_T = \frac{\frac{E_{\text{CNT}}}{E_{\text{matrix}}} - 1}{\frac{E_{\text{CNT}}}{E_{\text{matrix}}} + 2} \quad (2.9)$$

Both ROM and Halpin-Tsai models were tested on HDPE-MWCNT data (0.11 - 0.44 vol%) by Kanagaraj et al. (2007). They found Eq. 2.4 values varied from experimental data up to a maximum relative error of 4%, whereas Eq. 2.7 gave better agreement to E data, to within

2%. Both models were effective in estimating E for V_{CNT} below 0.2%. Kanagaraj et al. (2007) used the models as an indication that the interfacial interactions between HDPE and CNTs were strong, in line with the model assumptions. Qian et al. (2000) assessed Eq. 2.7 on PS-MWCNT (1 wt%) and found that the predicted values fell within $\sim 10\%$ of the experimental results.

At higher MWCNT loadings, up to 8 wt%, Via et al. (2012) found Eq. 2.7 overestimated E for PC-MWCNT. However, they reported a version of the Halpin-Tsai model for 3D randomly oriented fibers, expressed as

$$E = E_{\text{matrix}} \left(\frac{1}{5} \frac{1 + \frac{2l}{D}\eta_L V_{\text{CNT}}}{1 - \eta_L V_{\text{CNT}}} + \frac{4}{5} \frac{1 + 2\eta_T V_{\text{CNT}}}{1 - \eta_T V_{\text{CNT}}} \right) \quad (2.10)$$

which was found to agree with E measurements for the loadings tested. Overestimates of E with Eq. 2.7 were also reported for PA6-MWCNT (6 wt%) (Meinke et al., 2004) and PP-MWCNT (5 wt%) (Bhuiyan et al., 2013).

Although CNT aspect ratio is accounted for in Eqs. 2.5, 2.7, and 2.10, CNTs are assumed to be solid rods. Thostenson and Chou (2003) reasoned that since MWCNTs have a hollow centre, only the CNT outer walls were carrying any load. Hence, they suggested a modified E_{CNT} in Eq. 2.7 to reduce the cross-sectional area supporting the load by considering the CNTs wall thickness and its diameter. Their predictions were in agreement with the experimental data. The model showed the sensitivity of E to CNT diameter, and more specifically, the CNT diameter distribution. In addition, TEM and SEM micrographs of CNTs embedded in nanocomposites have consistently shown curved CNTs, hence Fisher and co-workers (2002) attempted to capture CNT waviness using a micromechanical model (Mori-Tanaka) and found that experimental data of PS-MWCNT (10 wt%) were closer to predictions of bent CNTs relative to straight rod CNTs.

2.6 Electrical properties

2.6.1 Carbon nanotubes

Early theoretical investigations of the electrical properties of CNTs suggested that they could be either metallic or semiconducting in nature by varying two characteristics: (1) tube diameter, which is inversely related to the energy gap for semiconductor behaviour, and (2) the chiral angle which determines the lattice configuration of a rolled tube (Saito et al., 1992). Ebbesen et al. (1996) confirmed theoretical predictions when they observed both metallic and non-metallic conductivity behaviour with 4 probe measurements on individual MWCNTs. They reported resistivities ranged from 5.1×10^{-6} to $9.8 \times 10^{-4} \Omega \text{ cm}$ (representative of metallic resistivity) and 10^{-3} to $6 \Omega \text{ cm}$ (representative of semiconductor resistivity). This work showed a clear relation between nanotube structure and electrical properties. The resistivity measured for SWCNT ropes was found to be between 0.03×10^{-3} and $0.10 \times 10^{-3} \Omega \text{ cm}$ (Fischer et al., 1997). SEM and spectroscopy enabled the examination of electrical properties with respect to the structure of individual SWCNT, using images with atomic resolution, and confirmed theoretical predictions of the influence of tube diameter and wrapping angle (Wildöer et al., 1998).

2.6.2 Thermoplastic-CNT nanocomposites

Electrically conductive polymer composites are valued in applications such as anti-static packaging and electronic applications. Nanocomposites filled with CNTs have the potential for substantially increased electrical conductivity compared to virgin polymers. This occurs because the CNTs provide a pathway for electrons. Electrical properties are strongly affected by filler loading content, filler orientation, filler-filler and polymer-filler interactions. The minimum loading of conductive filler which provides the transition from insulator to conductor is known as the electrical percolation threshold. Beyond this threshold there is a continuous 3D network formed by the filler. Therefore, electrical measurements have been used in several studies as an indicator of the presence of a percolated network structure within the polymeric matrix.

Table 2.1 presents electrical volume resistivity of selected nanocomposites reported in literature to show the enhancements of properties relative to pure matrix with the presence of

CNTs at various filler loading contents; the focus is on melt processed nanocomposites, consistent with the process history of materials in this study. CNTs have the ability to provide conductivity at lower filler concentration relative to traditional fillers like CB. For instance, Meincke et al. (2004) used a potentiometer to compare volume resistivity of PA6-MWCNT and PA6-CB at identical filler content of 5 wt %; the nanocomposite measured 3 magnitudes lower than that of CB-filled system.

TABLE 2.1: Electrical properties of selected MWCNT-polymer nanocomposites

Matrix type	CNT loading (%)	Processing methods	Testing method	Voltage supply (V)	Volume resistivity (Ω cm)	Reference
PC	0	Twin screw extruder	In-house clamps	500	10^{13}	Pötschke et al. (2002)
	2			1	10^3	
PC	0	Twin screw extruder	Four point probe	500	10^{15}	Pötschke et al. (2004)
	2			1	10^3	
	3			1	10^1	
PA6	0	Twin screw extruder	Potentiometer		$>10^{10}$	Meincke et al. (2004)
	6				$>10^7$	
	12				$>10^1$	

2.6.2.1 Influence of CNT network morphology

Pötschke et al. (2002) measured volume resistivity in a PC-MWCNT system, and found a step-wise change in resistivity arising from the electrical pathway of the CNT network, identified as the electrical percolation threshold at 2 wt% CNT content, as shown in Fig. 2.9. Similar behaviour was observed by Du's group with poly(methyl methacrylate) (PMMA)-SWCNT at 0.4 wt% (Du et al., 2004). Both studies found that the electrical properties are dependent on the filler loading. Du and co-workers used a power relation

$$\sigma \propto (m - m_c)^{\beta_c} \quad (2.11)$$

where σ is electrical conductivity, m is mass loading content, m_c is the percolation threshold and β_c is the critical exponent, to determine the electrical percolation threshold. This threshold is influenced by the CNT-CNT distance and the contribution from the limited metallic portion of CNTs for electron transport (Du et al., 2004; Pötschke et al., 2004). The minimum

distance between neighbouring nanotubes must be <5 nm for a conductive network to form, assuming that an electron hopping mechanism is responsible for the electrical conductivity in PMMA-SWCNT (Du et al., 2004).

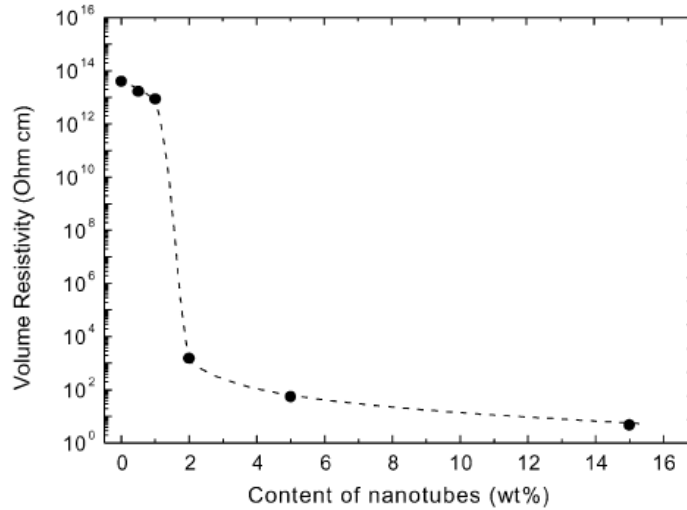


FIGURE 2.9: Volume resistivity dependence on MWCNT loading content for PC-MWCNT (adapted from Pötschke et al. (2002))

Orientation and alignment of CNTs was found to decrease electrical conductivity of PC-MWCNT fibers (Pötschke et al., 2005). They explained that the alignment of CNTs, evident from TEM images, decreases the probability of CNT-CNT contact to form a conductive pathway, thus resulting in the increase in electrical resistivity. Bai and Allaoui (2003) observed from dielectric measurements that increasing the CNT aggregate size and the CNT length, improved electrical conductivity and decreased the percolation threshold. They postulated that an increase in CNT length increased the probability of CNT entanglements and aggregate connections.

Electrical conductivity was also found to be influenced by MWCNT shape. The aspect ratio of a CNT is the ratio of the length of the CNT to its diameter. The modified aspect ratio, to account for CNT waviness, was identified as a mesoscopic shape factor and determined through the framework of static bending persistent length (l_{sp}), which is defined as the maximum straight length that is not bent permanently (Han et al., 2011). They performed the study using MWCNTs that were produced by CVD, over a temperature range of 600 - 700 °C to obtain MWCNTs with varying l_{sp} . The percolation threshold was found to be inversely related to the shape factor whereas electrical conductivity increased proportionally with the shape factor.

Sung et al. (2006) investigated the effects of CNT surface treatment on electrical resistivity. TEMs showed that functionalisation with hydrogen peroxide followed by drying treatments provided less entanglement of CNTs relative to untreated MWCNTs. Functionalised MWCNTs decreased the percolation threshold by about 2 - 3 wt% compared with untreated CNTs. The increase in conductivity was explained through the increase in filler-filler interactions, indicated by the increase in network stiffness in rheological measurements (Sung et al., 2006). This study shows the potential to employ electrical and rheological characterisation to infer CNT dispersion. In contrast to Sung's work, Gojny et al. (2006) found that electrical conductivity decreased and the percolation threshold increased with the addition of functionalised MWCNTs in an epoxy system. They suggested the decrease in conductivity was caused by the presence of an insulating polymer layer on the CNT surface due to increased affinity between the functionalised filler and matrix, hindering electron transport.

2.6.2.2 Influence of processing parameters

The influence of processing parameters for melt compounding and melt forming (IM and CM) were introduced in Section 2.2. The references reviewed showed that electrical resistivity measurements could be used to gain information regarding CNT network morphology (i.e. levels of dispersion and orientation). This is perhaps attractive to industry as the technique is non-destructive and could potentially be employed as a quality control measure.

The work reviewed in this Section highlights the development of the idea of CNT network destruction and reformation during processing. Pegel et al. (2008) investigated the influence of compression moulding on MWCNT network formation after masterbatch dilution of PC-MWCNT (0.875 wt%). They found that low pressing speed and high moulding temperature increased electrical conductivity due to the formation of loosely packed secondary agglomeration, evident from TEM images. The same study found that increasing the mixing speed during masterbatch dilution determined the final CNT agglomerate size. It was suggested that the relationship between mixing speed and agglomerate size distribution is due to simultaneous CNT network destruction and formation. The process helps to connect individual CNTs or clusters.

The influence of IM parameters was studied by Lellinger et al. (2008) on PC-MWCNT (2 wt%) and PA12-MWCNT (4 wt%). They measured the inline (melt in the mould) and offline (moulded parts) electrical conductivities using in-house constructed electrical sensors

that were fitted to a custom made mould. Three parameters of IM were focused on: V_{inj} , T_{melt} and T_{mould} . Both systems showed similar trends whereby V_{inj} and T_{melt} significantly affected electrical conductivity, whereas the influence of T_{mould} was minimal. Inline measurements were consistently higher than offline measurements. They explained the findings through a dynamic percolation framework, a destruction and re-formation of CNT network. V_{inj} and T_{melt} had opposite effects on conductivity due to the competition between the formation (faster at increased T_{melt}) and the destruction (more intense shear forces at higher V_{inj}) of the network during injection. When the melt is rapidly cooled in the mould, the CNT state is "frozen" (particularly at the mould surface), thus, the CNT network recovery is small.

Lew et al. (2011) performed a study to identify the main processing parameters that influence the volume and surface resistivity of injection moulded PC-MWCNTs (3 wt%). The IM parameters effect on electrical resistivity has been reviewed in Section 2.2.2, but their study into the role of the matrix is reviewed here. Five different matrices of molar mass M_w ranging between 12500 and 21500 g mol⁻¹ were injection moulded into bars. They reported volume resistivity to be inversely related to M_w , up to the higher M_w s (> 19500 g mol⁻¹), where volume resistivity levels off. On the other hand, as M_w increased, surface resistivity initially decreased until 14500 g mol⁻¹, and then increased with M_w . They suggested two possible explanations for the trend observed: (1) increasing M_w increases the shear gradient in steady state shear flows, thus, promoting CNT migration towards the core of the IM samples and reducing CNT presence at the sample surfaces; (2) higher M_w increases shear stress at the wall sections resulting in CNT orientation near sample surfaces. The latter is more plausible and verified by Villmow et. al's (2008a) TEMs in Fig. 2.3.

2.6.2.3 CNT network formation mechanism

In order to further understand the relationship between CNT dispersion/distribution and electrical conductivity, Alig and co-workers (Alig et al., 2007, 2008.; Pegel et al., 2008) carried out simultaneous rheological and electrical measurements in the melt regime. Alig et al. (2007) found that (1) CNTs arrange to rebuild a percolating network after destruction of the previous network by mechanical shear deformation; (2) CNT-filled systems are shear history dependent. The latter is evident from Fig. 2.10 illustrating TEMs of the same specimen of an injection moulded PC-MWCNT plate (5 wt%) with surface conductivity of 0.1 S cm⁻¹ that increases to 3 S cm⁻¹ after annealing for 1 hour at 300 °C. During melt mixing,

the primary agglomerates are broken up by rupture and erosion processes to disperse the CNTs. Depending on the processing parameters reviewed in Section 2.2, reformation of CNT aggregates, known as secondary agglomeration, occurs due to strong CNT-CNT interactions.

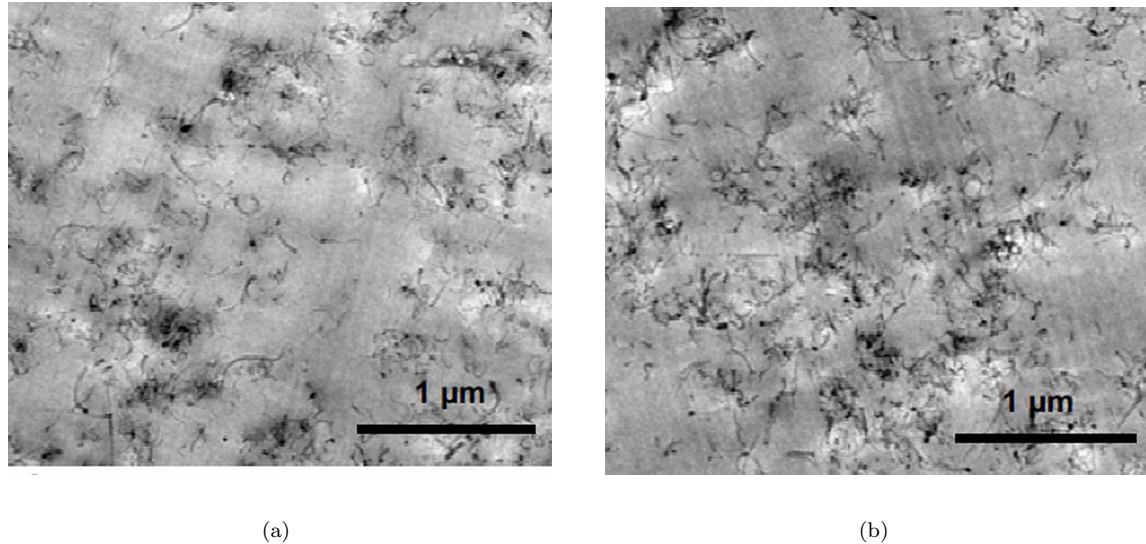


FIGURE 2.10: TEM images of (a) PC-MWCNT (5 wt%) injection moulded sheets of surface resistivity = $10 \Omega \text{ m}$ (b) after annealing for 1 hour at $300 \text{ }^\circ\text{C}$ giving surface resistivity = $10^{-1} \Omega \text{ m}$ (adapted from Alig et al. (2008c))

Alig et al. (2008) investigated the influence of melt processing parameters, particularly melt temperature and mass throughput, on electrical conductivity. They developed a measurement slit die that housed dielectric, pressure and temperature sensors and connected it to the twin screw extruder outlet. Deformation in the extruder was dominant to the slit die. Firstly, it was observed that conductivity during extrusion was small due to the shearing that disrupted the CNT network. Interestingly, when the extrusion stopped and a period of isothermal annealing was imposed, the recovery behaviour of CNTs increased the conductivity to a plateau. They found that increasing (1) annealing temperature, (2) filler loading content and (3) throughput, all reduced the period taken to reach a conductivity plateau. This was attributed to the lower melt viscosity promoting secondary agglomeration that increased CNT-CNT or CNT-to-cluster contact and minimised the destruction of the CNT network, respectively. The phenomenon observed was identified as dynamic percolation because of the time dependence for recovery of electrical conductivity. Closer inspection of the recovery, reproduced in Fig. 2.11, shows two processes. The first process recovered with an initial higher rate to a low conductivity where the recovery rate reduces; at this point, the

second process exhibits a high recovery rate up to a plateau. Alig et al. (2008) focused on explaining the latter process, which was described by combining percolation theory and a model for cluster aggregation where the clusters consist of CNT agglomerates, and very close CNT-CNT distances are assumed.

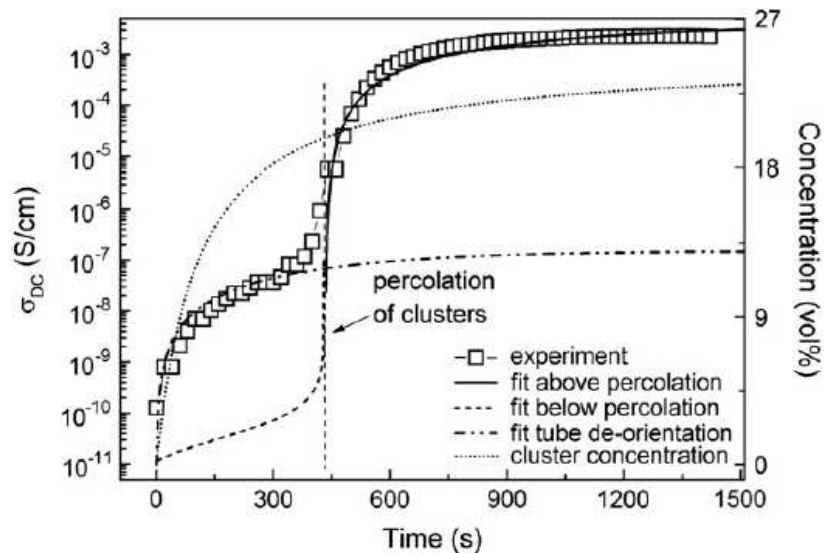


FIGURE 2.11: Electrical conductivity recovery measurements of PC-MWCNT (0.875 wt%) at 260 °C (square symbols). The electrical conductivity below the percolation threshold was calculated with percolation theory (dashed line) and a cluster aggregation model (solid line) was used for filler concentrations above the percolation threshold. The initial increase in conductivity was calculated using an empirical relaxation function for shear flow oriented CNTs (dash-dot-dot line) (adapted from Alig et al. (2008))

Zeiler et al. (2010) developed Alig et al.'s work by studying the influence of molar mass and temperature on the formation of the CNT network whilst considering the superposed effects of CNT network destruction and diffusion-controlled CNT cluster formation during the application of shear. They confirmed that the CNT network consists of weakly bonded clusters that break up and reaggregate to form a conductive pathway through combined electrical and rheological testing, as illustrated in Fig. 2.12, suggesting that the destruction of CNT-CNT bonds is reversible. Focusing on the influence of molar mass, they found that the formation of a CNT network is enhanced with a matrix of lower molar mass and at higher temperature.

The influence of thermal and mechanical history on time-dependent electrical conductive CNT networks was studied by Skipa et al. (2010) using simultaneous electrical and rheological measurements. They found that isothermal heating increases conductivity slightly and that the level of conductivity is dependent on the initial state of dispersion or agglomeration. However, an imposed shear results in a significant increase in conductivity, with CNT



FIGURE 2.12: Schematic of PC-MWCNT with CNT agglomerates (within circles) that cluster to form a pathway for electrical conductivity (reproduced from Zeiler et al. (2010))

agglomerated samples showing a minimum point in electrical conductivity with respect to time, as shown in Fig. 2.13.

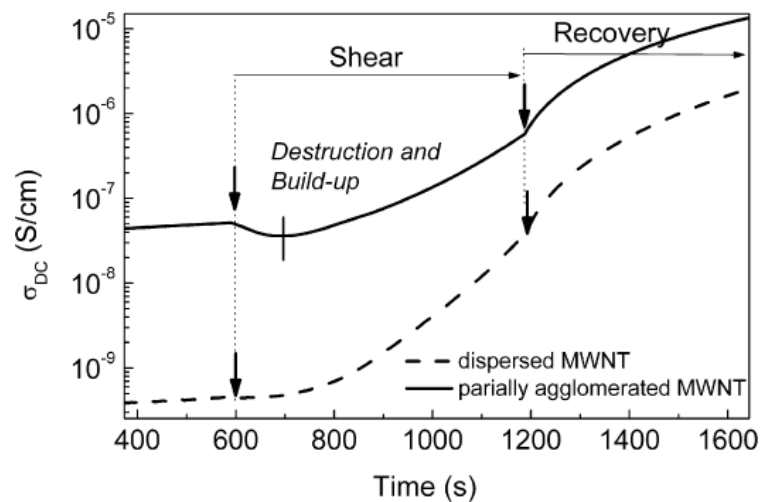


FIGURE 2.13: Electrical conductivity time dependence measured for 2 hours of annealing followed by a steady shear rate of 0.02 rad s^{-1} for 600 s and a quiescent recovery. The solid lines represents partial MWCNT agglomeration whereas dashed lines represent well dispersed MWCNTs (adapted from Skipa et al. (2010))

A local minimum for conductivity can be explained by the destruction of the network formed in the annealing phase prior to the application of shear. As shearing continues, the smaller agglomerates start to build-up a new conductive network through individual tubes or agglomerates being "picked up" to form connections. When there is sufficient time for recovery, the conductivity can reach equilibrium. The same trend was seen even when CNT loading content was increased, although the plateau value during the annealing phase increased. The

simultaneous measurement suggested that the electrical conductive network and the mechanical network are different. Skipa and co-workers (2010) used steady state shear as a tool to study the effects of CNT dispersion levels on electrical conductivity of PC-MWCNT systems. They found that regardless of the initial level of CNT dispersion, an equilibrium conductive network is reached after a sufficient period of shear, illustrated in Fig. 2.14. They proposed a model based on a kinetic equation and the generalised effective medium theory to capture the time dependence and shear induced electrical response.

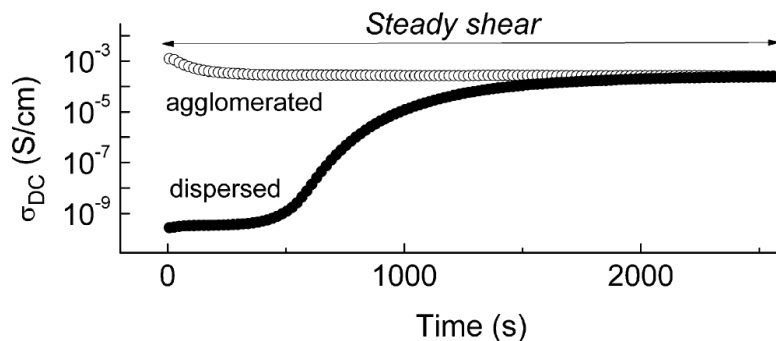


FIGURE 2.14: Electrical conductivity of initially dispersed (solid circles) and agglomerated CNT (hollow circles) under steady shear rate of 0.02 rad s^{-1} for 1 hour (adapted from Skipa et al. (2010))

Electrical investigations on nanocomposite melts have shed light into the mechanisms of the formation of the CNT network, and on what are the critical parameters for melt processing required to obtain secondary agglomeration favouring electrical conductivity. This understanding of CNT network formation can be employed to help to understand material properties such as thermal and mechanical response of the final product.

2.7 Rheology

Rheology is the study of the response of materials to flow. For polymers, it can provide an insight into the macromolecular structure of the polymer across a wide temperature range. This is crucial in determining the processability of filled thermoplastics polymers. One of the rheological measurement techniques of concern to this work is dynamic oscillatory rheology, where a specimen is subjected to sinusoidal deformations, and the material's response is measured as a function of time and/or frequency. The sinusoidal oscillation is imposed via controlled shear stress or shear strain, and the resultant shear strain or shear stress is measured. In the linear region, shear stress is proportional to shear strain. A phase difference,

δ can develop between the stress and strain sinusoids. This information is transformed into quantities such as storage modulus, G' , loss modulus, G'' , and complex viscosity, η^* for a given frequency.

G' measures the energy stored in the sample, representing the elastic behaviour, and is expressed as (Mezger, 2011)

$$G' = \frac{\tau_o}{\gamma_o} \cos \delta \quad (2.12)$$

where τ_o is the stress amplitude and γ_o is the strain amplitude

G'' measures the energy loss in the sample, representing the viscous behaviour, and is expressed as (Mezger, 2011)

$$G'' = \frac{\tau_o}{\gamma_o} \sin \delta \quad (2.13)$$

Oscillatory shear tests are divided into two categories: small amplitude oscillatory shear (SAOS) and large amplitude oscillatory shear (LAOS). SAOS probes the linear viscoelastic properties at small strains, typically up to 10% strain for unfilled polymers. Below this value the viscoelastic modulus is independent of strain amplitude. LAOS investigates non-linear viscoelastic properties where the material response is no longer sinusoidal (Mezger, 2011). It is used to gain structural information for when strains exceed the linear range, for example, when a polymer is injection moulded into shape (Hyun et al., 2011).

Rheometry has been employed to investigate several varieties of polymer nanocomposites embedded with nanometre-sized fillers to gain information on the interactions between filler and polymer. In much the same way as the properties reviewed in the previous Sections, the nanocomposite viscoelastic response is affected by similar factors. The final properties of any polymeric product depend on the processing methods that induce melt-state deformations. Thus, measurements of the non-linear region provides useful additional data for industrial processing where deformations can be significant and rapid, resulting in the dispersion, agglomeration and alignment of the fillers.

2.7.1 Linear rheology of thermoplastic-CNT nanocomposites

The initial step of any rheological study is to determine the effect of the filler's presence on the linear viscoelastic response of the base matrix. The strain amplitude imposed during oscillatory tests must not exceed the maximum strain for linear viscoelastic behaviour. Hence,

oscillatory shear amplitude sweeps at a constant frequency are performed to determine the limit of the linear region. The presence of CNTs have been found to decrease the linear viscoelastic range in thermoplastic-CNT nanocomposites (Abdel-Goad and Pötschke, 2005; Du et al., 2004; Meincke et al., 2004; Pötschke et al., 2002; Wu et al., 2007). Isothermal frequency sweeps have been used to study the change in structure between the filled and unfilled matrix. The frequency range should be as broad as possible to understand the relaxation mechanisms of the nanocomposite system (Nobile, 2011).

2.7.1.1 Effect of CNT loading content

Increasing CNT loading content in the matrix induces a step-wise change in the viscoelastic behaviour, similarly to electrical response. This point is known as the rheological percolation threshold and represents the transition from liquid to solid-like behaviour. The identification of this threshold has been performed through various means: (1) observing an exponential increase in G' against loading content (Abbasi et al., 2009; Du et al., 2004), (2) a significant increase in G' against frequency (Pötschke et al., 2004, 2002), (3) Cole-Cole plot (the imaginary part of η^* as a function of the real part) (Wu et al., 2007), (4) modified Cole-Cole plot (G' as a function of G'') (Pötschke et al., 2002) and (5) the van Gorp-Palmen plot (phase angle, δ as a function of complex modulus, G^*) (Meincke et al., 2004; Nobile et al., 2007; Pötschke et al., 2004; Wu et al., 2007).

As the formation of a filler network structure is responsible for both rheological and electrical properties of nanocomposites, the process parameters discussed in Section 2.6.2 are also relevant to the rheological response. Du et al. (2004) found that the rheological percolation threshold for PMMA-SWCNT system was lower than that of the electrical percolation threshold, and postulated that the difference was due to the CNT-CNT distance required between electrical conductivity and mechanical structure. Similar observations were recorded for PA6-MWCNT systems by Meincke et al. (2004). However, similar percolation thresholds have also been reported in LDPE-MWCNT and HDPE-MWCNT (Valentino et al., 2008), attributed to weak polymer-CNT interactions.

2.7.1.2 Oscillatory shear studies

Frequency dependence of a MWCNT nanocomposite's rheological response was initially studied by Pötschke et al. (2002) on PC-MWCNT with varying filler loadings of from 0.5 to 15 wt%. Dynamic rheological experiments were performed at 260 °C, and some of their results are reproduced in Fig. 2.15. They observed an increase of G' and G'' with frequency for all filler concentrations, and an increase of G' and G'' with concentration at any given frequency, as is clear from Fig. 2.15(a) and (b). The effect of CNT concentration on the moduli was more pronounced at low frequencies than at high frequencies. They found that η^* , shown in Fig. 2.15(c), was increased substantially at low frequencies by the addition of CNTs and that the effect reduced with increasing frequencies. Interestingly, η^* at low CNT loadings (<1 wt%) responded to frequency in a manner that was very similar to the unfilled PC. This indicated that rheological response of PC with low filler loading was relatively unaffected by the presence of CNTs. They attributed the change in η^* to the increase in G' . The significant increase in G' for samples with >2 wt% CNT was accounted for by the formation of an interacting CNT structure appearing at a critical concentration. Satapathy et al. (2007) performed similar rheological tests to characterise the CNT percolation threshold and dispersion in PC-MWCNT nanocomposites. They observed the same significant shift in G' and η^* at 2 wt% CNT loading from the pure PC samples as seen by Pötschke et al.. The lack of a dependence of moduli or frequency at low frequencies led them to conclude that the system was already rheologically percolated.

The plateau at low frequencies, seen in Fig. 2.15, suggests that the CNT network affects the relaxation of polymer chains (Du et al., 2004) and masks the contribution of polymer entanglements to the moduli (Pötschke et al., 2004). Several studies on different matrices have reported similar observations to those of Pötschke whereby the rheological percolated nanocomposites exhibit frequency-independent moduli at low frequencies. This was observed in PA-MWCNT (Meincke et al., 2004), PBT-MWCNT (Wu et al., 2007), and PE-MWCNT (Nobile et al., 2007).

Recently, Han et al. (2011) found that bending, or waviness of CNTs (characterised by the longest length without permanent bending, l_{sp}) also affects rheological properties: an increase of l_{sp} , increased G' .

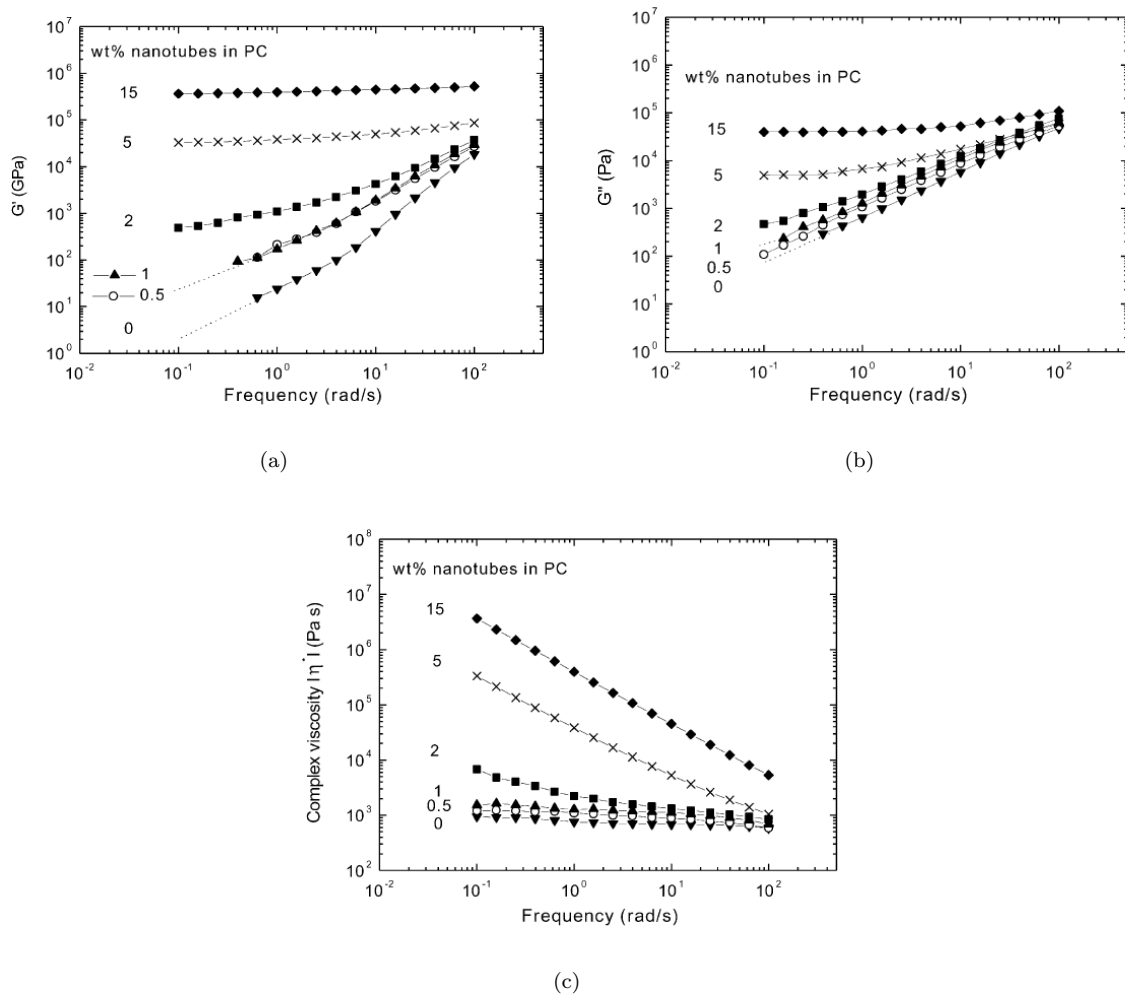


FIGURE 2.15: (a) Storage modulus, G' , (b) loss modulus, G'' and (c) complex viscosity, η^* as a function of frequency and increasing MWCNT (0.5-15 wt%) loading in PC, at $T = 260$ °C (adapted from Pötschke et al. (2002))

2.7.1.3 Influence of temperature

Pötschke et al. (2004) found that rheological properties of PC-MWCNT were significantly temperature-dependent. They investigated the frequency dependence of G' , G'' , η^* and loss tangent of PC-MWCNT nanocomposites at temperatures of 170 - 280 °C. Fig. 2.16 presents G' as a function of frequency at varying temperatures. The magnitude and shape of the G' against frequency curves were notably different at as temperature increased. Thus, the percolation threshold was found to be temperature-dependent. They suggest that the polymer-CNT network and the superposition of an entangled polymer network dictate the rheological properties. They assumed the interaction between polymer chains and CNTs to be more stable than those between entangled polymer chains. Therefore, the disentanglement

time for the polymer in the nanocomposite becomes larger than the characteristic time for loss of polymer-polymer entanglements (Abdel-Goad and Pötschke, 2005).

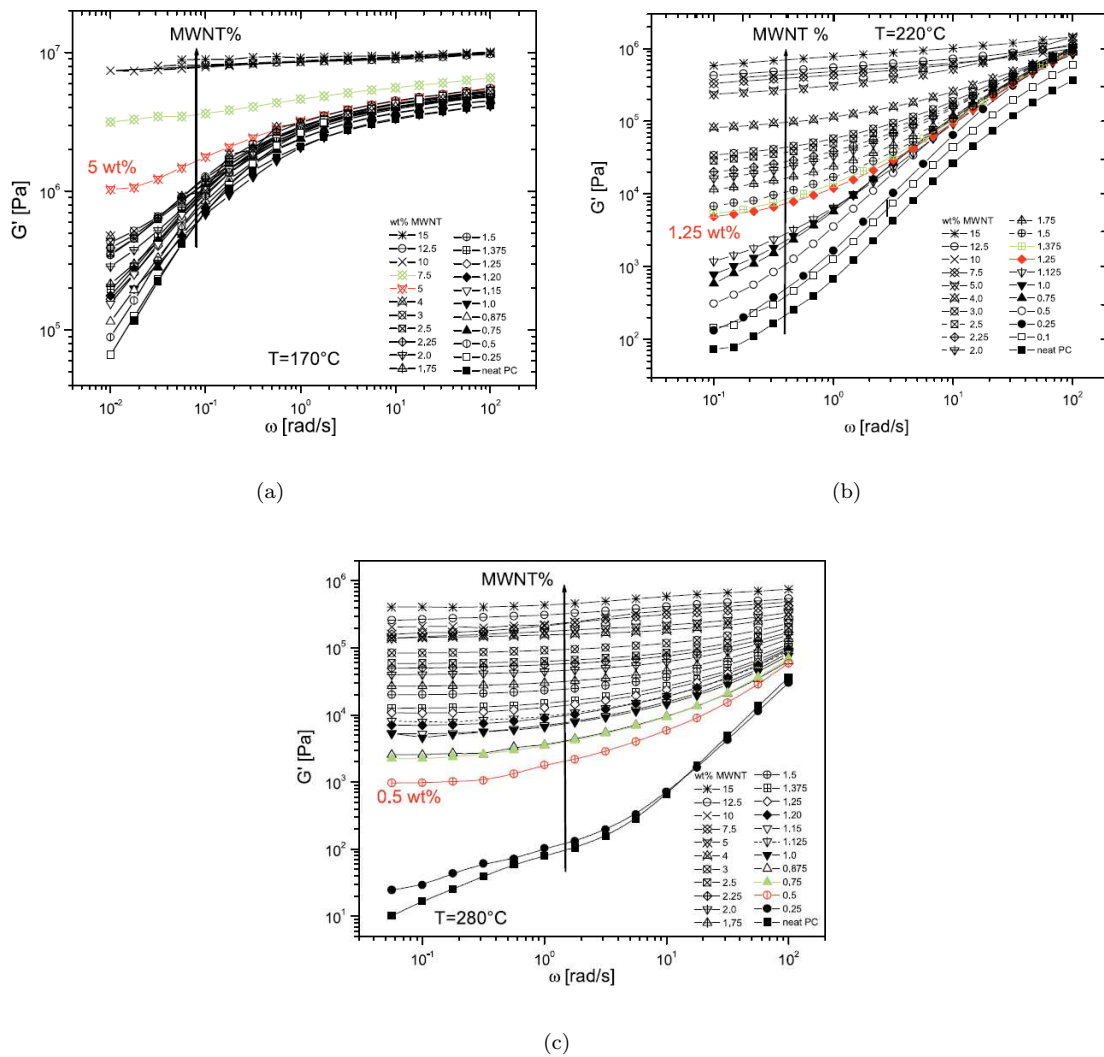


FIGURE 2.16: Frequency dependence of storage modulus with increasing temperature at (a) 170 °C, (b) 220 °C and (c) 280 °C (adapted from Pötschke et al. (2004))

2.7.1.4 Influence of matrix molar mass

One of the earliest studies into the role of the matrix on nanocomposites was that by Fornes et al. (2001). They studied the effect of molar mass of PA6-organoclay on the rheological behaviour. Although the filler in the reference is dissimilar from that of those in this work, the emphasis on the role of the matrix is of interest. Three different polymer matrices with M_n ranging from 16400 to 29300 g mol⁻¹, representing low (LMW), medium (MMW) and high molar mass (HMW) grades were studied. Two main observations were reported from dynamic

rheological measurements: (1) an increase in η^* and steady state shear viscosity, η with increasing molecular weight, as reproduced in Fig. 2.17, (2) and a change in the behaviour at low frequency oscillation. These LMW and MMW exhibited fluid-like behaviour, whereas the HMW revealed solid-like behaviour. The G' curves shown in Fig. 2.17(d) exhibit terminal slopes, which were attributed to the degree of exfoliation of the organoclay within the matrix. The greater degree of exfoliation increases the polymer-filler interactions leading to solid-like behaviour.

The Cox-Merz relation, expressed in Eq. 2.14, is an empirical observation for polymer melts that relates η and η^* (oscillatory shear viscosity), for analogous shear rate, $\dot{\gamma}$, or angular frequency, ω (Mezger, 2011).

$$\eta(\dot{\gamma}) = |\eta^*(\omega)| \quad (2.14)$$

Fig. 2.17 shows $|\eta^*|$ for (a) LMW, (b) MMW and (c) HMW. It was observed for all three molar masses of PA that the Cox-Merz relation failed for the nanocomposite. This was also reported for PC-MWCNT by Pötschke et al. (2002). This means that steady state η does not correspond to the η^* determined in oscillatory shear. Hence, the Cox-Merz relationship can't be used to predict shear viscosity of nanocomposites from complex viscosity data and vice versa. The ability to predict η is desirable because it is difficult to obtain the data experimentally at high shear rates due to factors such as sample fracture.

Fornes et al. (2001) postulated that high melt viscosity produces greater shear stress in the melt, and in turn, provides better exfoliation of the filler. This suggests that increasing the molecular weight of a given matrix could also provide a better dispersion of CNT agglomerates. On the other hand, Abdel-Goad and Pötschke (2005) found that the rheological percolation threshold was observed to occur in PC-MWCNT at CNT loadings of 0.25 - 0.5 wt%. This is lower than the 2 wt% obtained by Pötschke's earlier work in 2002 and Satapathy's group later in 2007. They suggested that the difference was due to the lower molar mass of PC, the higher rheological measuring temperature, as well as the higher mixing temperatures and longer mixing time. Zeiler et al. (2010) measured a higher storage modulus for nanocomposites with lower matrix viscosity (i.e. lower molar mass) and proposed that the shorter polymer chains encouraged higher density of CNT-CNT contact to form, resulting in a CNT network with higher stiffness; this was supported by higher electrical conductivity measurements at lower PC molar mass.

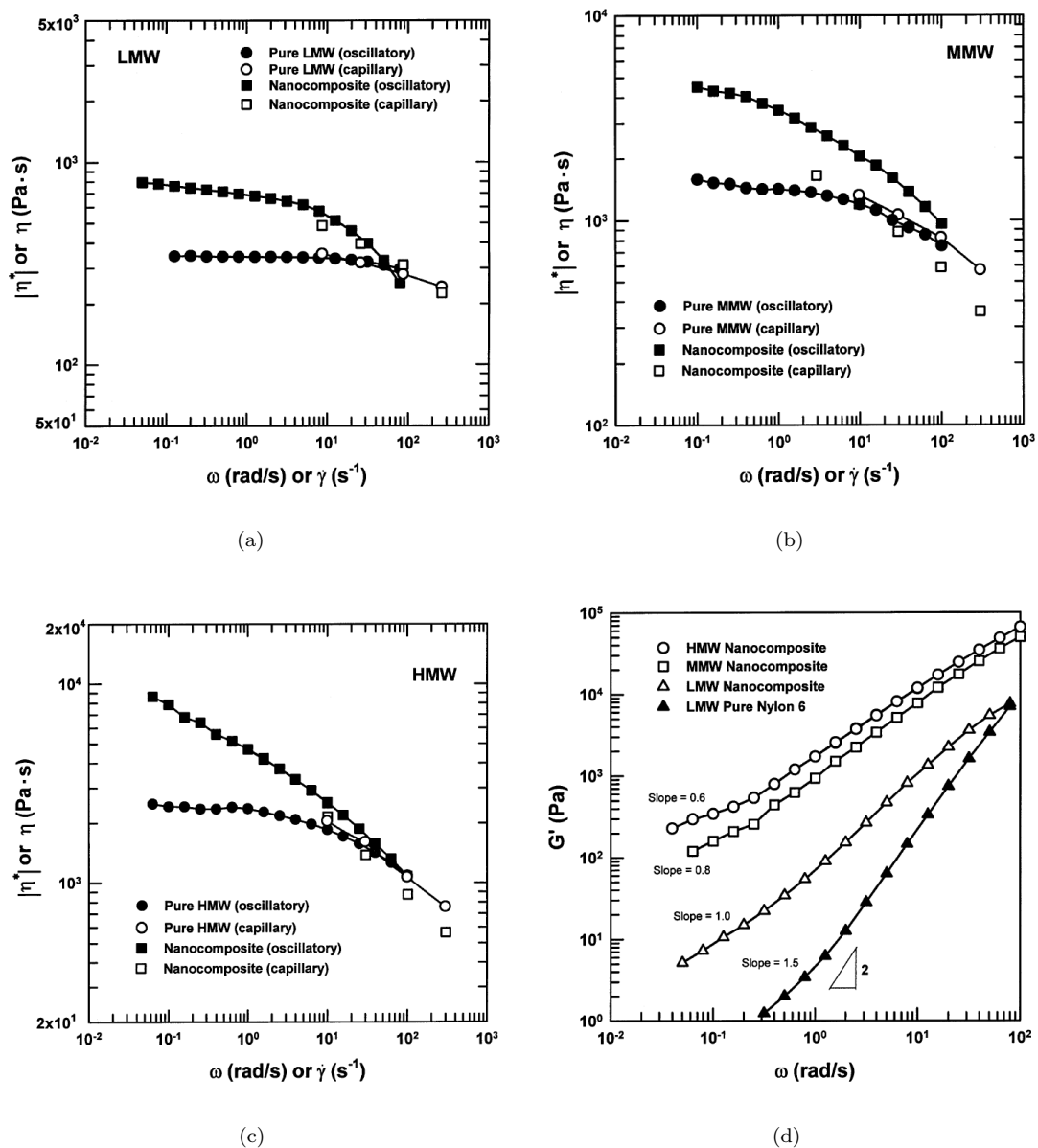


FIGURE 2.17: Complex viscosity as a function of frequency for increasing molar mass: (a) low molar mass ($M_n = 16400 \text{ g mol}^{-1}$), (b) medium molar mass ($M_n = 22000 \text{ g mol}^{-1}$), and (c) high molar mass ($M_n = 29300 \text{ g mol}^{-1}$). (d) Storage modulus as a function of frequency for increasing molar mass (adapted from Fornes et al. (2001))

Work on PMMA-SWCNT by Du's group (2004) found that the nanocomposites with a higher matrix molar mass had a smaller low frequency G' slope and larger G' at low frequencies. The authors postulated that if the rheological response was dominated by the CNT network, the viscoelastic response of samples with the same loading content should be identical. Fig. 2.18 shows their data, which contradicts to this postulate. This led them to the conclusion that the CNT network constrained polymer chain motions of the higher molar mass matrix. This is in contrast to Fornes's group, who suggested that greater CNT dispersion could be achieved

with higher PC molar mass. On the other hand, Nobile et al. (2007) observed an insignificant effect of molar mass on the rheology of PE-MWCNT. They attributed the behaviour to a lack of filler-matrix interactions.

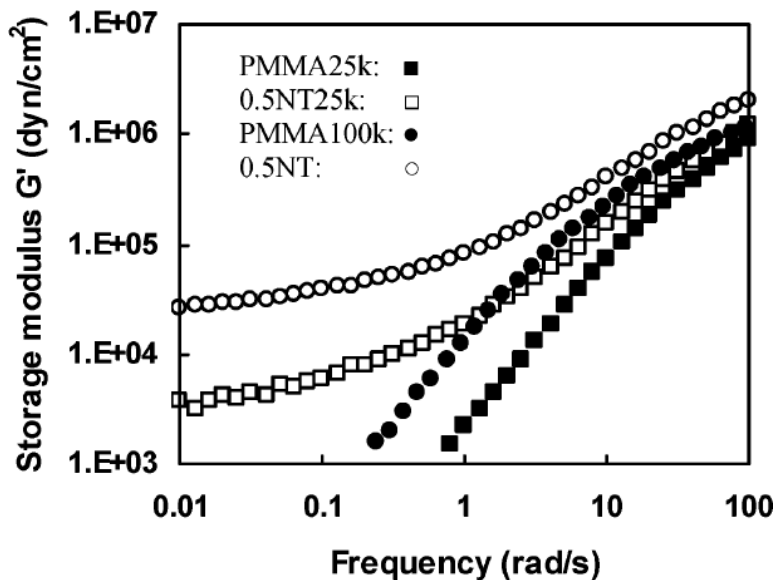


FIGURE 2.18: Viscoelastic response of PMMA-SWCNT with 0.5 wt% for two different polymer molar mass. PMMA25K = 25000 g mol⁻¹; 0.5NT25K (filled) = 25000 g mol⁻¹; PMMA100K = 100000 g mol⁻¹; 0.5NT100K (filled) = 100000 g mol⁻¹ at $T = 200$ °C (adapted from Du et al. (2004))

2.7.1.5 Influence of orientation and dispersion of CNTs

Du et al. (2004) measured the influence of CNT dispersion and CNT alignment on the rheological behaviour on PMMA-SWCNT. They observed that good CNT dispersion increased G' as a function of frequency. CNT alignment reduced filler-filler contact, reducing reinforcement of the matrix and leading to lower G' at low frequencies. The effect of CNT orientation induced by different processing methods was in agreement with the literature. High shear methods such as micro-injection moulding resulted in lower G' and significantly increased percolation thresholds relative to compression moulded samples (Abbasi et al., 2009). In addition, Sung et al. (2006) and Wu et al. (2007) both measured higher G' for functionalised MWCNTs compared to pure MWCNTs, showing that CNT treatment can also affect the rheological response.

2.7.2 Non-linear rheology of thermoplastic-CNT nanocomposite

2.7.2.1 Transient, steady state and elongational shear

The previous section showed that the presence of CNTs within a matrix leads to the formation of a CNT-CNT network that affects the viscoelasticity of the base matrix. However, non-linear melt rheology is more relevant to typical processing methods in industry. Methods such as transient and steady shear, and elongational shear are required to achieve similar shear rates and flow as the processing conditions. Information from these methods sheds light on the behaviour of the CNT network during melt processing.

Kharchenko et al. (2004) performed steady-state shear measurements on PP-MWCNT (2.5 vol%) and reported viscosity decreasing with increasing shear rates, indicating strong shear thinning. Similar observations of shear thinning were reported for PC-MWCNT (3 wt%) (Lew et al., 2011), HDPE-MWCNT (2.5 wt% and 5 wt%) (Nobile, 2011) and poly(ethylene oxide)(PEO)-SWCNT (Chatterjee and Krishnamoorti, 2008). Lew et al. (2011) found that both unfilled and MWCNT-filled PC exhibit shear thinning behaviour that is dependent on M_w (12500-21500 g mol⁻¹). They observed that filled PC follows the power-law fluid model. Shear viscosities of all filled PC converged to their unfilled counterparts and crossed over to record lower values, as shear rates increased from 50 to 5000 s⁻¹. Additionally, the rate of shear thinning decreased with increasing CNT loading content (1.8 - 4 wt%), and also followed a power law. They attributed both findings to interface chain slippage as a result of CNT orientation during flow, and suggested that exfoliation of CNT agglomerates could lead the CNT walls to behave as a plasticising agent.

Wu and co-workers (2007) performed the transient shear stress studies on PBT-MWCNT (5 wt%) to investigate the shear deformation history of the CNT network. They suggested a procedure: to shear PBT-MWCNT for 300 s at a fixed shear rate (0.5 s⁻¹), and keep the melt quiescent for a period (up to 120 s), prior to shearing the sample in the *reverse* direction. They found that the magnitude of stress overshoot increased with the quiescent period and reached the same plateau regardless of rest times. The overshoot is associated to the polymer chain entanglement resistance to flow (Nobile, 2011). This implied (1) that the destroyed CNT network had rearranged during the imposed rest time, resulting in an overshoot when the shear was reversed; (2) that CNTs are difficult to roll over under steady shear flow (Wu et al., 2007). Nobile and co-workers performed transient shear stress on HDPE-MWCNT

(2.5 wt% and 5 wt%) and also observed a stress overshoot for shear rates between 0.2 and 2.0 s⁻¹.

Chatterjee and Krishnamoorti (2008) applied a continuous shear stress on PEO-SWCNT for shear rates ranging between 1 and 5 s⁻¹. For all shear rates, they found an initial stress overshoot that reached to plateau after a time period, without applying any oscillatory shear. The overshoot was attributed to the rearrangement of the CNT cluster network structure, induced by shear.

The destruction and reformation of a CNT network structure in PC-MWCNT (0.875 wt%) was investigated in detailed by Alig et al. (2008) using a combined rheological and dielectrical setup. They annealed the melt for 7200 s and applied defined transient shear to PC-MWCNT to destroy the CNT network. Both the modulus and the conductivity recovered to original values after a rest time. This phenomenon was attributed to the destruction and reformation of CNT agglomerates that were described as spherical objects consisting of loosely packed MWCNTs. The same group (Skipa et al. (2010)) then investigated the CNT network under steady shear. They found that the nanotube network, relating to rheological and electrical properties, reached a steady state value after long shear periods, regardless of the initial CNT dispersion levels, as illustrated in Fig. 2.19. The constant moduli and conductivities suggest that a stationary CNT network is formed under steady shear conditions (Skipa et al., 2010). They also found that the transient viscosity showed a shear overshoot, attributed to the destruction of the CNT network, and evident from X-ray measurements. The time dependence of G' and G'' in a quiescent melt, quasi steady-state shear and oscillatory shear can be explained through the competition of breakup and formation of agglomerates under shear, which have been described through kinetic models by Alig et al. (2008). These findings highlight that steady-state shear is not always destructive to the CNT network.

Transient elongational shear of PC-MWCNT (2 wt%) was investigated by Handge and Pötschke (2007). The experiments were carried out at $T = 190$ °C, up to a Hencky strain of 2.4 (stretch ratio, $\lambda = 11$) for Hencky strain rates between the range of 0.1 and 1.0 s⁻¹. In comparison to unfilled PC, the presence of CNTs only had moderate influence on the transient elongational viscosity. They attributed the finding to the higher stresses in the matrix relative to the stresses induced by the MWCNTs. PC-MWCNT elongation behaviour is analogous to oscillatory behaviour at high frequency, where the matrix dominates the modulus (Handge and Pötschke, 2007).

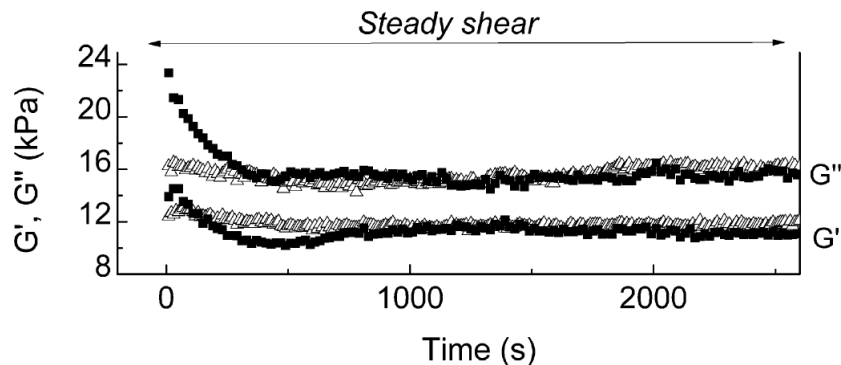


FIGURE 2.19: Storage modulus, G' and loss modulus, G'' of initially dispersed (solid squares) and agglomerated CNT (hollow triangles) under steady shear rate of 0.02 rad s^{-1} for 1 hour (adapted from Skipa et al. (2010)). The corresponding electrical conductivity measurement is presented in Fig. 2.14

In the same study, transient recovery after stretching was also investigated. Upon reaching λ , samples were immediately cut at one end while the opposite end remained clamped, and left free for 3600 s. They reported that the recovery of PC-MWCNT was less than that of unfilled PC, due to the CNT network restricting the recovery of the large extensions of the polymer chains, and giving rise to a yield stress in PC-MWCNT. TEM images of elongated PC-MWCNT showed that the individual CNTs were oriented in the flow direction, but returned to a random orientation after the recovery period.

2.7.2.2 Non-linear oscillatory shear

Wu et al. (2007) performed frequency sweeps ($0.02\pi - 20\pi \text{ rad s}^{-1}$) on PBT-MWCNT (3 wt%) at strains of 1% with increasing pre-shear shear rates of 0.5 up to 5 s^{-1} for $T = 240 \text{ }^\circ\text{C}$. They found that G' and G'' decreased as shear rates increased, particularly in the terminal region. When the CNTs were not oriented (no pre-shear), PBT-MWCNT showed solid like behaviour at low frequency. After the pre-shear treatment, $G'' > G'$ for all frequencies, indicating liquid-like behaviour. They suggested that the MWCNTs were very sensitive to shear flow and resulted in CNT orientation that decreased filler-filler interactions, and that led to a transition from solid to liquid-like behaviour.

Wu's group (2007) then performed the same frequency sweeps on PBT-MWCNT (3 wt%) but at higher strains, ranging from 10 up to 50%, and without pre-shearing. In contrast to the pre-shear experiments described earlier, they found G' to be independent of low frequency, as presented in Fig. 2.20(a). This is observed in spite of the rise of $\tan \delta$ with increasing strain amplitude, demonstrating that the viscosity of PBT-MWCNT increases

with strain levels. They reconcile the finding by suggesting that during LAOS: (1) CNTs oriented by shear are hard to rotate or roll over; (2) rigidity of CNTs and the decrease in chain entanglements around the CNTs results in transient phase separation; and (3) long term CNT relaxation behaviour. Cole-Cole plots are a method used to illustrate viscoelastic properties of materials using the shape of the curve (Mezger, 2011). The semi-arc shape of the Cole-Cole plot exhibited in Fig. 2.20(d) indicates (3) whereas the upturn at low viscosities indicated by the arrows in the circle verifies (2).

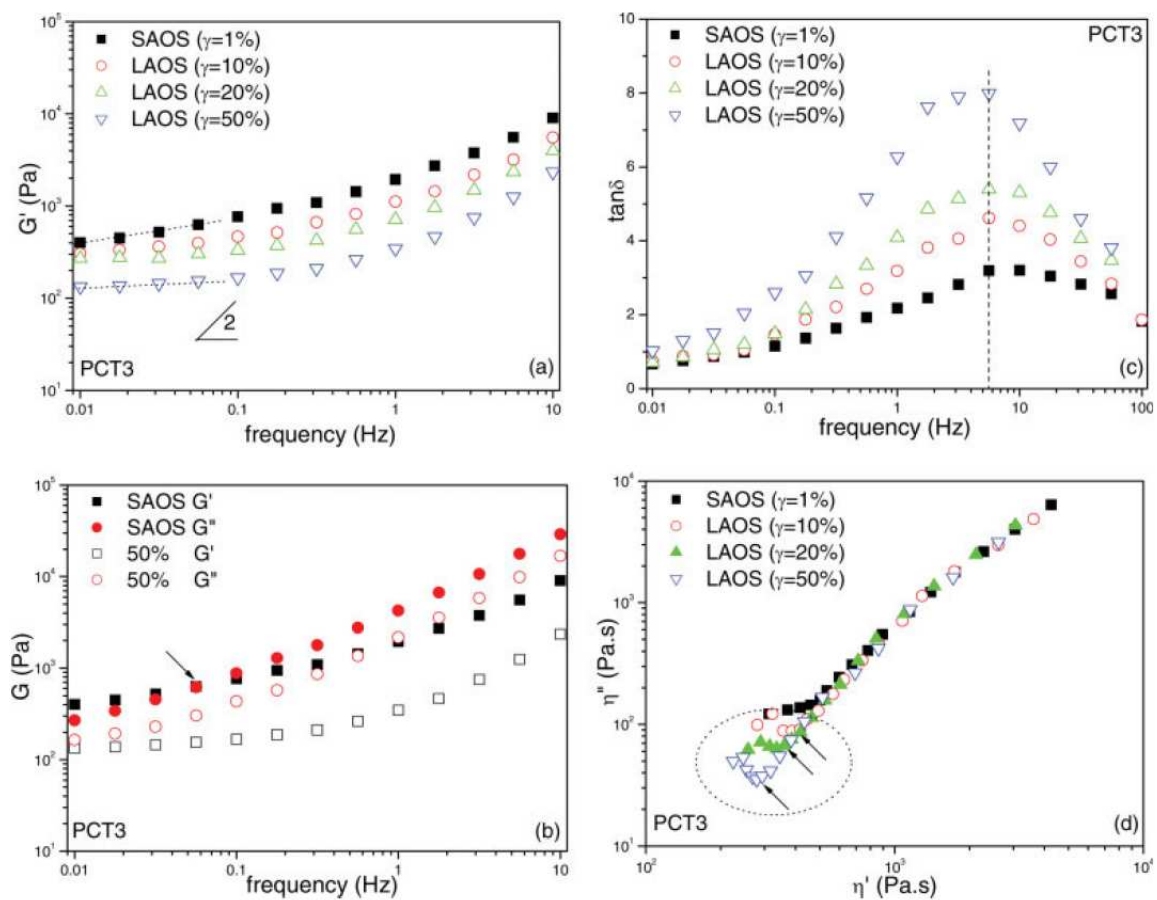


FIGURE 2.20: (a) Storage modulus, G' of PBT-MWCNT (3 wt%) at different levels of strain. (b) Comparison of SAOS and LAOS measurements of G' , and (c) $\tan \delta$. (d) Cole-Cole plot of complex viscosity, η^* (the imaginary part η'' of as a function of the real part η') at different levels of strain (reproduced from Wu et al. (2007))

2.8 Summary

This chapter has presented existing relevant literature on the thermal, mechanical, electrical and rheological properties of thermoplastic and CNT based nanocomposites, with attention

given to processing parameters effects. The constituent materials of the nanocomposite concerning this work were introduced in Section 2.1.

Section 2.2 presented the processing routes for thermoplastic-CNT nanocomposite, with emphasis on the melt processes. Two categories of melt processes are focused: melt compounding and melt forming (or moulding). The first process is concerned with the mixing of the nanocomposite constituent materials, which is then formed to required shape using second process. The parameters of both processes influence the morphology of nanocomposites and ultimately, their final properties. Previous work on the relationship between various processing parameters and the CNT network morphology in nanocomposite systems has presented. The literature on quantifying the state of CNT dispersion in the matrix using OM micrographs was summarised in Section 2.3.

Section 2.4 provided an overview of literature on the thermal conductivity and thermal degradation of thermoplastic-CNT nanocomposites. Factors that influence the thermal behaviour and the proposed degradation mechanisms for CNT-nanocomposite available in literature were reported. Currently, there is no unified agreement on which factors affect thermal degradation due to the complexity of the degradation mechanism in nanocomposite systems.

Previous work on mechanical properties of CNT nanocomposites has been reviewed in Section 2.5. The literature is used to highlight the factors affecting mechanical properties that can be divided into processing and material related parameters. Processing dictates the CNT network structure and morphology whereas material parameters include CNT characteristics and matrix chemistry. Investigations into these parameters facilitate an understanding of the mechanical reinforcement and of failure mechanisms of filled systems.

Section 2.6 reviewed the electrical resistivity of CNT nanocomposites. Factors influencing electrical resistivity are similar to those influencing mechanical properties, processing and material related parameters. The development of a dynamic percolation framework, that is, the destruction and reformation of the CNT network, for electrical conductivity was presented in Sections 2.6.2.2 and 2.6.2.3. The influence of processing on electrical resistivity and combined electrical and rheological studies have enabled an understanding of CNT network formation. This can explain how specific properties may be optimised through different CNT network morphology.

Rheological studies have been reviewed in two parts: linear and non-linear rheology. Section 2.7.1 reported on the influence of CNT loading content, of melt temperature, and of matrix molar mass, on the linear rheological properties of CNT nanocomposites. Dynamic oscillatory measurements were used to study the relaxation of the base matrix and to provide an indication of the state of dispersion and orientation of CNTs in the melt state. Section 2.7.2 reviewed the non-linear rheological behaviour of CNT nanocomposites. The transient and elongational shear investigations revealed that CNT nanocomposites are shear thinning and that the CNT network can re-form after shear deformation. This is further evidenced by combined electrical and rheological studies demonstrating that steady state shear is not necessarily destructive to the CNT network.

Chapter 3

Materials and preparation

3.1 Materials

3.1.1 Polymer matrix materials

The polymer matrix materials used in this study are PC resins ranging from low viscosity to high viscosity. Low viscosity grades Makrolon[®] 2205 and 2405, medium viscosity grade Makrolon[®] 2805 and high viscosity grade Makrolon[®] 3105 were supplied by Bayer MaterialScience AG, Germany. The Makrolon[®] family has characteristics such as high toughness, transparency, good electrical insulating properties, good heat resistance and are easily processed with various moulding methods. These characteristics currently serve commercial applications that includes lighting components, optical lenses, cosmetic packaging and medical devices (i.e. injection systems and surgical instruments).

The melt flow rate (MFR) is a measure of the flow of polymer melts and is typically used in industry for evaluations as an indication of polymer viscosity. A similar quantity to MFR is the melt volume rate (MVR) that is beneficial if the melt density, ρ_{melt} of the polymer is unknown. MFR relates to MVR through the expression

$$\text{MFR} = \text{MVR}(\rho_{\text{melt}}) \quad (3.1)$$

Table 3.1 presents MFR and MVR determined by Bayer MaterialScience AG (2012) under conditions of 300 °C and a load of 1.2 kg, and the calculated melt densities for the corresponding temperature using Eq. 3.1.

TABLE 3.1: Melt flow rate, melt volume rate and melt density of PC matrix at 300 °C (Bayer MaterialScience AG, 2012)

Material	MFR ($\text{g } 10 \text{ min}^{-1}$)	MVR ($\text{cm}^3 10 \text{ min}^{-1}$)	ρ_{melt} (g cm^{-3})
PC 2205	37	34	1.1
PC 2405	20	19	1.1
PC 2805	10	9.0	1.1
PC 3105	6.5	6.0	1.1

3.1.2 Filler material

The MWCNTs used in this work were manufactured and supplied by Nanocyl S.A., Belgium via catalytic CVD process, identified as grade NC7000. Carbon purity levels of 90% were reported by the manufacturer (Nanocyl S.A., 2009a). The median diameter and median length of NC7000 nanotubes as received from the manufacturer were measured as 10 nm and 1341 nm respectively by TEM, as shown in Fig. 3.1 (Castillo et al., 2011; Krause et al., 2011). The CNTs were dispersed in chloroform by ultrasonic treatment for 3 minutes prior to imaging.

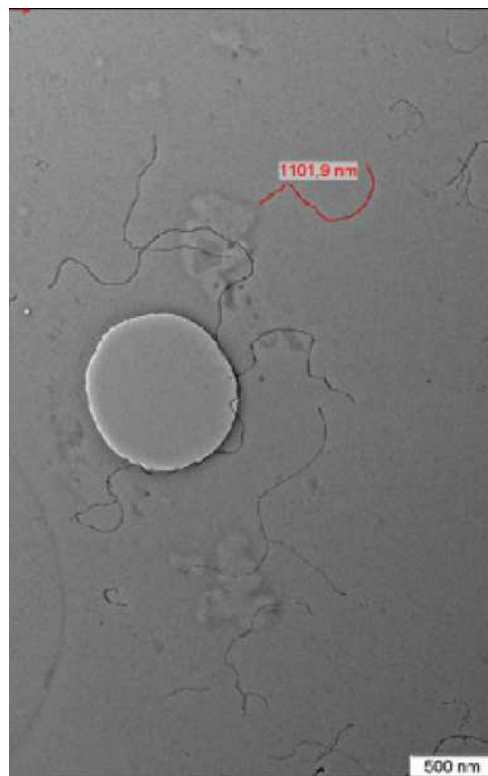


FIGURE 3.1: A TEM image of NC7000 MWCNTs obtained by merging two images for the measurement of the length and diameter of CNTs. A typical measurement of a CNT length is identified in red (Krause et al., 2011)

3.2 Melt compounding

PC-MWCNTs were melt compounded by Nanocyl S.A. using an Industrial Leistritz ZSK-MAXX co-rotating twin-screw extruder with a proprietary screw profile with a length to diameter ratio of 48:1. The MWCNTs were gravimetrically fed into PC melt through a twin-screw side feeder with a nominal mass fraction of 3 wt% for all PC resins. The extrusion screw speed was fixed at 300 rpm and the compounding temperature varied between 230 and 290 °C. The extrudate was pelletised into granules for subsequent forming processes to specific geometries.

The melt mixing was performed to prepare three separate categories of filled materials. Firstly, four grades of PC resin of different molecular weight melt were filled with a constant mass fraction of MWCNTs and compounded at a fixed temperature of 280 °C, in order to study the role of the matrix on the behaviour of the filled materials. In the second category, PC 2205 was compounded with MWCNTs at extrusion temperatures between 230 and 290 °C in 10 °C increments, in order to explore the influence of compounding temperature on the materials properties. Lastly, to assist the determination of possible degradation of the matrix during compounding, virgin PC 2205 was put through the twin-screw extruder under the same conditions as for the nanocomposites compounded at 280 °C. This grade of PC was identified as PC 2205 1-pass. Table 3.2 lists all the PC grades used in this study that were melt compounded.

TABLE 3.2: Melt compounded materials of different PC grades

Material	Filler content (wt%)	Compounding temperature (°C)
PC-MWCNT 2205	3	230 - 290
PC 2205 1-pass	0	280
PC-MWCNT 2405	3	280
PC-MWCNT 2805	3	280
PC-MWCNT 3105	3	280

3.3 Preparation methods

After melt compounding and extrusion, sample needs to be formed into specific geometries prescribed by the characterisation methods of interest. Sample preparation methods are crucial in determining the microstructures of the specimens as the methods could influence

the orientation and distribution of the fillers in the matrix (see Section 2.2.2). Compression moulding is an effective laboratory method to produce isotropic samples. Injection moulding, on the other hand, is an established industrial manufacturing method for processing thermoplastics. The two methods induce different thermal and shear histories on the material, resulting in different microstructures, and ultimately affecting the final properties of the material.

3.3.1 Compression moulding

Compression moulding was the primary technique used in this work to shape specimens for subsequent testing. The moulds used were flash moulds, consisting of interlocking parts producing the desired cavity shape, as shown in Fig. 3.2. Additionally, they are easily disassembled, and can produce multiple specimens per moulding cycle. The advantage of using flash moulds is the elimination of post-moulding sample preparation for specific tests that may in turn affect the structure and thermal history of the polymer specimen prior to testing (De Focatiis, 2012). Pressure applied to the mould is distributed over the surface of the mould and the inserts; it is not directly exerted onto the samples. Instead, the pressure forces the excess polymer to flow away from the cavity, leaving the molten polymer in the cavity to form to shape.

Different specimens geometries may be obtained from this method. Fig. 3.2(a) illustrates circular samples that are used for rheological characterisation and thermal measurements. Fig. 3.2(b) shows samples prepared for tensile testing, the cavity shape of the mould corresponding to Type 1BA (75 mm × 5 mm × 2 mm) of the standard BS EN ISO 527-2:2012 (British Standard, 2012). Rectangular bars, as shown in Fig. 3.2(c), can be used for microscopy studies or other characterisation tests such as creep or DMA measurements.

Prior to each moulding process for all materials, granules were dried at 80 °C for a minimum of 12 hours. The moulds consisted of an upper and lower stainless steel sheet, 200 mm × 200 mm × 2 mm, an upper and lower disposable aluminium foil, 200 mm × 200 mm × 0.15 mm, and the stainless steel flash mould with the desired shape cavity, 200 mm × 200 mm. The specimen thickness required dictates the thickness of the mould. The aluminium foils were used to ease the release of the sample from the flash mould, by avoiding the specimens from adhering to the stainless steel sheets. The surfaces of the mould and the disposable aluminium foil, cut from aluminium rolls, were cleaned with acetone and sprayed with dry

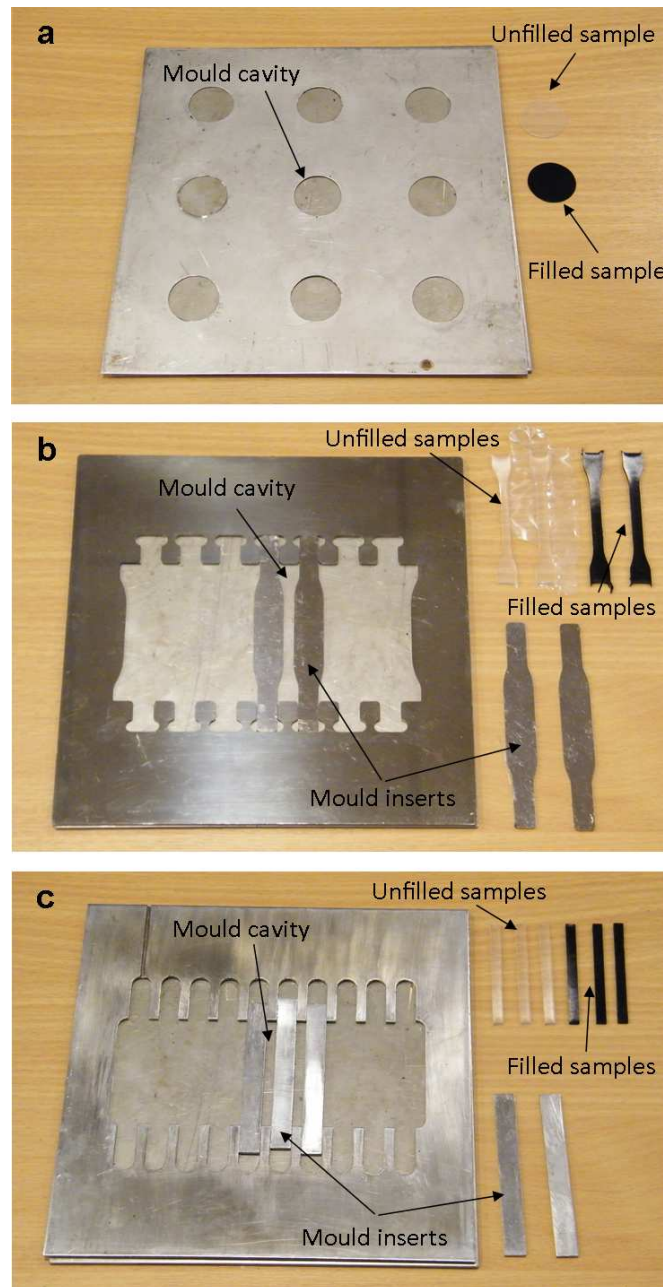


FIGURE 3.2: Multiple specimens mould capable of producing (a) circular specimen of 25 mm in diameter and 0.5 mm in thickness; (b) dog-bones with gauge length of 25 mm and 2 mm in thickness exhibited with sample prior to flash removal; (c) rectangular bars with dimensions of 60 mm \times 5 mm \times 2 mm shown with samples without flash. The specimens illustrated are PC-MWCNT 2205 and PC 2205

PTFE spray lubricant to aid sample removal from the mould. Dried granules of the material were distributed in the mould cavity with a slight excess of the filled or unfilled polymer, and sandwiched between sheets of aluminium foil and stainless steel sheets as illustrated in Fig. 3.3(a). The filled mould was then positioned in between the platens of a hand operated hydraulic heated press as shown in Fig. 3.3(b). The platens were pre-heated to 250 °C. Heat reaches the mould and polymer granules via conduction.

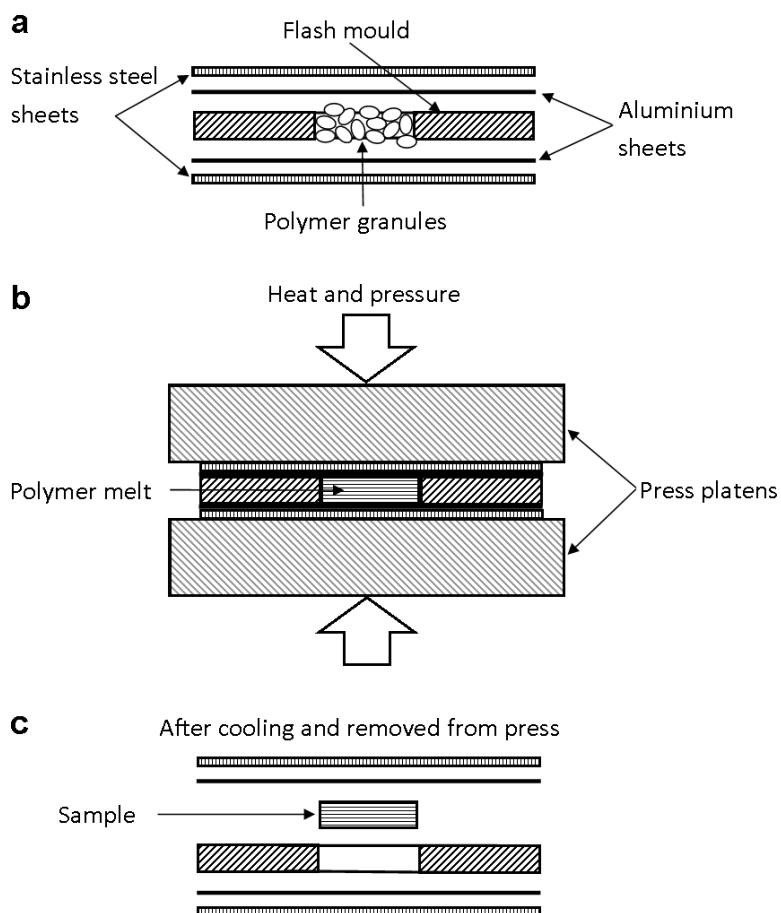


FIGURE 3.3: A schematic diagram of the moulding process: (a) the mould arrangement with the mould cavity filled with polymer granules; (b) the mould is transferred to the heated press and the pressure cycle is applied; (c) the mould is then cooled and removed from the press to release the moulded specimens from the cavity.

The moulding procedure, illustrated in Fig. 3.4, consisted of 10 minutes of warm-up time (heating rate of $\sim 32 \text{ }^\circ\text{C min}^{-1}$), followed by 5 minutes of pressure cycling between 0 and 100 bar to help spread the polymer within the cavity and to dislodge any air voids, and 5 minutes of holding at 100 bar of pressure. After the holding time, the cooling procedure is imposed by forcing cold water through cooling channels within the platens until the press is at $\sim 80 \text{ }^\circ\text{C}$. The final temperature of the mould ensures that the polymer samples are well below the glass transition temperature, T_g , and not a burning hazard when removing the specimens from the cavity. The cooling rate of the mould was measured as $\sim 20 \text{ }^\circ\text{C min}^{-1}$. The heating and cooling rates were determined from monitoring the temperature of the melt in the mould with a thermocouple. The samples are then carefully removed from the mould after the cooling process as seen in Fig. 3.3(c). Excess polymer, or flash, on the samples is removed with a sharp knife and specimens were prepared to shape with fine grade of wet and dry sand-paper.

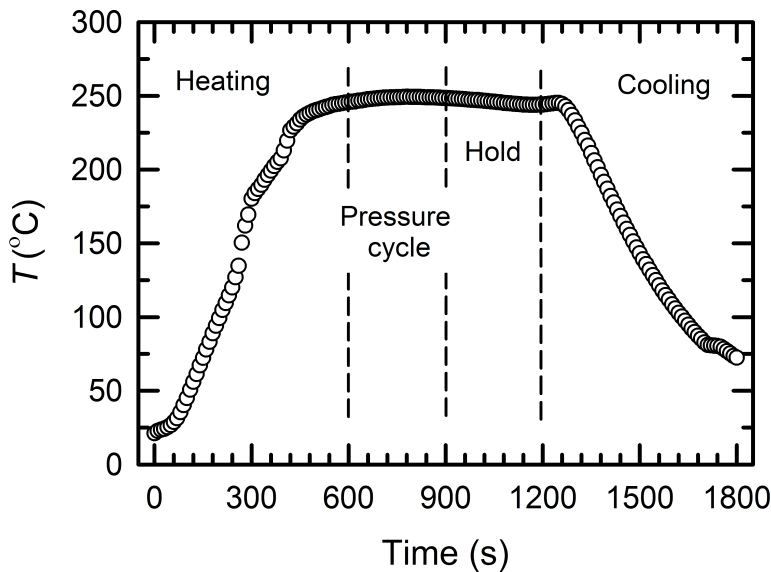


FIGURE 3.4: The moulding procedure and the moulding temperature as a function of time

3.3.2 Injection moulding

In the interest of determining the influence of the compounding temperature and moulding technique on the behaviour of the PC-MWCNT, a grade of material was selected for injection moulding. PC-MWCNT 2205 samples extruded between 230 and 290 °C were injection moulded using an Engel Victory 80 ton injection moulding machine. Samples were moulded into dog-bones by Nanocyl S.A. in accordance with ASTM D638 standard for tensile testing that is the equivalent to Type 1B sample dimensions (gauge section: 50 mm \times 10 mm \times 4 mm) of the standard BS EN ISO 527-2:2012 (British Standard, 2012).

3.4 Molar mass distribution

The molar mass distribution of the supplied unfilled PC grades was measured using gel permeation chromatography (GPC), by passing polymer dissolved in a solvent through a column packed with porous material (where the pore size is similar to the macromolecules) that separates polymer chains based on molecule size (McCrum et al., 1997). Measurements for unfilled PC were performed in tetrahydrofuran (THF) eluent relative to polystyrene standards, using an Agilent Technologies PC-GPC 120. Three repeats were carried out on each grade. Table 3.3 reports the molar mass averages, M_n and M_w with two standard errors referring to a confidence level of 95%.

TABLE 3.3: Molar mass averages obtained via GPC for the PC materials

Material	M_n (g mol ⁻¹)	M_w (g mol ⁻¹)	PDI
PC 2205	13900 ± 3000	33600 ± 1020	2.5 ± 0.4
PC 2205 1-pass	11900 ± 230	32900 ± 330	2.7 ± 0.1
PC 2405	14200 ± 490	38700 ± 570	2.7 ± 0.1
PC 2805	18000 ± 4120	45700 ± 730	2.6 ± 0.5
PC 3105	21400 ± 2420	50500 ± 470	2.4 ± 0.3

3.4.1 Influence of melt compounding on molar mass

A comparison between the molar mass of PC 2205 and PC 2205 1-pass was performed to establish if melt compounding had caused any changes to the molar mass of the virgin PC. The molar mass measurements are presented in Table 3.3. Although the molar mass averages of PC 2205-1 pass were slightly lower, than those of PC 2205, the measured values are within the measurement error. This suggests that the melt compounding process did not affect virgin PC significantly.

3.4.2 Influence of CNT presence on polymer degradation

In order to evaluate the possibility of polymer degradation due to the presence of CNTs, PC was extracted from PC-MWCNT to compare to virgin PC 2205 via molar mass measurements. During a study to characterise the dispersability of the MWCNTs in various solvents, Pötschke et al. (2003) observed that the CNTs dispersed in THF solution. This observation implied that it was not possible to perform GPC testing with nanocomposites, as the CNTs would obstruct and clog the pores in the GPC column. Pötschke's procedure of separating the filler from PC-MWCNT consisted of immersing the material for four consecutive days whilst changing the solvent each day and finally filtering the dispersion to obtain the nanoparticles. They then extracted PC for further evaluation to detect any changes in the molar mass of PC after processing with the addition of CNTs and to assess the loading content of the filler in the nanocomposite. Details of the filtration (such as membrane pore size) were not available.

In this work, PC was extracted from the nanocomposite using Soxhlet extraction. PC-MWCNT 2205 weighing 10.06 g was dissolved in chloroform (~250 ml) and passed through a Soxhlet apparatus. The MWCNTs were collected in a cellulose thimble with a porosity of 20 μm . The procedure was performed continuously for 24 hours. The solvent was then removed

by a rotary evaporator, leaving the recovered PC flakes, identified as PC_{extc}. PC recovery from PC-MWCNT was achieved with ease and in a shorter period compared to the filtering technique.

Molar mass of PC_{extc} was measured in chloroform relative to polystyrene standards using GPC to ascertain change in molar mass after melt compounding with the addition of MWCNTs. The thimble containing the CNTs was dried in a vacuum oven for a period of 48 hours. PC_{extc} and PC 2205 were dissolved in chloroform eluent for molar mass measurements presented in Table 3.4. A single measurement was carried out.

TABLE 3.4: Molar mass measurements of extracted PC 2205 (PC_{extc}) and virgin PC 2205

Solvent	Material	M_n (g mol ⁻¹)	M_w (g mol ⁻¹)	PDI
Chloroform	PC 2205	11100	26400	2.4
	PC _{extc}	11700	27000	2.3

The close similarity between the measured weight average molar mass, M_w of PC 2205 with both PC_{extc} and PC 2205 1-pass, dissolved in chloroform and THF respectively, suggests that there was no significant effect on the virgin polymer due to the presence of CNTs or the melt mixing process to produce the nanocomposites. This finding supports Pötschke et al.'s (2003) view that direct addition of the CNTs into polymer melt during compounding to produce PC-MWCNT with a certain filler concentration, is favoured over the masterbatch dilution method. The masterbatch dilution method consists of diluting commercially available masterbatches of PC-MWCNT (with high filler concentrations of up to 15 wt%) with the pure polymer using the melt mixing process. Pötschke et al. (2003) observed that this method produced lower matrix molar mass for the same filler concentration as the direct addition method due to the increase in mixing times (and extended shearing) of PC-MWCNT, evidenced by GPC measurements.

A different eluent was used in comparison of molar mass averages because PC_{extc} precipitated in THF. The precipitation could have been caused by additive residue (such as a plasticiser) that required longer periods in THF to dissolve completely. Chloroform was attempted as an alternative eluent and was found to completely dissolve PC_{extc}. Due to constraints on the availability of GPC columns, chloroform was selected for the comparison study between PC 2205 and PC 2205 1-pass.

3.5 Independent filler content determination

3.5.1 Soxhlet extraction

The Soxhlet extraction method allows retention of filler in the thimble, for which the contents are typically discarded as residue. The MWCNTs captured in the thimble in this work were used to confirm the loading content in the nanocomposites. Differences in weight of the thimble before and after the PC recovery from PC-MWCNT 2205 are recorded in Table 3.5. The filler loading fraction was found to be 3.6 wt%, which is in good but not perfect agreement to the MWCNT content reported by Nanocyl S.A.

TABLE 3.5: Measurement of filler loading content in PC-MWCNT 2205

Extraction stage	Contents	Weight, W (g)	ΔW (g)
Before	Empty thimble	8.20	
	PC-MWCNT+thimble	18.26	
After drying 48 hours in vacuum oven	PC-MWCNT		10.06
	MWCNTs+thimble	8.56	
	MWCNTs		0.36

The slight discrepancy (+0.6 wt%) between the measured filler concentration and that reported by the manufacturer may be attributed to inhomogeneous mixing of the filler and the matrix.

3.5.2 Density measurement

A non-destructive means to estimate the filler content is through density measurement. Density of PC 2205 and PC-MWCNT 2205 were measured with a Precisa XT220A analytical balance fitted with a density kit. The density kit functions on Archimedes' principle, that states that the buoyant force acting on an immersed solid object in a water is equivalent to the weight of the fluid displaced. Compression moulded disc samples with dimensions of 30 mm in diameter and 0.5 mm thickness were weighed in air and in water at ambient temperature. Reverse osmosis water was used as the fluid medium. The water temperature was recorded for each specimen with a mercury thermometer prior to carrying out the density measurement. Care was taken to ensure no air bubbles were stuck to the surface of the specimens during the weight measurements in water. At least three consecutive measurements were repeated on each of three separate specimens of each grade. The surfaces of the specimens were

thoroughly dried with tissue paper prior to the repeat measurements. Table 3.6 presents the density measurements of PC 2205 and PC-MWCNT 2205, with two standard errors from the mean.

TABLE 3.6: Average density measurements of PC 2205 and PC-MWCNT 2205

Material	Weight, W (g)	Density, ρ (g cm^{-3})
PC 2205	0.45 ± 0.001	1.18 ± 0.002
PC-MWCNT 2205	0.46 ± 0.004	1.20 ± 0.002

Density of PC was determined from specimens without voids. Since the filled PC specimens are opaque it is difficult to ascertain if the specimens contain any voids. The density of MWCNT was not readily available from the manufacturer. It can be appreciated that due to structural characteristics of MWCNTs, determining the density of individual carbon nanotubes is not trivial. Among those who have attempted to measure the density of MWCNTs are Lu and co-workers (2006), who used gradient sedimentation and reported densities of 2.09 g cm^{-3} and 2.11 g cm^{-3} for nanotubes manufactured by CVD (similar to this work) and arc discharge methods respectively. Huang et al. (2005) quoted the nanotube manufacturer, Shenzhen Nanotech Port Co. Ltd for their work on barium titanate composites and reported a density of 2.10 g cm^{-3} , but no further information on synthesis method or density measurement technique was provided.

The total mass of nanocomposite, M , is given by the mass of PC, M_{PC} , and of the nanotubes, M_{CNT}

$$M = M_{\text{PC}} + M_{\text{CNT}} \quad (3.2)$$

The specific volume of PC-MWCNT, defined as $\frac{1}{\rho}$, can be expressed as the total volume (i.e. the volume of PC matrix, V_{PC} , and the volume of CNTs, V_{CNT}) divided by the total mass of nanocomposite, M

$$\frac{1}{\rho} = \frac{V_{\text{PC}} + V_{\text{CNT}}}{M} \quad (3.3)$$

In order to determine the mass of the PC, M_{PC} and of the nanotubes, M_{CNT} , it is conveniently expressed as follows

$$\frac{1}{\rho} = \left(\frac{V_{\text{PC}}}{M_{\text{PC}}} \cdot \frac{M_{\text{PC}}}{M} \right) + \left(\frac{V_{\text{CNT}}}{M_{\text{CNT}}} \cdot \frac{M_{\text{CNT}}}{M} \right) \quad (3.4)$$

Simplifying Eq. 3.4 by defining the mass fraction of PC as $1-x$ and mass fraction of MWCNTs as x , and expressing densities of PC and MWCNTs as, ρ_{PC} and ρ_{CNT} correspondingly, gives

$$\frac{1}{\rho} = \frac{1-x}{\rho_{\text{PC}}} + \frac{x}{\rho_{\text{CNT}}} \quad (3.5)$$

Rearranging Eq. 3.5 estimates the mass fraction of CNTs in filled PC as

$$x = \frac{\rho_{\text{CNT}}(\rho - \rho_{\text{PC}})}{\rho(\rho_{\text{CNT}} - \rho_{\text{PC}})} \quad (3.6)$$

Substituting the densities of PC-MWCNT and PC of $\rho = 1.20 \text{ g cm}^{-3}$ and $\rho_{\text{PC}} = 1.18 \text{ g cm}^{-3}$ respectively (see Table 3.6); and CNT density values from literature $\rho_{\text{CNT}} = 2.09 \text{ g cm}^{-3}$ and 2.11 g cm^{-3} (Lu et al., 2006) into Eq. 3.6, the MWCNT content was determined as 3.8 wt%. The filler content, similar to Section 3.5.1, is found to be in good agreement but slightly higher than the loading content reported by Nanocyl.

The deviation of +0.8 wt% between the filler content calculated through density measurements and that reported by the manufacturer could be attributed to the assumption of no voids in the density measurement of PC-MWCNT specimens and the use of literature values for CNT density in the absence of the density of NC 7000 nanotubes. If there was significant voids in the filled specimens, the measured density of PC-MWCNT will increase, yielding a higher value of filler content. Thus, the small deviation suggests that the presence of significant voids in the compression moulded PC-MWCNT samples is not likely. This finding validates that the compression moulding procedure is able to produce repeatable samples that are free of significant voids.

3.6 Conclusions

Sections 3.1 and 3.2 introduced the materials used in this work and described the melt compounding process that was used to disperse the MWCNTs in the PC base matrix.

Section 3.3 described the techniques that were employed to prepare the samples prior to characterisations experiments. Attention was given to compression moulding as it is the primary techniques used throughout this study. Filled and unfilled samples were formed to shape using in-house flash moulds.

Section 3.4 presents the molar mass distribution measurements that were performed on all material grades to facilitate the understanding of the structure-property relationship before considering the complexity introduced by the CNT network structure in the nanocomposites. The Soxhlet extraction technique enabled recovery of PC from the nanocomposite in order to determine the influence of melt compounding with CNTs on the molar mass. It was found that both the addition of MWCNTs and the melt compounding parameters had no significant degradative effects on the base PC matrix.

In an effort to independently determine the filler loading content of PC-MWCNT, two techniques were employed in Section 3.5. The first method is the Soxhlet technique that successfully separated the filler from PC-MWCNT. The second method is based on the density measurements of moulded specimens, detailed in Section 3.5.2. The filler content determined from both methods was in good agreement to that reported by the manufacturer. Using a MWCNT density values from literature in the second method indicated that no significant voids were present in the compression moulded PC-MWCNT samples. This finding validated compression moulding as a technique that is able to produce multiple and repeatable specimens with minimal post-moulding processing requirements for subsequent testing.

Chapter 4

Thermal properties

4.1 Introduction

This chapter describes a range of experimental techniques used to investigate the thermal properties of PC-MWCNT. Section 4.2 reports calorimetric measurements and discusses the effect of the addition of CNTs on the glass transition, measured using differential scanning calorimetry (DSC). In Section 4.3, the thermal transport properties of PC and PC-MWCNT are determined using the transient plane source measurements and discussed with reference to the role of CNTs in heat transport. Thermal stability and degradation of PC and PC-MWCNT are measured using thermogravimetric analysis (TGA) in both nitrogen and air atmospheres in Section 4.4; possible mechanisms affecting the thermal properties of PC due to the presence of CNTs are discussed.

4.2 Influence of CNTs on the glass transition temperature

The glass transition temperature, T_g , of a polymer is the temperature at which the amorphous matrix transitions from a hard and brittle state (otherwise known as the glassy state) to a rubber-like state. This occurs due to the restriction on molecular motion when the polymer is cooled, freezing the conformations of molecular segments (McCrum et al., 1997). As the behaviour of materials changes significantly at T_g , it is important to characterise T_g of PC with the addition of CNTs. One of the techniques to measure T_g is DSC. This method

measures the heat capacity of a matrix as it goes through the transition in the range of temperature scanned. The glass transition is not a true phase transition because it depends on the local segmental motions of the polymer chains. Hence, DSC measurements are influenced by parameters such as heating rate and sample mass.

4.2.1 Method

Calorimetric scans of MWCNT-filled and unfilled PC of varying molar mass ($M_w = 33600 - 50500 \text{ g mol}^{-1}$) were carried out with a Thermal Analysis (TA) Instruments DSC Q10. Test specimens pellets were cut with a sharp knife to obtain a weight of approximately 10 mg. The specimens were then encapsulated in standard DSC hermetic aluminium pans. Nitrogen purge gas with a flow rate of 100 ml min^{-1} was used to prevent oxidation and contamination of the samples. The specimens were heated at a rate of $10 \text{ }^\circ\text{C min}^{-1}$ from room temperature to $250 \text{ }^\circ\text{C}$, followed by cooling at a rate of $10 \text{ }^\circ\text{C min}^{-1}$ to $50 \text{ }^\circ\text{C}$, and a second heating at a rate of $10 \text{ }^\circ\text{C min}^{-1}$ through to $250 \text{ }^\circ\text{C}$. Three repetitions were performed on each material in the standard heat/cool/heat cycle. The initial heat cycle erases the thermal history of the sample, and the sample is then cooled at a controlled rate, during which the sample goes from a rubbery to an isostructural glassy state. The controlled cooling allows the polymeric material to reach a repeatable enthalpic state associated with a specific T_g . The subsequent heat cycle with a defined thermal history is then used to determine the T_g .

The baseline was determined with an empty DSC cell. The baseline is performed prior to experiment to check for noise levels in the instrument, typically caused by contamination of the DSC cell or purge gas flow issues such as inconsistent gas flow rate or presence of moisture in the gas (Hatakeyama and Quinn, 1999). For the determination of T_g , the baseline signal is subtracted from the specimen result to improve the resolution of the transition investigated (Hatakeyama and Quinn, 1999). Fig. 4.1 presents a typical derivative of heat flow vs. temperature plot, after subtracting the baseline.

T_g of filled and unfilled PC of all grades were determined using TA Universal Analysis software. The normalised heat flow-temperature curve was smoothed using a least-squares averaging technique with a smoothing width of $2 \text{ }^\circ\text{C}$ before analysis to remove oscillations typical of these traces. There are two methods to determine T_g . The first method determines the inflection of the heat flow-temperature curve between the three tangent lines, illustrated in Fig. 4.2, between the data limits selected by the user. The second method determines the

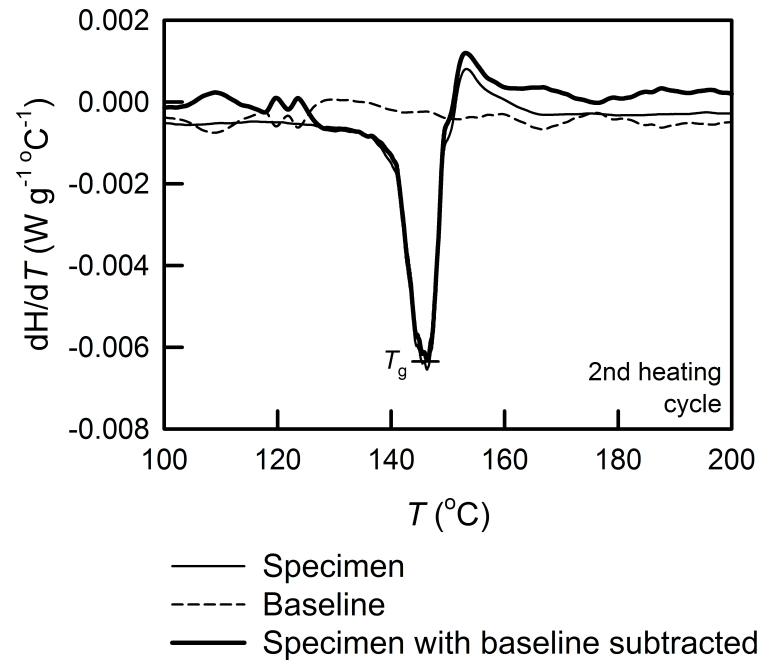


FIGURE 4.1: An illustration of the derivative heat flow as a function of temperature of the baseline; the specimen of grade PC 2205; and the subtraction of the baseline from the specimen measurement

peak of the temperature derivative of the heat flow-temperature curve as shown in Fig. 4.2. The latter method was selected for the determination of T_g in this work as it was less user dependent.

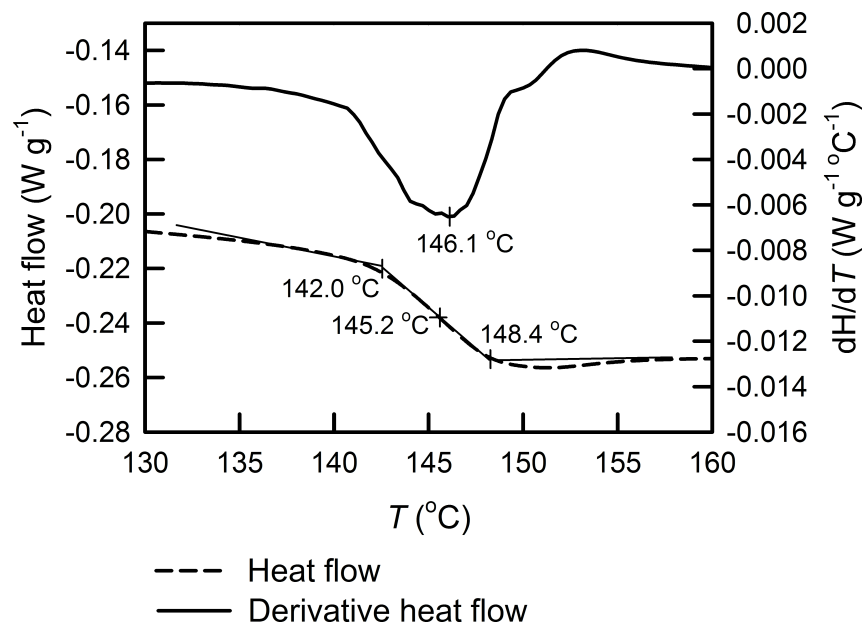


FIGURE 4.2: Example of the determination of T_g using the peak of derivative heat flow and the inflection step change of heat flow as a function of temperature

TABLE 4.1: Glass transition temperatures, T_g , determined from the peak of derivative heat flow with respect to temperature for all materials (\pm two standard errors)

Material	T_g ($^{\circ}\text{C}$)
PC 2205	146.0 ± 0.2
PC 2405	147.4 ± 0.2
PC 2805	146.5 ± 0.4
PC 3105	147.6 ± 0.4
PC-MWCNT 2205	146.0 ± 0.5
PC-MWCNT 2405	146.5 ± 0.2
PC-MWCNT 2805	145.2 ± 0.7
PC-MWCNT 3105	147.0 ± 0.8

4.2.2 Results and discussion

The average glass transition temperatures for all filled materials and the corresponding virgin matrices are reported in Table 4.1 with 95% confidence levels. The unfilled PC generally showed a small increase in T_g as molar mass increased, as expected. However, the increment was not consistent as PC 2805 exhibited a decrease in T_g relative to the previous lower molar mass. This trend was also observed in T_g measurements of filled PC. A possible explanation for the trend is the commercial nature of the materials leading to experimental variations due to batch differences or additives. Comparisons between the T_g of filled and unfilled PC of the corresponding grade shows that the addition of CNTs had no effect on PC 2205, whereas T_g of PC 2405, PC 2805 and PC 3105 marginally decreased by 0.9 $^{\circ}\text{C}$, 1.3 $^{\circ}\text{C}$, and 0.6 $^{\circ}\text{C}$ respectively.

A decrease in T_g implies a greater degree of mobility which could occur due to an addition of free volume arising from the density of chain ends. Polymer chain ends are surrounded by regions that are characterised by imperfect packing, giving rise to greater free volume in comparison to that between chain segments (Aklonis and Macknight, 1983). Hence, an increase in the number of chain end density yields a higher free volume. The number density of chain ends is inversely proportional to the number average molar mass, M_n . At high molar mass, T_g will tend to a constant value because of the negligible concentration of chain ends in the polymer. Using the Fox-Flory equation, T_g can be expressed as (Aklonis and Macknight, 1983)

$$T_g = T_g^{\infty} - \frac{C}{M_n} \quad (4.1)$$

where T_g^{∞} is the glass transition temperature at infinite polymer chain length and C is an empirical constant that is polymer specific.

In order to highlight the influence of the addition of CNTs, measurements of T_g were plotted against the inverse of M_n for both unfilled and filled PC in Fig. 4.3. The experimental scatter could be attributed to impurities introduced during or after melt-compounding, particularly since the nanocomposites were produced industrially. The reduction in T_g for PC-MWCNT is consistent with reported findings the in literature for a wide range of PC nanocomposite systems (Castillo et al., 2011; Samuel et al., 2009) similar to those studied in this work.

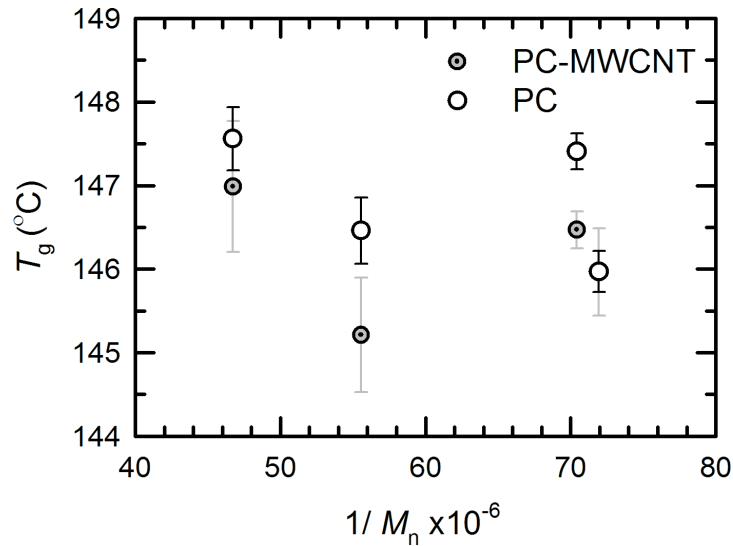


FIGURE 4.3: Relationship between glass transition temperatures determined from signal peak in derivation of heat flow as a function of $\frac{1}{M_n}$ for MWCNT-filled (3 wt%) and unfilled PC

Studies on polymer films demonstrated higher mobility of chains extends from the free surface (air) to several tens of nanometers of the film interior resulting in a T_g gradient (Ellison and Torkelson, 2003). In nanocomposite systems, it has been suggested that a confined or adsorbed layer of polymer on the surface into the nanofiller reduces the mobility of polymer chains, thus it would lead to a rise in T_g , as reported for filled elastomers (Heinrich et al., 2002). Hence, one may expect a rise in T_g of PC-MWCNTs.

Measurements obtained from DSC reported in Table 4.1 indicate a small but discernible *reduction* in T_g with the addition of MWCNTs that contradicts the expected rise. This suggests that the confined layer of PC chains on the surface of MWCNTs, if any, does not constrict the mobility of the bulk of PC chains. On the contrary, the reduction of T_g with the addition of CNTs implies an enhancement of PC chain mobility. Since no specific surface modification of MWCNTs was performed in this study, chemical interactions between matrix and CNTs are likely to be weak. An explanation is that the reduction in T_g in PC-MWCNT

is caused by a lack of wettability between the PC and the surface of the nanotubes which gives rise to additional free volume.

Castillo and co-workers (2011) used the change in heat capacity, ΔC_p , from DSC measurements, to understand the reduction of T_g of PC-MWCNT with various CNT loadings. This is because polymer confinement at the nanotube surfaces may affect the amount of polymer that contributes to the glass transition, resulting in the decrease of ΔC_p . Thus, the proportional relationship between ΔC_p and polymer mobility allows one to analyse the amount of polymer that is involved in the glass transition. ΔC_p for all grades of filled and unfilled PC in this work were determined using the inflection method as described in Section 4.2.1. Fig. 4.4 presents the relationship between ΔC_p and M_w of the unfilled PC and the corresponding filled grades.

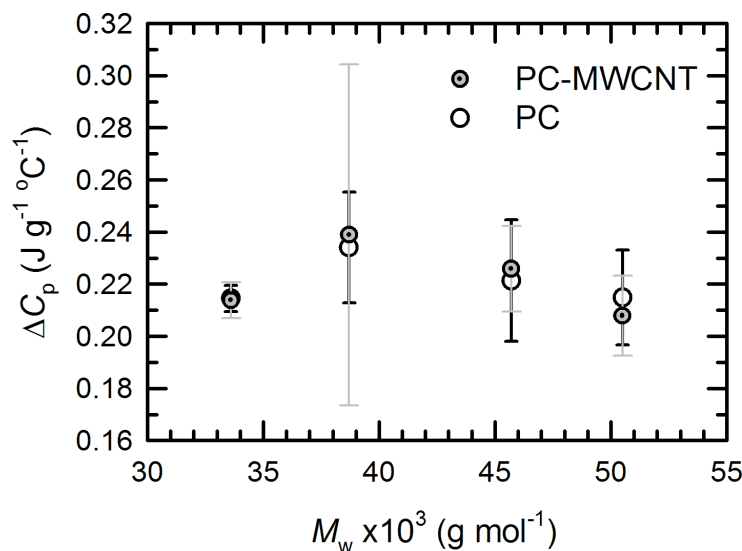


FIGURE 4.4: Change in heat capacity, ΔC_p of MWCNT-filled (3 wt%) and unfilled PC as a function of the weight-average molar mass. Error bars represent two standard errors

The difference between ΔC_p of filled and unfilled PC varied with increasing M_w . The experimental scatter can be attributed to the user dependent method and the commercial nature of PC. At the lowest molar mass, ΔC_p of PC remained unchanged with the addition of CNTs. As molar mass increased, ΔC_p of PC-MWCNT 2405 and PC-MWCNT 2805 (corresponding to base matrices $M_w = 38700$ and 45700 g mol⁻¹) were greater than the base matrix by $\sim 5 \times 10^{-3}$ J g⁻¹ °C⁻¹. The increase of ΔC_p implies that more polymer participated in the glass transition, resulting a decrease T_g ; as reported in Table 4.1. This is further evidence that the bulk PC chains for $M_w = 33600 - 45700$ g mol⁻¹ were not immobilised by individual tubes and the CNT network mobility, and that the polymer-CNT

interactions are favourable. Similar observations were reported by (Castillo et al., 2011) for comparable nanocomposite systems.

Contrary to the previous PC grades, the CNT presence in PC 3105 reduces both ΔC_p and T_g . Similar observations have been reported with the increase of CNT concentration in PC-MWCNT systems (Castillo et al., 2011; Samuel et al., 2009), similar to this study, implying that less polymer participated in the glass transition (i.e. an increase in T_g). Castillo and co-workers found ΔC_p of PC (Makrolon 2600) to be $0.29 \text{ J g}^{-1} \text{ }^\circ\text{C}^{-1}$ whereas the corresponding PC-MWCNT, of identical CNTs and loading content as of this work, recorded $0.18 \text{ J g}^{-1} \text{ }^\circ\text{C}^{-1}$ with large error bars that overlap with the measurements of unfilled PC. They postulated, specifically for PC-MWCNT systems, that the increase in polymer mobility could arise from an effect known as the correlation hole. This effect is observed when the layer of polymer chains between the immobilised chains on the CNT surface and the bulk polymer has increased mobility due to a reduction of entanglement density in this layer relative to the bulk entanglement density. Our findings suggest that the correlation hole effect in PC-MWCNT systems may occur when a critical polymer chain length is reached, although the large error bars prevent a definite conclusion.

Although Castillo's and Samuel's studies concluded that the reduction of T_g was most likely attributed to polymer degradation during melt processing, both studies did not recover the matrix from the nanocomposite to assess for degradation. The same cannot be concluded in this study since the PC recovered from PC-MWCNT using Soxhlet recorded no significant degradation following GPC measurements, as detailed in Section 3.4.2.

4.3 Thermal transport properties

Thermal properties such as thermal conductivity, κ , thermal effusivity, e , and thermal diffusivity, d are important parameters to consider when processing polymeric material. Such parameters can dictate the cost and the speed of manufacture owing to the high temperatures required for traditional plastic forming methods. A material with low κ would need a higher temperature or longer processing period to mould the material to shape. The thermal properties can ultimately affect the properties of the final product, as the morphology of the nanocomposite structure may change as the material cools.

The parameter κ is a measure of the heat flow as a function of time through the thickness of a material whereas e is a measure of the material's capacity to exchange heat with the surrounding environment (Salazar, 2003). The technique used to measure κ and e is the transient plane source. This method applies an electrical pulse to a sensor element that heats the specimen causing a small temperature perturbation at the interface between the specimen and the sensor element; the rate of change in the resistance of the sensor due to temperature difference is employed to determine thermal transport properties (Gustafsson, 1991). Hence, the sensor element is used to generate heat and to monitor temperature. The thickness of the specimen must be sufficient to be considered as an infinite solid to prevent heat penetrating through the specimen. The transient plane source technique also indirectly measures d and heat capacity, C_p . The thermophysical parameter d describes the rate of heat propagation when temperature changes over a time period (Salazar, 2003).

4.3.1 Method

The thermal transport properties of filled and unfilled PC 2205 were determined using a C-Therm TCi Thermal Conductivity Analyzer. Only a single PC grade was studied as the thermal transport properties of the virgin PC grades is unlikely to change significantly with increasing molar mass, and the MWCNT concentration for all filled grades are constant.

The specimens were compression moulded into a disc geometry with 30 mm diameter and 2 mm thickness. Water was used as the interface medium between the sensor and specimen; a weight of 500 g was loaded on the specimen to ensure good contact between the heat reflectance sensor and the specimen. A blotter test was performed to determine the specimen thickness required to prevent heat transferring to the weight. This test involves inserting a foam block (77 mm \times 77 mm \times 13 mm) between the sample and the weight. If the measurements without the presence of the foam block is consistent to the blotter test, then the specimen thickness is sufficient. A Pyrex glass block (25 mm \times 25 mm \times 13 mm) was used as the calibration material before performing κ measurements. All measurements were conducted at ambient temperature. Two specimens of the filled and unfilled PC were measured. Measurements of five repeats for each specimen were performed to verify for repeatability.

4.3.2 Results and discussion

Table 4.2 reports measured e and κ values of PC 2205 and PC-MWCNT 2205. Specific heat capacity, C_p measures the heat required by per unit of the material to change the material temperature by one degree. Using e and κ , C_p can be determined following the expression

$$C_p = \frac{e^2}{\kappa \cdot \rho} \quad (4.2)$$

where the density, ρ for filled and unfilled PC was determined in Section 3.5.2.

With the values of κ , ρ and C_p , d was calculated as

$$d = \frac{\kappa}{C_p \cdot \rho} \quad (4.3)$$

Both C_p and d values of PC 2205 and PC-MWCNT 2205, reported in Table 4.2, were calculated from Eqs. 4.2 and 4.3 respectively. The change of e , κ , d and C_p of PC due to the presence of CNTs is determined by calculating the difference between PC-MWCNT and PC values, represented as $\Delta\text{MWCNT} = \text{PC-MWCNT} - \text{PC}$ and is presented in Table 4.2.

TABLE 4.2: Thermal effusivity, e , thermal conductivity, κ , thermal diffusivity, d , and heat capacity C_p of PC 2205 and PC-MWCNT 2205 (\pm two standard errors). Δ MWCNT is the difference obtained by subtracting PC from PC-MWCNT

Material	e ($\text{Ws}^{1/2} \text{ m}^{-2}\text{K}^{-1}$)	κ ($\text{W m}^{-1}\text{K}^{-1}$)	d ($\times 10^{-6}$) ($\text{m}^2 \text{ s}^{-1}$)	C_p ($\text{J kg}^{-1}\text{K}^{-1}$)
PC 2205	579.7 ± 1.5	0.2616 ± 0.0012	0.2036 ± 0.0008	1089 ± 0.6
PC-MWCNT 2205	635.1 ± 0.4	0.3068 ± 0.0004	0.2334 ± 0.0002	1114 ± 0.2
ΔMWCNT	55.40 (+10%)	0.0452 (+17%)	0.0298 (+15%)	25.00 (+2%)

The addition of MWCNTs changes the thermal properties, increasing e by 10%, κ by 17%, d by 15%, and C_p by 2%. This is attributed to the formation of an CNT network in a percolated system giving rise to several pathways for phonon transport responsible for conducting heat. The increase of κ in the nanocomposites is desirable for applications that require heat dissipation such as electronic packaging.

King et al. (2012) employed the hot plate method at 55 °C to measure κ of injection moulded PC system filled with MWCNT (melt diluted to attain 1 wt% and 5 wt% filler content). The hot plate method measures the heat flux of the specimen located between heating and cooling

plates. They reported an increase in κ of 5% (for 1 wt%) and 24% (for 5 wt%) relative to pure PC respectively. Thus, the increase of 17% obtained in this work for 3 wt% MWCNT is consistent with their measurements. There are several differences between King's study and this work, such as the different measurement techniques, loading content in PC-MWCNT compounding methods and in specimen manufacture methods. Although the differences between King's study and this work are evident, the increment in $\kappa_{\text{PC-MWCNT}}$ found in this work is still within the range of enhancement of $\kappa_{\text{PC-MWCNT}}$ reported by King's group.

4.3.3 Predicting thermal conductivity of PC-MWCNT

Two simple two-phase models can be used to calculate upper and lower bounds of the thermal conductivity of nanocomposites. The first model is based on the inverse of ROM (or parallel model) (Gojny et al., 2006), whereby both phases are perpendicular to the heat flow direction, as illustrated in Fig. 4.5(a),

$$\frac{1}{\kappa} = \frac{V_{\text{CNT}}}{\kappa_{\text{CNT}}} + \frac{V_{\text{PC}}}{\kappa_{\text{PC}}} \quad (4.4)$$

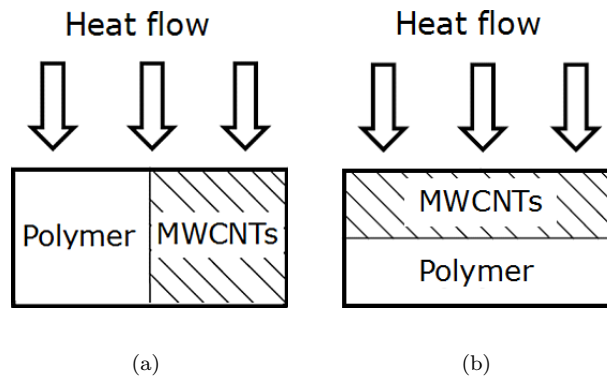


FIGURE 4.5: A schematic illustration of the (a) parallel and the (b) series two-phase models to estimate thermal conductivity of PC-MWCNT 2205 (adapted from Kochetov (2012))

The second model uses ROM (or series model) (Gojny et al., 2006) that considers both phases to be in parallel to the heat flow direction, as illustrated in Fig. 4.5(b), and is expressed as

$$\kappa = (\kappa_{\text{CNT}})(V_{\text{CNT}}) + (\kappa_{\text{PC}})(V_{\text{PC}}) \quad (4.5)$$

In order to calculate the bounds of κ for PC-MWCNT 2205, $V_{\text{CNT}} = 0.021$ ¹, $\kappa_{\text{PC}} = 0.2615 \text{ W m}^{-1}\text{K}^{-1}$ (from Table 4.2), $\kappa_{\text{CNT}} = 20 \text{ W m}^{-1}\text{K}^{-1}$ (Yi et al., 1999) were substituted

¹Calculated with $\rho_{\text{MWCNT}} = 1.75 \text{ g cm}^{-3}$ (Shaffer and Windle, 1999)

into Eqs. 4.5 and 4.4. The value κ_{CNT} was taken from the reference as the CNTs were similar to this work. The two-phase models calculated κ of PC-MWCNT 2205 to be in the range of $0.2671 \text{ W m}^{-1}\text{K}^{-1}$ (series model) to $0.6761 \text{ W m}^{-1}\text{K}^{-1}$ (parallel model).

The measured $\kappa_{\text{PC-MWCNT}}$ value ($0.3068 \text{ W m}^{-1}\text{K}^{-1}$) is within the range estimated by the models, and is 15% higher than the lower bound. The close proximity of $\kappa_{\text{PC-MWCNT}}$ to the lower bound suggests that the nanocomposite was unable to effectively harness the high conductivity of CNTs. This perhaps could be expected due to the complexities highlighted by Das et al. (2008): (1) agglomeration of MWCNTs leads to poor dispersion preventing exploitation of the κ_{MWCNT} in the matrix; (2) the transport of heat by phonons through individual CNTs and through the CNT network structure is affected by the gaps between both the neighbouring nanotubes and the MWCNT network, resulting in the interruption of thermal transport.

Thermal resistance at the interfaces, also known as Kapitza resistance, affects thermal transport at the polymer-filler interface and filler-filler contact (Das et al., 2008). The aspect ratio of the CNTs also influences Kapitza resistance (Aljaafari et al., 2011). A rise in CNT aspect ratio increases the filler-filler contacts, favouring phonon transport. The scattering effect of phonon transport, such as interfacial boundary scattering arising from the large surface area of the MWCNTs, dominates thermal conduction. However, phonon conduction is affected by defect scattering, and the large surface area of commercially synthesised MWCNTs (as used in this work) have a relatively high density of defects. Gojny et al. (2006) suggested that weak interfacial adhesion between the filler and polymer increases the effectiveness of MWCNTs as thermal conductors due to a smaller effect on the damping behaviour of the phonons' vibrational amplitude at the interface. The marginal increase in thermal transport properties of PC-MWCNT presented in Table 4.2 does not agree with Gojny's view. A plausible explanation is that the random orientation of the agglomerated MWCNTs within PC, as a result of the compression moulding procedure, may have led to a lower filler-filler contact that impeded the transport of phonons.

In an effort to estimate κ_{CNT} from the thermal conductivity measurements of filled and unfilled PC, Eq. 4.5 was rearranged to obtain κ_{CNT} as

$$\kappa_{\text{CNT}} = \frac{\kappa - (\kappa_{\text{PC}})(V_{\text{PC}})}{V_{\text{CNT}}} \quad (4.6)$$

whilst Eq. 4.4 was rearranged to give

$$\kappa_{\text{CNT}} = \frac{(\kappa)(\kappa_{\text{PC}})(V_{\text{CNT}})}{\kappa_{\text{PC}} - (\kappa_{\text{CNT}})(V_{\text{PC}})} \quad (4.7)$$

From calculations of Eqs. 4.6 and 4.7, κ_{MWCNT} in this work is predicted to be between 0.3 and 2.4 W m⁻¹K⁻¹. Literature reports κ values for MWCNTs between 20 and 3000 W m⁻¹K⁻¹ (Chiu et al., 2005; Small et al., 2003; Yi et al., 1999). The estimated κ_{CNT} range is considerably lower than those reported in the references. This is because the calculations do not account for several factors that influence thermal transport in nanocomposites, such as the aspect ratio of MWCNTs and the morphology of the filler network within the matrix. Gojny et al. (2006) found κ of PP-MWCNT decreases with a reduction of the aspect ratio of MWCNTs. Melt mixing, employed in this work, has been shown to reduce the lengths of MWCNTs (Krause et al., 2011). Consequently, this reduces the aspect ratio of MWCNTs and decreases filler-filler contact which can explain the reduction of κ_{MWCNT} predictions relative to literature values.

4.4 Thermal degradation and stability

Knowledge of degradation of a polymer is crucial for determining suitable processing parameters since the final properties, and hence the applications of the material, are dependent on processing. The high thermal stability of CNTs presents the potential for the filler to improve the thermal stability of the base matrix in a nanocomposite. PC has high thermal stability, compared to most thermoplastics, and is used in fire retardant applications by itself or with the addition of fillers (Jang and Wilkie, 2005). Thermogravimetric analysis (TGA) is a technique for monitoring the change of mass in a specimen as it is heated through a pre-defined temperature history (Brown, 2001). The technique is commonly employed to study polymer stability, composition of blends, flame retardancy, and determination of additive amount (Chiu, 1968; Groves et al., 1993).

4.4.1 Method

Thermal degradation and stability of the MWCNT-filled and unfilled PC 2205, as received from the manufacturers, were measured using a SDT (simultaneous DSC and TGA) Q600

TA, but only employed in TGA mode. The tests were performed from ambient temperature up to 900 °C with a ramp rate of 10 °C min⁻¹ in both nitrogen and air atmospheres. The purge gas functioned to (1) maintain a constant atmosphere, (2) remove potential gases emitted during a test, and (3) minimise condensation of reactive products on the balance (Brown, 2001). The samples were cut from pellets using a sharp knife and the weight of each sample range between 10 mg and 15 mg. Platinum pans were used both as reference and to contain the sample. All pans were cleaned using a blow torch before TGA measurements to remove any residue material from previous tests and to ensure the pans are dry prior to the experiment. The samples measured in a nitrogen atmosphere were placed in the furnace for 5 minutes with the flowing purge gas prior to the start of each test in order to displace other gases from the furnace.

The results were analysed using the TA Universal Analysis software. $T_{5\%}$ is defined as the temperature at 5% weight loss, that is used to indicate the onset of degradation, a measure of thermal stability. T_{\max} is defined as the temperature at the maximum rate of weight loss that is identified by the peak of the $\frac{dW}{dT}$ curve. Percentage of char residue is calculated as the final char weight divided by the specimen weight at ambient temperature.

4.4.2 Results and discussion

4.4.2.1 TGA under nitrogen atmosphere

Fig. 4.6 presents typical TGA curves illustrating percentage weight change as a function of temperature, for filled and unfilled PC 2205 over the range 200 - 900 °C under nitrogen atmosphere. The TGA measurements characterised by $T_{5\%}$, T_{\max} and percentage of char residue for filled and unfilled PC are presented in Table 4.3. The influence of the CNTs on the TGA measurements of PC is determined by the difference between the measured values of PC-MWCNT and PC, defined as $\Delta\text{MWCNT} = \text{PC-MWCNT} - \text{PC}$ (for Tables 4.3 and 4.7).

Decomposition of materials under nitrogen atmosphere takes place as a one-step process leaving a char residue. An earlier study on the degradation of PC in nitrogen performed by Jang and Wilkie (2004) measured $T_{5\%} \sim 520$ °C and $T_{\max} = 540$ °C. The difference between Jang's reported measurements and of this work is 38 °C and 20 °C for $T_{5\%}$ and T_{\max} respectively, could be attributed to the dissimilar heating rate, sample size and purge

gas flow rate. They suggested that the PC degradation pathway under nitrogen is mainly caused by the chain scission of the isopropylidene linkage and the hydrolysis/alcoholysis of carbonate linkages. These products rearrange and react to form char residue (Jang and Wilkie, 2004).

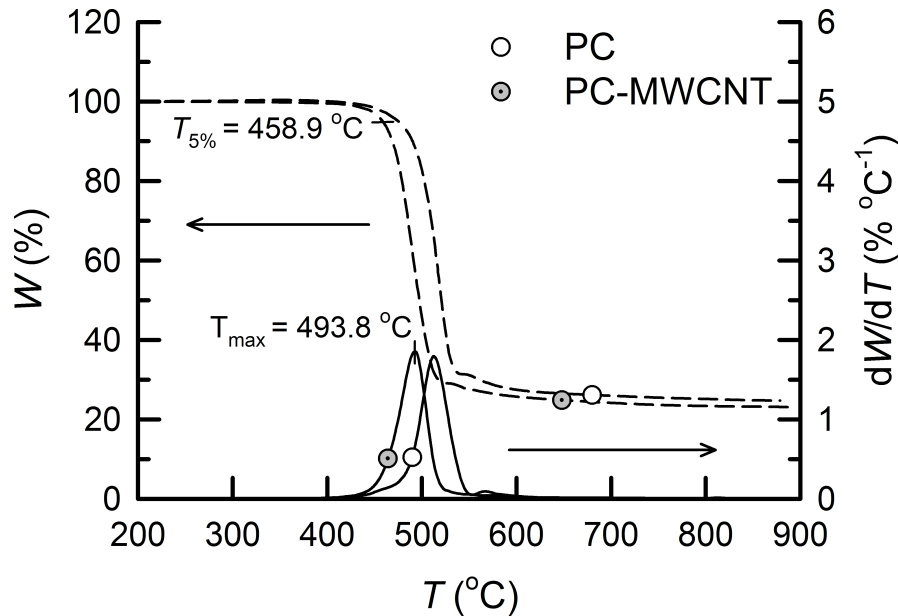


FIGURE 4.6: Typical TGA curves for a specimen of PC 2205 and PC-MWCNT 2205 heated at $10\text{ }^{\circ}\text{C min}^{-1}$ under nitrogen atmosphere

The onset of degradation occurs earlier in PC-MWCNT relative to PC, by $23\text{ }^{\circ}\text{C}$. T_{max} is also lower by $27\text{ }^{\circ}\text{C}$ and the char residue obtained at $900\text{ }^{\circ}\text{C}$ decreased. The evidence from Table 4.3 shows that the addition of CNTs actually decreases the thermal stability of PC, as well as the quantity of char formed under nitrogen atmosphere. ScharTEL and co-workers' (2008) carried out investigations on PC-MWCNT systems comparable to those in this study. They reported a lower temperature at 10% weight loss, $T_{10\%}$ and a decrease in T_{max} as CNT content increased. In ScharTEL's work, PC systems with 2 wt% and 4 wt% MWCNT loading content exhibited a difference between filled and unfilled PC of $\Delta T_{10\%} = -44\text{ }^{\circ}\text{C}$ and $-52\text{ }^{\circ}\text{C}$ respectively whereas $\Delta T_{\text{max}} = -58\text{ }^{\circ}\text{C}$ and $-71\text{ }^{\circ}\text{C}$. The greater reduction in T_{max} of PC-MWCNT for ScharTEL's work relative to this work is speculated to arise from the different MWCNTs dimensions and the purge gas flow rate.

One explanation for the decrease of $T_{5\%}$ and T_{max} in this work could be the increase in thermal conductivity of the bulk nanocomposite due to the addition of the fillers as evidenced in Section 4.3. A greater thermal conductivity could lead to an earlier onset of degradation and a decrease in T_{max} , for a given heating rate. It has been postulated in literature for

TABLE 4.3: Thermal analysis of unfilled and MWCNT-filled (3 wt%) PC under nitrogen atmosphere obtained at $10\text{ }^{\circ}\text{C min}^{-1}$

Material	$T_{5\%}$ ($^{\circ}\text{C}$)	T_{max} ($^{\circ}\text{C}$)	Residue at $900\text{ }^{\circ}\text{C}$ (%)
PC 2205	482 ± 5	520 ± 2	24.7 ± 0.1
PC-MWCNT 2205	459 ± 1	493 ± 1	23.8 ± 0.7
Δ MWCNT	-23 (-5%)	-27 (-5%)	-0.9 (-4%)

other nanocomposites (Barus et al., 2010; Su et al., 2011) that an increase in T_{max} could be attributed to the barrier effect of the CNT network that reduces the rate of diffusion of degradation products from the matrix. However, our measurements show that MWCNT accelerates the diffusion of degradation products from PC, prior to the formation of char on the specimen surface. TGA curves in Fig. 4.6 suggest that the degradation rate of PC is not significantly affected by the presence of MWCNTs. This is possibly due to the formation of char that creates an effective barrier that inhibits further decomposition of materials beneath the char (Kashiwagi, 1994). The formation of char has been shown to be affected by the CNT content, as reported by Scharrel et al. (2008), with the final residue increasing with CNT content. However, low CNT loadings ($\leq 3\text{ wt}\%$) can lead to a decrease of char residue, as shown by Scharrel's group and in this work. It is likely that low CNT loadings, in contrast to highly filled systems, are unable to promote the formation of char and the CNT network is too sparse to provide an effective barrier. In this context, the presence of CNTs with a high thermal conductivity actually promotes the degradation of PC.

Feng et al.'s (2010) study on the degradation of PC filled with 6 wt% bisphenol A bis(diphenyl phosphate) (a flame retardant) and 2 wt% organo-montmorillonite clay nanoparticles (OMMT) recorded a decrease in $T_{5\%}$ relative to unfilled PC, attributed to the modifying surfactant in OMMT. However, they reported an increase in T_{max} arising from the barrier properties of OMMT, and an increase in char residue. In contrast to this study, Gedler's work on PC-graphene showed that the filler improved the thermal stability of PC under nitrogen atmosphere (Gedler et al., 2012). The inconclusive findings suggest that the thermal properties of nanocomposites can be very specific to each individual system.

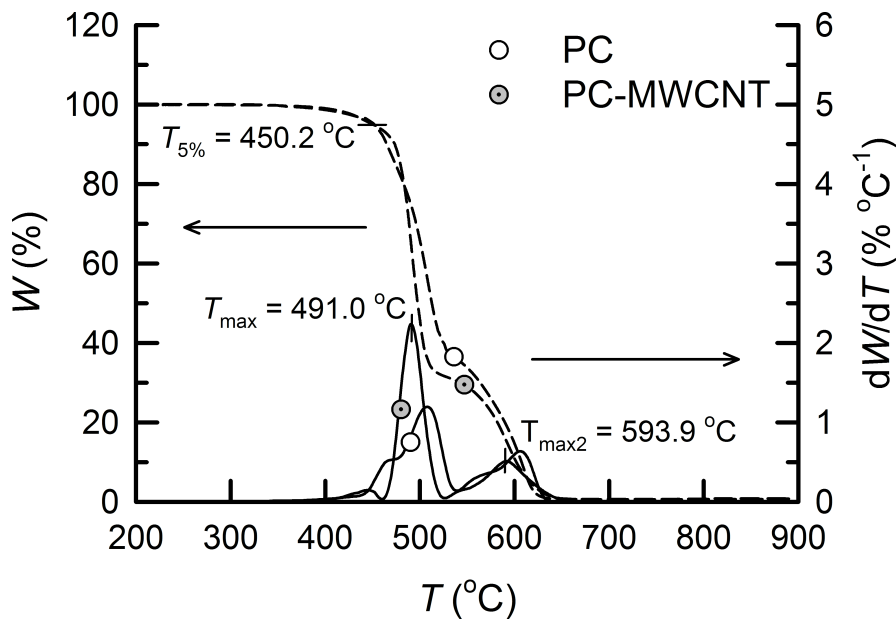
4.4.2.2 TGA under air atmosphere

Degradation of polymers is commonly investigated in inert atmospheres. However, studies of the nanocomposite behaviour in atmospheric conditions are equally important because this provides information for practical applications of the material. Fig. 4.7 illustrates a typical

TABLE 4.4: Thermal analysis of unfilled and MWCNT-filled (3 wt%) PC under air atmosphere obtained at $10\text{ }^\circ\text{C min}^{-1}$

Material	$T_{5\%}$ ($^\circ\text{C}$)	T_{max} ($^\circ\text{C}$)	T_{max2} ($^\circ\text{C}$)	Residue at $900\text{ }^\circ\text{C}$ (%)
PC 2205	449 ± 4	506 ± 3	608 ± 2	0.5 ± 0.2
PC-MWCNT 2205	451 ± 1	489 ± 3	596 ± 3	0.6 ± 0.6
ΔMWCNT	2 (+0.4%)	-17 (-3.4%)	-12 (-2.0%)	0.1 (+20%)

TGA curve for the decomposition of filled and unfilled PC under an air atmosphere. The degradation occurs in a two-step decomposition, with virtually no char residue. The first step of the decomposition corresponds with the thermo-oxidative degradation of unfilled PC that occurs on a similar pathway to that of degradation in nitrogen atmosphere (Jang and Wilkie, 2005). The peak of the $\frac{dW}{dT}$ curve in the second step of decomposition is identified as T_{max2} . This peak arises from the degradation of both the PC that was protected by the char formed during the first step of decomposition and the char layer itself (Gedler et al., 2012). Table 4.4 presents the TGA measurements characterised by $T_{5\%}$, T_{max} , T_{max2} and percentage of char residue for filled and unfilled PC under air atmosphere.

FIGURE 4.7: Typical TGA curves for a specimen of PC 2205 and PC-MWCNT 2205 heated at $10\text{ }^\circ\text{C min}^{-1}$ under air atmosphere

The onset of degradation is slightly delayed by the addition of MWCNT into PC, by $2\text{ }^\circ\text{C}$, whereas T_{max} decreases by $17\text{ }^\circ\text{C}$, and T_{max2} is also lowered by $12\text{ }^\circ\text{C}$. The char residue obtained at $900\text{ }^\circ\text{C}$ is relatively unchanged. The results show that the addition of CNTs marginally improves the thermal stability of PC in air, but decreases the temperature at maximum rate of weight loss both before and after the formation of char.

The results from Table 4.4 suggest that MWCNTs do not function as an effective barrier to hinder the thermo-oxidation of PC. The steeper slope of the change in PC-MWCNT weight as a function of temperature (Fig. 4.7) shows that the rate of weight loss is increased with the addition of CNTs. Li's (2006) work on PA 6-MWCNT showed that MWCNTs improved the thermal stability of the matrix, delaying the start of degradation by 18 °C. The same increase in thermal stability for the PC nanocomposite of this study was not observed. This could be explained by two mechanisms: (1) the presence of thermally conductive MWCNTs improving heat distribution within PC-MWCNT, promoting PC decomposition, and (2) the temporary protection provided by the MWCNT network breaking down upon reaching T_{\max} , resulting in the acceleration of degradation (Marosfői et al., 2006). It is postulated that weak interactions between polymer-filler and filler-filler are unable to physically or chemically adsorb the decomposition products to shift degradation to higher temperatures (Su et al., 2011). This could be an explanation for the close proximity of $T_{5\%}$ values of filled and unfilled PC in this work, since no surface modifications to MWCNTs were performed. Another explanation is that poorly-dispersed fillers do not enhance the barrier effects needed to slow down the transport of decomposition products as efficiently as highly dispersed fillers (Wu et al., 2008). This implies that the MWCNTs could be distributed within the PC matrix with a low level dispersion resulting in a lack of thermal stability improvement.

Gedler et al. (2012) reported an increase in $T_{5\%}$, T_{\max} , $T_{\max2}$ and in the percentage of char residue of PC with the addition of graphene (0.5 wt%) for degradation in air. The graphene acted as a barrier, delaying both oxygen from reaching the PC and the escape of volatile gases during degradation. Choi et al. (2005) observed increased thermal stability PC with the addition of 10 to 25 wt% vapour grown carbon nanofibers (VGCF). Similarly to Gedler's group, Choi and co-workers also found that the residue coincided with the filler content. This was not observed in the present work with PC-MWCNT, and could be attributed to the degradation of CNTs in air above 600 °C (Marosfői et al., 2006) and to the presence of defects along the MWCNTs leading to oxidative instabilities (Bom et al., 2002).

In comparison with nitrogen atmosphere, $T_{5\%}$ and T_{\max} for unfilled PC in air shifted upwards by 33 °C and 14 °C respectively; while $T_{5\%}$ and T_{\max} for PC-MWCNT in air also shifted upwards by 8 °C and 4 °C respectively. The final char residue at 900 °C remained constant up to the end of degradation in nitrogen but it continued to decrease in air, reaching close to zero at 900 °C. Contrary to the findings in nitrogen, the addition of MWCNTs had no significant effect on the thermal stability of PC in air. For PC, the rate of weight loss is

reduced in air relative to nitrogen. This is because oxygen primarily reacts with the surface of samples, forming the protective char layer faster than in samples degrading in nitrogen (Jang and Wilkie, 2005). For PC-MWCNT, the rates of weight loss in nitrogen and in air (first step of degradation) are similar. This suggests that the presence of MWCNTs *hindered* the formation of char in air, leading to faster degradation compared to unfilled PC.

4.5 Conclusions

The glass transition temperatures of PC and PC-MWCNT with different matrix PC grades, reported in Section 4.2, were measured using DSC. It was found that T_g increases with increasing molar mass for both MWCNT-filled and unfilled PC, although the increments were small. A plot of T_g as a function of $\frac{1}{M_n}$ showed that T_g decreases with increasing density of chain ends regardless of the presence of CNTs, in accordance to the free volume theory. The addition of MWCNTs to PC produced a discernible reduction of T_g . The addition of CNTs appears to enhance chain mobility, leading to a lower T_g . GPC measurements in Section 3.4.2 of PC extracted from PC-MWCNT confirm that the observed decrease in T_g cannot be attributed to matrix degradation during processing. A possible explanation for the decrease in T_g of PC-MWCNT is attributed to the lack of wettability between the PC and the surface of CNTs, giving rise to additional free volume.

Section 4.3 presented the thermal transport properties of PC 2205 and PC-MWCNT 2205 determined using the transient plane source technique. This was performed to study the role of CNTs on the transport of heat. The presence of MWCNTs alters the thermal transport properties of PC matrix increasing κ by 9%, e by 17%, d by 15%, and C_p by 2%. Two two-phase models, the parallel model and the series model, were employed to determine the upper and lower bounds of $\kappa_{\text{PC-MWCNT}}$, based on the κ measurements and the CNT volume fraction. $\kappa_{\text{PC-MWCNT}}$ was estimated to be between $0.27 \text{ W m}^{-1}\text{K}^{-1}$ and $0.68 \text{ W m}^{-1}\text{K}^{-1}$. The measured $\kappa_{\text{PC-MWCNT}}$ was found to be within the predicted bounds. The closeness of $\kappa_{\text{PC-MWCNT}}$ to the lower boundary could be explained by the CNT agglomeration and the presence of gaps (between both the neighbouring individual nanotubes and the MWCNT network) that interrupts the transport of heat by phonons.

Section 4.4 described the thermal degradation and stability measurements of PC and PC-MWCNT carried out using TGA under nitrogen and air atmospheres. Degradation in nitrogen occurred as a one-step process whereas degradation in air took place in two steps. In an inert atmosphere, the addition of CNTs increase the onset of degradation and decreases thermal stability of PC. This is likely due to improved heat distribution as a result of the presence of CNTs that promotes PC degradation. Thermo-oxidation tests found a marginal increase in the onset of PC degradation temperature with the addition of CNTs. The explanation for the close proximity of the thermal stability of filled and unfilled PC could be attributed to two factors. Firstly, the weak polymer-filler and filler-filler interactions may not be effective in adsorbing the degradation products either physically or chemically. This is expected since no surface modification was performed on the CNTs. The second factor is that the CNT barrier protection is only temporary and breaks down upon reaching T_{\max} .

When PC degrades, a layer of char forms on the material surface that acts as a protective barrier. Comparing the rates of weight loss in air and nitrogen of PC and PC-MWCNT, it was observed that the degradation rate was reduced for PC in air whereas PC-MWCNT exhibited similar degradation rates regardless of the atmospheres. The reduction of degradation rate of pure PC is attributed to the faster formation of char in air relative to nitrogen. This means that the presence of CNTs delayed the formation of char in air, and hence promote degradation. This accelerated degradation occurs after the temporary barrier of the CNT network breaks down.

Chapter 5

Melt rheology

The previous chapter has determined the thermal stability of PC and PC-MWCNT that provided the upper boundary of the temperature range for the investigation the viscoelastic properties of MWCNT-filled and unfilled PC melts in this chapter. This chapter is based on the article "Viscoelastic melt rheology and time-temperature superposition of polycarbonate-multi walled carbon nanotube nanocomposites" published in *Rheologica Acta* (Choong et al., 2013). Section 5.2 introduces the rheological procedures and methods. Section 5.3 investigates the effect of the presence of MWCNTs on linear viscoelasticity of PC. Preparatory frequency sweep tests are presented in Section 5.4 to study the influence of test conditions on shear experiments such as temperature ramp direction and nanocomposite melt processing on the materials rheological response. Section 5.5 describes the shifting procedures for time-temperature superposition (TTS) employed to extend the viscoelastic response of all materials over a broad range of frequencies. Mastercurves for both unfilled PC and PC-MWCNTs are presented in Section 5.6. Section 5.6.3 is concerned with large amplitude oscillatory shear measurements to study the effects of shear and temperature history on the rheological behaviour of PC-MWCNT. The aim is to elucidate the roles played by nanotubes and by the matrix polymer on several aspects of the viscoelastic response: time-temperature superposition and vertical shifting, dynamic strain amplitude, relaxation processes, and strain and temperature history.

5.1 Introduction

Several authors have specifically studied the melt rheology of PC-MWCNT nanocomposites (Abdel-Goad and Pötschke, 2005; Pötschke et al., 2002; Sung et al., 2006). Pötschke and co-workers were one of the earliest groups to carry out investigations on the frequency dependence of the linear viscoelastic moduli of PC-MWCNT for various filler concentrations, as reported in Section 2.7.1. Zeiler et al. (2010) studied the influence of polymer viscosity and of polymer-nanotube interactions on network formation by exploring both the linear and the non-linear viscoelastic regions using simultaneous rheological and electrical measurements. They performed flocculation experiments at 190 °C and 250 °C and observed that the formation of both rheological and electrical networks was faster at higher temperature, as well as in nanocomposites with a matrix of lower molar mass. Thus, they linked speed of the network formation to viscosity, with lower viscosity promoting faster network formation. Comparing two molar masses of PC, they measured a higher storage modulus in PC-MWCNT (2 wt% and 3 wt%) with the lower molar mass matrix for low frequencies at a single temperature (250 °C), and suggested that the shorter polymer chains facilitated CNT-CNT contacts, giving rise to a stiffer nanotube network. They concluded that the breakup of CNT clusters and the diffusion-controlled clustering of CNTs are two opposite processes which superpose, and that the timescale of the diffusion-controlled clustering is not influenced by oscillatory shear flow. Thus, it is apparent that the polymer matrix can have a strong influence on the rheological properties following breakup of CNT clusters. More recently, Handge et al. (2011) applied a fractional Zener model for predictions of linear viscoelastic properties of PC-MWCNT melts to the experimental data of Zeiler et al. (2010) for filler concentrations of 0.5 - 5 wt% (for $T = 250$ °C), and they were successful in describing the storage modulus over a wide frequency range, but less so for the loss modulus.

TTS is a methodology integral to most modelling efforts that combines the effects of time and temperature and that relies on the principle of thermorheological simplicity. Materials are considered thermorheologically simple when all relaxation mechanisms present have the same temperature dependence (Dealy and Plazek, 2009). In polymer melts, the temperature dependence of relaxation times allows frequency dependent or time-dependent viscoelastic data to be shifted to any reference temperature through an appropriate shift factor. This process is normally referred to as horizontal shifting. The viscoelastic modulus of polymer melts is also weakly dependent on temperature because of its effect on density. When a

temperature correction is applied to the modulus, it is known as vertical shifting (Rubinstein and Colby, 2003).

There have been mixed conclusions on the application of TTS to nanocomposites. Handge and Pötschke (2007) attempted to shift the frequency dependence of viscoelastic moduli of PC-MWCNTs (2 wt%) measured at 190 °C and 210 °C, and observed that the data superposed unsatisfactorily. They suggested that the failure of TTS implied that the relaxation processes of the pure polymer and of the filler network had different temperature dependence, and attributed the influence of interactions between polymer and filler more to the entropy elasticity of the melt than to the temperature. Solomon et al. (2001) successfully applied TTS to melt-compounded PP filled with organophilic nanoclay in the presence of a compatibiliser. They observed a similar temperature dependence of shift factors in the nanocomposites as in the base polymer. Reichert et al. (2001) found that the application of TTS was possible with extruded and injection-moulded PP filled with organophilic layered silicates that were annealed, but interestingly that TTS was not possible without the annealing step. They used the shifting procedure as a tool for the investigation of clay platelet network formation, and observed that the annealing process improves exfoliation and facilitates the formation of a thermodynamically stable structure. Wu et al. (2007) observed that TTS was possible in PBT-MWCNT nanocomposites in a narrow temperature window of 230 to 240 °C, but not at higher temperatures up to 260 °C. They attributed the successful superposition at higher reduced frequencies to dominant local chain dynamics, and the failure of superposition at lower reduced frequencies to the different temperature dependence of the percolated network.

None of the reported studies attempted any application of vertical shifting. This chapter investigates the linear and non-linear viscoelastic melt rheology of a range of PC-MWCNT nanocomposites of constant filler content but varying matrix viscosity and of the matching pure melts.

5.2 Experimental

5.2.1 Materials

Four grades of PC (2205, 2405, 2805 and 3105) ranging from low to high viscosity as received and the matching grades of MWCNT-filled (3 wt%) polymers were investigated. CM disc

specimens of 30 mm in diameter and 0.5 mm in thickness were produced, with CM parameters detailed in Section 3.3.1.

Dynamic rheometry was performed using a Bohlin C-VOR Instruments rheometer fitted with an environmental chamber. Measurements were performed in stress-controlled oscillatory shear using a 25 mm parallel plate geometry with a 0.5 mm gap size in an air atmosphere. Parallel plates were selected due to ease of specimen loading to ensure consistent contact between the plates and the specimen disc, although there is a disadvantage in the presence of strain gradient. Each moulded disc was allowed to acclimatise at the highest temperature of testing for a period of 5 minutes and trimmed to size with a sharp blade prior to commencing the test. The thermal compensation and auto-tension options were enabled during the tests to control the gap and to compensate for thermal expansion of the specimen and parallel plates. A thermal equilibration time of 300 s followed by a 30 s buffer delay was imposed before beginning each isothermal test run.

5.2.2 Amplitude sweep procedure

Isothermal amplitude sweeps at logarithmically increasing shear strains between 0.01% and 100% were performed at a fixed frequency of $2\pi \text{ rad s}^{-1}$ on PC 2205 and PC-MWCNT 2205. The sweeps were conducted in decreasing 20 °C steps between 260 and 160 °C for all grades of pure PC, and between 300 and 160 °C for all nanocomposite grades. Thermal degradation studies in air atmosphere reported in Section 4.4.2.2 exhibited the onset of degradation from temperatures above 400 °C. Thus, the temperature range for rheological investigations of the material is well below the temperature at the onset of degradation.

5.2.3 Frequency sweep procedure

Isothermal frequency sweeps were carried out in decreasing 20 °C steps between 260 and 160 °C for all grades of pure PC, and between 300 and 160 °C for all nanocomposite grades, at logarithmically increasing frequencies from 0.2 to $80\pi \text{ rad s}^{-1}$, at a fixed strain amplitude of 0.5%, determined from amplitude sweeps. Isothermal frequency sweeps were also performed at strain amplitudes of 0.05%, 5% and 50% for PC-MWCNT 2205 only. Limited preparatory experiments were performed in increasing 20 °C steps to evaluate the influence of the change of temperature ramp direction on the measurements.

5.3 Amplitude sweeps

5.3.1 Determination of the linear viscoelastic range

Fig. 5.1 reports the storage modulus, G' and the loss modulus, G'' , both normalised with respect to their measured values at 0.5% strain, $G'_{0.5\%}$ and $G''_{0.5\%}$ respectively for both unfilled and filled PC 2205, as a function of strain amplitude, measured at $2\pi \text{ rad s}^{-1}$ for all temperatures investigated. The normalisation is intended to facilitate the determination of a strain amplitude for which both filled and unfilled PC are within the linear viscoelastic (LVE) region.

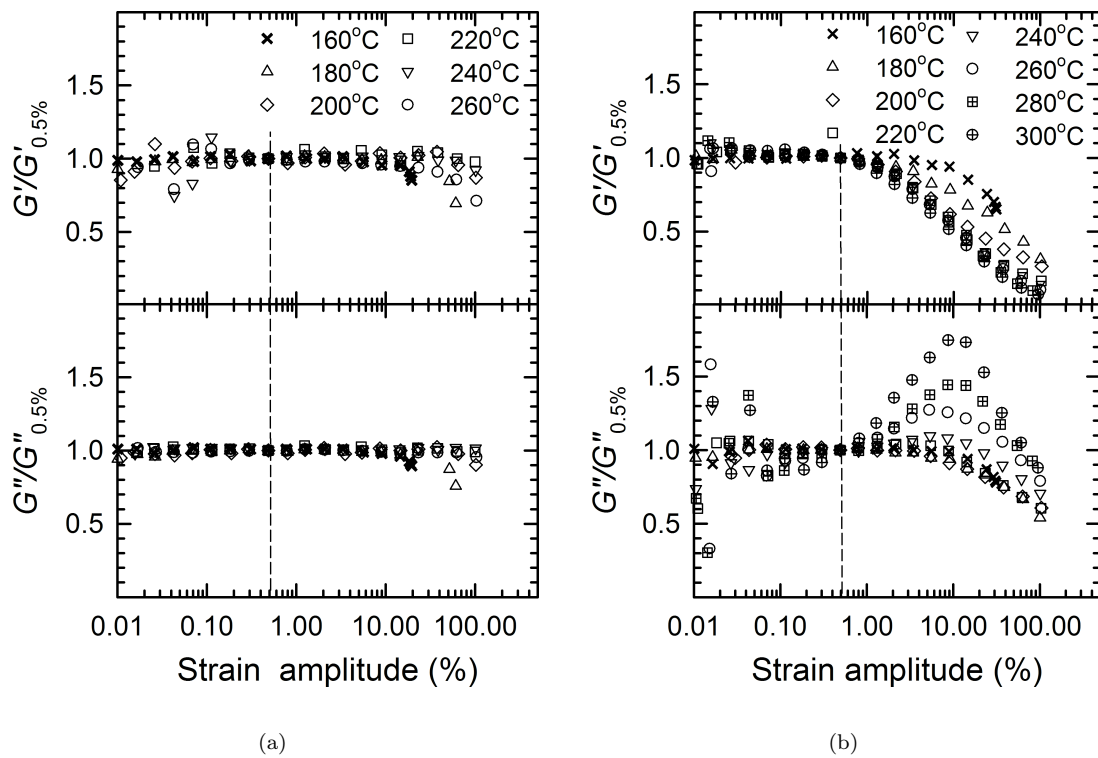


FIGURE 5.1: Amplitude sweeps of normalised storage modulus G' and loss modulus G'' measured at $2\pi \text{ rad s}^{-1}$ of (a) unfilled PC 2205 at temperatures 160 - 260 °C and of (b) PC-MWCNT 2205 (3 wt%) at temperatures 160 - 300 °C. The vertical dashed line indicates the linear viscoelastic limit

Very small strain amplitudes, $< 0.1\%$, result in noisier measured signals, as the torques and angular velocities approached the limits of the resolution of the instrument. A region where moduli are independent of strain amplitude then appears with increasing amplitude, extending to strains beyond 10% strain for the unfilled PC, but only to 0.5% strain for the filled PC. The earlier onset of nonlinearity has been previously attributed to the effect of strain amplification: the matrix experiences a higher local strain than the macroscopic

strain due to the presence of the stiff nanotubes (Costa et al., 2008; Richter et al., 2009). This effect is generally enhanced by confinement of polymer chains located near the surface of a nanotube (Stöckelhuber et al., 2011; Vilgis, 2005). Since no specific surface modification of MWCNTs was performed in our materials, chemical interactions between matrix and CNTs are likely to be weak. Nevertheless, the confined or adsorbed layer should be detectable by its reduction to the mobility of chains, leading to a rise in T_g . Measurements obtained from DSC reported in Section 4.2 indicate a small but discernible reduction in T_g with the addition of MWCNTs.

At larger strain amplitudes, the most striking difference in the response arising from the presence of filler is a strain overshoot in loss modulus. This overshoot reaches a maximum at shear strains of 5 - 10%, and is followed by shear thinning behaviour at even larger strains. Similar overshoots were previously observed in PA-6 clay nanocomposites (Wan et al., 2005) and have been attributed to and can be modelled by the different amplitude dependence of the rate of cluster formation relative to that of cluster destruction (Hyun et al., 2011). A cluster in this context can be thought of as a region of material in which there is increased CNT connectivity. The overshoot is greater at higher temperatures. This is consistent with the rate of cluster formation being a temperature dependent process. The destruction of CNT clusters with increasing strain amplitude also provides an explanation for the earlier onset of non-linearity in storage modulus in the filled materials.

In subsequent experiments, linear viscoelasticity was explored through isothermal frequency sweeps performed at a strain amplitude of 0.5%, indicated in Fig. 5.1, where both filled and unfilled PC are within the LVE at all temperatures of interest. It is noted that while the LVE limit was explored using a fixed frequency of $2\pi \text{ rad s}^{-1}$, the applicability across a wide temperature range suggests that it will be equally appropriate across a wide frequency range.

5.4 Preparatory experiments for isothermal frequency sweeps

5.4.1 Time dependence of structural build up

Initial exploratory frequency sweeps suggested that in order to explore the full viscoelastic spectrum, the presence of CNTs in the nanocomposites might require higher test temperatures. However, performing rheology at very high temperatures is challenging since polymer degradation can occur during the experiment. In order to investigate possible polymer degradation in CNT-filled PC samples at the highest measuring temperature, an annealing experiment was conducted prior to performing oscillatory test measurements at a constant frequency. This test is known as a flocculation test (Richter et al., 2009). A single PC-MWCNT 2205 sample was annealed at 280 °C at a single frequency (1 Hz) and 0.5% strain (still within the LVE at this temperature) for 4 hours. The plot of storage modulus and loss modulus against time is shown in Fig. 5.2. The plot is shown using a linear scale to emphasize any change in the value of the viscoelastic moduli.

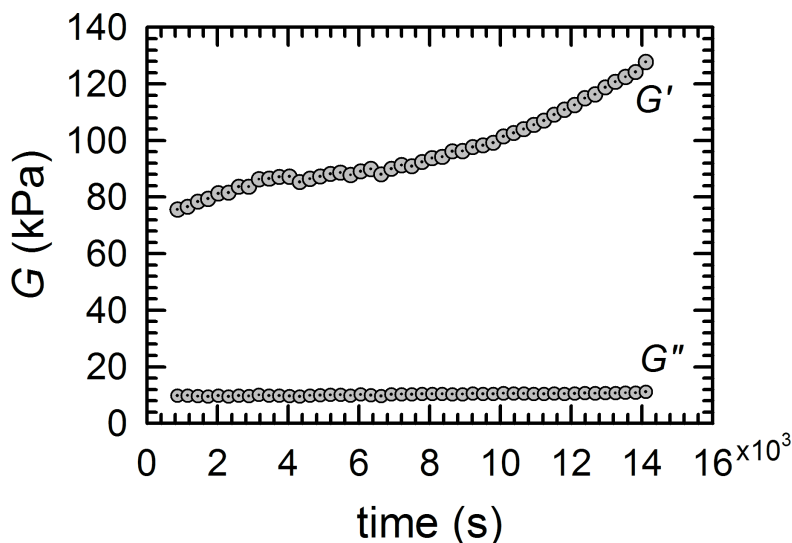


FIGURE 5.2: Storage modulus, G' and loss modulus, G'' of PC-MWCNT 2205 annealed at 280 °C at a single frequency (1 Hz) and 0.5% strain

At 280 °C, G' increases almost by a factor of 2 over a 4 hour period, whereas G'' remained constant. Degradation would be expected to decrease G' and an increase in G'' at a given temperature and frequency, due to a shortening of the molecules. The fact that G'' remains constant and that the increase is limited to G' suggests that the dominant change in the structure is due to rearrangement of the nanotubes to form a network. This gradual build

up of structure with time has also been reported in studies on similar PC-MWCNT systems by Alig et al. (2008) and Richter et al. (2009).

The break-up of this network can also be seen indirectly in the amplitude sweeps of through the reduction in modulus of the nanocomposites with increasing strains in (Fig. 5.1) and it is reasonable to attribute this to a form of Payne effect ordinarily seen in filled rubbers.

5.4.2 Effect of temperature step direction

A frequency sweep was performed starting at the highest temperature, 300 °C and decreasing in temperature steps of 20 °C or 40 °C through to 160 °C, followed by a reverse series of steps increasing temperature back to 300 °C in 20 °C or 40 °C steps. This experiment was intended to determine whether the sequence of the temperature steps has an influence on the viscoelastic properties of PC-MWCNT, perhaps through either a build-up of structure, or degradation of the polymer itself. G' of PC-MWCNT 2205 was measured over a frequency range of 0.1 - 40 Hz at 0.5% strain, at temperatures between 160 - 300 °C, as illustrated in Fig. 5.3. The almost perfect overlap between increasing and decreasing steps shows that direction of the temperature steps has virtually no effect on the magnitude of the recorded modulus for all temperatures and frequencies.

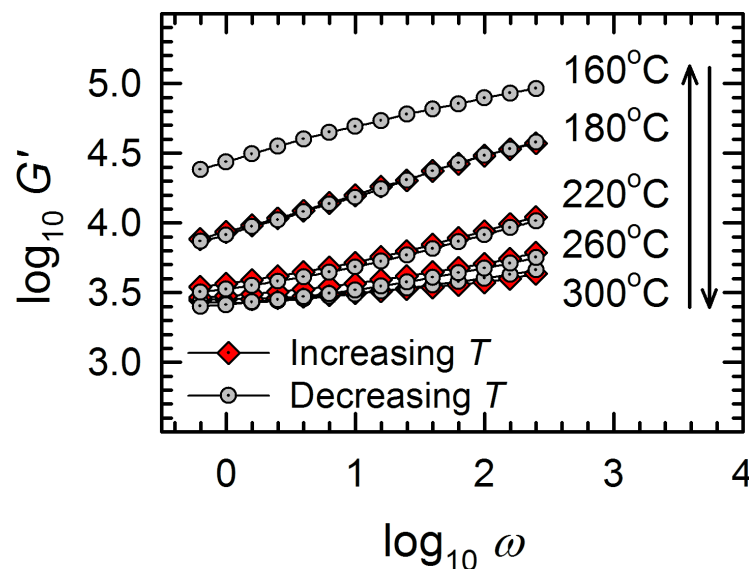


FIGURE 5.3: Storage modulus, G' against frequency of PC-MWCNT 2205 at different temperature step directions. Arrows indicate temperature direction, initially decreasing followed by an increase. Lines are guide to the eye following increasing and decreasing step

The downward temperature ramp was chosen for all subsequent frequency sweeps as it was easier to trim the specimen discs at higher temperatures.

5.4.3 Role of melt processing on rheology

In order to attempt to quantify this effect, the viscoelastic response of PC 2205 (as supplied in granules from Bayer MaterialScience) was compared to that of PC 2205 1-pass, the unfilled PC that had experienced the same extrusion conditions as the nanocomposites. Fig. 5.4 illustrates the two responses of G' as a function of frequency. They are virtually indistinguishable. This suggests that the extrusion conditions do not cause a reduction in molar mass of the matrix polymer, when PC is processed alone. Nevertheless, through this experiment alone, we cannot exclude the possibility that degradation could arise as a result of the presence of the nanofillers during compounding.

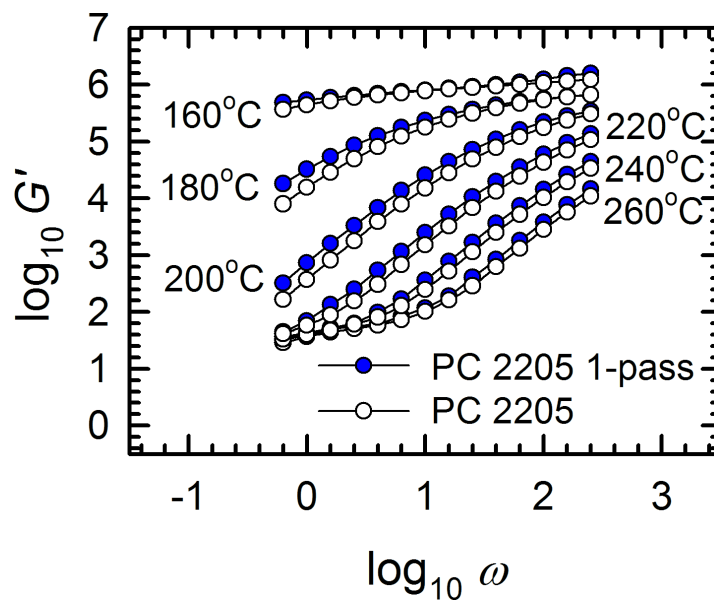


FIGURE 5.4: Storage modulus, G' against frequency of PC 2205, as received from the supplier, and of PC 2205 1-pass, material that had experienced identical melt mixing conditions as PC-MWCNT without the addition of the filler, for $T = 160 - 260$ °C. Lines are guide to the eye

The recovery of PC from the nanocomposite through Soxhlet extraction and the molar mass measurement, presented in Section 3.4.2, supports the view that no degradation of the matrix polymer within the nanocomposite took place during melt compounding, even with nanoparticles present.

5.5 Time-temperature superposition and construction of mastercurves

5.5.1 Vertical shifting

Dealy and Plazek (2009) recommended the use of the van Gorp-Palmen (VGP) plot of phase angle, δ vs complex modulus, G^* to ascertain thermorheological simplicity of a material. The VGP plot does not require a shift in frequency to a reference temperature to produce overlapping curves, but only a shift in modulus with temperature (van Gorp and Palmen, 1998).

Fig. 5.5(a) illustrates unshifted isothermal frequency sweeps at 0.5% strain for both filled and unfilled PC 2205 as a VGP plot. The measurements on unfilled PC exhibit a reasonably good but not perfect overlap across the temperature range; the measurements on PC-MWCNT show a distinct lack of overlap.

A common method for accounting for changes in modulus with temperature T in pure polymer melts is to apply a density correction to the modulus such that the relationship

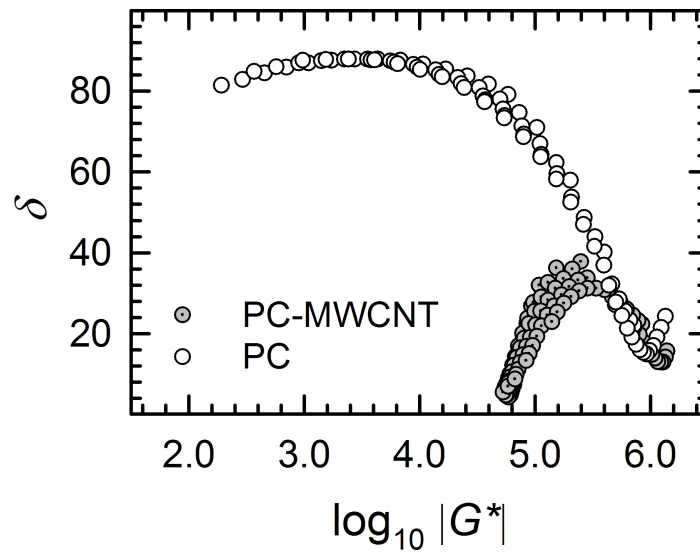
$$\frac{G^*(T_{\text{ref}})}{\rho_{\text{ref}}T_{\text{ref}}} = \frac{G^*(T)}{\rho T} \quad (5.1)$$

is satisfied, where T_{ref} is the reference temperature and ρ_{ref} is the density at this reference temperature. The ratio $\rho_{\text{ref}}T_{\text{ref}}/\rho T = b_T$ is the vertical shift factor (noting that in practice it results in a horizontal shift in a VGP plot). A convenient expression for the density of PC ρ_{PC} was obtained by Zoller (1982) from isothermal dilatometry experiments as

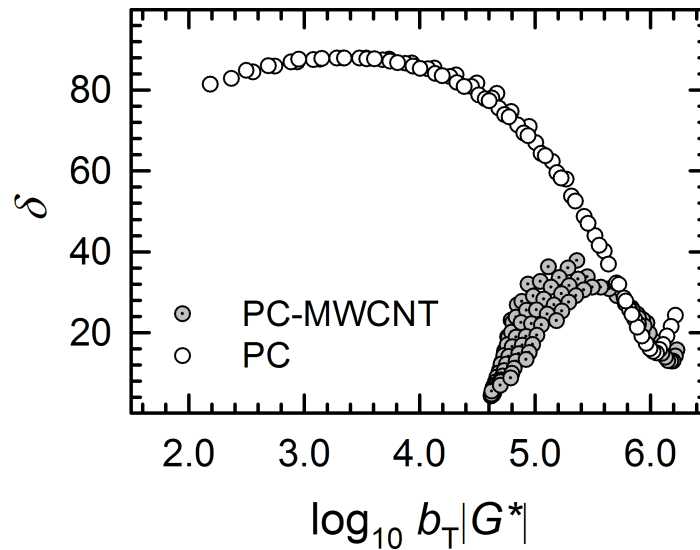
$$\rho_{\text{PC}} = \exp[0.307 - 1.859 \times 10^{-5}(T + 273)^{3/2}] \quad (5.2)$$

Variations in density with molar mass are small and neglected here. The computed value of b_T is shown in Fig. 5.6. Using Eqs. 5.1 and 5.2, a reduced modulus ($b_T G^*$) VGP plot for unfilled PC 2205 at $T_{\text{ref}} = 200$ °C is produced and shown in Fig. 5.5(b). A small improvement to the overlap between temperatures can be observed in the pure polymer relative to the unshifted data in Fig. 5.5(a).

A similar approach was attempted with the nanocomposite. To the authors knowledge, there are no reports in the literature of variation in density with temperature of MWCNTs. Hence,



(a)



(b)

FIGURE 5.5: (a) The van Gurp-Palmen plot of phase angle against complex modulus over a temperature range of 160 - 260 °C for PC 2205 and of 160 - 300 °C for PC-MWCNT 2205 (3 wt%). (b) Same plot with the reduced complex modulus at $T_{\text{ref}} = 200$ °C

a constant density of CNT $\rho_{\text{CNT}} = 1.75 \text{ g cm}^{-3}$ (Shaffer and Windle, 1999) was used across the temperature range. The density for PC-MWCNT was determined from the nominal nanotube mass fraction using Eq. 3.6 in Chapter 3.

The computed value of b_T based on density is also shown in Fig. 5.6 for PC-MWCNT grades. It is virtually indistinguishable from that of the pure PC due to the small fraction of CNTs

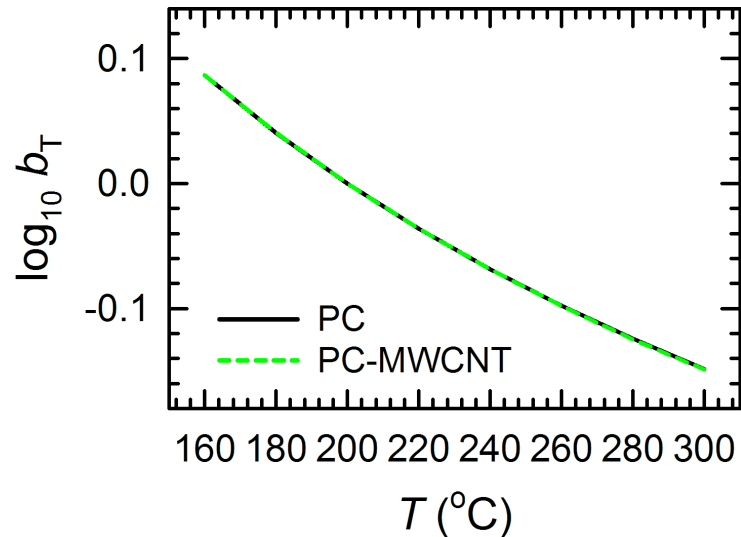


FIGURE 5.6: Vertical shift factors at reference temperature $T_{\text{ref}} = 200$ °C determined for unfilled PC based on a density correction using Eqs. 5.1 and 5.2 (thick solid line), and for PC-MWCNT using Eqs. 5.1 and 3.5 in Chapter 3 (green dashed line)

in these nanocomposites. A reduced modulus VGP plot for filled PC 2205 at a reference temperature of 200 °C using the density correction is shown in Fig. 5.5(b). The correction is actually slightly detrimental to the quality of the superposition, suggesting that there may be a different reason for the change in modulus with temperature in the filled systems.

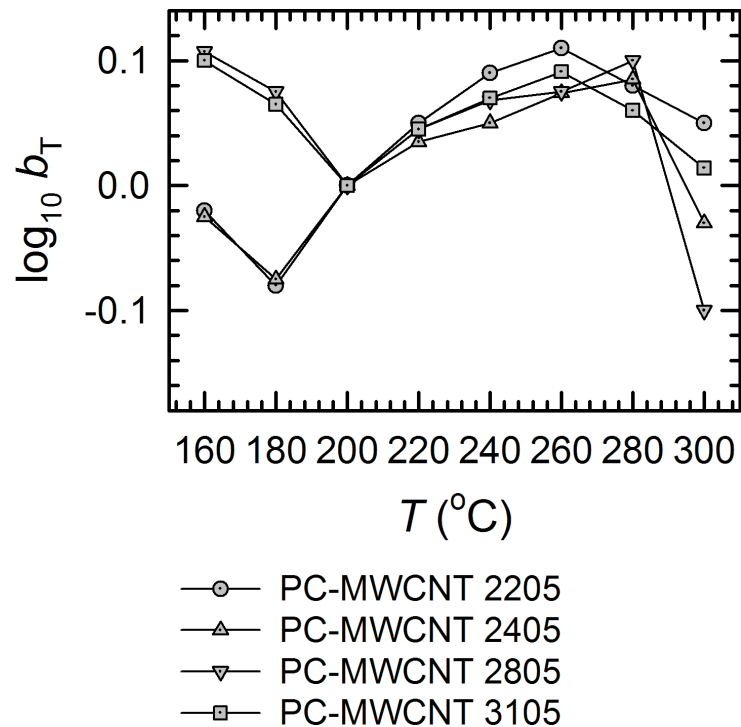


FIGURE 5.7: Vertical shift factors obtained by manual shifting using the van Gorp-Palmen plots for all PC-MWCNT grades. The thin lines are guides to the eye

As a step towards understanding this process, the vertical (or modulus) shift factors, b_T are obtained by determining the (horizontal) shift in complex modulus required to superpose the measurements in the VGP plot. b_T was obtained manually, from a visual assessment of the overlap for measurements on all filled grades, as shown in Fig. 5.8 for all filled PC. The values of b_T are shown in Fig. 5.7. Although it is possible to achieve good overlap in the low frequency region of the measurements, it is challenging to do so in the high frequency range, for all temperatures except for 160 °C. There are no significant differences in either b_T or the quality of fit between matrix grades at temperatures above 200 °C; at temperatures below 200 °C there appears to be some effect of molar mass, although the reason for this is unclear at present.

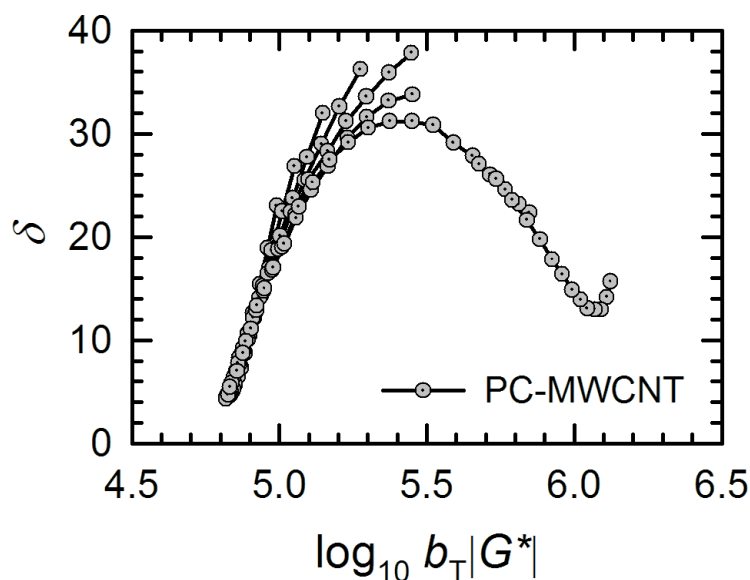


FIGURE 5.8: Shifted van Gorp-Palmen plot for PC-MWCNT 2205 (3 wt%) at a reference temperature of $T_{\text{ref}} = 200$ °C used to determine the vertical shift factor. The lines are guides to the eye

5.5.2 Horizontal shifting

A numerical procedure was developed to determine the optimal amount of horizontal shift in the frequency domain of the reduced moduli required to attempt the production of a mastercurve. For every measurement T , a horizontal shift factor a_T was identified relative to a fixed T_{ref} that minimises the error in the overlap of the shifted moduli measurements relative to the adjacent measured temperature. The method is based on that suggested by Gergesova et al. (2010). It is aimed at removing the ambiguity normally present in manual shifting of viscoelastic experimental data. The method relies on numerical optimisation technique that

seeks to identify the shift factor that minimises the area enclosed by overlapping moduli between viscoelastic data measured at adjacent temperatures.

The first step in the procedure is the definition of T_{ref} . A Matlab optimisation subroutine is then used to identify the coefficients of a set of polynomials $f_{T_i}^{b_T G'}$ ($\log \omega$) and $f_{T_i}^{b_T G''}$ ($\log \omega$) that best fit each set of measured values of reduced $\log G'$ and $\log G''$ as a function of \log frequency, for each measured temperature. In the present data, a third order polynomial was found to be satisfactory. Fig. 5.9 illustrates the polynomial fitting of experimental data of viscoelastic moduli for PC 2205 measured at $T = 160 - 260$ °C. The polynomials are used in the subsequent shift factor optimisation instead of the measured experimental data in order to minimise the consequences of experimental scatter.

For each pair of temperatures T_i and T_{i+1} , an overlap region is identified for both storage and loss moduli. Each region is enclosed by the two polynomials obtained from the data at the two temperatures of interest on the left and right boundaries. The lower boundary is defined by the value of the polynomial functions

$$f_{T_i}^{b_T G'}(\min(\log \omega)) \text{ and } f_{T_i}^{b_T G''}(\min(\log \omega)) \quad (5.3)$$

where $\min(\log \omega)$ is the log of the smallest frequency recorded experimentally for T_i . The upper boundary is defined similarly by the values of the polynomial functions

$$f_{T_i}^{b_T G'}(\max(\log \omega)) \text{ and } f_{T_i}^{b_T G''}(\max(\log \omega)) \quad (5.4)$$

where $\max(\log \omega)$ is the log of the highest frequency recorded experimentally at T_{i+1} . An optimisation routine is scripted in Matlab to identify the value of the shift factor, a_T such that when the shifting is applied to the polynomials, giving $f_{T_i}^{b_T G'}(\log a_T \omega)$ and $f_{T_i}^{b_T G''}(\log a_T \omega)$ the sum of the magnitudes of the overlap regions obtained simultaneously from storage and loss moduli data is a minimum.

The construction of a single such bound area is illustrated on real experimental data for pure PC 2205 in Fig. 5.9, with $T_i = 200$ °C and $T_{i+1} = 220$ °C. Each area was computed numerically using the trapezium rule. A shift factor was obtained between each pair of neighbouring temperatures, and the values reported are relative to the quoted reference temperature.

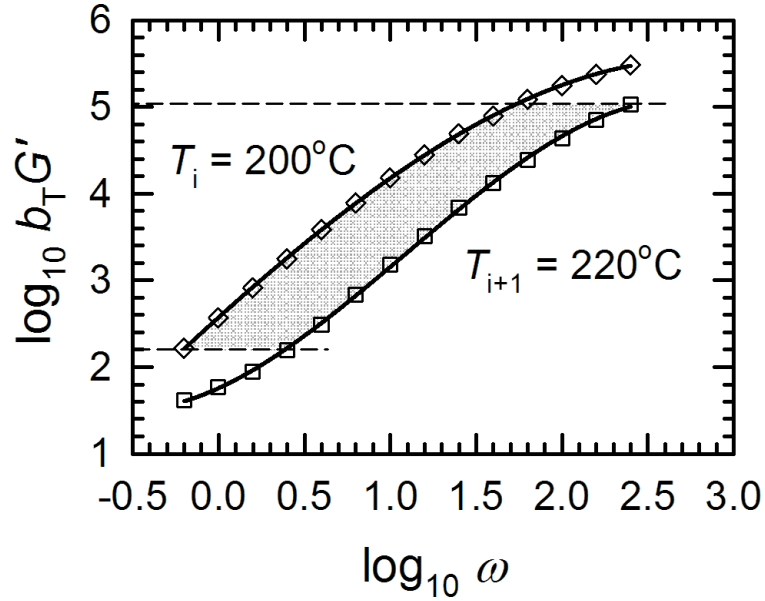


FIGURE 5.9: Illustration of the construction of the area (shaded) minimized to determine the optimum shift factor. Solid lines are polynomial functions. Dashed lines represent the upper and lower boundaries of the overlapping area

Horizontal shift factors obtained using this procedure are shown in Fig. 5.10 for unfilled grades, and in Fig. 5.11 for filled grades. The shift factors for unfilled PC can be described by the Williams-Landel-Ferry (WLF) equation

$$\log(a_T) = \frac{-C_1(T - T_{\text{ref}})}{C_2 + (T - T_{\text{ref}})} \quad (5.5)$$

where C_1 and C_2 are empirical constants that are dependent on the selected reference temperature, T_{ref} . The WLF fit for all grades of unfilled PC is shown in Fig. 5.10 for $T_{\text{ref}} = 200^\circ\text{C}$, yielding $C_1 = 4.14$ and $C_2 = 93.2$.

Fig. 5.10 exhibits horizontal shift factors to be relatively independent of the matrix polymer. For sufficiently entangled unfilled polymer melts this is expected since relaxation times of the polymer chains change with temperature in the same way. Although the horizontal shift factors for PC-MWCNT are not perfectly described by WLF, as shown in Fig. 5.11, it is in close agreement to the unfilled PC. The similarity of shift factors between the filled and pure materials is evidence that the relaxation processes probed in this temperature range all have the same temperature dependence (even though the moduli do not).

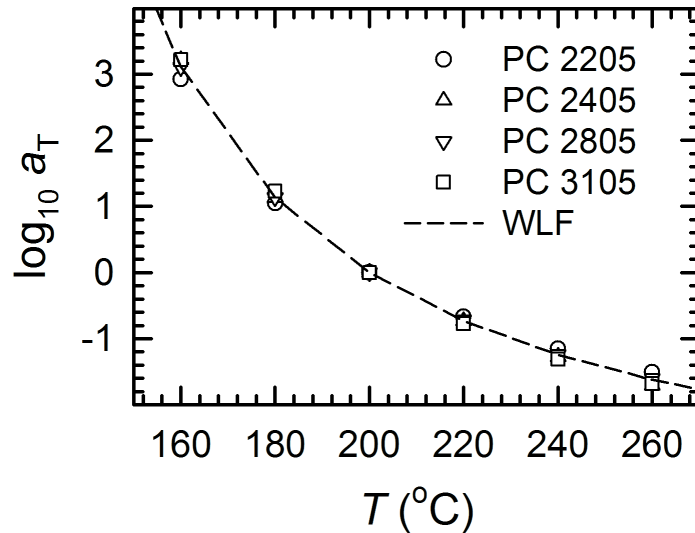


FIGURE 5.10: Shift factors determined using an automated technique at $T_{\text{ref}} = 200$ °C for unfilled PC. The dashed line represents the WLF fit as defined in Eq. 5.5

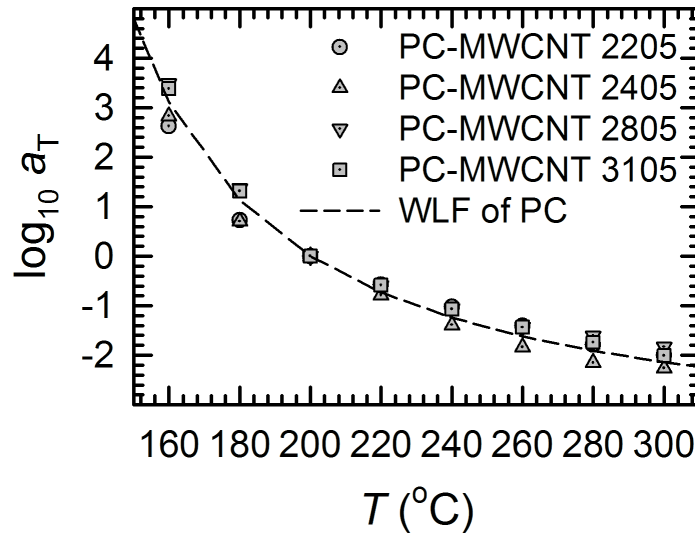
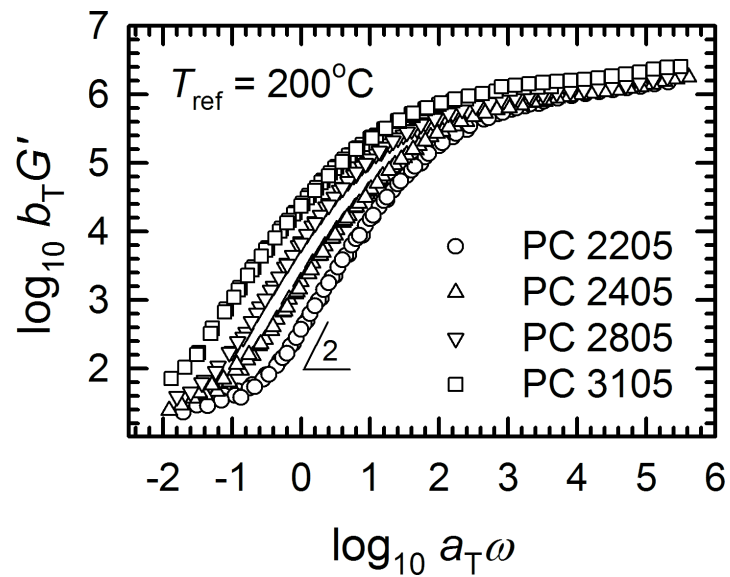


FIGURE 5.11: Shift factors determined using an automated technique at $T_{\text{ref}} = 200$ °C PC-MWCNT (3 wt%). The dashed line represents the WLF fit as defined in Eq. 5.5 for unfilled PC

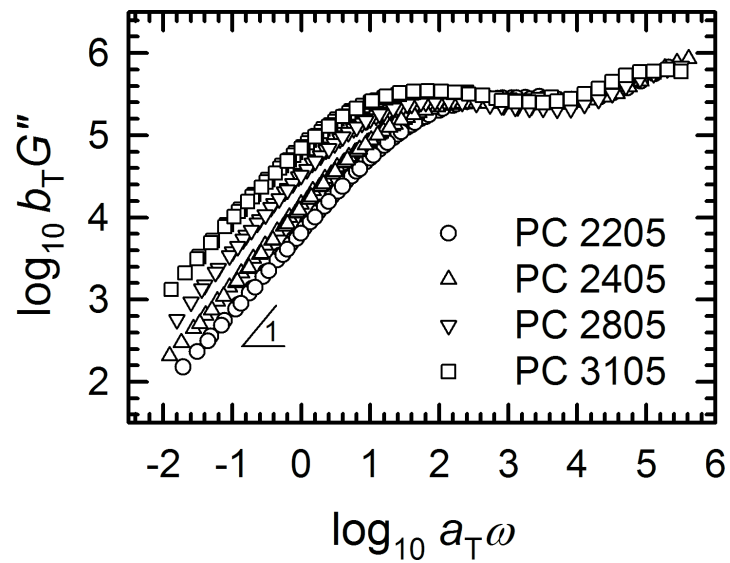
5.6 Frequency sweeps

The shift factors shown in Figs. 5.6 and 5.10 are used to produce reduced frequency-modulus mastercurves for the different grades of unfilled PC used in this study. These are illustrated in Fig. 5.12. As is well known in the literature on polymer melts, the width of the rubbery plateau increases with increasing molar mass and flow occurs at a lower reduced frequency. In unfilled PC, at low reduced frequencies, G'' is always higher than G' and the materials exhibits liquid-like properties typical of polymer melts with the characteristic gradients in the terminal zone of $G' \propto \omega^2$ and $G'' \propto \omega$, as shown in Figs. 5.12(a) and (b) respectively.

The slight plateau of G' seen at the lower limit of the reduced frequency range, particularly for PC 2205 and 2405 could be an artefact attributed to the torque limit of the instrument.



(a)



(b)

FIGURE 5.12: Reduced frequency mastercurves of (a) storage modulus and (b) loss modulus of unfilled PC of varying molar mass ($M_w = 33600 - 50500 \text{ g mol}^{-1}$) at a strain amplitude of 0.5%

A plateau of G' known as the plateau modulus, G_N^0 is observed at high frequencies. This modulus is related to the molecular weight between entanglements, M_e by

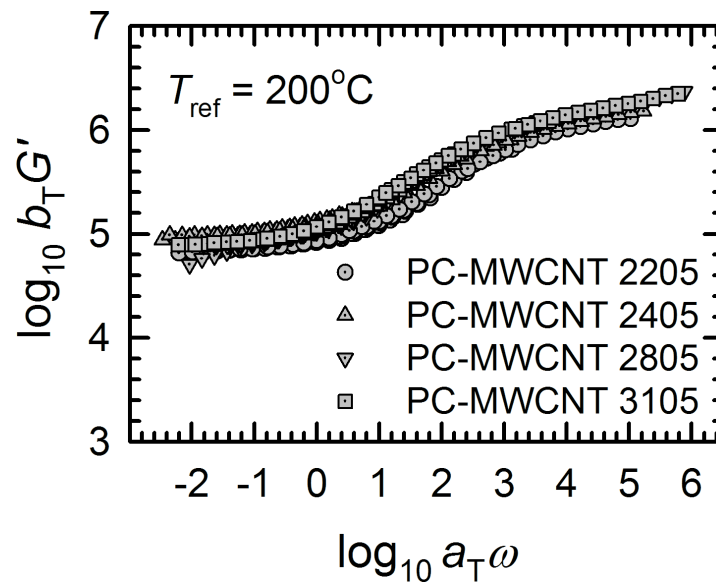
$$G_N^0 = \frac{\rho RT}{M_e} \quad (5.6)$$

where ρ is the density at temperature, T and R is the universal gas constant ($8.314 \text{ J K}^{-1} \text{ mol}^{-1}$). From the measurements shown in Fig. 5.12, G_N^0 for the PC grades (determined at $160 \text{ }^\circ\text{C}$) is between 1.6 and 2.5 MPa. Using Eq. 5.6, M_e is calculated to be between 1700 and 2700 g mol^{-1} . These values are consistent with literature value of 2500 g mol^{-1} for PC (Jordan and Richards, 2000).

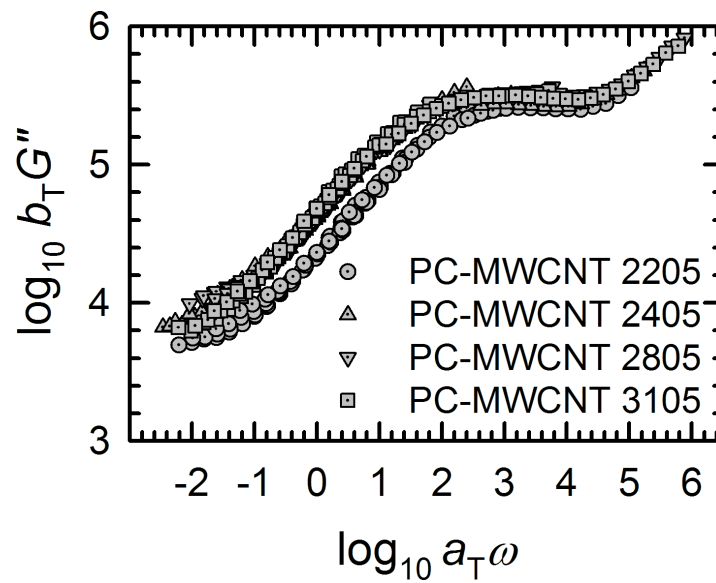
The shift factors shown in Figs. 5.7 and 5.11 are used to produce reduced frequency-modulus mastercurves for the range of nanocomposites. These are illustrated in Fig. 5.13. These mastercurves exhibit two important differences relative to those of the equivalent matrix polymers: (1) the presence of a second plateau instead of a zone of terminal flow; and (2) a loss tangent that is less than unity throughout the extended frequency range. At low reduced frequencies the second plateau has a modulus of $\sim 10^5 \text{ Pa}$ (see Fig. 5.13(a)). This behaviour was first observed by Pötschke et al. (2002) for PC-MWCNT nanocomposites with more than 2 wt% filler content, sufficient to form a percolated network within the matrix system. Similar observations of network percolation for PC-MWCNT were reported in the work of Alig et al. (2008) and of Skipa et al. (2010). This second plateau has a modulus, approximately 1.5 orders of magnitude smaller than the rubbery plateau arising from the entanglement network, and suggests the presence of an interconnected network of nanotubes, and hence of rheological percolation.

5.6.1 Application of a two-phase model to the viscoelastic data

Song and Zheng (2010) proposed a two-phase model to predict the elastic moduli of polymers filled with nanoparticles. This model is parameterised through a strain amplification factor parameter, A_f , storage G'_{CNT} and loss G''_{CNT} moduli parameters representing the filler network, and an exponent α related to the frequency dependence of this filler network. The model includes immobilised chains on the rigid filler surface and the interphase, if any, into the filler phase. This is because the chain confinement or chain absorption is localised to the filler surface and generally does not affect the behaviour of the bulk polymer.



(a)



(b)

FIGURE 5.13: Reduced frequency mastercurves of (a) storage modulus and (b) loss modulus of PC-MWCNT (3 wt%) of varying molar mass ($M_w = 33600 - 50500 \text{ g mol}^{-1}$) at a strain amplitude of 0.5%

A_f describes the hydrodynamic effect of exaggerated strain of the polymer chains in the presence of rigid fillers. Song and Zheng's approach assumes perfect bonding between the filler and matrix interface, and thus A_f is only dependant on the filler loading content as the relaxation timescale of the filler phase is beyond the range of frequencies that can be experimentally tested. The filler phase is treated as an elastically rigid network structure,

and in accordance to a microrheological model based on fractal concept, G' of the filler phase is weakly dependent on frequency whereas G'' is almost independent of frequency (Song and Zheng, 2010). The contribution of the matrix and the filler phases are combined to estimate G' and G'' of nanocomposites, expressed by (Song and Zheng, 2010)

$$G'(\omega) = A_f \sum_{i=0}^n G'_{\text{matrix}}(\omega) + G'_{\text{CNT}} \omega^\alpha \quad (5.7)$$

$$G''(\omega) = A_f \sum_{i=0}^n G''_{\text{matrix}}(\omega) + G''_{\text{CNT}} \quad (5.8)$$

where n is the polynomial order

Song and Zheng's model was applied to the viscoelastic mastercurves of all matrix polymers and nanocomposites in order to identify the nature of the changes in structure arising between polymer and nanocomposite. Since G' of unfilled PC grades at the lower limit of the reduced frequency range were deemed to be an artefact, values that deviate from the relationship $G' \propto \omega^2$ were not considered in the model. In the case of PC-MWCNT, only data in the frequency range corresponding to the unfilled grades were applied to the model. Optimisation of the parameters was carried out with $n = 5$ using Matlab, and fitted results are shown in Fig. 5.14 for all grades of filled and unfilled PC.

Table 5.1 shows that A_f for all PC grades did not exceed 1.20. The stiffness of the nanotube network $G'_{\text{CNT}} \sim 10^5$ Pa for all grades, and $G''_{\text{CNT}} \sim 10^4$ Pa. The frequency dependence of the network was negligible, with $\alpha \sim 10^{-2}$. Thus, the model is consistent with the view that the present systems do not exhibit pronounced strain amplification, and that the nanotubes agglomerate into a mostly elastic network with stiffness $\sim 10^5$ Pa. The stiffness of this network is probably connected to nanotube bending modes (Rubinstein and Colby, 2003).

TABLE 5.1: Parameters obtained from Song and Zheng's two-phase model, with $n = 5$, applied to the data of all PC grades

Material	Strain amplification factor, A_f	Frequency exponent, α	$\log G'_{\text{CNT}}$	$\log G''_{\text{CNT}}$
2205	0.93	0.09	4.94	4.15
2405	1.20	0.04	5.08	4.26
2805	0.93	0.06	4.98	4.07
3105	0.71	0.01	4.95	3.90

The confinement of PC chains, if any, must therefore be localised to the surface of CNTs or CNT-agglomerates. This is consistent with the T_g measurements presented in Chapter

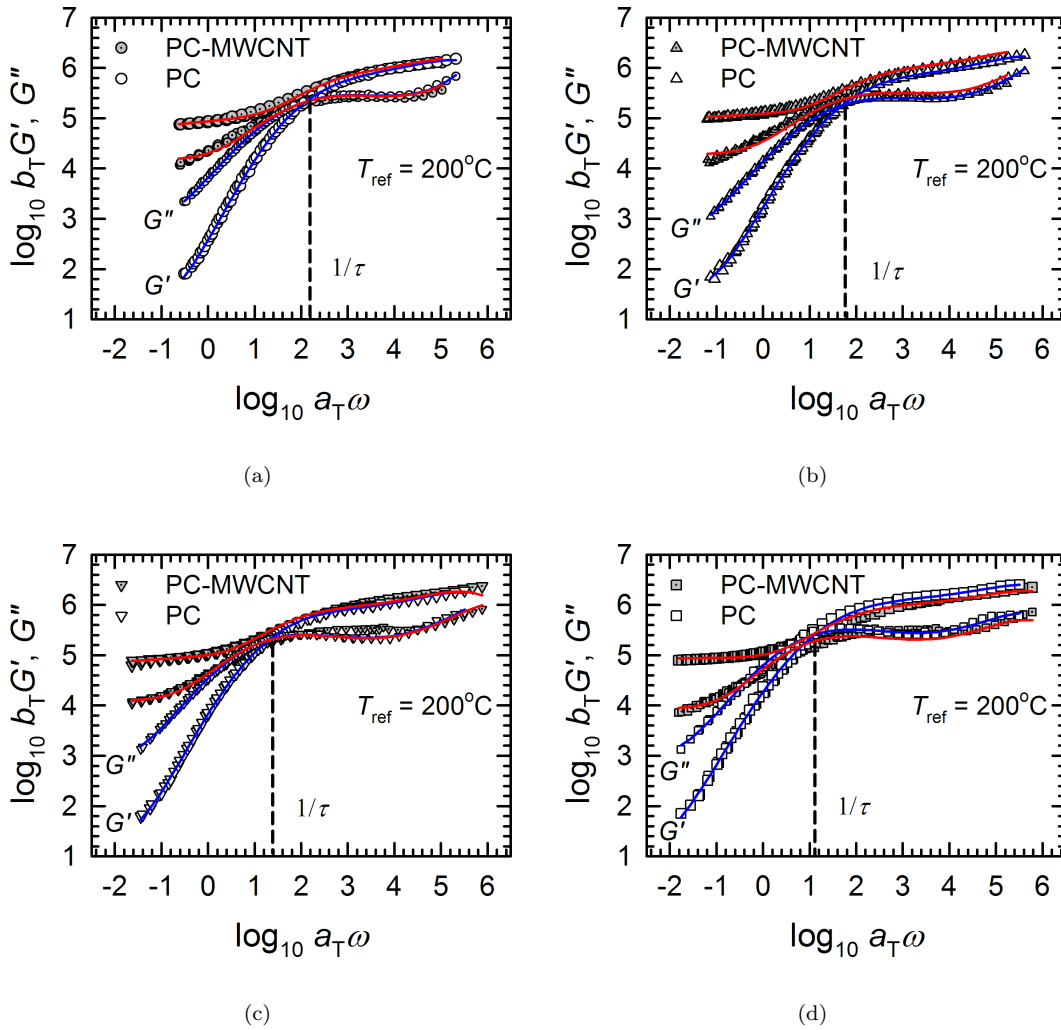


FIGURE 5.14: The polynomial fit of PC-MWCNT (red solid line) and unfilled PC (blue solid line) of grades (a) 2205 (circle), (b) 2405 (up triangle), (c) 2805 (down triangle) and (d) 3105 (square) employed in the two-phase model (Song and Zheng, 2010). Only unfilled PC data that followed the relationship $G' \propto \omega^2$, and the corresponding PC-MWCNT of the selected unfilled PC reduced frequency range were considered in the model. The cross-over frequency is used to determine the characteristic relaxation time

4, and suggests that the earlier onset of deviation from linearity observed during the amplitude sweeps in Fig. 5.1 for PC-MWCNT are caused by a destruction of the CNT network. Such a percolation network is known to exhibit gradual build-up with time in flocculation experiments, as observed in Section 5.4.1 and reported by Richter et al. (2009), arising from diffusion-controlled agglomeration of MWCNTs (Zeiler et al., 2010).

Fig. 5.15 illustrates the ratios of viscoelastic moduli of filled materials to those of pure materials as a function of reduced frequency. A ratio that deviates from unity is a signature that the nanotubes are influencing the viscoelastic response. The influence is greatest at

the lowest reduced frequencies, where the pure polymer undergoes flow but the filled system exhibits the second plateau. Here the ratio of storage moduli exceeds 10^3 and the ratio of loss moduli exceeds 10. At higher reduced frequencies the ratio is close to unity. A noteworthy feature is that the onset of the deviation from unity occurs at a lower reduced frequency (and hence longer timescale) with increasing molar mass of the matrix polymer. Due to the substantial differences in size between polymer chains and CNTs, it is not unreasonable to assume that polymer mobility is the main driver for any rearrangement of the filler network, and hence that the dominant relaxation mechanism observed is that of the polymer matrix.

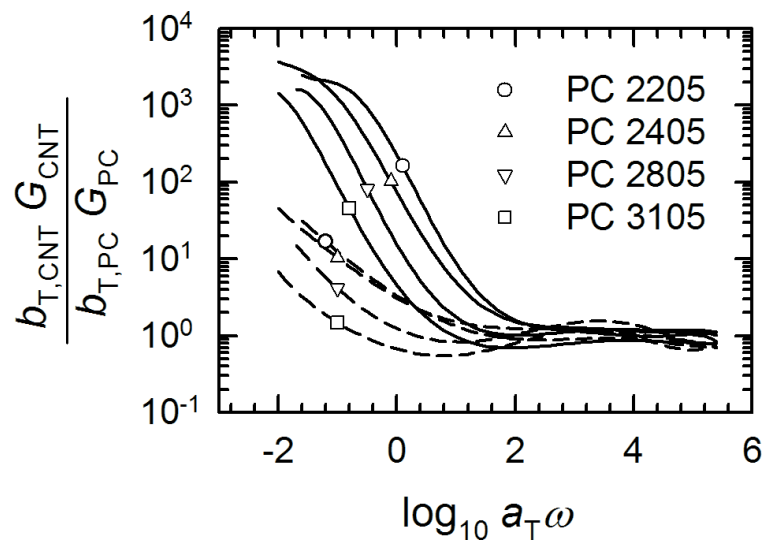


FIGURE 5.15: Ratios of storage modulus (solid line) and loss modulus (dashed line) of filled PC-MWCNT (3 wt%) to unfilled PC of matching matrix molar mass ($M_w = 33600 - 50500 \text{ g mol}^{-1}$) as a function of reduced frequency, determined at a strain amplitude of 0.5%

5.6.2 Relaxation times

In the pure PC melts, a characteristic relaxation time, τ was estimated from the inverse of the cross-over frequency for each grade, as shown in Fig. 5.14. Linear regression was employed to identify the coefficient n of a power-law relationship of the form $\tau \propto M_w^n$ as shown in Fig. 5.16. n was identified as 5.66 ± 0.22 (where \pm refers to the standard deviation). This value is somewhat higher than the generally reported literature values for PC of 3.4 - 3.75 (Jordan and Richards, 2000) and 4.22 (Dobkowski, 1982). It is probable that the difference originates from the polydispersity of the commercial resins, but the data shows clear power-law behaviour.

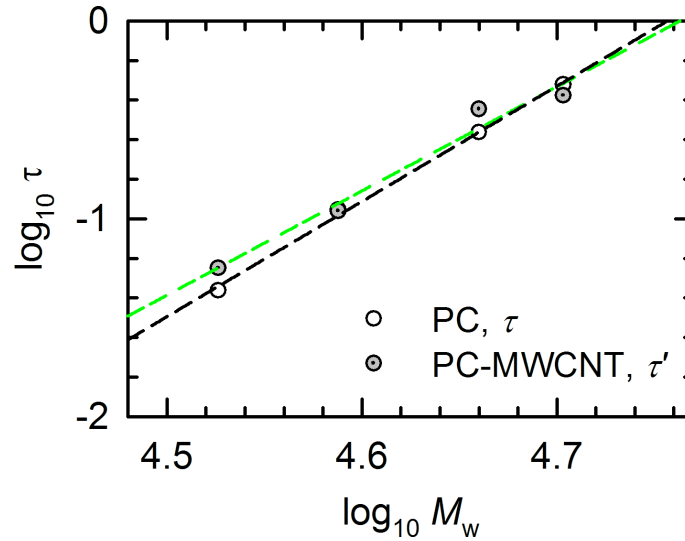


FIGURE 5.16: Characteristic relaxation times obtained from the cross-over frequency in unfilled PC (hollow symbols) and from the peak in $\tan \delta$ in the PC-MWCNT (3 wt%) (dotted, grey symbols), as a function of molar mass. Dashed lines (black: unfilled PC; green: filled PC) represent linear regressions through the data sets

In the filled PC melts, it is not possible to obtain a characteristic relaxation time from the crossover frequency since no cross-over occurs, as illustrated in Fig. 5.14. Nevertheless, the change in molar mass of the matrix polymer influences the mastercurves by shifting the frequency at which the reduction in the moduli takes place. Instead, a timescale τ' is determined corresponding to the inverse of the frequency at which the peak in $\tan \delta$ occurs. The frequency is obtained for all grades on unshifted experimental data at 200 °C using a peak fitting algorithm, as exhibited in Fig. 5.17. Linear regression was employed to identify the coefficient n of a power-law relationship of the form $\tau' \propto M_w^n$, and n was identified as 5.25 ± 0.62 (where \pm refers to the standard deviation), as shown in Fig. 5.16.

The two power-law coefficients are remarkably similar. In fact, by carrying out a paired Students t-test on the differences in relaxation times between filled and unfilled materials of equal matrix molar mass, we could not reject the hypothesis that the relaxation times are unaffected by the presence of nanotubes at a 90% confidence level (two-tailed t test, $t = 0.48$, $n = 4$). This supports the view that the same relaxation mechanism applies to both pure PC melts and to nanocomposites. This implies that the molar mass of the matrix polymer affects the timescale of the relaxation process observed in the nanocomposites in the same way as it affects the pure polymers. The relaxation mechanism normally associated with polymer melts is reptation, although this generally scales with a lower power of molar mass than that recorded here.

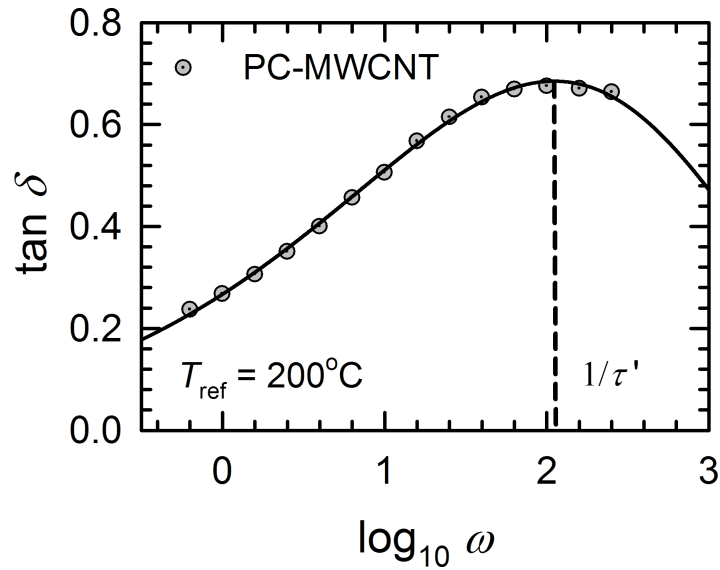


FIGURE 5.17: A typical example of fitting a Weibull (4 parameter) peak fitting algorithm (solid line) to the $\tan \delta$ data. The data shown here is of PC-MWCNT 2205

Three types of interactions can be expected in a polymer nanocomposite: (1) polymer-polymer interactions (dominated by the relaxation of the entanglement network), (2) nanoparticle-nanoparticle interactions, and (3) polymer-nanoparticle interactions (Pötschke et al., 2004). Only one type (polymer-polymer) is present in the unfilled polymers. The similarity in the scaling with molar mass of the relaxation processes observed is perhaps unsurprising evidence of the key role played by polymer-polymer interactions in these filled systems. Although no conclusive evidence can be presented, it is reasonable to assume that nanotube-nanotube interactions are slow (given their size relative to polymer molecules) and limited in extent (by the small volume fraction), and that polymer-nanotube interactions are probably dominated by the faster relaxation of the polymer chains, and hence that they also scale with molar mass in the same way as the polymer-polymer interactions. Further evidence to support this is also available in the work of Zeiler et al. (2010), who observed an influence of molar mass of the matrix on the dynamics of network formation in nanocomposites.

Although no estimate of relaxation time of a nanotube-nanotube network can be made, the fact that these materials can be melt-compounded and extruded is clear evidence that they will flow if sufficient shear stress is applied. Another interpretation of this is that the applied stress reduces the relaxation time of the nanotube network to the timescale of the experiment (Costa et al., 2008; Richter et al., 2009).

5.6.3 Large amplitude response

In order to probe the material response in the non-linear regime, mastercurves were constructed from isothermal frequency sweeps conducted at strain amplitudes of 0.05%, 5% and 50%, by appropriate vertical and horizontal shifting. Vertical shifting was performed manually using VGP plots, and the vertical shift factors are illustrated in Fig. 5.18 as a function of strain amplitude. Horizontal shift factors were subsequently determined for each strain amplitude using the automated technique, and are shown in Fig. 5.19.

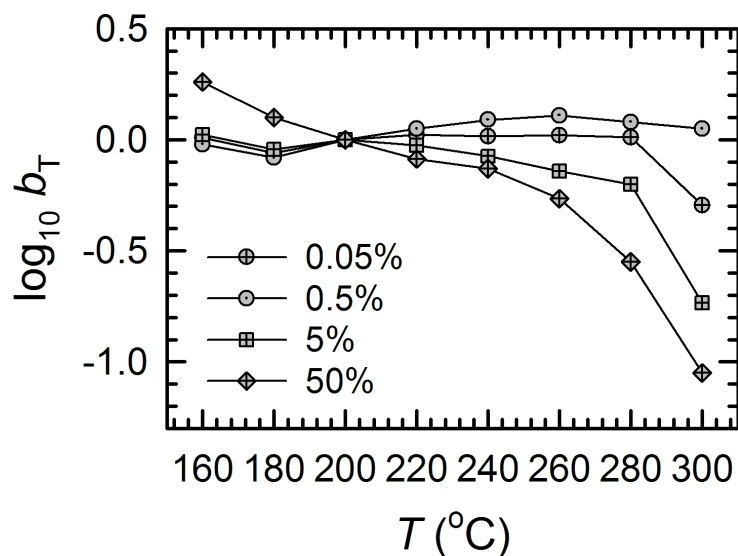


FIGURE 5.18: Vertical shift factors obtained from isothermal frequency sweeps at strain amplitudes of 0.05%, 0.5%, 5%, and 50% at $T_{\text{ref}} = 200$ $^{\circ}\text{C}$. Lines are a guide to the eye

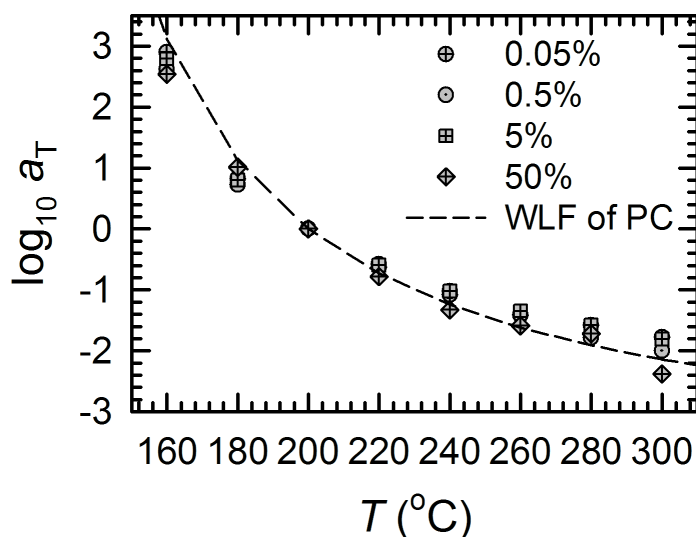


FIGURE 5.19: Horizontal shift factors obtained from isothermal frequency sweeps at strain amplitudes of 0.05%, 0.5%, 5%, and 50% at $T_{\text{ref}} = 200$ $^{\circ}\text{C}$. The dashed line is the WLF fit using unfilled PC parameters

The effect of increasing the strain amplitude is much greater on the vertical shift factors than on the horizontal shift factors. The small effect on the horizontal shift factors, and the closeness to the WLF fit, suggests that strain amplitude is not significantly affecting the relaxation mechanisms and their temperature dependence. This is consistent with the view that polymer matrix relaxation is the dominant mechanism, and with the small amplitude dependence observed on moduli from the amplitude sweeps on pure PC in Fig. 5.1.

The vertical shift factors are most affected by amplitude at the highest test temperature, where shifting to a lower reference temperature requires a reduction of modulus. This can be understood by considering a nanotube network that is affected by two processes: strain amplitude (setting the degree of network disruption), and temperature (affecting the kinetics of network formation). Thus, the higher the test temperatures (where the network will approach an equilibrium state more quickly), the stiffer the equilibrium state of the nanotube network for a given strain amplitude. At lower test temperatures the state of the nanotube network will be further from equilibrium, and hence more history dependent.

Mastercurves constructed from shifted isothermal frequency sweeps performed across the range of strain amplitudes on PC 2205 shifted to a reference temperature of 200 °C are shown in Fig. 5.20. There is little difference between the 0.05% and 0.5% strain amplitudes other than the increased noise at 0.05% because of smaller torque and angular velocity signals. When the amplitude increases to 5%, it is still possible to construct a mastercurve with good overlap between the test temperatures. There is evidence of shear thinning, with moduli reducing by almost one order of magnitude across the extended reduced frequency. At 50% strain amplitude the procedure of constructing the mastercurve is more challenging as there is less overlap between temperatures. The moduli are as much as two orders of magnitude smaller at 50% strain amplitude than at 0.5%.

The reduction in moduli across the reduced frequency range indicates that the strain amplitude is affecting both the nanotube network and the entanglement network. For a given strain amplitude, however, the effect is larger at the low reduced frequency end of the spectrum, where the nanotube network dominates, than at the high reduced frequency end where the entanglement network dominates.

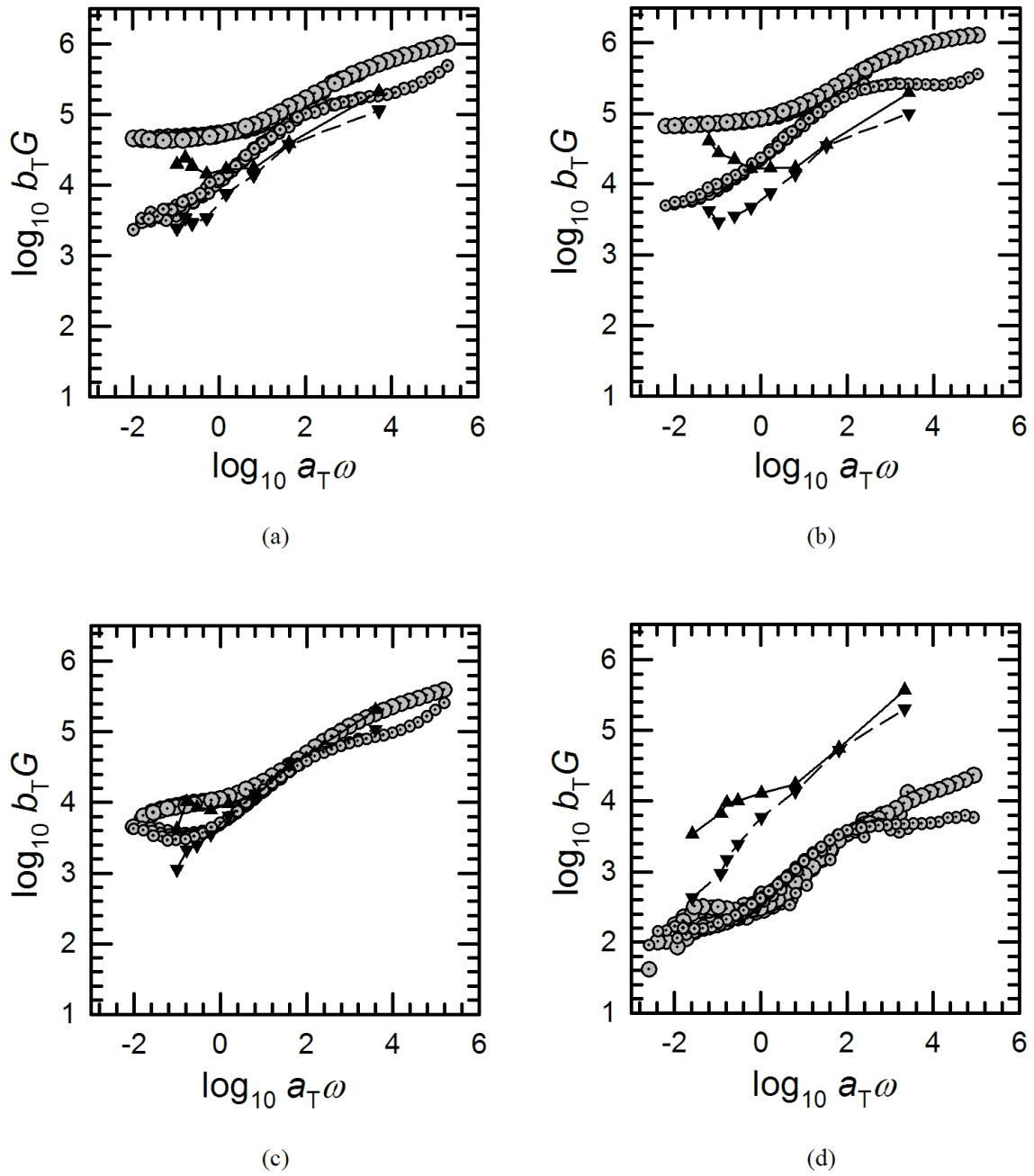


FIGURE 5.20: Mastercurves for filled PC-MWCNT 2205 (3 wt%) (G' : large dotted grey circles; G'' : small dotted grey circles) for strain amplitudes of (a) 0.05%, (b) 0.5%, (c) 5% and (d) 50%, at $T_{\text{ref}} = 200$ °C. Corresponding measurements obtained from amplitude sweeps (G' : up triangles; G'' : down triangles) measured at 2π rad s^{-1} . Solid and dashed lines are a guide to the eye

5.6.4 Roles of strain and temperature history

The strain and temperature history experienced by a nanocomposite plays an important role in defining the extent to which the nanotube network is developed, and hence the extent to which it contributes to the response. This build-up is readily observable through flocculation

experiments such as in the present work (Fig. 5.2) and those of Richter and co-workers (2009). The effect is also observable in the present experiments by comparing the responses measured at identical reduced frequencies and strain amplitudes obtained from frequency sweeps and from amplitude sweeps.

Moduli obtained during the amplitude sweeps at a range of temperatures shown in Fig. 5.1 measured at strain amplitudes closest to 0.05%, 0.5%, 5% and 50% at fixed frequency $2\pi \text{ rad s}^{-1}$ were first shifted vertically according to the shift factors shown in Fig. 5.18. Then, TTS was employed to shift the frequency to a reference temperature of 200 °C, to allow a direct comparison with the large amplitude frequency sweeps. These measurements are also shown in Fig. 5.20.

Differences in strain and temperature history are responsible for the differences in moduli between the mastercurves based on frequency sweeps and those extracted from amplitude sweeps. It is worth restating that the amplitude sweeps were performed on a single specimen across a reducing temperature range from 300 °C through to 160 °C, with each temperature experiencing increasing strain levels through to 100% prior to cooling and acclimatising at the next temperature. This means that the history of every amplitude sweep measurement except the first (at 300 °C) is of a nanotube structure that has been disrupted by the brief application of 100% strain at the previous temperature, and that has re-formed to a certain degree during the allowed acclimatisation time of 5 minutes. Frequency sweeps were instead performed across the same reducing temperature range from 300 °C through to 160 °C, but each specimen experienced a fixed strain amplitude (of 0.05%, 0.5%, 5% and 50%) at all temperatures.

By comparing the mastercurves obtained from the two methods, it is apparent that only the moduli measured at 5% strain are almost identical whereas the moduli obtained at 0.05%, 0.5% and 50% strain are not so. The implication of the nearly identical moduli at 5% strain is that the structure of the nanotube network must be comparable. In the case of the frequency sweep, it has experienced a 5% strain amplitude throughout the frequency range at each temperature, followed by a recovery period whilst changing temperature. In the case of the amplitude sweep, it has experienced up to 100% strain amplitude at the previous measurement temperature, followed by a recovery period whilst changing temperature, and a rising amplitude through to 5%. Thus, we can speculate that the level of network disruption and build-up obtained following a constant 5% strain amplitude is similar to that obtained

following a brief 100% disruption, a recovery period of 5.5 minutes in which the temperature is reducing and settling, and a rising amplitude through to 5% strain.

The same moduli are not obtained following the two histories through to the other strains. For the smaller strain amplitudes 0.05% and 0.5%, the disruption caused during the amplitude sweeps at 100% strain at the previous test temperature results in a lower modulus. For the larger strain amplitude 50%, there is greater disruption to the network during the constant 50% amplitude frequency sweep than during the rising amplitude sweep.

This comparison between amplitude sweep and frequency sweep measurements serves as a reminder of the particular challenges of characterising a material whose properties are very sensitive to strain and temperature history, and highlights the need for detailed methodologies of characterisation to enable reproducible results and thorough understanding to be achieved.

5.7 Conclusions

This chapter has investigated the linear and non-linear viscoelastic response of four grades of PC melt-compounded with 3 wt% MWCNTs, and of the matching matrix polymers. Section 5.3 has indicated that the nanocomposites deviate from linear viscoelasticity at much smaller strains relative to the pure polymers. Although this has been attributed to strain amplification, where the matrix polymer experiences a higher local strain than the macroscopic strain due to the presence of the stiff nanotubes network, evidence suggests that disruption of the nanotube network at increasing strain amplitudes is responsible. The evidence arises from the strain amplification factor parameter from the Song and Zheng's two-phase model discussed in Section 5.6. This is consistent with a lack of change of mobility interpreted from T_g measurements reported in Chapter 4. Filled materials also exhibit a strain overshoot in loss modulus not seen in the pure polymer.

Section 5.5 has presented isothermal frequency sweeps carried out on both MWCNT-filled and pure materials. The effect of temperature on modulus was accounted for by employing a density correction to the modulus in pure materials, and a shift obtained from van Gurp-Palmen plots in the filled materials. Mastercurves were then constructed in Section 5.6 by employing an automated shifting procedure to identify horizontal shift factors for time-temperature superposition. The horizontal shift factors were found to be relatively independent of both matrix polymer and the presence of nanotubes, suggesting that relaxation

processes have the same temperature dependence in filled and pure materials. The filled mastercurves exhibit two distinct differences from the pure polymer: a second plateau at low reduced frequency with a modulus of $\sim 10^5$ Pa, associated with a percolated nanotube network, and a loss tangent less than unity across the extended frequency range. Evidence of the filler networks contribution to the modulus was observed through application of Song and Zheng's two-phase model. Relaxation timescales of both unfilled and filled materials, explored in Section 5.6.2, were approximated from the inverse of the cross-over frequency and the frequency at the peak in the loss tangent respectively. All these timescales scale with molar mass through a power-law with very similar coefficients, further evidence that the dominant relaxation mechanism in the nanocomposites is associated with the polymer network itself.

Isothermal frequency sweeps carried out at varying strain amplitudes from 0.05% to 50%, and horizontal and vertical shift factors obtained to produce mastercurves have been explored in Section 5.6.3. There was a considerable effect of strain amplitude on the vertical shifting, arising from the different levels of disruption to the nanotube network from the strain amplitudes. The effect of strain amplitude on horizontal shifting was small, even at 50% strain. A comparison of moduli obtained at the same reduced frequency and amplitude from two different experiments was carried out to illustrate how strain and temperature history can affect the magnitude of the viscoelastic response of nanocomposite materials.

Chapter 6

Microscopic investigation

This chapter presents the use of microscopic techniques for the characterisation of the state of dispersion and of the microstructure of PC-MWCNT nanocomposite. Section 6.2 discusses with the quantification of CNT dispersion and distribution using optical micrographs and digital image analysis. Micrographs of polished specimens are presented in Section 6.2.2 to determine the presence of voids in specimens formed by compression moulding and by injection moulding. Section 6.3 is concerned with the qualitative evaluation of CNT dispersion using SEM. Section 6.4 describes the use of focused ion beam and SEM techniques for morphology characterisation in PC-MWCNTs.

6.1 Introduction

Quantification of the CNT-nanocomposites morphology can be separated into factors comprising (1) the dispersion of the CNTs (i.e. the individualisation of the nanotubes) and (2) the CNT distribution (i.e. the spread of the nanotubes) in the base matrix. Characterising the dispersion and distribution of CNTs in the matrix helps to understand the structure-property relationship of the nanocomposite, particularly for electrical and mechanical properties of PC-MWCNT to be presented in Chapters 7 and 8 respectively. Such information is beneficial in optimising polymeric processing conditions.

The characterisation of the level of CNT dispersion in nanocomposites has been attempted through OM, SEM and TEM. The dispersion of individual CNTs is categorised as nanodispersion whereas macrodispersion refers to the dispersion of CNT agglomerates or bundles

(Green, 2010). OM and SEM were used to study the macrodispersion of thermoplastic-CNT systems (Kasaliwal et al., 2009, 2010; Kashiwagi et al., 2004; Liu et al., 2004; Pegel et al., 2008), while TEM was employed for nanodispersion studies, owing to its nanometer resolution capability (Liu et al., 2004; Pegel et al., 2008, 2009; Pötschke et al., 2004). However, there is a lack of standards or of a unified approach for quantitative analysis of CNT-filled systems that hinders a direct comparison between different studies.

In this work, the state of CNT nanodispersion in PC-MWCNT is expected to be limited. This is attributed to the direct incorporation of pure MWCNTs into PC through melt compounding that favours the formation of CNT agglomerates. This is evident from the investigation of PC-MWCNTs in the melt state by Alig and co-workers (2012) that reported the shear-induced destruction and reformation of agglomerations of CNTs. Thus, the properties of melt compounded nanocomposites are more likely to be dictated by the macrodispersion of CNTs rather than the levels of CNT nanodispersion. Furthermore, industry tends to utilise OM as a means to investigate the filler dispersion levels in the filled polymer systems due to the ease and speed of the method compared to other microscopy techniques. Therefore, this chapter is focused on OM and SEM techniques relevant to CNT macrodispersion.

6.1.1 Optical microscopy sample preparation and techniques

OM can provide an estimate of the volume fraction of macrodispersed CNTs, as the CNT agglomerates can be easily distinguished from the matrix using visible light. The advantages of using OM relative to SEM and TEM include the short times for specimen preparation and the relative ease of the test procedure. In addition, the information provided by OM can represent the bulk material with significantly less number of images compared to electron microscopy. As highlighted in Section 2.3.1, the disadvantage of OM is that the 2D analysis cannot describe the absolute dispersion of CNTs which is a 3D structure. However, OM is carried out in this work to evaluate the relative change of CNT dispersion for the different melt processes and as such, the quantification of the CNT macrodispersion is sufficient.

Micrographs can be analysed using image processing algorithms that are extensively used by other scientific communities, for instance the biological and medical fields. Digital image processing have been adapted to analyse CNT materials, as demonstrated by Pegel and co-workers with PC-MWCNT systems (Pegel et al., 2011). Such algorithms allow rapid

processing of a large number of micrographs to obtain a statistically confident description of the level of filler dispersion in a CNT-nanocomposite.

Among the quantitative methods using OM that have been attempted on CNT-nanocomposite materials are thresholding method (Kasaliwal et al., 2010; Krause et al., 2009) and quadrat-based method (Haslam and Raeymaekers, 2013). The first method uses the feature-based approach that correlates the threshold with the number of objects that has a roundness of <0.5 (Pegel et al., 2011). A selected threshold value is then used to quantify the agglomerate area fraction, defined as the ratio between the cumulative area of the CNT agglomerates and the total area of the micrographs in thin sections (Pegel et al., 2011). The technique has been employed for PC-MWCNT (Kasaliwal et al., 2009, 2010; Pegel et al., 2011), and for systems similar to these employed in this work such as PLA-MWCNT (Villmow et al., 2008*b*) and PP-MWCNT (Krause et al., 2010). The quadrat method consists of dividing a micrograph into sections with a mesh size of choice. CNT dispersion is defined by the standard deviation of the filler concentration in the sections. Haslam and Raeymaekers (2013) proposed the inclusion of the calculation for the agglomerates size distribution to the quadrat method, where the CNT dispersion is quantified as an index calculated with equal consideration to the agglomeration size and spatial distribution. The thresholding method was selected to evaluate PC-MWCNT in this work as there were similar CNT systems to compare to in the literature and the result is not biased by the mesh size, which may be of concern when large particles cross between two or more sections of the grid in the quadrat method.

A crucial part of OM is the specimen preparation where thin slices, otherwise known as sections, of the CNT specimen are observed in transmission mode. Microtoming is the preparation of sections between 1 and 40 μm in thickness that must be thin, undeformed, and flat (Sawyer et al., 2008). In order to obtain sections, a specimen is mounted on the microtome by either embedding in a mould or by self-support using a chuck. Securing the specimen in the chuck is crucial to prevent any movement during microtomy and facilitates consistent section thickness. If embedding is required, an epoxy can be used for this purpose. The cutting knife is typically selected based on the desired section thickness and material. For example, polymers may be sectioned with tungsten carbide (1 - 15 μm) and diamond (0.5 - 3 μm) (Delaware Diamond Knives, 2013). Curled sections, a possible effect of sectioning, can be uncoiled through several techniques such as manually using a soft brush and forceps, heating the section on a hot plate to relax it or floating the section on water.

There are problems limiting microtoming that can affect the structure of the polymer section. Common artifacts on the sections includes striations, non-uniform thickness, wrinkling and chatter marks. Generally, these artifacts are caused by knife-related factors (i.e. damaged, incorrect angle, blunt) and procedure-related factors (i.e. sectioning speed, section thickness, cutting surface size, specimen temperature, presence of contaminants) (Sawyer et al., 2008). These defects are undesirable as they will interfere with the image analysis of the micrographs. There are remedies for some defects such as knife related factors that can be avoided by using sharp knives or selecting an appropriate knife material based on the application. However, the process of minimising defects are also dependent on the skill of the operator preparing the specimens and on the material under investigation.

6.1.2 SEM sample preparation and techniques

SEM can be conducted on cryofractured surfaces (Du et al., 2004; Logakis et al., 2009) to provide information on CNT dispersion and orientation. It should be noted that SEM is dependent on the compositional and topographical contrast of the materials investigated. Although SEM micrographs are able to infer CNT orientation (Abbasi et al., 2009) or confirm the presence of a CNT network structure (Du et al., 2004), the topological contrast of a fracture surface makes quantification of CNT dispersion via image processing unfeasible. The qualitative interpretation of SEM images is therefore subjective and a reasonable number of images is required to deduce the CNT dispersion of the bulk material.

An SEM specimen requires a conductive surface and a path to ground. Specimen preparation for polymers typically involves fracturing a larger specimen to attain the suitable dimensions to fit into the vacuum chamber of a SEM. This is followed by the application of a conductive coating to allow electron transmission, to minimise radiation damage and to avoid charging of the specimen (Schrand, 2005). Coatings can be applied with gold, platinum or carbon. The coating thickness should be minimal as a thick coating layer results in a granular and cracked appearance (Sawyer et al., 2008). Care must be taken to ensure that the specimen is free of contaminants as other material on the surface of interest can lead to misinterpretation of the specimen microstructure.

The combination of a focused ion beam (FIB) and SEM is a method that allows in-situ sectioning to obtain cross-sections of materials. The 2D images can then be used to infer 3D

structural information via image processing. This technique has been successfully attempted on clay nanocomposites (Ray, 2010) as shown in Chapter 2 (Fig. 2.5).

6.2 Optical microscopy

In OM, the light transmitted or reflected by the specimen is channeled through a system of lenses to produce an image at magnifications ranging from $2\times$ to $2000\times$ (Sawyer et al., 2008). The resolution of the image is limited by the wavelength of visible light (400 - 700 nm), the objective lens and features of the specimen itself. For CNT-filled polymer systems, OM can provide information on filler agglomerates such as shape, size, and distribution. A digital camera attached to the microscope is used to record the images for processing and analysis.

Two techniques of polymer sample preparation for OM investigation in this work. The first technique is the preparation of sliced sections that allows the specimens to be studied with transmitted light. This was pursued in the effort to quantify the CNT dispersion in filled PC materials. The second technique is the grinding followed by the polishing of the specimen surface of interest for inspection with reflected light. This method is employed to determine the presence of voids in the PC-MWCNTs samples.

6.2.1 Characterisation of CNT dispersion

6.2.1.1 Section preparation methods

Rectangular bar specimens of PC-MWCNT 2205 with dimensions $60\text{ mm} \times 5\text{ mm} \times 2\text{ mm}$ were manufactured by compression moulding at $250\text{ }^\circ\text{C}$. Thin sections of the specimens were prepared using the microtome to obtain sections with thickness of $2\text{ }\mu\text{m}$ and $4\text{ }\mu\text{m}$. The rectangular specimen was cut to a length of 30 mm and embedded in a circular mould filled with EpoFix epoxy and left to cure overnight at room temperature.

Microtoming was performed with two instruments. The first instrument was a Reichert Jung 2050 SuperCut rotary microtome using a tungsten carbide knife. The cutting speed was fixed at 6 mm s^{-1} and the cutting surface was perpendicular to the length of the specimen. Slices were placed on microscope slides and manually uncurled using a soft brush. Microtoming was also performed using an MC PowerTome employing a glass knife. The block face of the

cutting surface (similar to the rotary microtome) was trimmed prior to sectioning. A boat containing distilled water, attached to the cutting edge of the glass knife, is used to float the sections away from the knife edge and to collect the specimens. The sections are transferred to a microscope slide using a tool consisting of an eyelash and placed on a gently heated stage (~ 50 °C) to evaporate the water. Whilst heating, the eyelash tool is used to uncurl the specimens. Although attempts were made to uncoil the curled sections, the section's edge that made the initial contact with the knife's cutting edge remained curled. Optical investigations of such areas were omitted.

6.2.1.2 OM investigation

OM was conducted using a Olympus BX-51 microscope in transmission with a $10\times$ lens. A digital camera, Q Imaging Fast 1396, was used to record the images. The Q Capture software was used to control exposure time. Light intensity was fixed for all images. Each micrograph represents an area of ~ 1.26 mm².

6.2.1.3 OM micrographs of thin sections

As PC is translucent in thin sections, it will appear bright, providing an obvious contrast to the CNT agglomerates that appear black. For the purpose of this technique, only CNT agglomerates above ~ 1 μm in diameter are detectable due to resolution limit of OM.

Fig. 6.1 shows representative optical micrographs of 2 μm thick sections obtained using the tungsten carbide knife. A wide variety of defects are visible. The bright areas suggest tearing of the matrix, and the hazy or blurry parts are attributed to a non-uniform surface. The tungsten carbide knife was considered unsuitable for the preparation of slices as it was difficult to differentiate between defects and CNT agglomerates.

Fig. 6.2 shows optical micrographs of 2 μm and 4 μm sections obtained using a glass knife. Knife scratches are the dominant defect and the surfaces are still not perfectly planar. Comparing Fig. 6.2 with Fig. 6.1 there is, however, an improvement in the quality of sections. Hence, sections obtained with the glass knife are used for further analysis in this work.

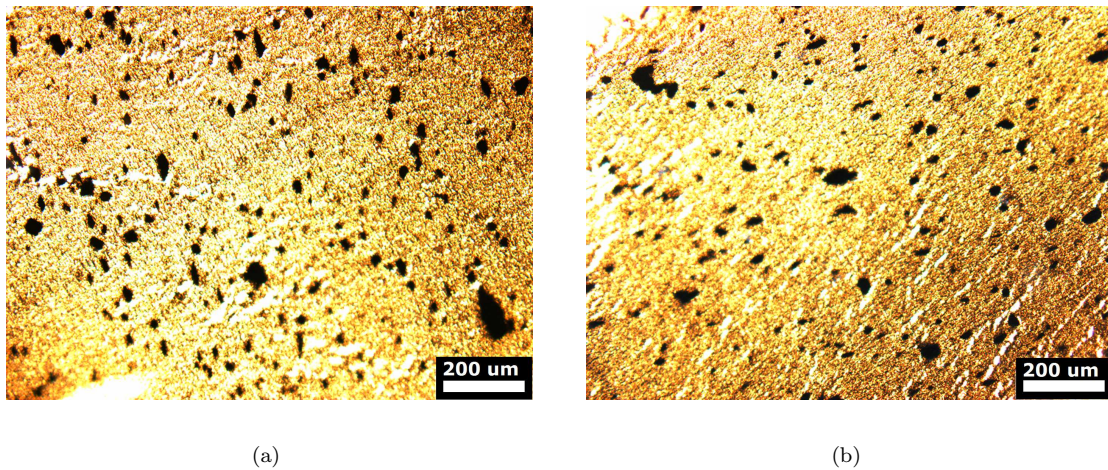


FIGURE 6.1: Optical micrographs of PC-MWCNT 2205 sections of thickness $2\ \mu\text{m}$, obtained with a tungsten carbide knife

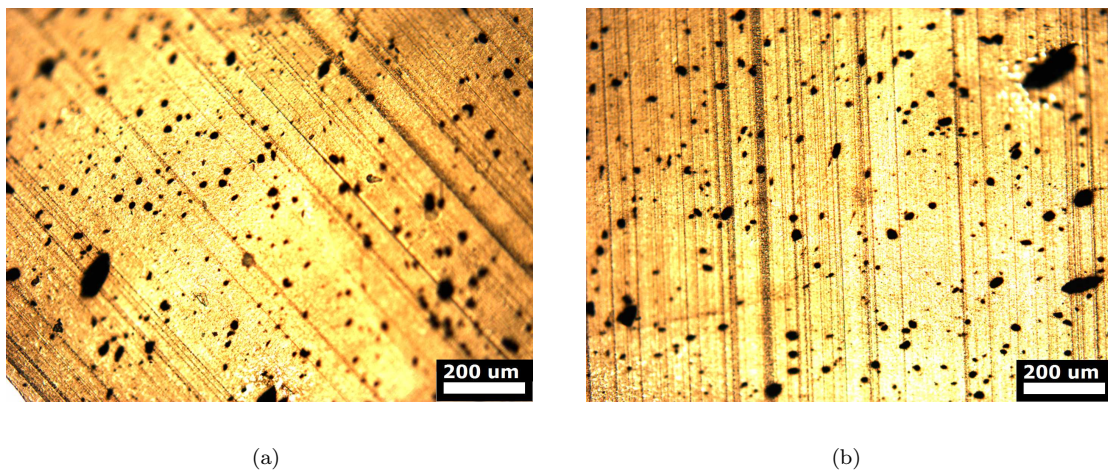


FIGURE 6.2: Optical micrographs of PC-MWCNT 2205 sections of thickness (a) $2\ \mu\text{m}$ and (b) $4\ \mu\text{m}$, obtained with a glass knife

6.2.1.4 Attempts to produce an improved specimen surface

A procedure was attempted to improve the surface. A slice is sandwiched between two slide covers and placed on a heated Linkam stage that was mounted on a microscope. A top cover enclosed the device to reduce the loss of heat from the stage to the surrounding environment. A window seal on the top cover allowed real-time observation of the heat treatment of the specimen. The sandwich assembly was heated to $170\ ^\circ\text{C}$ (above T_g) at a rate of $30\ ^\circ\text{C}\ \text{min}^{-1}$. The temperature was selected to allow the PC to flow while minimising possible re-agglomeration of CNTs. At $160\ ^\circ\text{C}$, a small weight of $5\ \text{g}$ was placed on the slide covers and the specimen was observed over 15 minutes.

Fig. 6.3 illustrates micrographs of microtomed $2\ \mu\text{m}$ sections of PC-MWCNT 2205 at various times during the heat treatment. The images are blurred because of the uneven surface and due to the temperature of the air in the device. Striations formed on the sections as seen in Fig. 6.3(b) - (d), hence the procedure was found to be unsuitable to produce planar sections.

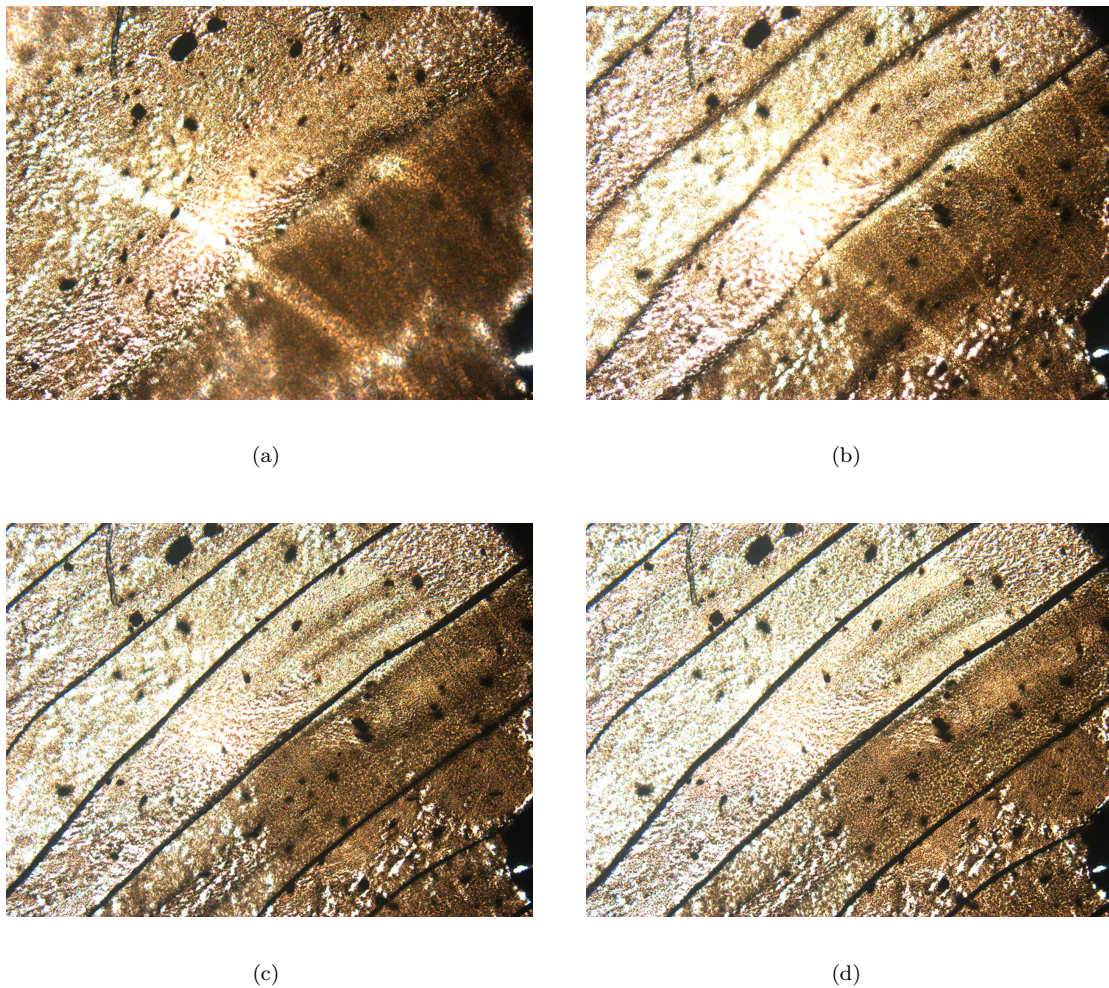


FIGURE 6.3: Optical micrographs showing the heat treatment of a $2\ \mu\text{m}$ section of PC-MWCNT 2205 at 10x magnification. At $170\ ^\circ\text{C}$, a weight of 5 g was placed on the section and the images were obtained at several intervals showing (a) the specimen just after application of the load ($t = 0$). The formation of striations appearing at (b) $t = 3$ minutes, and remaining after (c) $t = 6$ minutes and (d) $t = 10$ minutes

6.2.1.5 Image analysis

The optical micrographs were analysed with image processing software, ImageJ (Rasband, 1997). An image processing procedure for CNT agglomeration from OM micrographs was

developed by Pegel et al. (2011) that consisted of the following steps: background correction, binarising the image and identifying an appropriate threshold to quantify the CNT agglomerates. Both Pegel and Kasaliwal successfully applied the procedure to analyse low concentrated PC-MWCNT (1 wt%) and obtained estimates of CNT agglomeration areas. This method is employed in this work to determine the degree of dispersion using OM D_{OM} that is expressed as (Kasaliwal et al., 2009)

$$D_{\text{OM}} = 1 - \frac{f \left(\frac{A_{\text{CNT}}}{A_{\text{o}}} \right)}{V_{\text{CNT}}} \quad (6.1)$$

where f is the packing density of CNTs ($f = 0.25$ (Kasaliwal et al., 2009)), A_{CNT} is the agglomerate area, A_{o} is the total observed area and V_{CNT} is the CNT volume fraction in percentage.

6.2.1.6 Image processing procedure

The image processing procedure used in this work is based on Pegel et al. (2011). The first step is background correction of an OM image (converted to an 8-bit image) to reduce the effects of illumination gradient, typically found on micrographs. A mean filter is applied to a duplicate of the original image using a radius (in pixels) corresponding to the largest agglomerate in the image. This smooths the duplicated image by substituting each pixel with the surrounding mean. The filtered image is then subtracted from the original image to remove the brighter pixels in the original image. The same mean filter is applied to the new image and divided by the original image to remove any illumination gradient.

The corrected image is then binarised in the second step. Pegel and co-workers' (2011) developed a feature-based algorithm that determines the relationship between the threshold value and the quantity of objects, yielding a histogram. This was pursued because the grey-scale based algorithms, typically used to determined threshold values, were not sufficient to identify small CNT agglomerates due to the weak distinction of the agglomerates from the background (Pegel et al., 2011). Therefore, the threshold value for binarisation is obtained using the triangle algorithm, whereby a line is constructed between the minimum and maximum value on the histogram (Wu et al., 2008). The furthest normal distance between this line and the histogram identifies the threshold value.

Lastly, a morphological filter is applied to the binarised image to perform an erosion process followed by a dilation process. An erosion process removes the pixels from the edges of a black object, each pixel in the image with the smallest pixel value in that pixels neighborhood, employing a 3×3 square structuring element. The dilation process is the opposite of the erosion, replacing of each pixel in the image with the highest pixel value found surrounding it. The open morphology operation helps to remove isolated pixels and smooths the agglomerate boundaries.

6.2.1.7 Quantification of CNT dispersion

Figs. 6.4(a) and (b) illustrate the original image of a PC-MWCNT (3 wt%) section and the filtered image respectively. The feature based algorithm applied to Fig. 6.4(b) produced the histogram, shown in Fig. 6.5, yielding the grey scale threshold value of 116.

Pegel's binarisation method was found to be unsuitable for the current work as the feature-based algorithm picked up the less circular shapes associated to the dominant scratch defects, shown in Fig. 6.4(c). The agglomerate area fraction, A_{ag} for Fig. 6.4(c), with the defects visible, is 4.9% for a $2\mu\text{m}$ thick section. When visible defects were excluded by selecting regions of interest for the quantification of CNT dispersion levels, A_{ag} is estimated to be 4.6%. A higher value of A_{ag} indicates a lower level of CNT dispersion. There is a relationship between the section thickness and A_{ag} , hence the CNT agglomerate volume fraction can be obtained by determining A_{ag} for of range section thickness. Due to the technical difficulties and user dependence of separating defects from CNT agglomerates in the OM micrographs, no further evaluations using this method was performed to quantify CNT dispersions of these systems.

Since A_{CNT} could not be evaluated, D_{OM} cannot be determined using the current micrographs. It should be noted that Pegel and co-workers highlighted that the error for D_{OM} increases with high CNT agglomerate volume fractions. Furthermore, the uncertainty of the appropriate packing density f value for CNT agglomerates contributes to this error. Hence, obtaining a reliable estimate of agglomerate volume fraction for percolated PC-MWCNT systems is not trivial. Although a quantitative measure could not be achieved for PC-MWCNT (3 wt%), the image can be qualitatively inferred as having poor dispersion due to the high density of CNT agglomerates visible.

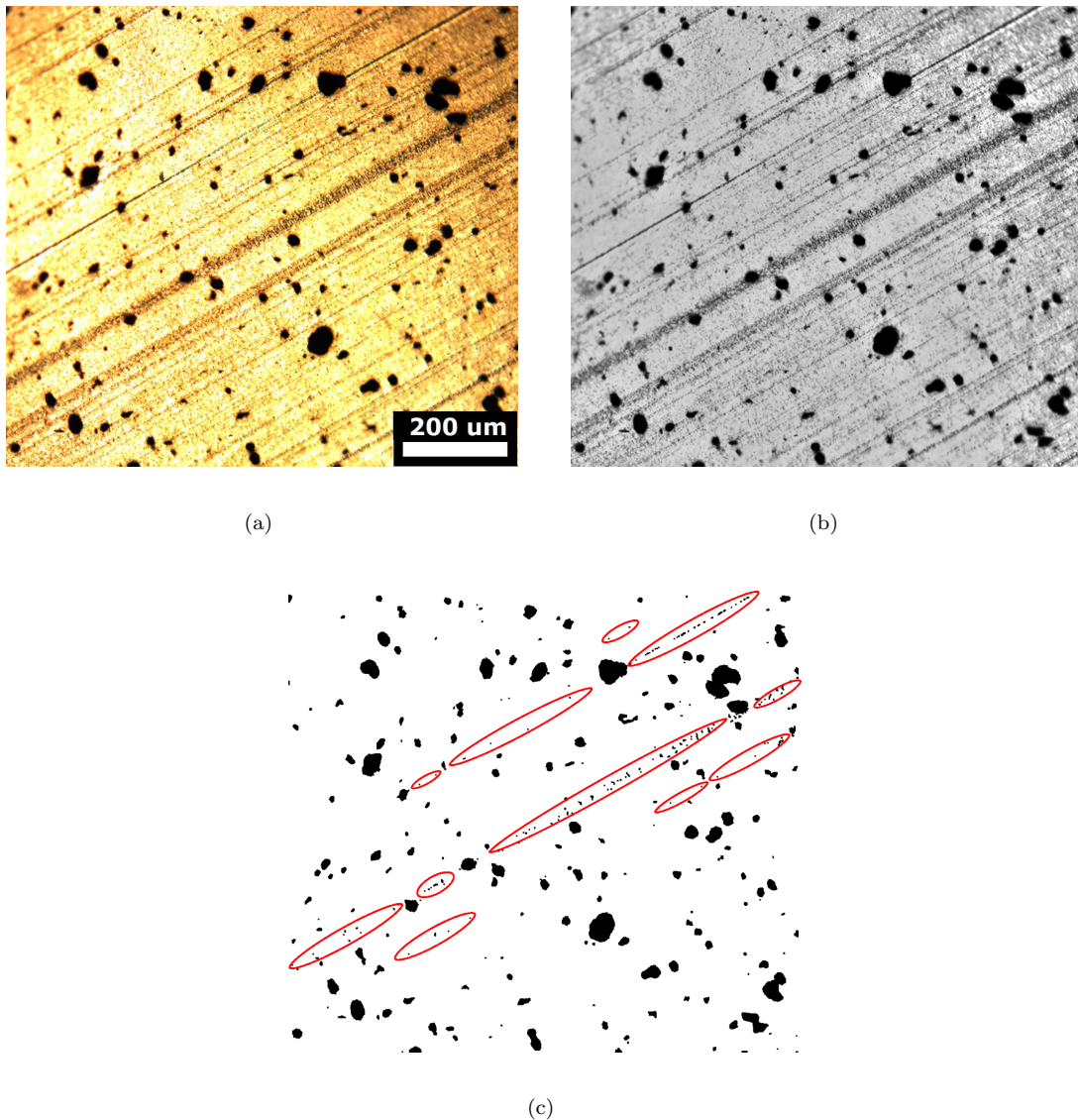


FIGURE 6.4: The background correction procedure applied on the (a) original image of PC-MWCNT (3 wt%) with thickness of $2 \mu\text{m}$ to obtain the (b) new filtered image with minimised illumination gradient. A feature based algorithm (Pegel et al., 2011) is applied to (b) to yield the (c) binarised image with artifacts still visible as indicated by the red *ellipses*

In the present case, image processing and analysis fell short owing to damage during specimen section preparation. There are considerable practical challenges in producing thin, flat and artifact-free specimen sections of saturated PC-MWCNT for microscopy. The technique requires a high level of skill and a reasonable number of sections, in order to represent the bulk structure of the specimens. OM sample preparation technique is destructive and laborious, and highlights the difficulties of implementing OM in commercial processes or as a service-life inspection of CNT filled thermoplastics.

There is a demand for non-invasive optical and imaging processing methods to characterise

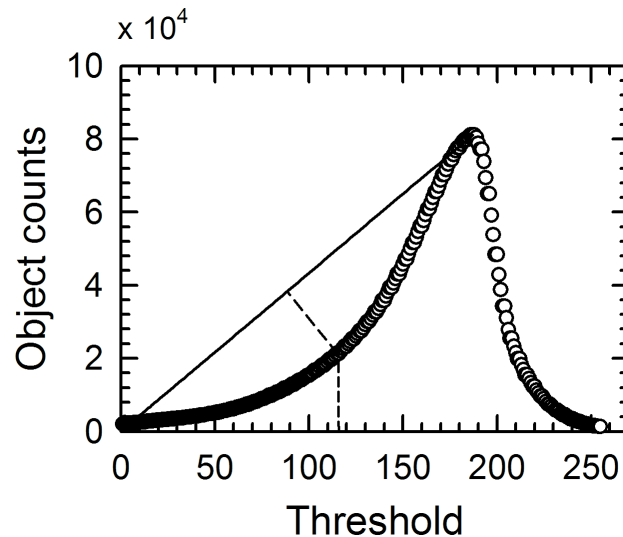


FIGURE 6.5: An illustration of the triangle algorithm, described in Section 6.2.1.6, to determine the threshold value for Fig.6.4(c)

CNT dispersion in the matrix. Recently, techniques based on optical diffraction and diffusion mechanisms such as optical coherence tomography, oscillatory photon correlation spectroscopy and Fraunhofer wavefront correlation have been developed and applied on nanoclay and MWCNT nanocomposites (Broughton et al., 2013). They developed these methods to be used in production lines and as an inspection tool during nanocomposites' product lifetimes.

6.2.2 Void determination

6.2.2.1 Grinding and polishing procedure

Three specimens of varying processing conditions were used to determine the presence of voids: compression moulded PC 2805 and PC-MWCNT 2205, and injection moulded PC-MWCNT 2205. The specimens were cut to a length of 20 mm and embedded in a circular mould filled with polyester resin. The resin was mixed with 0.3% and 1% (of the resin weight) of NL 49P accelerator and Butanox catalyst respectively. The resin was left to cure overnight at room temperature.

Grinding and polishing was performed using a Struers DAP-7 equipped with a Struers Pedemin-S specimen mover that holds the specimen in position with a spring loaded contact and rotates in conjunction with the polishing wheel. The wheel speed was fixed at 125 rpm. The grinding process was performed with wet and dry paper of grades P800, P1200, P2500 and P4000 that corresponds to median particle diameters of 22 - 2.5 μm . Water was used

as a coolant. The polishing process was performed with a soft cloth and a solution of water and Buehler 1 μm deagglomerated alumina polishing abrasives. The solution was applied intermittently during the polishing period. The polished surface was rinsed with water and left to dry.

6.2.2.2 OM investigation

OM was conducted using a Olympus BX-51 microscope in reflection with a $4\times$ lens. A digital camera, Q Imaging Fast 1396, was used to record the images. The Q Capture software was used to control exposure time. Light intensity was fixed for all images. Each micrograph represents an area of 7.8 mm^2 .

6.2.2.3 OM micrographs of polished sections

Fig. 6.6 shows representative optical micrographs of the polished surface perpendicular to the specimen length. The striations and scratch marks are likely due to the abrasives of the wet and dry paper, and the alumina solution. Fig. 6.6(d) exhibits the identical position as Fig. 6.6(c) with the intention of focusing on the bright spots to highlight the feature. These bright areas seen in Figs. 6.6(b) and (d) may possibly be voids since such features were not observed for unfilled PC specimen. The voids diameter range between $10 \mu\text{m}$ and $70 \mu\text{m}$. It can be speculated that these small voids may have influenced the density measurements reported in Section 3.5.2, though the effect was not significant. The voids would have a greater effect on the materials's mechanical behaviour as will be discussed in Chapter 8.

6.3 Scanning electron microscopy

SEM uses a probe to focus an electron beam across the specimen in a high vacuum environment in order to form images (Sawyer et al., 2008). It functions as a generalised reflection method, because it detects electrons emitted from the specimen surface. The advantage of SEM arises from the higher resolution that allows for higher magnification compared to OM. In order to prevent charging up of the electron beam for non-conductive materials, the specimen requires a conductive coating, low accelerating voltage or a variable pressure environment. The field emission gun (FEG) is used as the source of the electron beam,

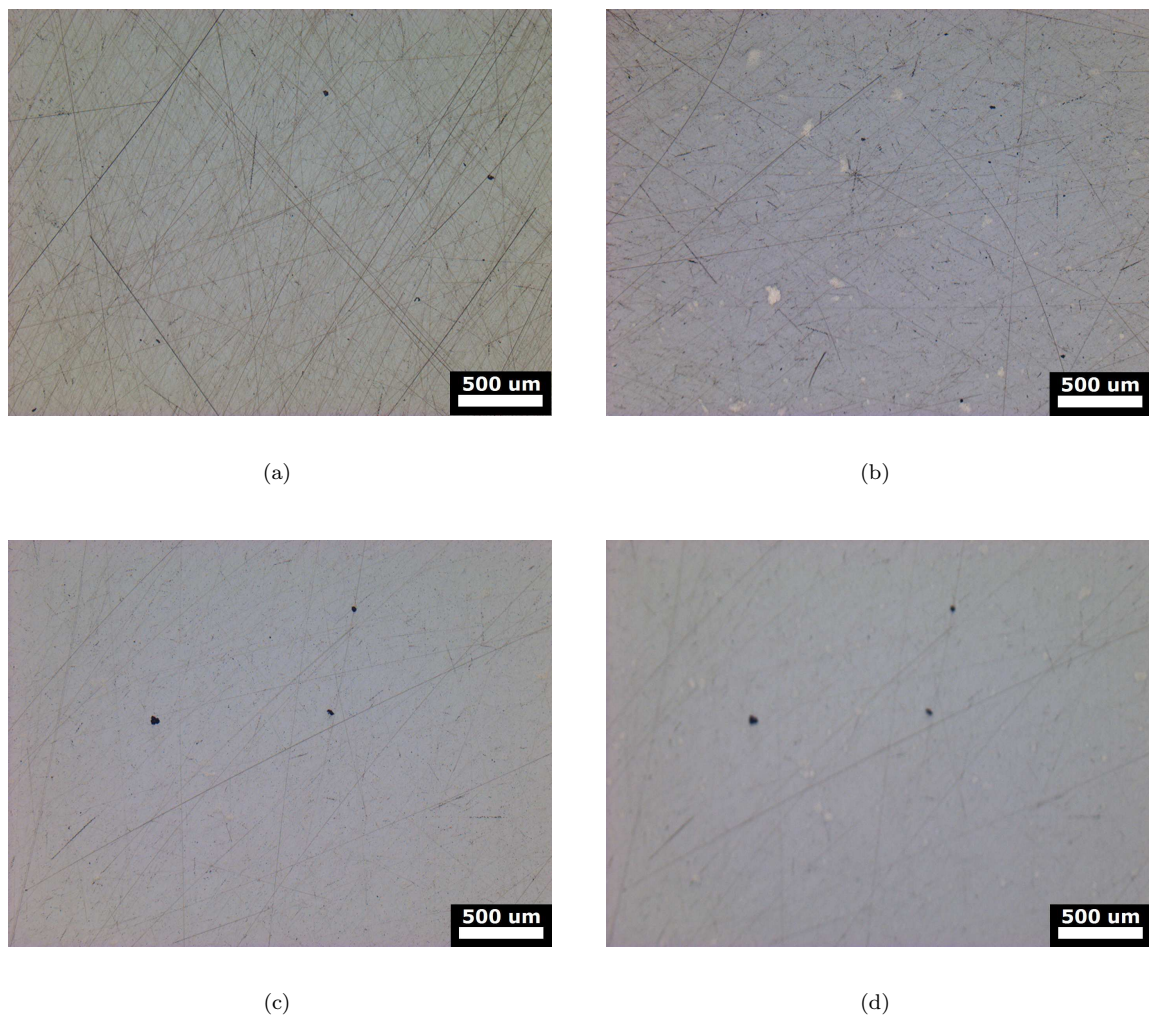


FIGURE 6.6: Optical micrographs showing the polished surfaces of (a) compression moulded PC 2805, (b) compression moulded PC-MWCNT 2205, (c) and (d) injection moulded PC-MWCNT 2205 at 4x magnification; (d) exhibits the identical location as (c) but the focus was adjusted to emphasize the bright features

typically with tungsten as the electron emitter. SEM is used in this work in order to provide a qualitative interpretation on the dispersion of CNTs within the matrix.

6.3.1 Method

SEM was performed using a Philips XL30 SEM-FEG operating at 20 kV. PC-MWCNT 2205 bars were cryofractured to a length of ~ 20 mm and mounted onto a stub using double-sided carbon tape prior to sputter coating with platinum (Pt) for ~ 90 s to ensure high electrical conductivity. SEM images were obtained on the fractured surface.

6.3.2 SEM micrographs

Fig. 6.7 shows a set of representative SEM images of PC-MWCNT cryofractured surfaces at different levels of magnification. The images show extruded strands that are likely to be individual nanotubes. The average CNT diameter in Fig. 6.7(b) was found to be 54.7 ± 4.5 nm. This is much higher than the average nanotube diameter of 9.5 nm according to the MWCNT manufacturer. This discrepancy is likely due to either an excessive Pt coating or to PC adhering to the CNT surface. The presence of bright spherical objects in Fig. 6.7(b) and the crack appearance of the Pt coat in Fig. 6.7(d) suggests a thick coating layer that may be concealing details of the fracture surface and obscuring protruding CNT strands. Therefore, the state of CNT dispersion and alignment is inconclusive.

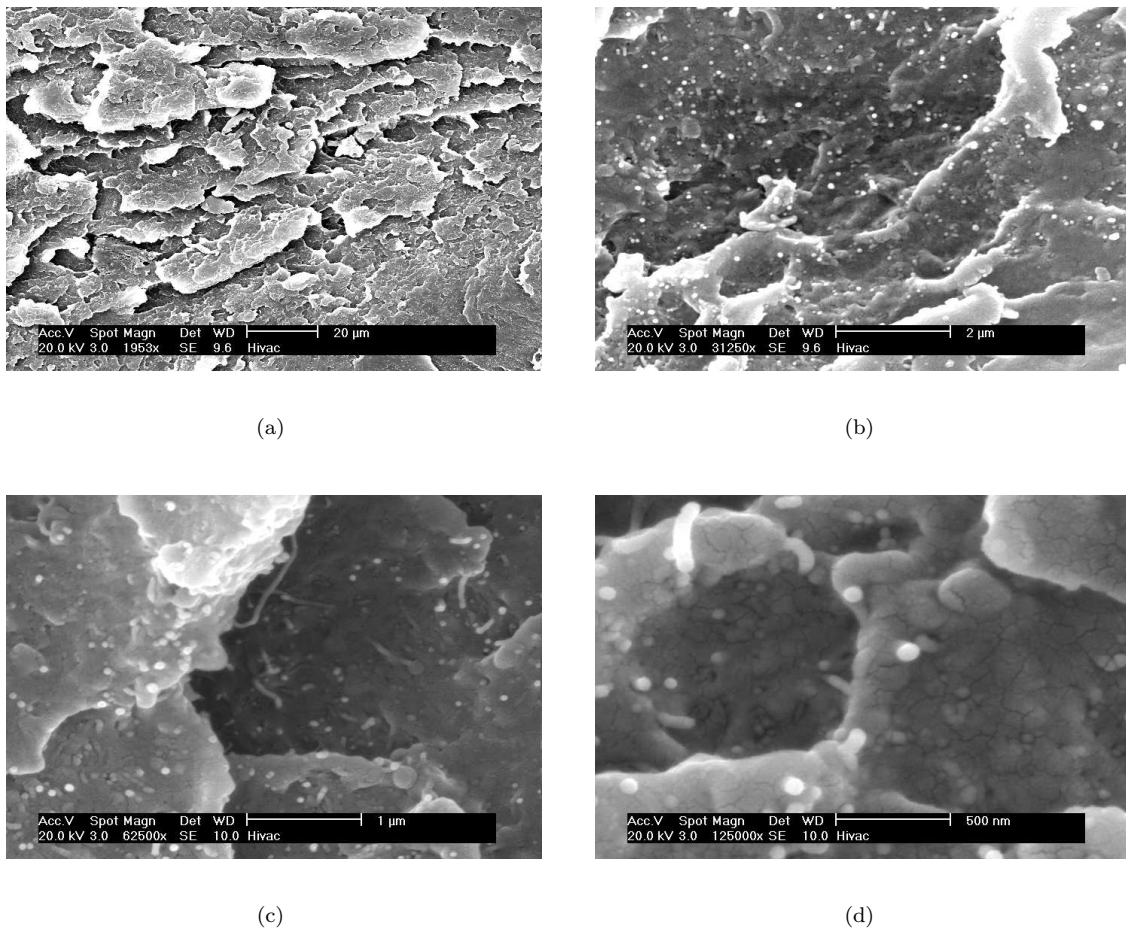


FIGURE 6.7: SEM micrographs of cryofractured PC-MWCNT 2205 at different magnifications showing the (a) fracture surface, (b) MWCNTs protruding from the cryofractured surface and platinum deposits, (c) and (d) MWCNT strands

Several references (Du et al., 2004; Logakis et al., 2009; Nobile et al., 2007; Prashantha et al.,

2008) have reported the use of coating for SEM imaging of CNT nanocomposites but did not specify the coating times or coating layer thickness. As such, in order to identify a suitable amount of coating for our PC-MWCNT systems, a heuristic approach was required. Due to SEM-FEG availability constraints, a thinner Pt coating was not attempted. Instead, there was an opportunity for a limited study of CNT dispersion of PC-MWCNT using focused ion beam-SEM that allows in-situ preparation to view the surface of interest. This method was pursued without sputter coating in order to prevent the coating layer from obscuring information of the surface investigated. Other studies have successfully obtained SEM images *without* the use of coatings on fractured PC-MWCNT surfaces (Pötschke et al., 2004, 2005) and on MWCNTs only (Kasaliwal et al., 2010; Kashiwagi et al., 2004; Pötschke et al., 2005; Socher et al., 2011). Furthermore, the literature has not consistently reported the use of coatings on CNT nanocomposites for SEM studies (Lew et al., 2009; Liu et al., 2004; Socher et al., 2011).

6.4 Focused ion beam-SEM

FIB-SEM is a combined technique that uses a high current ion column to precisely prepare a sample by removing or depositing material at a rapid rate in small defined areas, whilst using SEM to provide images of the underlying material (Sawyer et al., 2008), as illustrated in Fig. 6.8. This technique is commonly used in the semiconductor industry for failure analysis, and has been adapted by the material science community to prepare TEM specimens and for cross-section evaluations of various polymeric materials (Langford, 2006; Ray, 2010). Ray (2010) used successfully used FIB-SEM on poly[(butylene succinate)-co-adipate] filled with silicate to obtain cross-sectional views of different planes. The images were then reconstructed digitally to infer the 3D morphology of the silicate network structure (see Fig. 2.5). Bhuiyan et al. (2011) used FIB-SEM to report on the presence of CNT agglomerates and to interpret interfacial strength measurements in PP-MWCNT (1 wt%). FIB-SEM was pursued in this study to characterise the CNT dispersion distribution in PC-MWCNT, with the potential to obtain a 3D reconstruction of the CNT network. This information may be used to relate the morphology of the CNT network to the mechanical and electrical properties of PC-MWCNT.

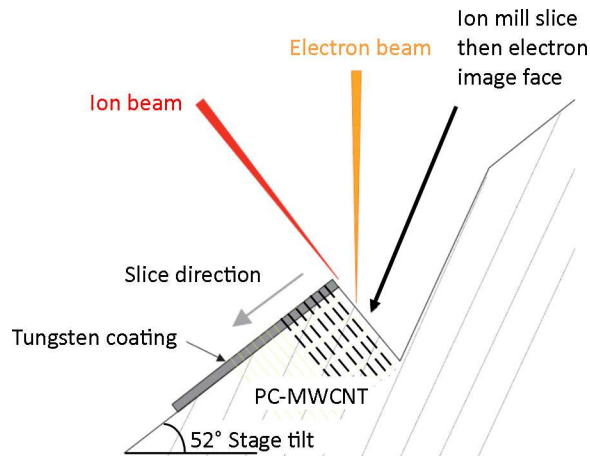


FIGURE 6.8: Schematic side view of the ion beam and electron beam with respect to the PC-MWCNT specimen (adapted from Bushby et al. (2011))

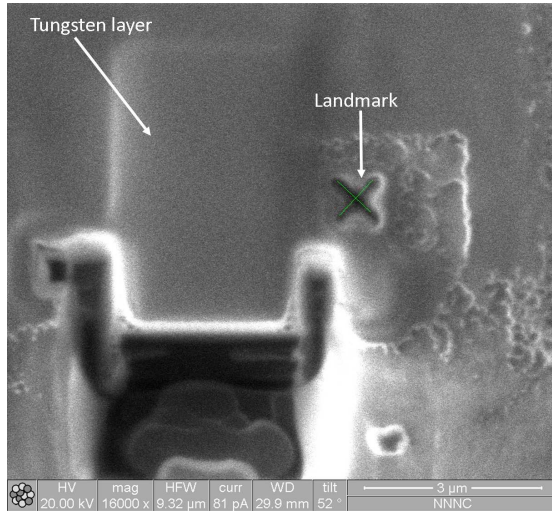
6.4.1 Method

This study was performed using a FEI Quanta 200 3D DualBeam. A PC-MWCNT bar measuring $20\text{ mm} \times 6\text{ mm} \times 0.9\text{ mm}$ was attached to a specimen stub using double-sided copper tape. A layer of tungsten was deposited on the area of interest prior to ion beam milling to prevent curtaining effect. This effect is observed as striations across the specimen cross-section. When the ion beam passes over an uneven surface topography, the variation in height steps can change the sputter yield, resulting in the curtain effect (Langford, 2006). The tungsten layer creates a planar surface that allows the ion beam to mill a clean cross-section and provides a protective layer for the specimen surface during milling. The stage containing the stub and the specimen is then tilted to 52° in the vacuum chamber. An ion beam of 0.16 nA was used to etch the specimen with a layer spacing of 100 nm . The SEM operated with an accelerating voltage of 20 kV .

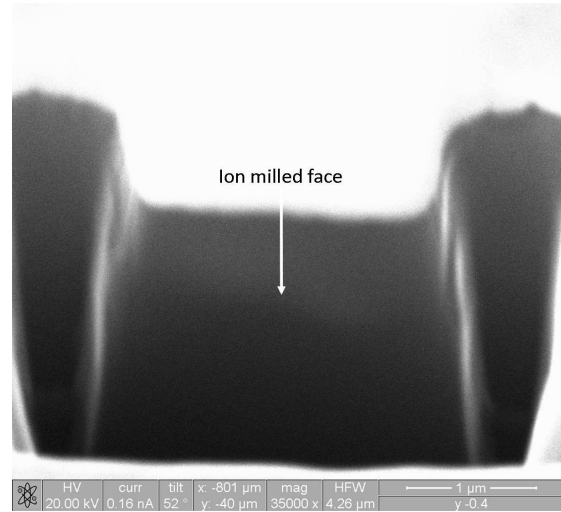
6.4.2 FIB-SEM images

Figs. 6.9(a) and (b) illustrates the site window with a layer of tungsten and the cross-section of PC-MWCNT 2205 that has been milled with the ion beam. It was not possible to identify individual MWCNTs due to the lack of contrast between filler and matrix. Successive slices revealed very similar images. Backscattered electrons (BE) are electrons from an electron beam that are elastically scattered by the specimen's atoms (Sawyer et al., 2008). As the production of BE is dependent on the atomic number of the material, a higher atomic number element will appear brighter. The detection of BE was attempted to differentiate CNTs from

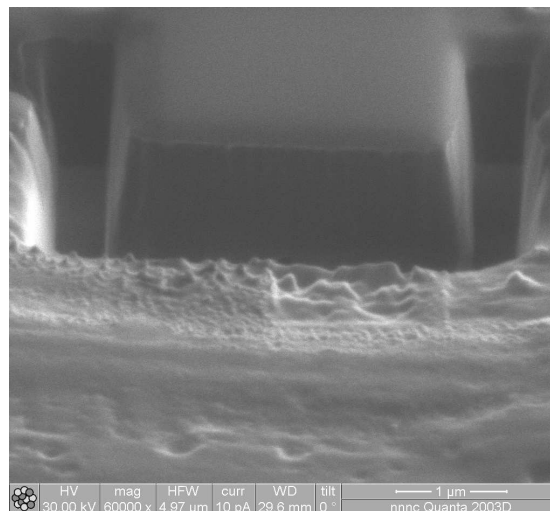
the matrix. Fig. 6.9(c) shows one such BE image. Even this technique was not sufficient to distinguish the filler from the matrix. This can be attributed to the similar densities and similar atomic compositions of PC and of MWCNTs.



(a)



(b)



(c)

FIGURE 6.9: (a) The site window with a layer of tungsten on the surface of PC-MWCNT 2205, with a landmark (X) to identify the specific site on the specimen. (b) SEM image of PC-MWCNT 2205 cross-section obtained with ion beam milling. (c) Backscattered electrons image of PC-MWCNT 2205 cross-section

6.5 Conclusions

The OM investigation to characterise and quantify the CNT dispersion of PC-MWCNT (3 wt%) was presented in Section 6.2. The glass knife yielded thin sections with less defects relative to the tungsten carbide knife. However, the heat treatment attempted to produce planar sections formed striations, complicating the OM analysis. Digital image processing applied to the micrographs of the sections obtained with a glass knife was unable to remove artifacts. Direct observation of the OM micrographs shows large CNT agglomerates, indicating poor dispersion within the matrix. Considerable technical expertise is required to produce specimens for OM analysis, that are suitable for quantitative analysis. Section 6.2.2 showed that the PC-MWCNT samples obtained by compression moulding and injection moulding may have small voids that would affect the mechanical behaviour.

Section 6.3 described the SEM investigation for qualitative evaluation of CNT dispersion. The cracked appearance of the Pt coating layer, the presence of bright spherical objects on the PC-MWCNT fractured surface and the enlarged CNT diameter suggests that the conductive coating layer was too thick. The thick layer may have concealed details of the fracture surface and the CNTs.

FIB-SEM was performed on PC-MWCNT, detailed in Section 6.4, to assess the technique for the possibility of obtaining images without coating, as well as for a 3D reconstruction. The ion beam was used to mill the specimen to reveal a cross-section of the specimen, while the SEM was utilised to image. It was not possible to distinguish between PC and CNTs, even with imaging with back-scattered electrons, due to a lack of contrast between the MWCNTs and the matrix. This can be explained by the comparable densities and atomic components of the filler and matrix. Therefore, the state of CNT dispersion is inconclusive.

Chapter 7

Electrical resistivity

7.1 Introduction

The influence of melt processing on electrical resistivity of CNT-nanocomposites and its dependence on various forming processes parameters has been introduced in Section 2.6. So far, most studies on the electrical behaviour of PC-MWCNT have been focused on the effects of CNT loading content, and nanocomposites were primarily produced in laboratory environments.

In order to achieve commercialisation of these materials, there is a need to investigate the influence of traditional polymer processes, that typically involves high shear rates and fast cooling rates. In industry, filled thermoplastics are compounded, pelletized and re-melted during secondary polymeric processes such as IM, which forms the final product. Although the forming processes determine the final electrical behaviour of the nanocomposite, it is not yet known whether the initial state of CNT dispersion or the conductive CNT network obtained from extrusion will influence the final electrical properties of percolated PC-MWCNT systems. This is potentially of interest for manufacturers seeking to tailor electrical properties of thermoplastic-CNTs systems utilising traditional polymeric processes.

This chapter briefly reviews the various electrical resistivity measurement techniques that can be used to characterise the electrical behaviour of nanocomposites. The development of an in-house fixture is then described. Exploratory experiments are performed with the in-house fixture to identify and minimise sources of error.

The chapter then focuses on the effects of processing history on the volume resistivity of PC-MWCNT 2205 (3 wt%). Materials were compounded with varying extrusion temperatures and formed to shape using two processes leading to different shear and cooling rates, IM (high rates) and CM (low rates). Measurements of volume resistivity are compared to highlight the effects of flow and temperature history on percolated PC-MWCNT systems. The commercial nature of the raw materials and of the manufacturing processes (compounding and IM) renders this study of particular industrial value for PC-MWCNT applications.

7.2 Resistivity measurements methods

Materials are typically categorised into three families, according to their electrical resistivity: (1) conductors ($<10^3 \Omega \text{ m}$), (2) antistatic ($<10^3 - 10^9 \Omega \text{ m}$) and (3) insulators ($<10^9 \Omega \text{ m}$) (Blythe, 1984). Bulk resistivity ρ , in line with EN ISO 3915:1999, is a combination of volume and surface resistivity but the effects of the latter are usually negligible (British Standard, 1999). As such, ρ will be referred to as volume resistivity throughout this chapter.

Resistivities measured in the laboratory are typically performed on especially shaped specimens by devising uniform electric fields through the specimen (Blythe, 1984). The inclusion of MWCNTs into insulating PC imparts electrical conductivity to the nanocomposite system. Since the electrical resistivity is known to be affected by polymeric processing methods and parameters, resistivity measurements can provide indirect information on the state of CNT dispersion. Moreover, electrical measurement techniques are non-destructive, making them attractive as screening tools.

7.2.1 Two-terminal method

The two-terminal method, illustrated in Fig. 7.1, is the simplest technique to measure volume resistivity of a material. There are two ways to perform the measurement: (1) using electrodes at the ends of a rectangular or cylindrical shaped specimen; and (2) positioning probes on the flat specimen surface (Blythe and Bloor, 2005). The contacts function as the voltage source, V_s , and the current, I , through the specimen is measured to determine the material's resistance, R . Contacts that exhibit Ohmic behaviour, where the relationship of current and voltage passing across the contacts is linear, are preferred.

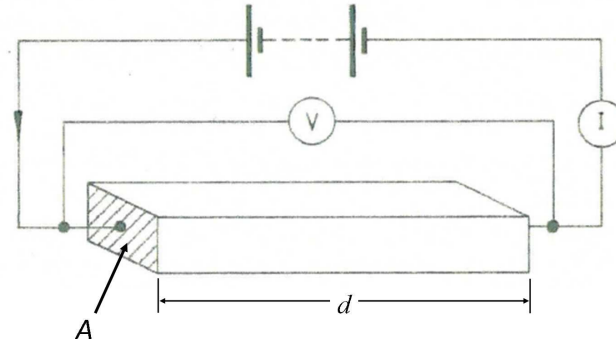


FIGURE 7.1: Two-terminal method for volume resistivity measurement (adapted from Blythe (1984))

The specimen R is determined as

$$R = \frac{V}{I} \quad (7.1)$$

With information of the specimen cross-sectional area, A , and the distance between the terminals, d , ρ is obtained from R using the expression (Blythe and Bloor, 2005),

$$\rho = \frac{RA}{d} \quad (7.2)$$

and has units of Ohm meters (Ω m), although Ω cm is often used in the literature.

The disadvantage of this method arises from the inclusion of contact resistance in the resistance measurements. The contact resistance arises from the junction between the terminal and the specimen (Blythe and Bloor, 2005). Additional resistance can arise from resistance of the electrode terminals, resistance of the connecting wires and resistance of the instrumentation device. This technique is more appropriate for comparative tests, where changes between sample resistivities are of interest.

7.2.2 Four-terminal method

Fig. 7.2 illustrates the four-terminal method, that utilises two outer electrodes to supply current to the specimen, while two inner electrodes are in contact with the specimen to measure the voltage drop, ΔV between the inner probes (Blythe and Bloor, 2005). All four terminals are positioned along the specimen. This method is preferred relative to two-terminal method because it avoids the issue of contact resistance by separating the current supply and voltage measurement (or sensing) electrodes. This leads to negligible current flow in the sensing electrodes, yielding accurate voltage measurements across R .

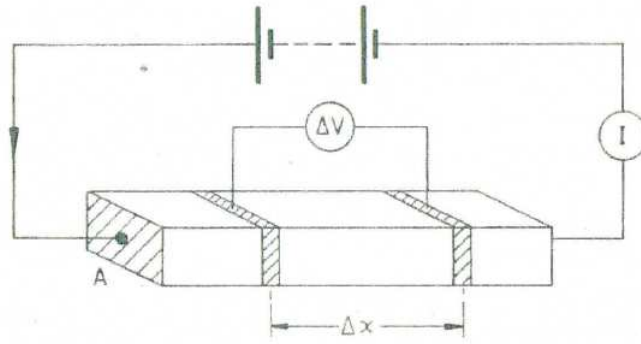


FIGURE 7.2: Four-terminal method for volume resistivity measurement (adapted from Blythe (1984))

7.2.3 Van der Pauw method

The van der Pauw method was devised to determine ρ of semi-conductors (van der Pauw, 1958). The technique is analogous to the four-terminal method. Two small contacts deliver a constant I into the specimen, while two other contacts measure ΔV across the contacts. The difference between four-terminal method and the van der Pauw method is the location of the contacts. In the van der Pauw technique, the contacts are located at the periphery of a shaped specimen.

The advantage of this technique is its ability to determine resistivity of irregularly shaped specimens. Specimen geometries commonly used with this method are clover-leaf and square, as shown in Fig. 7.3. Greek cross and bridge-type shapes can also be used. An important requirement is that specimens must not be perforated in order maintain specimen homogeneity. The favoured geometry is the clover leaf because the incisions reduce errors related to the size of the contacts. The specimen surface must be flat. If the specimen is homogenous and symmetric, then only one measurement is required. For greater accuracy, or to average over specimen inhomogeneity, the polarity and positions of contacts supplying current and measuring ΔV are changed around the specimen to give a total of eight separate measurements (Keithley Instruments, 2004), as shown in Fig. 7.4.

The four positions illustrated on the left of Fig 7.4 measures R_1 as

$$R_1 = \frac{V_2 + V_4 - V_1 - V_3}{4I} \quad (7.3)$$

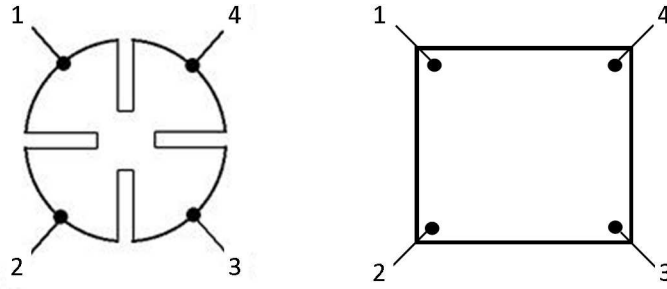


FIGURE 7.3: Clover-leaf and square geometry specimen for van der Pauw resistivity measurement

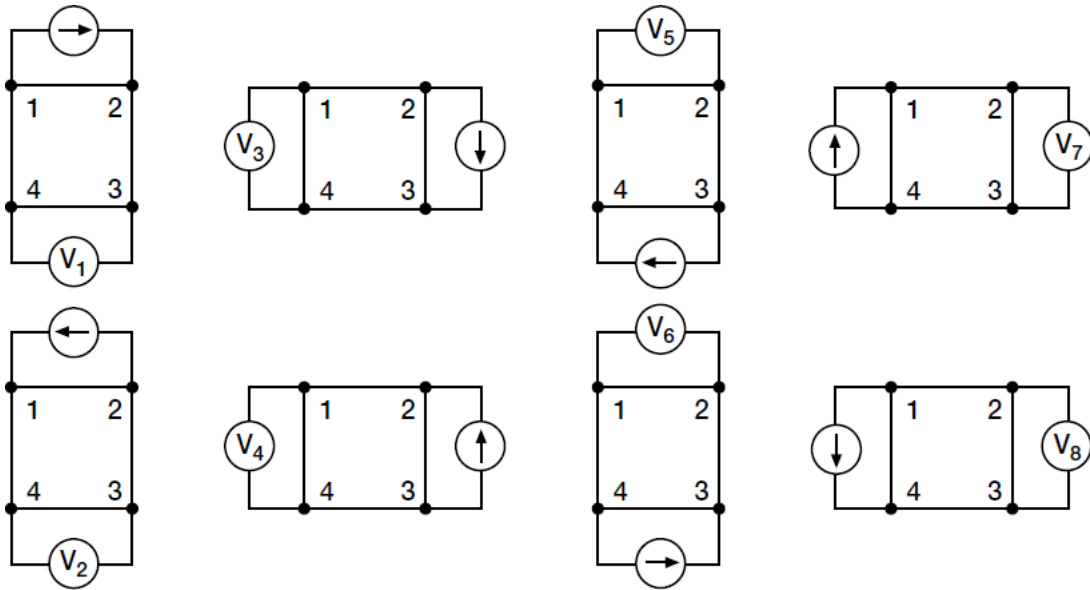


FIGURE 7.4: Eight measurement positions for the van der Pauw method to determine volume resistivity (adapted from Keithley Instruments (2004))

The other four positions illustrated on the right of Fig 7.4 repeats the previous measurements on the opposite positions to determine R_2 , follows

$$R_2 = \frac{V_6 + V_8 - V_5 - V_7}{4I} \quad (7.4)$$

Hence, the average R of the specimen is determined as

$$R_{\text{avg}} = \frac{R_1 + R_2}{2} \quad (7.5)$$

If R_1 and R_2 differ by more than 10%, it is recommended that these values be rejected because the large variation indicates that the specimen is not adequately uniform to provide consistent and repeatable resistivity measurement (Keithley Instruments, 2004).

ρ of the specimen, for a given thickness t and R_{avg} calculated from Eq. 7.5, is (van der Pauw, 1958)

$$\rho = f \left(\frac{\pi R_{\text{avg}} t}{\ln 2} \right) \quad (7.6)$$

where f is a geometric factor that is a function of the ratio $\frac{R1}{R2}$. Since all specimens used in this study are symmetrical, $f = 1$.

7.3 In-house two-terminal resistivity fixture

It must be noted that initial exploratory experiments with the four-terminal method and van der Pauw methods highlighted the technical challenges of the resistivity measurement techniques, such as achieving good contact between the pointed probes and the specimen. Therefore, only the two-terminal method was pursued for this work as means of carrying out comparative measurements on $\rho_{\text{PC-MWCNT}}$ of CM and IM dog-bone specimens. The following sections will describe the construction of the fixture and the calibration procedure to minimise potential errors to electrical measurements related to the two-terminal method.

This section describes the design of an in-house two-terminal fixture for measurement of electrical resistivity. Fig. 7.5 shows a labelled photograph of the fixture developed for two-terminal method for ρ measurements on specimens of rectangular geometry. The fixture employs surface contacts on the specimen, to both supply voltage and measure current flowing through the specimen. An electrometer, used as a power supply and ammeter, is connected to the fixture through the crimp ring terminals. V_s is monitored by the multimeter using crocodile clips attached to the connection junctions between the electrometer and the copper plates.

In a two-terminal measurement, the ideal contact geometry would apply a voltage at planes A_i and B_i , as shown in Fig. 7.6, but this is not always practical, for instance, in a thin bar geometry of thickness ≤ 1 mm. Hence, larger surface contacts are used on the top and bottom surfaces of the specimen, at locations A_p and B_p , to maximise contact area between the terminals and the specimen.

The cross-section of one entire terminal is illustrated in Fig. 7.7. Conductive elastomers are employed between the copper contacts and the specimen surface to improve surface contact between the two rigid bodies. The top surface contacts are spring loaded to provide

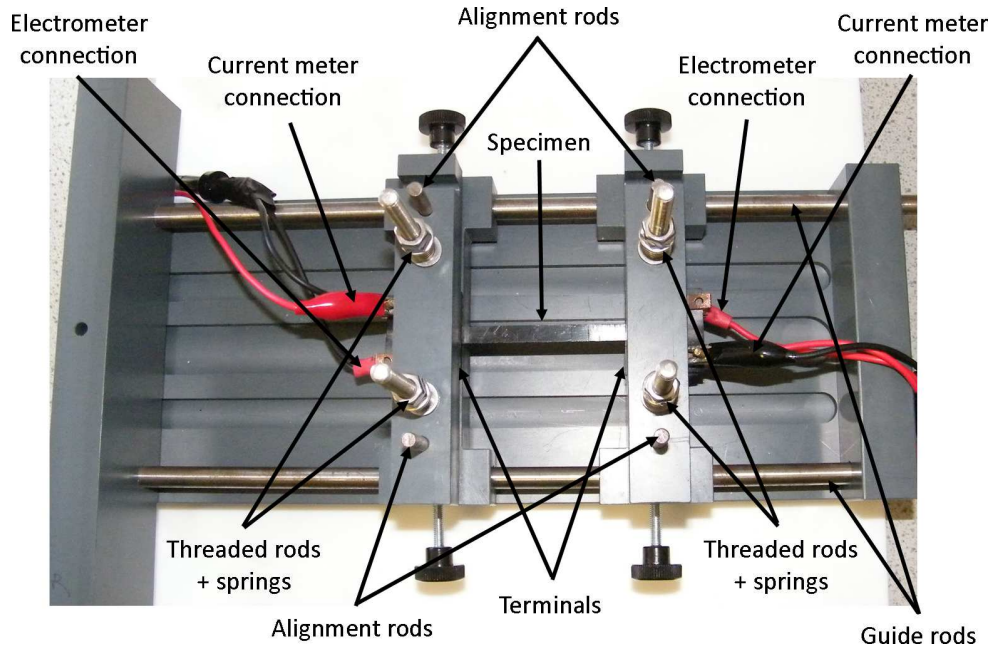


FIGURE 7.5: Two-terminal fixture setup with specimen positioned for resistivity measurement

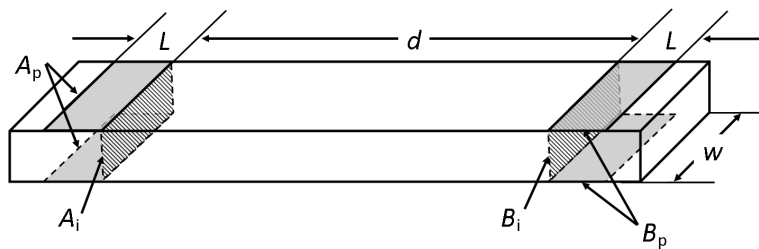


FIGURE 7.6: Specimen with practical contact locations A_p and B_p and the corresponding ideal contact locations A_i and B_i

a consistent force between each specimen and terminal surface, ensuring a good, repeatable contact. A specimen is sandwiched between the upper and lower sections. The fixture accommodates specimens of various lengths, from 60 mm up to 200 mm, widths up to 20 mm, and thickness between 1 mm and 4 mm. Full technical details of the fixture will be provided in Section 7.3.1.

The flow of current from the contacts to the specimen is not perfectly uniform, as illustrated schematically in Fig. 7.7. As the distance for current transfer increases further along the contact, the current reduces to zero at the far edge. This phenomenon is known as current crowding. The length between the edge of the contact and the point of no current along the contact is known as the transfer length, L_t . When current is transferred away from the contacts, the current flow will subsequently converge along the length of the specimen, and can be assumed to be uniform.

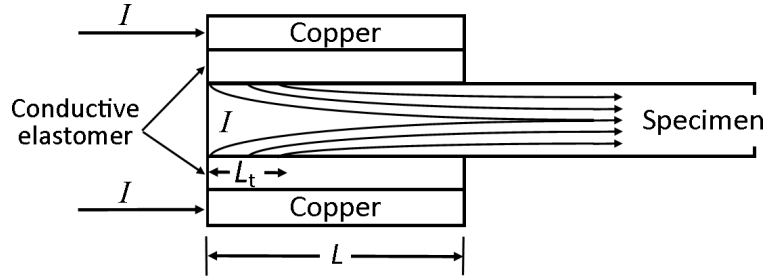


FIGURE 7.7: A cross section of the terminal showing the electrode components and the contact interface with the specimen; and schematic of the current distribution from the contacts to the specimen. The transfer length, L_t , the length over which current transfers between the contact and the specimen. L_t was determined as 67.6 mm using the extrapolation method, presented in Section 7.5.1.4

Table 7.1 presents the symbols and definitions that are used to describe the equivalent circuit representing the fixture, shown in Fig. 7.8.

TABLE 7.1: Symbols and its definitions to describe the equivalent circuit of the two-terminal fixture

Symbols	Definitions
R_s	specimen resistance
R_{cu}	copper resistance
R_{ce}	conductive elastomer resistance
R_{cu-ce}	resistance of the copper-conductive elastomer interface
R_{ce-s}	resistance of the conductive elastomer-specimen interface
R_w	copper wire resistance
R_{meter}	meter resistance
R_t	resistance of an individual surface contact (an upper or a lower section of a terminal)
$R_{terminal}$	resistance of one entire terminal
R_T	total resistance of the two-terminal circuit

R_t is determined as

$$R_t = R_{cu} + R_{cu-ce} + R_{ce} + R_{ce-s} \quad (7.7)$$

R_{cu} is negligible because copper has much lower resistivity ($\sim 10^{-8} \Omega \text{ m}$) compared to the other resistances.

$R_{terminal}$ consists of two R_t connected in parallel, and is calculated from

$$\frac{1}{R_{terminal}} = \frac{1}{R_t} + \frac{1}{R_t} \quad (7.8)$$

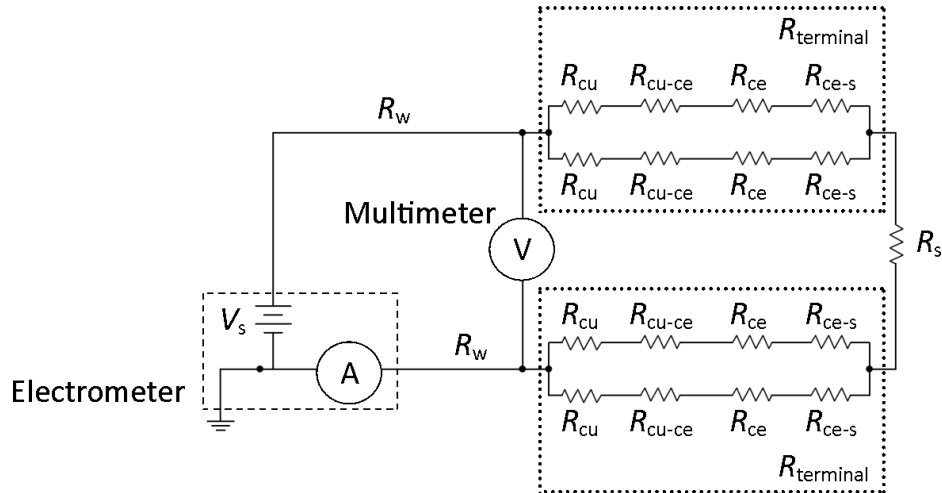


FIGURE 7.8: The circuit diagram of two-terminal method for the in-house fixture for resistivity measurements. Symbols are defined in Table 7.1

Rearranging Eq. 7.8 gives

$$R_{\text{terminal}} = \frac{R_t}{2} \quad (7.9)$$

The total resistance of the two-terminal circuit, according to Fig. 7.8 is

$$R_T = 2R_w + 2R_{\text{terminal}} + R_s + R_{\text{meter}} \quad (7.10)$$

R_w is significantly smaller than the other resistances as the wires are made of copper. By substituting Eq. 7.9 into Eq. 7.10, R_T , the measured resistance, can be expressed as

$$R_T \simeq R_t + R_s + R_{\text{meter}} \quad (7.11)$$

The determination of R_t and R_{meter} will be presented in Section 7.5.1.3. Volume resistivity of the specimen is calculated by substituting R_s into Eq. 7.2.

The dominant resistance contributing to the contact resistance, R_c is expected to arise from the interfaces $R_{\text{cu-ce}}$ and $R_{\text{ce-s}}$. The latter is dependent on the material of the specimen. However, due to the circuit configuration, it is not possible to separately determine $R_{\text{cu-ce}}$, R_{ce} , and $R_{\text{ce-s}}$.

7.3.1 Technical description of a two-terminal fixture

Fig. 7.9 shows the two-terminal fixture in a typical configuration for ρ measurement of a specimen.

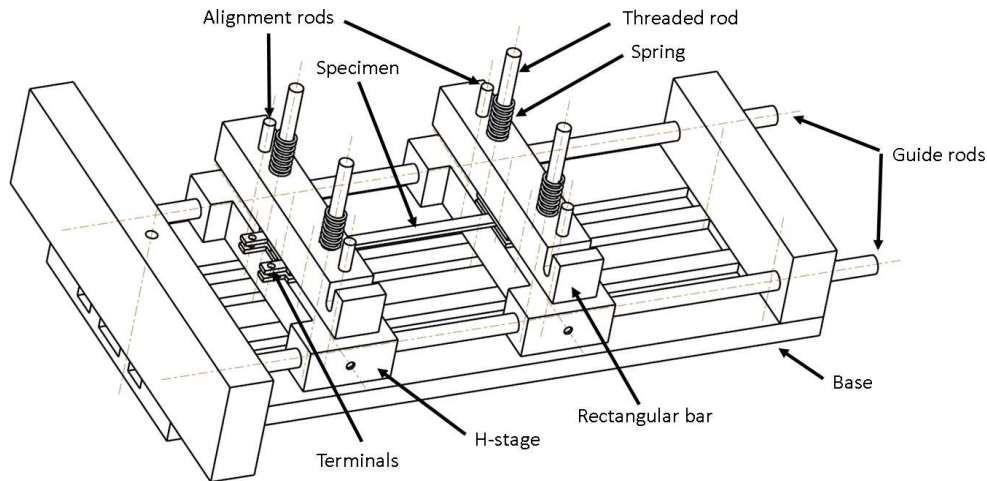


FIGURE 7.9: A typical experiment configuration to determine electrical resistivity of the specimen using the two-terminal method

Fig. 7.10 presents the cross section of one entire terminal that is divided into two surface contacts, giving the upper and lower terminal. The upper terminal contact is fixed to a spring loaded rectangular bar while the lower terminal is fixed to an H-shaped bar, seen in Fig. 7.10. Two parallel threaded rods run through the upper and lower bars, each housing a compression spring with a constant of 1.34 Nm^{-1} . This provides a consistent force between each specimen and terminal surface, ensuring a good, repeatable contact. Two nuts were used to set the compression length of the spring, one nut held the spring at the desired length while the other functions as the locking nut. Nylon lockings nuts were used to prevent the threaded bars from contacting the base of the fixture.

A copper contact plate and a conductive carbon-filled silicone elastomer sheet (Laird Technologies C5-9134) are attached to the respective bars using two M2 counter sunk brass screws. The elastomer is employed to provide a good surface contact between the rigid specimens and the copper plate. Each copper plate is connected to an insulated crimp ring terminal with a brass M5 set screw and nut. The crimp ring terminal is soldered to one end of a copper core cable 60 mm long while the other end is soldered to an insulated socket. Another copper wire cable, with a 4 mm banana plug at one end and a crocodile clip in the opposite end, is used to connect the test fixture terminals to the electrometer via a triaxial cable.

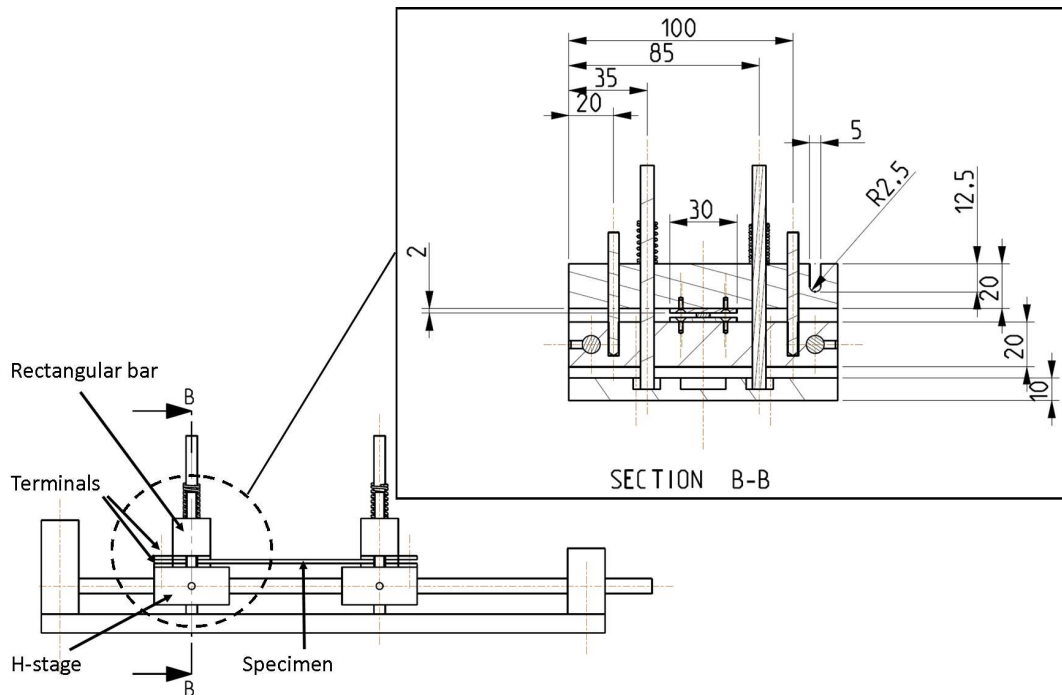


FIGURE 7.10: Side view of the two-terminal fixture. The inset shows the cross-sectional view of one entire terminal in the inset. Dimensions are in mm

The H-stage slides on two 8 mm diameter silver steel guide rods, that run horizontally along the length of the fixture base, shown in Fig. 7.11. This allows the fixture to accommodate specimens of various lengths, from 60 mm up to 200 mm. Each spring loaded rectangular bar is aligned to the H-shaped bar using two 5 mm diameter alignment rods, made from silver steel.

The bars and base of the fixture are made from PVC, a good electrical insulator. A sheet of PTFE is used as a protective insulating sheet between the test fixture and the workbench.

7.4 Errors in electrical measurements using custom test fixtures

7.4.1 Considerations for current measurements

Current leakage occurs through stray resistance paths when the voltage sources in close proximity to the measuring circuit, thus, affecting current measurements (Keithley Instruments, 2004). In order to reduce the possibility of current leakage, a Keithley 6517B electrometer is used as both the voltage source and the current meter by employing the Meter-Connect

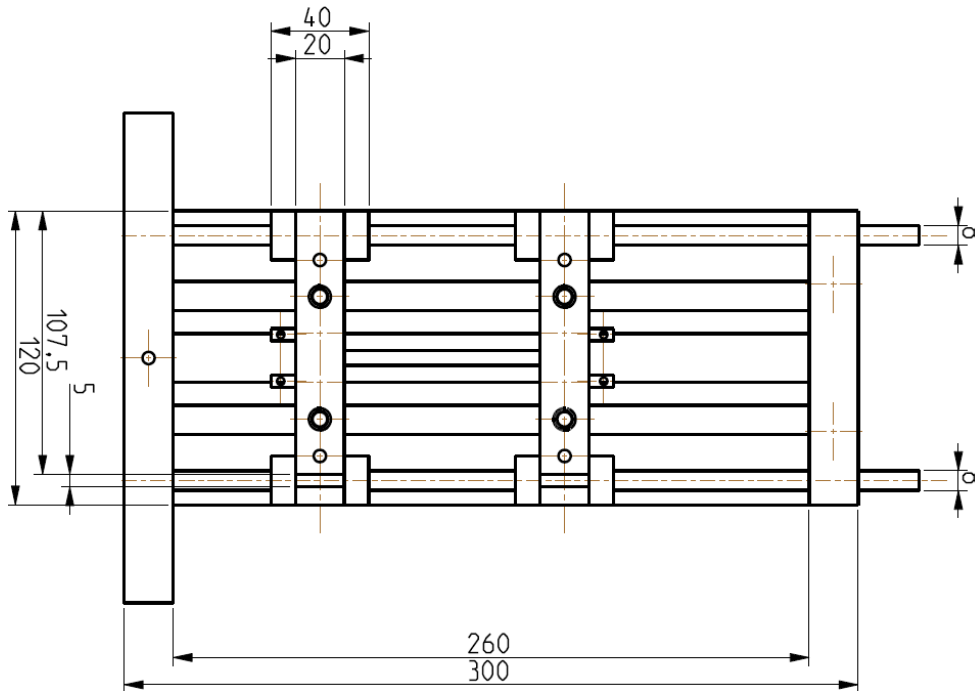


FIGURE 7.11: Top view of the two-terminal fixture. Dimensions are in mm

option. This internally connects the voltage source to the ammeter. A disadvantage of employing the Meter-Connect option is the potential for an increase in noise in the voltage source due to an input amplifier. Therefore, a Keithley 2100 digital multimeter was connected in parallel to the circuit to monitor the voltage burden of the current meter during the test period. Voltage burden is the voltage drop across the input terminals that is caused by the internal R of the current meter. The internal resistance of the multimeter is set to $>10^9 \Omega$ to prevent drawing current from the circuit.

Input bias current arises from an offset current flowing through the ammeter, and only ideal ammeters have zero input bias current. This could potentially affect low current measurements. The input bias current for a Keithley 6517B, as used in our work, is rated as less than 3 fA (Keithley Instruments, 2009). As currents measured with the fixture are typically between 10^{-4} A and 10^{-2} A , this error is negligible.

The device connections are crucial to minimise the signal loss between the instrumentation and the test fixture. A triaxial cable is typically used with a source measurement unit (e.g. an electrometer). It has two layers of shielding and insulation, protecting the center conductor from electrostatic interference. However, friction between the conductor and the insulator in the cable through flexing or movements, may generate triboelectric currents that can affect ρ measurements (Keithley Instruments, 2004). A low noise cable, Model 237-ALG-2 triaxial

cable with an internal graphite coating, is used to prevent errors due to such effects. The triaxial cable was secured in a fixed location during tests, in order to inhibit movement that could generate triboelectric voltages. The test fixture was connected to safety earth through the triaxial cable.

Extraneous currents can be internally generated in the test circuit, leading to errors in measurements. Undesirable currents can be introduced through contamination from body oils, salt, solder flux and moisture (Keithley Instruments, 2004). Such error was minimised by ensuring (1) the fixture is of rigid construction and made from insulating and water-resisting materials (i.e. PVC) and (2) maintaining clean fixture terminals. The latter was achieved by avoiding manual handling with bare hands, and using compressed air to remove any foreign matter between the conductive elastomer and the specimen.

The measuring devices were controlled remotely using a custom LabVIEW interface. The software is used to set input parameters, to perform zero checks on the devices, and to record data files. The zero checks, conducted prior to R measurements, reconfigure the measuring devices to shunt the input signal to low.

Contact resistances in the fixtures come from several sources: (1) contact of the terminals with the specimen, (2) copper plate and conductive elastomer interface, (3) oxide layers on copper, (4) connections between the triaxial cable and the terminals (i.e. soldered and brass-ring terminal junctions), and (5) connecting wires. Sources (1) and (2) were limited by with the application of consistent pressure using compression springs. Further investigation into the magnitude of contact resistances (1) and (2) will be presented in Section 7.5. Formation of an oxide layer on the surfaces of the copper is inevitable, and hence, care was taken to prevent puncture of the oxide layer to attain repeatable measurements. All soldered junctions and crocodile clip connections were insulated using PVC electrical tape. Connecting wires were crimped to insulating ring terminals.

7.4.2 Temperature effects

Thermoelectric electromagnetic fields (EMF) are the voltages that arises from the different materials connected within a circuit and the temperature differences at the connections (which are dependent on the type of material) (Keithley Instruments, 2004). This introduces

errors into the voltage measurements. As the custom test fixture was constructed from various materials, care was taken to minimise this error with practical steps such as warming up the test instruments prior to use. The sum of all the connections in the circuit provides the total EMF voltage. One method to address thermoelectric EMF is to perform the first measurement and then reverse the voltage source, V_s to read the second measurement (Keithley Instruments, 2004). This test was conducted on the test fixture and will be presented in the Section 7.5.1.1. By reversing V_s , the polarity of the signal of interest is reversed but the EMF voltages remain unchanged. Therefore, averaging the first and second measurements cancels the EMF voltages.

Temperature is known to affect current measurements through, for instance, the contraction or expansion of the fixture materials or connections with measuring devices. Hence, prior to performing ρ measurement, all measuring devices were switched on for a minimum of an hour to attain thermal stability. All measuring devices and the fixture were kept away from direct sunlight. Resistivity measurements were performed between 16 °C and 18 °C.

Device heating affects ρ measurements as high current density in a specimen can increase or decrease the resistance of a specimen, depending on the material. Assuming a closed system, electrical power, P that can be converted to heat within a specimen is given by

$$P = I^2 R \tag{7.12}$$

Following the relationship in Eq. 7.12, if the current flowing through the specimen increases, the power dissipated will increase the square of the current. Therefore, the most effective way to minimise heating effects is to use a smaller current through the specimen.

7.5 Exploratory experiments

7.5.1 Two-terminal method

7.5.1.1 Thermoelectric effect

In order to verify and validate the fixture's function, a series of exploratory tests were performed. The first experiment was to change the polarity of V_s to determine the thermoelectric

EMF effect in the circuit. As the fixture terminals are constructed from different materials, it is not possible to discount a priori a thermoelectric EMF effect.

The setup to probe the effect consisted of two solid copper bars with the dimensions of 50 mm \times 10 mm \times 2 mm connected to a TENMA 72-7270 resistance decade box (tolerance of 1%) using copper wires and crocodile clips. The copper bars were positioned at the center of the terminal contacts. The copper dimensions were chosen to replicate the surface contact area between the terminals and PC-MWCNT specimen. A force of 28 N was applied on the terminals using the compression springs. The resistance of the two copper bars is negligible.

V_s of 1 V to 0.25 V was supplied to the circuit in decreasing steps of 0.25 V. Each voltage step was applied for 20 s at positive polarity and a further 20 s at negative polarity. Fig. 7.12 presents the plot of I_{meas} as a function of time for V_s between 0.25 V and 1 V. If there is a temperature effect on the specimen due to the voltage supply, the magnitude of the measured current would vary significantly with the change in voltage polarity. The findings show no evidence of measurable thermoelectric effect. Hereafter, tests were conducted with voltage of positive polarity only.

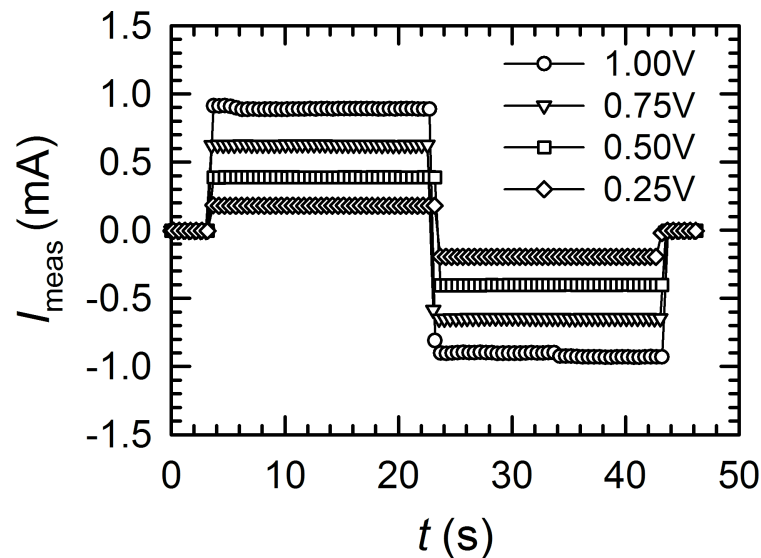


FIGURE 7.12: Current flow as a function of time for voltage supply between 0.25 V and 1 V, applied to the fixture in decreasing order of 0.25 V steps, at different polarities

7.5.1.2 Heating of specimen

A high current density can potentially heat a material. The change in temperature, ΔT is estimated through calculations, with the assumption that all energy is converted to heat in

a closed system. The electrical energy, E in the circuit can be determined using P from Eq. 7.12, and the duration for when the voltage is applied in the circuit, t , through

$$E = Pt = VIt \quad (7.13)$$

The conversion of E to thermal energy, Q due to the resistance of electrical current flowing through the specimen is referred to as Joule heating. The relationship between ΔT of the specimen induced by Joule heating and E is given by

$$E = Q = mC_p\Delta T \quad (7.14)$$

where m is the mass and C_p is the specific heat capacity of the material under test.

Joule heating can be induced by current crowding at the terminal or by high current density. In an attempt to detect the effects of Joule heating, a test was performed to monitor for temperature of a PC-MWCNT 2205 bar (100 mm \times 6 mm \times 0.9 mm) while a current is flowing through the specimen. A type K thermocouple was insulated with PVC electrical tape from the current, and secured on the PC-MWCNT bar, at \sim 5 mm from the edge of one terminal. A voltage of 9 V was supplied for 60 s, giving a current density of 12 A mm⁻². These parameters were chosen to amplify any temperature effect.

According to Eqs. 7.13 and 7.14, under adiabatic conditions, the expected temperature rise ΔT is 4.9 K, (using C_p for PC-MWCNT of 1114 J kg⁻¹K⁻¹ as calculated Section 4.3). The calculation of ΔT represents the worst case scenario when the heat generated by Joule heating is conserved within the specimen. The thermocouple recorded no measurable temperature change. This observation was verified using an infra-red temperature gun. Instead, it was observed that the current flowing through PC-MWCNT increased from 5.7 mA, at the start of the test, by \sim 1.2 mA. This may indicate a temperature effect since the same was not found in Section 7.5.1.1 for the test period of 40 s.

The measurement of the specimen temperature was challenging due to the need to isolate the thermocouple from the current passing through the specimen, that was achieved with the electrical tape. However, the tape also acts as a thermal insulator, which could have contributed to the lack of measurable temperature change. In reality, any heat within the specimen could have dissipated more quickly than we can measure, with the thermocouple or

the infra-red temperature gun, since the fixture terminals were good electrical and thermal conductors.

The change in current as a function of time could be explained by the localised temperature change of the CNT agglomerates within the matrix, thus decreasing the volume resistivity of the specimen. Since the agglomerates are surrounded by insulating matrix, an increase in temperature of the agglomerates does not necessarily increase the temperature of the bulk specimen, making it challenging to monitor the change in temperature of the specimen.

This test has shown that high current density leads to a reduction in R . The calculation for ΔT is used as a check to minimise the likelihood of any significant Joule heating affecting subsequent resistivity measurements.

7.5.1.3 Non-ideal contacts and resistance sources in the fixture

Tests were carried out to evaluate the suitability of the fixture for the measurement of the R range of interest, between 1000 Ω and 15000 Ω . Two separate experiments were performed: (1) variation of V_s between 0.2 and 3 V, in a downwards direction and without any external resistance load; and (2) applying an external resistance load ranging from 1000 Ω to 15000 Ω at two fixed V_s of 5 V and 10 V. Experiment (1) assessed the behaviour of the contacts as a function of current flow whereas experiment (2) validated the function of the fixture for the resistance range of interest.

The fixture configuration to perform experiments (1) and (2) is identical to that described in Section 7.5.1.1. For both experiments, V_s was applied onto the copper bars for 20 s. Experiment (1) was performed to determine the relationship of R_{terminal} and the electrometer's internal resistance, R_{meter} as a function of current flow. Since a copper bar was used as the specimen, R_s is negligible. Following Eq. 7.10, R_T for this experiment is

$$R_T = R_t + R_{\text{meter}} \quad (7.15)$$

The difference between V_s and the voltage measured by the multimeter, V_{meas} yields the voltage burden attributed to the ammeter, identified as V_{meter} . R_{meter} is determined as $\frac{V_{\text{meter}}}{I_{\text{meas}}}$, where I_{meas} is the average current monitored for 20 s at a fixed voltage. Fig. 7.13 presents R_{meter} as a function of I_{meas} for V_s ranging from 0.25 to 2.5 V. The finding shows

that R_{meter} increases as I_{meas} decreases; but the rise of R_{meter} is more pronounced at the lowest current (2 mA). A third order polynomial function was sufficient to reflect the data observed, with a coefficient of determination, R^2 of 0.997. This function allows estimation of R_{meter} for a given I_{meas} .

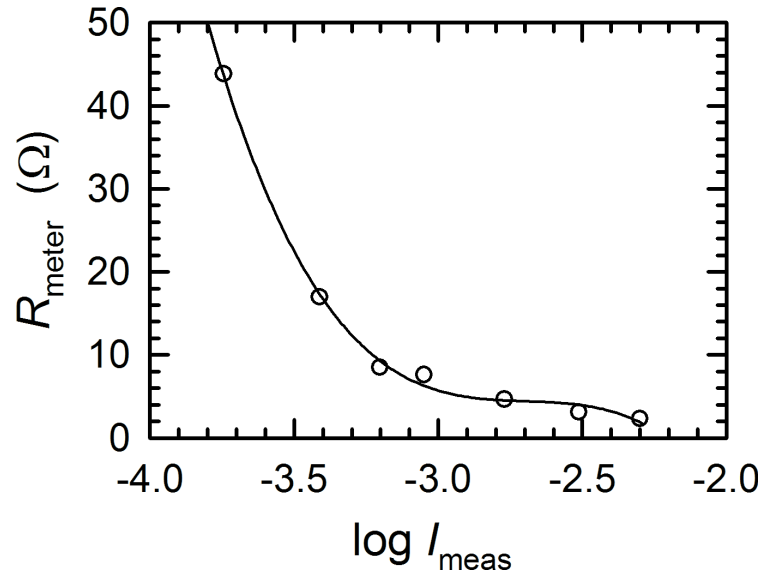


FIGURE 7.13: Electrometer internal ammeter resistance as a function of current flow. The solid line represents the third order polynomial function

R_{terminal} was determined to evaluate its contribution to the total resistance, R_T of the circuit as a function of current. R_{terminal} was calculated as $\frac{V_{\text{meas}}}{I_{\text{meas}}}$. Fig. 7.14 presents the relationship between R_{terminal} and I_{meas} for the circuit. The plot shows that the terminals exhibit non-Ohmic behaviour, probably due to the conductive elastomer-copper interface. Although non-Ohmic contacts are not ideal, the use of conductive elastomer as an interface between the specimen and the copper plates is necessary due to the rigidity of the copper terminals and of the PC-MWCNT. It would be difficult to obtain intimate surface contact between the terminals and specimen in the absence of the flexibility of the conductive elastomer. A second order polynomial function was satisfactory to describe the experimental data, with $R^2 = 0.995$. This function approximates R_{terminal} for a given I_{meas} .

Experiment (2) was performed to verify that the contribution of R_{meter} and R_{terminal} to R_T . Using the resistance box, a range of resistances between 1000 Ω and 15000 Ω , were evaluated at V_s of 10 V. The procedure was repeated with a reduced V_s of 5 V. Fig. 7.15 compares the measured resistance, R_{estimate} , accounting for R_{meter} and R_{terminal} , to the known resistance loads, R_{actual} . The test for 1000 Ω at 10 V was omitted because the energy consumption was above 1 J, which could potentially heat the specimen, thus corrupting the R measurement.

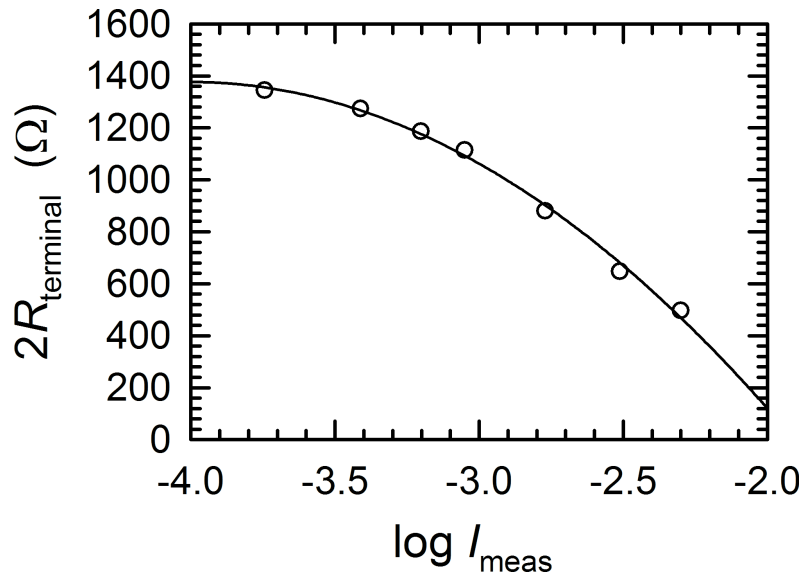


FIGURE 7.14: Total terminal resistance of the circuit as a function of current flow. The solid line represents the second order polynomial function

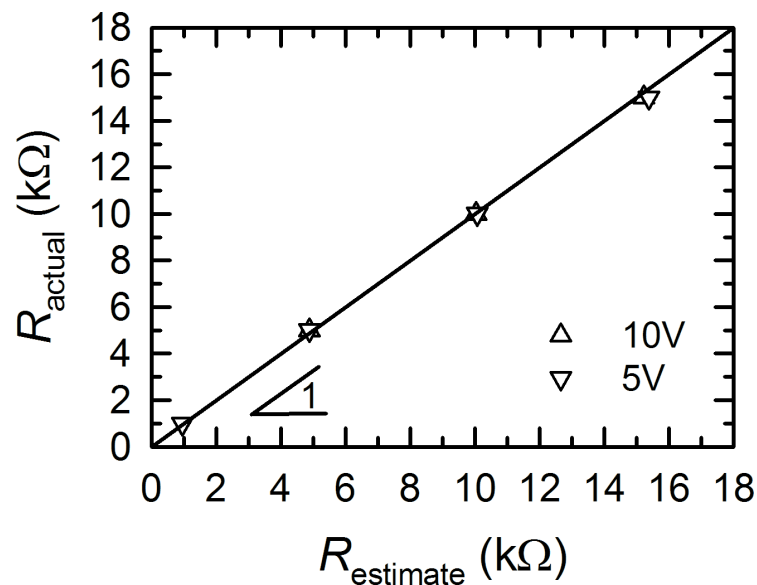


FIGURE 7.15: The comparison between the known resistance load, R_{actual} and the calculated resistance load, R_{estimate} for voltages of 5 V and 10 V. R_{estimate} is determined from the measured resistance, using the fixture, and accounting for the meter and terminal resistances

We can make two observations in Fig. 7.15. Firstly, R_{estimate} and R_{actual} were in agreement for both voltage supply values. Secondly, reducing the voltage supply from 10 V to 5 V had no significant change in the similarity between R_{estimate} and R_{actual} . The variation between R_{estimate} and R_{actual} was found to be up to 2% for 10 V and up to 3% for 5 V; considering the accuracy of the resistance box is 1%, the agreement between R_{estimate} and R_{actual} is satisfactory.

7.5.1.4 Contact resistance and contact resistivity determination

Substituting the copper sheets with a PC-MWCNT 2205 bar in the fixture, the total resistance, R_T of the circuit is given by

$$R_T = R_t + R_{\text{PC-MWCNT}} + R_{\text{meter}} \quad (7.16)$$

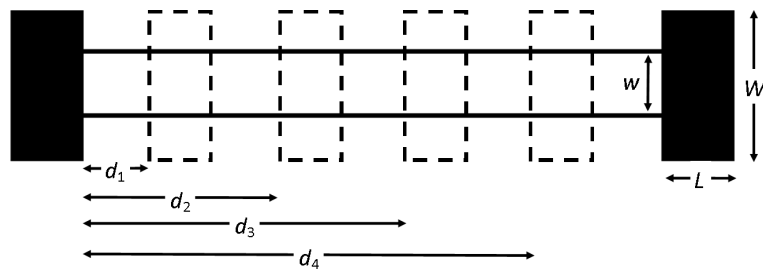
$R_{\text{ce-s}}$ is now the dominant contact resistance, R_c in the circuit. In line with common terminology used in the literature, henceforth R_t is described as $2R_c$. This is substituted into Eq. 7.16 to obtain

$$R_T = 2R_c + R_{\text{PC-MWCNT}} + R_{\text{meter}} \quad (7.17)$$

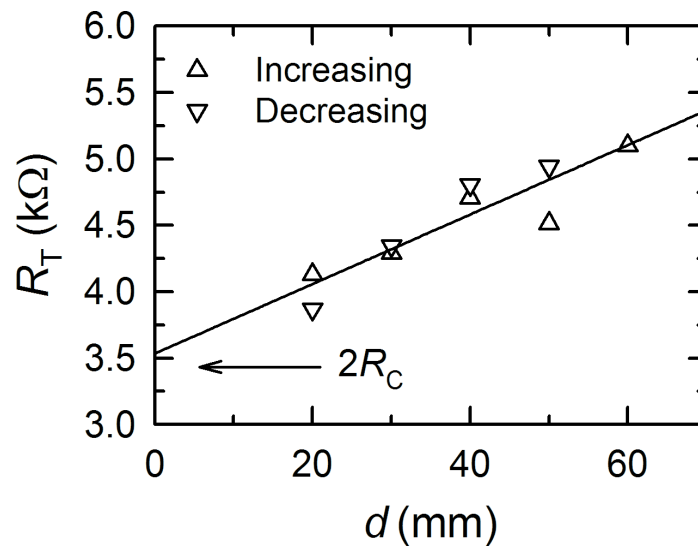
One way to determine R_c in semiconductors is by the extrapolation method (EM), shown in Fig. 7.16(a). This method measures the voltage distribution along a constant cross section semiconductor using a probe, and determines R_c by extrapolation the plot of voltage as a function of contact spacing, d (Berger, 1972). At the interface ($d = 0$), ΔV is theoretically zero for an ideal contact, thus, this point can be attributed to R_c . A derivative of this technique is the transfer length method (TLM). The difference between the TLM and the EM lies in the measurement method; in the TLM an array of identical planar contacts are deposited on the semiconductor at unequal spacing between the contacts, and the voltage is measured between adjacent contacts (Schroder, 2006).

The determination of R_c in this work is based on a hybrid of the methods: the EM method is used but with surface contacts, as in the TLM method. The relationship between R and d for PC-MWCNT 2205 is shown in Fig. 7.16(a), and yields R_c as the intercept of the ordinate. Instead of an array of contacts as with TLM, measurements were conducted by fixing the position of one terminal and moving the second terminal along the base to obtain d of 20 mm up to 60 mm. This procedure ensures that identical force is applied on the specimen at both terminal ends, and more importantly, is representative of the measurement procedure intended for resistivity measurements.

Measurement of R_T was performed by applying V_s of 3.05 V to the PC-MWCNT bar, providing a current density of 1 A mm^{-2} . The voltage was applied for 10 s. The experiment was conducted in increasing d in steps of 10 mm, and subsequently in decreasing steps to evaluate repeatability. The measurement at $d = 60$ mm was not repeated.



(a)



(b)

FIGURE 7.16: (a) Extrapolation method with surface contacts used to determine contact resistivity between the terminal and the PC-MWCNT specimen. (b) Total resistance of the circuit as a function of contact spacing. The solid line represents the linear regression through data of increasing and decreasing order of contact spacing

A plot of R_T as a function of d is presented in Fig. 7.16(b). The values of R_c were not significantly dependent on contact spacing measurement order. Thus, R_c is estimated from the measurements regardless of direction of contact spacing. Linear regression applied to the measurements yield $R^2 = 0.824$. At $d = 0$, the ordinate yields $2R_c = 3536 \Omega$, and hence $R_c = 1768 \Omega$. The slight variation of resistance along the length of the material may have arisen from the errors in d . The TLM employs the intercept of the abscissa, $R_T = 0$, to provide L_t . Therefore, comparison between L_t and the length of the contact, L provides an indication of the state of current flow. Current could be restricted to the edge of the contact or current may flow along L (Venugopal et al., 2010). L_t was found to be 67.6 mm that is greater than the actual L of 20 mm, suggesting that current flows along the length of the terminal.

The identical experiment could not be performed on both IM and CM dog-bone samples because CM dog-bones had a limited parallel length, l_p of constant cross section. The parallel length of IM dog-bones coincides with the minimum d of the test fixture, hence d cannot be varied in order to determine R_c using the EM method. In light of these practical issues, contact resistance was determined using the PC-MWCNT bar and the contact resistance for both CM and IM dog-bone specimens were calculated based on the specimen surface area in contact with the terminals. For the area of contact, A_c , the contact resistivity, ρ_c for PC-MWCNT bar is expressed as

$$\rho_c = R_c A_c \quad (7.18)$$

As a reminder, each terminal has two surfaces in contact with the PC-MWCNT. Therefore, A_c for one terminal is $2.4 \times 10^{-4} \text{ m}^2$. Substituting $R_c = 1768 \text{ } \Omega$ (from Fig. 7.16) and A_c into Eq. 7.18 gives $\rho_c = 0.42 \text{ } \Omega \text{ m}^2$.

The shape of CM dog-bones for determination of A_c includes the curved shoulders that complicate a physical measurement, thus A_c was determined using the computer-aided design software, Pro/Engineer. A_c for IM dog-bone in contact with the elastomer is determined by the width of the gauge length and the length of the terminal. Table 7.2 presents A_c and R_c for both CM and IM dog-bone specimens, with R_c calculated using Eq. 7.18 using ρ_c of the PC-MWCNT bar geometry.

TABLE 7.2: Contact resistance of compression moulded (CM) and injection moulded (IM) PC-MWCNT 2205 dog-bone specimens determined using Eq. 7.18 with the contact resistivity of bar geometry

Forming method	Area of contact for one terminal, A_c ($\times 10^{-4} \text{ m}^2$)	$2R_c$ (Ω)
IM	4.0	2122
CM	3.2	2627

The disadvantage of the EM method lies in: (1) the need to extrapolate data in order to obtain R_c and L_t , (2) the possibility of current crowding in the material under the contacts due to the diffusion width being smaller than the contact window (which may result of non-uniform current density leading to Joule heating), and (3) current from the terminal flowing laterally around the contacts, leading to erroneous R_c (Schroder, 2006). Errors (1) and (3) cannot be mitigated due to the design of the fixture. Error (2), however, can be checked through calculations of the energy consumption using Eq. 7.14 to estimate the possible magnitude of temperature rise. Based on the calculations, the adiabatic rise is 0.02 K, thus

error (2) is not considered. Moreover, the determination of $L_t \gg L$ presented earlier indicates that current crowding is not of concern.

7.5.1.5 Effects of contact location at the terminal and the external applied force

A batch of experiments was performed to check the effects of contact location and of the force applied on the spring loaded terminals on resistivity measurements. The experimental method and circuit configuration is identical to experiment (2), detailed in Section 7.5.1.3. A known resistance of 8000Ω is applied using the variable resistor. No repeats were performed. The use of a known resistance in these tests rather than filled PC specimens was intended to highlight the change in R as a result of the varying the contact location and of the external force.

The influence of contact location along the terminal width, W on the resistance measurements was checked by positioning the copper sheets at ~ 5 mm from the left and the right edges of the contacts. An external force of 28 N was applied through the spring loaded terminals. The change in position found R to vary by only 1%, showing that the location of the specimen along W has negligible effect on the measurements.

The influence of external force from the spring applied onto the contacts and specimen was assessed by varying the spring compression length. The lengths of the spring were determined with the specimen located in the terminals. R measurements were performed following the order of 15 mm, 18 mm and 22 mm corresponding to 28 N, 20 N and 9 N respectively. Since location was not of concern for R measurement with 28 N, the R recorded for the left edge was used in the analysis of this test. For the other external forces, R measurements were performed with the copper sheets in the centre of the terminals. It was found that reducing the force from 28 to 20 N yield no change, while further decrease in force to 9 N gave a 1% deviation in R from the previous force. The findings show that R is not sensitive to the external force applied. Subsequent measurements with PC-MWCNT 2205 were performed with a force of 28 N.

7.6 Experimental method

Following the exploratory experiments, R_c for the dog-bone specimens have been determined in Table 7.2 and R_{meter} is also known. The magnitude of the effects of thermoelectric EMF, device heating, specimen heating, specimen position and external force have been evaluated in Section 7.5.1. Repeatability of measurements using the in-house fixture has also been demonstrated. All these findings provide the confidence to employ the fixture to determine $\rho_{\text{PC-MWCNT}}$.

This study on the electrical behaviour of CM and IM PC-MWCNT is performed to understand the influence of the processing method on $\rho_{\text{PC-MWCNT}}$, and to assess the possibility of using electrical measurements as a tool to indicate the level of CNT dispersion.

CM dog-bone specimens with overall length of 75 mm (gauge length dimensions of 25 mm \times 5 mm \times 2 mm) were positioned in the fixture with the dog-bone grip section (tabs) contacting the terminals. The dog-bone tabs were placed along the length of terminals, with the flat end of the tabs aligned to the outer edges of the terminals. This was performed to locate the each specimen consistently for measurement. It should be noted that d (35 mm), is slightly greater than l_p (30 mm), giving an extension of 2.5 mm at both ends of the parallel section. Due to the small size of the CM dog-bones, it was difficult to repeatedly locate the specimens if $d = 30$ mm was employed. Using Pro/Engineer software and assuming that the curvature of the dog-bone shoulder for the extended length is a straight line, the angle between the curvature and the extended length was approximated as 4.8°. Hence, the width of the dog-bone is estimated to increase by a maximum of 0.42 mm. The dog-bone width increment is within the tolerance of the width of the gauge length (5 \pm 0.5 mm) as specified in BS EN ISO 527-2:2012 (British Standards, 2012). A constant V_s of 5 V was supplied for 20 s.

IM dog-bones have l_p of 60 mm. As the specimen is longer than the CM dog-bones, ρ measurements were performed on the parallel section of the specimens. The specimen is located in the fixture using spacers. This helps to ensure that the measurement location between specimens is maintained. Initial experiments performed with CM dog-bones showed that it was challenging to maintain a constant current density. Therefore, Eq. 7.2 is rearranged to give

$$R = \frac{\rho d}{A} \quad (7.19)$$

Substituting Eq. 7.19 into Eq. 7.1 and rearranging gives

$$\frac{V}{d} = \rho \frac{I}{A} \quad (7.20)$$

which shows that the voltage per unit length is related to the current density. In order to perform a comparative study between CM and IM specimens, the voltage per unit length for the specimens was fixed. Hence, a constant V_s of 2.86 V was supplied to IM dog-bones for 20 s, giving a voltage per unit length of 143 V m⁻¹.

For all ρ measurements, the spring loaded contacts applied a force of 28 N on each end of the specimen. R was measured at temperatures between 16 °C and 18 °C. The average current flow for the test period is computed to determine R , and the value is corrected for R_c as determined in Section 7.5.1. ρ was calculated using Eq. 7.2. A total of 5 specimens were measured for each compounding temperature, and for each forming method, and the average is reported.

Chandra et al. (2007) reported the change of volume resistivity along the length of IM samples, with typical observation of greater electrical conductivity as distance from the gate increases. Hence, a measurement of resistivity was performed in and against the direction of melt flow, by supplying a voltage of 2.86 V for 20 s to an IM specimen compounded at 230 °C in the melt flow direction and the reverse direction. No significant dependance of resistivity on flow direction was found.

7.6.1 Detecting outliers

The outliers for the data set of CM and IM specimens for each compounding temperature were determined using a formal outlier test. The test selected to analyse the R measurements, that can be approximated as a normal distribution, applies to a univariate data set where both the mean and variance of the sample are unknown. Using the Minitab software, the Anderson-Darling test (Stephens, 1974) at 5% significance level was applied to R measurements of IM PC-MWCNT 2205. The test revealed that the hypothesis of normality cannot be rejected, thus the measurements can be assumed to follow a normal distribution.

The Tietjen-Moore test (Tietjen and Moore, 1972) was used to identify a single outlier or multiple outliers in the data set of each compounding temperature. This method finds the deviations of the data points from the data mean, considering the standard deviation of the

data set. The test detects an outlier or outliers based on critical values depending on the significance levels.

A detail description of the normality and outlier tests for the R data set, with some examples, is presented in Appendix A.

7.7 Results

The resistivities of CM bars, across the compounding temperature range are presented in Fig. 7.17 with confidence levels of two standard errors. At a significance level of 5%, there were two CM specimen outliers for the compounding temperature of 230 °C, that were rejected from the data set. The lowest ρ was measured for CM specimens that were extruded at 280 °C, while the highest ρ was recorded for the compounding temperature of 270 °C. Generally, ρ increases as the extrusion temperature increases up to 270 °C. ρ decreases at 280 °C, but rises again at 290 °C. The uncertainty of ρ varies across the temperature range. There is no significant dependence of volume resistivity on compounding temperatures.

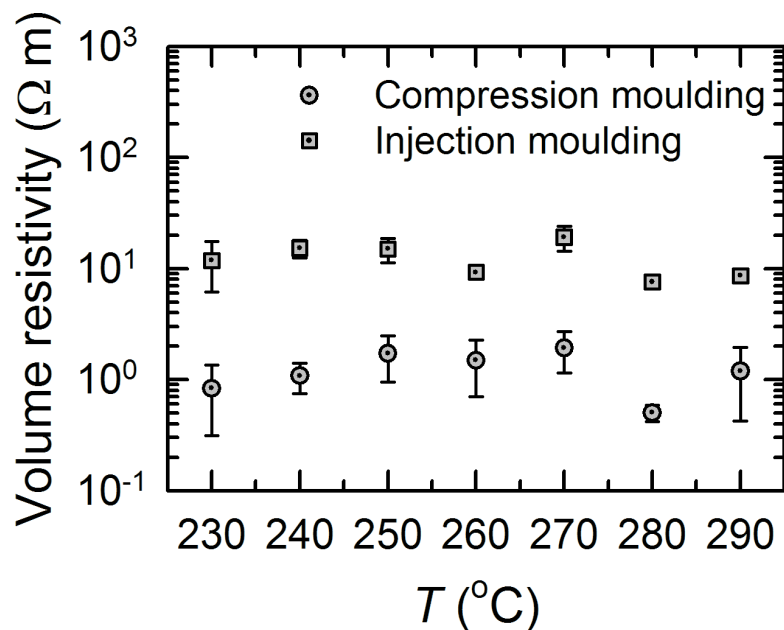


FIGURE 7.17: Electrical volume resistivity of PC-MWCNT 2205 (3 wt%) compounded at temperatures between 230 °C and 290 °C, and formed to shape by compression moulding and injection moulding

Fig. 7.17 shows measurements of ρ for IM PC-MWCNT 2205 for all extrusion temperatures. The outlier tests for 5% significance level determined one outlier for 270 °C and two outliers

for 280 °C. The minimum and maximum ρ is recorded for 290 °C and 270 °C respectively. The uncertainty of ρ generally reduced with increasing temperature. No significant dependence of ρ on the compounding temperatures was observed.

Comparing the two forming processes, ρ of CM bars is consistently lower than that of IM bars by one order of magnitude. The overall average ρ of CM and IM PC-MWCNT 2205 for all compounding temperatures is $1.26 \pm 0.80 \text{ } \Omega \text{ m}$ (\pm represents the standard deviation) and $12.20 \pm 4.58 \text{ } \Omega \text{ m}$, respectively. The uncertainty for CM PC-MWCNT 2205 is greater than for IM specimens. This may arise from the longer cooling process for CM that promotes secondary agglomeration, yielding a wider variation in the formation of a conductive CNT network compared to IM, where the CNT network is formed during rapid cooling of specimen, minimising the variability between specimens for each compounding temperature.

7.8 Discussion

IM increases ρ of PC-MWCNT 2205 by almost an order of magnitude in comparison to CM processed samples. This can be explained by the re-agglomeration of dispersed CNTs during CM (Kasaliwal et al., 2009). The increased time at high temperature allows the formation of a more percolated network in the CM bars, resulting in lower resistivity levels relative to IM PC-MWCNT. The rheological response presented in Section 5.6.2 showed that the time relaxation timescales of PC-MWCNT scale in the same way as the unfilled PC, indicating that the polymer mobility may be responsible for the CNT re-agglomeration process, as in the polymer relaxation mechanism is the dominant mechanism in PC-MWCNT. To a smaller degree, the orientation of CNTs during the IM process, results in a skin layer, as illustrated in Fig. 2.3 (Chapter 2), and contributes to the higher resistivity of IM bars. The deviation between CM and IM PC-MWCNT resistivities verify that secondary polymeric processes after compounding are critical in determining, and perhaps tailoring, the electrical behaviour of percolated thermoplastic-CNT systems.

Both ρ of CM and IM PC-MWCNT exhibited no significant dependence on the compounding temperatures. This finding is interesting as the extrusion temperature, affecting the viscosity of the matrix during compounding, is expected to lead to different levels of CNT dispersion. This in turn, determines the electrical behaviour of PC-MWCNT. Kasaliwal and co-workers (2009) found that high temperatures, when mixing in a laboratory extruder, are favourable

for obtaining lower resistivity in CM PC filled with 1 wt% CNT (close to the percolation threshold). They reported a reduction of 10 orders of magnitude in ρ as temperature increased from 240 to 260 °C. The increase in electrical conductivity was attributed to the reduced matrix viscosity, allowing it to penetrate primary CNT agglomerates and disperse the CNTs more than the higher viscosity matrix at the lower temperature. The higher temperature also promotes the formation of CNT network between the CNTs, as individual tubes or agglomerates, providing a conductive pathway in the nanocomposite.

Our findings for CM PC-MWCNT (3 wt% CNT) do not coincide with the Kasaliwal's observation on the relationship between volume resistivity and compounding temperature. An explanation is that the filler concentration in this work is above the electrical percolation threshold, which is reported in the literature to be in the range of 1 - 2 wt% (Bauhofer and Kovacs, 2009; Castillo et al., 2011), for comparable systems. This implies that a conductive network structure is more easily established within the matrix. Therefore, the lack of variability of ρ between the extrusion temperatures can be attributed to the presence of several conductive pathways within the matrix. Section 5.4.1 showed that the formation of the CNT network in PC melt is as a function of time (see Fig. 5.2). As such, the conductivity of CM specimens is expected to be higher than that of IM specimens, given that the CM has a slower cooling rate in comparison to IM.

We cannot discount that the state of CNT dispersion could vary with compounding temperature. However, the resistivity measurements suggests that the secondary processes, both CM and IM are not dependent on the temperature and shear history of the compounding procedure, resulting in similar ρ across the compounding temperature range investigated. Therefore, controlling or tailoring the electrical properties of percolated PC-MWCNT systems have to be achieved through manipulation of the secondary process parameters.

The volume resistivity of CM PC-MWCNT 2205 compounded at various temperatures are compared to resistivity values of other similar systems in Table 7.3. All PC-MWCNT systems from the literature in Table 7.3 are filled with 3 wt% commercial grade MWCNTs, with the exception of Spikowski's work, where information on the origin of the CNTs was not available. Castillo et al. (2011) evaluated the influence of five commercially available MWCNTs on PC-MWCNT electrical conductivity; one of the MWCNTs grades (NC7000) is identical to that used in this work. Castillo and co-workers obtained resistivity values lower than those reported in this work, by approximately an order of magnitude. The discrepancy could be

due to the measurement technique. This is supported by Spikowski and Kunzelman (2012) who employed the same measurement method as that used in this work (that is, to use surface contacts in the two-terminal configuration) and reported similar ρ to the values obtained in this work for CM specimens. Overall, there is good agreement between the reported literature values for CM PC-MWCNT and the measured volume resistivities of this work.

TABLE 7.3: Electrical resistivity of compression moulded PC-MWCNT (3 wt%)

Measurement method	Volume resistivity (Ω m)	Reference
Four-terminal	0.5	Pötschke et al. (2005)
	0.5	Socher et al. (2012)
	0.2	Kasaliwal et al. (2009)
	0.1	Pötschke et al. (2005)
	0.05 - 0.2	Castillo et al. (2011)
Two-terminal	~ 10	Abbasi et al. (2009)
	$\sim 0.4 - 1.6$	Spikowski and Kunzelman (2012)
	0.5 - 2	This work

Table 7.4 compares the volume resistivity of IM PC-MWCNT 2205 to the resistivity values of other similar systems recorded in the literature. The findings for IM PC-MWCNT 2205 are in agreement with the measured resistivity values reported by Mack and co-workers. Table 7.4 shows that there is a wide variation, up to 11 orders of magnitude, between resistivities of comparable systems of PC filled with 3 wt% MWCNTs. Perhaps the deviation is not surprising considering that Villmow's group reported ρ variations of up to 6 orders of magnitude for the same PC-MWCNT (2 wt%) system but with different IM processing conditions. The discrepancy of ρ for percolated PC-MWCNT in the references, emphasizes the sensitivity of ρ to the IM parameters.

TABLE 7.4: Electrical resistivity of injection moulded PC-MWCNT (3 wt%) determined with two-terminal method

Volume resistivity (Ω m)	Reference
$10^8 - 10^{10}$	Rios et al. (2011)
10^7	Abbasi et al. (2009)
$10^3 - 10^7$	Spikowski and Kunzelman (2012)
$10^3 - 10^4$	Chandra et al. (2007)
0.7 - 20	Mack et al. (2012)
~ 0.14	Lew et al. (2011)
9 - 15	This work

It should be highlighted that both Lew et al. (2011) and Mack et al. (2012) used the same MWCNTs grade (NC7000). This suggests that NC7000 MWCNTs yields the lowest ρ in PC-MWCNT systems among the CNTs available commercially. The same observation of

NC7000 obtaining the lowest ρ was also reported for a different matrix, PA 12, by Socher et al. (2011). Differences in the CNT grade may also contribute to the discrepancy in ρ in Table 7.4, as observed by Castillo et al. (2011).

The variation in resistivity values reported in Tables 7.3 and 7.4 is attributed to material- and process-related factors, and to measurement methods. Material related factors include CNT dimensions and CNT purity, which can vary between CNT manufacturers, and ultimately influence the electrical conductivity. Process related factors concern with the parameters of the melt mixing processes for compounding and moulding of test specimens. These parameters can consist of, and are not limited to, the melt temperature, screw speed, screw configuration, injection temperature and injection speed. These factors all play a role in the morphology of the CNT network, the level of CNT dispersion, CNT orientation and eventual CNT-CNT interactions that determine the electrical conducting pathway. Our study suggests that extrusion parameters do not have a significant effect on percolated CNT systems, but nevertheless that the final electrical properties are strongly dependent on the type of forming processes.

It should be mentioned that there have been limited reports of the measurement of ρ IM PC-MWCNT using the four-terminal method. Kasaliwal (2011) attempted the four-terminal method on IM PC-MWCNT (3 wt%) sheets but was limited by the capability of their measuring fixture. Spikowski and Kunzelman (2012) produced IM PC-MWCNT bar specimens but only reported ρ IM PC-MWCNT (5 wt%) discs measured with four-terminal method using surface and point probes. ρ measurements using the point probes were not attainable for discs obtained at high injection speed (76.2 mm s^{-1}), attributed to significant skin layer effect (Spikowski and Kunzelman, 2012). This effect was reduced with the increase of moulding temperature, and can be explained by the re-agglomeration of CNTs driven by polymer mobility as the disc cools.

Another disadvantage of using the four-terminal method is that the ρ in measurements are localised to the location of the probes, and thus, may not be representative of the bulk property of IM samples. A more reliable bulk measurement for IM specimens is obtained using the two-terminal method, as the surface contact probes are less sensitive to the skin effect. The disadvantage of using two-terminal configuration with surface contacts is the inability of the technique to detect variations of resistivity as the distance from the gate of the specimen increases. For example, both Chandra et al. (2007) and Spikowski and Kunzelman

(2012) found that resistivity typically decreases as distance from the gate increases, while Chandra et al. (2007) even reported variations across the width of the specimen. However, both studies had to machine or fracture their specimens in order to detect the variability in electrical resistivity. Hence, there is still value in measuring ρ with the surface contact technique, particularly when a non-destructive and rapid method is desired for purposes such as screening or comparison studies.

7.9 Conclusions

This chapter has presented the various resistivity measurement methods, the design and development of in-house resistivity fixtures, the exploratory experiments of the methods and the validation of the two-terminal method to measure resistivity of the materials in this study. The influence of compounding temperatures on the volume resistivity of PC-MWCNT 2205, formed by CM and IM processes, was investigated.

Section 7.2 introduced the different resistivity measurement methods for measuring volume resistivity and highlights each method's advantages and deficiencies. Section 7.3 has described the design and construction of a two-terminal fixture to measure resistivity of PC-MWCNT. The technical details of the fixture are presented in Section 7.3.1. The sources of error that affect electrical measurements, which can be divided into circuit-related and instrument-related factors, are outlined in Section 7.4. The section also includes the steps taken to reduce such errors in the fixture and the measurement procedure.

Potential sources of error for the two-terminal method such as thermoelectric effect, specimen heating and contact resistances were quantified in Section 7.5.1. Conductive elastomers were employed to ensure good surface contact between the two rigid bodies, PC-MWCNT and copper contacts. Comparison studies between known resistance loads and resistance measurements were conducted to validate the fixture. Contact resistivity arising between the terminals and specimens were determined in Section 7.5.1.4 using a hybrid of methods: EM method employing surface contacts (TLM method). This was performed with a PC-MWCNT bar due to the limitations of the fixture to accommodate dog-bone specimens for the hybrid method procedure. The contact resistance of dog-bone specimens were calculated based on the contact area between the terminal surface probes and the specimen.

Section 7.7 presented the resistivity measurements of PC-MWCNT 2205 showing an order of magnitude deviation between CM and IM. The overall volume resistivity of CM and IM samples recorded an average of 1.26 ± 0.80 and $12.20 \pm 4.58 \text{ } \Omega \text{ m}$ respectively. This can be explained by the re-agglomeration of CNTs and time-dependent build-up of the CNT conductive network during compression moulding that is most likely driven by polymer mobility, evidenced from the rheological investigation in Chapter 5. A smaller effect contributing to the higher ρ of IM PC-MWCNT is due to the oriented CNTs at the regions close to the mould wall (i.e. skin effect). The findings highlight the effect of shear rates and rapid cooling on the formation of the conductive CNT network structure in a percolated thermoplastic-MWCNT system. It was found that both forming process exhibited no significant dependence of ρ on the compounding temperatures. This is attributed to the multiple conductive pathways present in the percolated PC-MWCNT system. This suggests that the secondary process parameters play a greater role than compounding conditions, in determining or tailoring the electrical behaviour of these filled systems.

Chapter 8

Mechanical properties

The previous chapter has studied the effects of melt processing on the electrical resistivity of PC-MWCNT. This chapter investigates the influence of processing on the mechanical properties of PC-MWCNT, employing the specimens from the previous chapter. The raw materials were compounded between the temperatures of 230 and 290 °C, in 10 °C increment steps. Solid specimens were subsequently formed by injection moulding (IM) and by compression moulding (CM). The variation of extrusion temperatures and use of conventional moulding methods to produce the nanocomposite helps to relate the effects of flow and temperature history to the mechanical properties in percolated PC-MWCNT systems. The applicability of a well known micromechanical model to predict the modulus of CM and IM PC-MWCNT is then evaluated. The correlation between the mechanical properties and the electrical resistivity (as reported in Chapter 7) of the material formed by CM and IM are examined.

8.1 Introduction

Mechanical properties are crucial in determining application and performance envelopes for nanocomposites. The opportunity to exploit the high stiffness and strength of CNTs, in addition to the electrical conductivity of PC-MWCNT, has been the subject of interest to researchers and industry alike. While electrical properties of PC-MWCNT stem from the formation of a CNT network structure consisting of single CNTs or CNT agglomerates within the matrix, mechanical properties are achieved with good dispersion of individual CNTs in

the matrix. Individualised nanotubes increases the CNT surface area available for wetting by the matrix. This leads to an increase of CNT-matrix interaction and facilitates the efficient load transfer from the matrix to the CNTs.

Alig and co-workers (2012) determined that electrical conductivity of PC-MWCNT systems increases with CNT agglomeration. However, the enhancement of mechanical properties of CNT-nanocomposites arises from the tensile properties of the individual CNT and from the large surface area to volume ratio of the individual tubes. Hence, a balance is often necessary if a specific mechanical performance and electrical conductivity is required.

Alig et al. (2012) studied the dependence of electrical conductivity of thermoplastic-CNTs during melt deformations and postulated that there is competition between the shear-induced destruction and formation of a CNT network. The same group also highlighted that secondary agglomeration of CNTs is a thermally activated process that can be accelerated by shear flow. It is this same network that provides the mechanical reinforcement of the CNT-thermoplastic system. Achieving optimal CNT dispersion in the matrix through melt polymeric processes is challenging. CNT functionalisation may be employed to improve CNT dispersion in the matrix, but it is often not economical. Moreover, if specific electrical properties are required, then the filler concentration must be above the percolation threshold. CNT agglomeration increases with higher filler concentration. Hence, there is a need to address how existing processing methods can be tailored, to control the final mechanical properties of percolated CNT-thermoplastic systems for commercial application.

Our process uses compounded feedstock (pellets), re-melted to form the material to shape. Different stages of this process impose different levels of shear rate, as indicated in Table 8.1.

TABLE 8.1: Typical shear rates for polymeric processes (Mezger, 2011)

Process	Shear rates (s^{-1})
Extrusion (compounding)	10 - 10^3
Injection moulding	10^3 - 10^4
Compression moulding	1 - 10

To date, much research into the mechanical properties of PC-MWCNT systems have focused on the CNT loading content (Abbasi et al., 2009; Castillo et al., 2011; Eitan et al., 2006; King et al., 2012; Liu et al., 2010). These authors have prepared tensile testing specimen using various methods such as small batch mixing (Castillo et al., 2011), twin-screw extrusion

(Abbasi et al., 2009; King et al., 2012; Liu et al., 2010), CM (Castillo et al., 2011; Eitan et al., 2006; Liu et al., 2010), conventional IM (King et al., 2012), and micro-IM (Abbasi et al., 2009; Eitan et al., 2006).

Efforts to enable the commercialisation of these materials, with an emphasis on mechanical reinforcement, are beginning to garner more interest. Rios et al. (2011) investigated the influence of IM parameters of PC-MWCNT, as reviewed in Section 2.5.3.2. More recently, Mack and co-workers (2012) studied the influence of varying the compounding parameters on an industrial-scale twin screw extruder on the tensile properties of injection moulded specimens. They focused on the screw speed, screw design and throughput of the process parameters. Lower speed and higher throughput tended to yield lower mechanical properties, whilst screw design had no significant effect. The group also reported that increasing the filler concentration from 1 to 5 wt% increased the elastic modulus and tensile strength of PC-MWCNT.

This chapter investigates the influence of varying compounding temperatures of PC with a fixed MWCNT concentration of 3 wt%, formed by CM and IM, on the hardness and the tensile mechanical properties.

8.2 Specimen preparation for mechanical testing

A range of PC-MWCNT 2205 samples were extruded by Nanocyl S.A. at a range of temperatures, between 230 °C and 290 °C (at increments of 10 °C) under otherwise identical processing conditions and pelletised.

The materials were processed into dog-bone specimens for mechanical testing using two forming methods, IM and CM. Details of the procedures and conditions for both moulding methods are described in Section 3.3. As a reminder, the IM dog-bones were manufactured by Nanocyl S.A. while CM dog-bones were manufactured in-house with a flash mould. Comparison of these two families of materials facilitates (1) the understanding of the effects of polymer and filler orientation on mechanical properties and (2) whether the melt compounding history followed by remelting and reforming using different methods influences the end properties. The size of the CM specimens is limited by the dimensions of the heated press. Hence, a flash mould with removable inserts was designed to manufacture smaller samples

(length = 75 mm, thickness = 2 mm), 50% of the linear dimensions of the IM dog-bones, according to BS EN ISO 527-2:2012 (British Standards, 2012).

8.3 Vickers hardness

Hardness is the resistance of a material to deformation (Herrmann, 2011). The Vickers hardness method was used to determine the surface hardness of the IM and CM PC-MWCNT specimens. This procedure uses a diamond pyramid with a square base as the indenter. The opposite faces of the indenter are separated by an angle of 136° . Vickers hardness, HV, is calculated as the ratio of the applied indentation force, F_i , to the surface area of the indentation, A , as

$$HV = \frac{F_i}{A} \quad (8.1)$$

The units used for F_i in Eq. 8.1 are kilogram-force, kgf which can be converted to N by multiplying by standard gravity (9.8066 ms^{-2}). In this work, the units for HV are expressed as kgf mm^{-2} , to distinguish the measured values from other hardness methods such as Brinell, Rockwell and Shore hardness.

Fig. 8.1 illustrates typical micrographs of an indented surface of filled and unfilled CM dog-bone specimens.

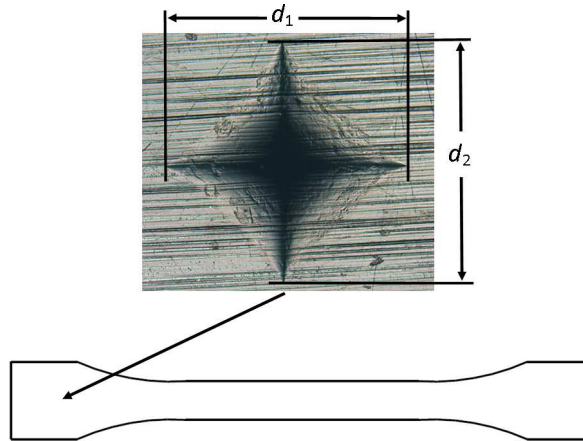


FIGURE 8.1: The location of hardness measurement of a CM dog-bone specimen with an inset of an optical micrograph at 10x magnification in reflection mode, exhibiting an indentation for PC-MWCNT 2205 obtained with 5 kgf (49.03 N). The diagonal lengths, d_1 and d_2 are used to calculate Vickers hardness

A , in mm^2 , is approximated using the arithmetic mean value, d of the diagonal lengths, d_1 and d_2

$$A = \frac{d^2}{2 \times \sin \frac{136^\circ}{2}} = \frac{d^2}{1.854} \quad (8.2)$$

The typical indentation depth for pure PC and PC-MWCNT is ~ 0.16 mm.

8.3.1 Method

A 5 kg weight is applied for 15 s. d_1 and d_2 were measured within a few minutes of the indentations using an ocular device. Three conditions were imposed to ensure that indentations for hardness measurements are valid: (1) the depth of penetration, D_p is sufficiently smaller than the specimen thickness, t ($D_p > \frac{t}{7}$), (2) the distance of the indentations from the edges of the dog-bones is $> 2.5d$; and (3) the distance between repeated indentations is at least $3d$.

Indentations were performed on the grip section of the dog-bones, as illustrated in Fig. 8.1, so that the same dog-bones could subsequently be used for tensile tests. A minimum of four indentations were performed on each specimen, giving a total of 20 measurements for each compounding temperature for the corresponding forming method. The average HV for each compounding temperature is reported. Error bars and \pm represent two standard errors, unless specified otherwise.

8.3.2 Results and discussion

Fig. 8.2 presents the average Vickers hardness for CM PC-MWCNT 2205 as a function of the melt compounding temperature. Generally, HV decreases as the compounding temperatures increases. There is a slight increase of 1% at 250 °C from the previous temperature before decreasing to a minimum at 270 °C ($15.26 \pm 0.17 \text{ kgf mm}^{-2}$). HV then increases at 280 °C and 290 °C. The maximum HV of $15.57 \pm 0.04 \text{ kgf mm}^{-2}$ is obtained for PC-MWCNT processed at 230 °C. The hardness of PC-MWCNT 2205 across the compounding temperature range changes by around 3%.

For comparison, HV of unfilled CM PC 2205 is measured as $15.08 \pm 0.20 \text{ kgf mm}^{-2}$. All CM PC-MWCNT 2205 materials recorded higher HV relative to the unfilled CM PC 2205. This is attributed to the presence of CNTs, increasing the stiffness of the surrounding matrix.

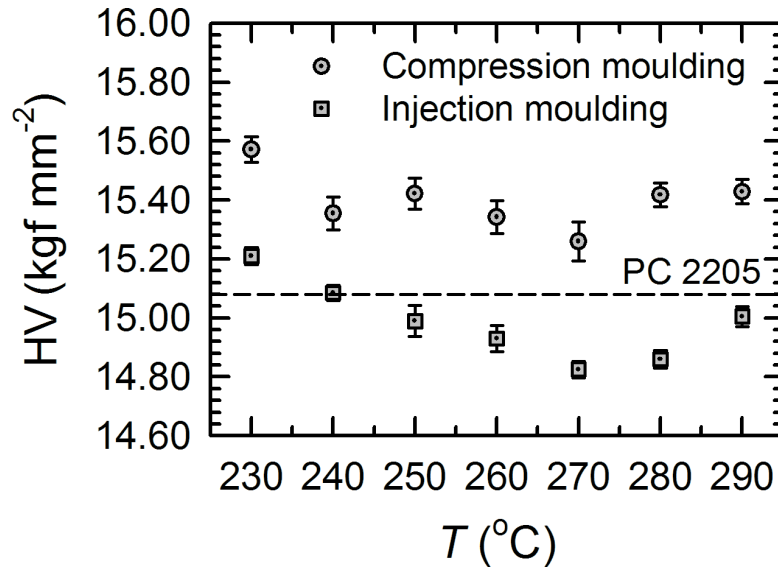


FIGURE 8.2: Vickers hardness of compression moulded and injection moulded PC-MWCNTs 2205 compounded at temperatures between 230 °C and 290 °C, the error bars represent two standard errors. The dashed lines represents the Vickers hardness of compression moulded unfilled PC 2205

The change in HV with the addition of CNTs is not substantial, increasing only by 1 to 3%. Liu et al. (2010) reported an increase in Shore hardness of $\sim 11\%$ for CM PC-MWCNT with comparable filler concentration. The discrepancy between the referenced work and our measurements could be due to differences in MWCNT manufacturer and compounding parameters; Liu and co-workers' employed small batch mixing to produce PC-MWCNT.

The limited hardness difference relative to the unfilled PC could be attributed to (1) agglomeration of the CNTs (likely promoted by the percolated nanocomposite systems and driven by the polymer mobility) yielding poor CNT dispersion in the matrix leading to softer matrix-rich regions, and (2) poor interfacial bonding between the CNT and the polymer chains resulting in ineffective stress transfer from the matrix to the stiffer CNTs. The overall average of HV for CM PC-MWCNT 2205 is 15.41 ± 0.17 kgf mm⁻² (\pm represents the standard deviation). The observation that we can make with the results is that the addition of CNTs above the percolation threshold, at processing conditions used in this work, yields a small change in HV as evidenced by the low deviation of HV measurements.

Fig. 8.2 presents the HV of IM PC-MWCNT 2205 as a function of the compounding temperature. The hardness decreases as the compounding temperature increases from 230 to 270 °C, and subsequently increases up to 290 °C. PC-MWCNT processed at 230 °C corresponds to the maximum HV of 15.21 ± 0.06 kgf mm⁻² whereas the minimum HV of

$14.83 \pm 0.07 \text{ kgf mm}^{-2}$ is measured for filled PC processed at $270 \text{ }^\circ\text{C}$. There is a difference of 3% between the maximum and minimum values, with an overall average of $14.99 \pm 1.43 \text{ kgf mm}^{-2}$ (\pm represents standard deviation). The decreasing and increasing trend of HV is not currently understood.

Across the compounding temperature range, CM results in a higher hardness relative to IM samples, seen in Fig. 8.2. This is attributed to alignment of CNTs in the direction of flow, induced by the high shear rates and fast cooling rates of IM, particularly at the surfaces of the mould. Villmow et al. (2008a) observed, for similar nanocomposite systems to this study, that the highest degree of CNT orientation during IM occurs on the surfaces of the moulded part. Since the indentations are performed on the surface of the specimens, that is, in a direction perpendicular to the flow direction, the indenter load is applied perpendicular to oriented CNT tube axes, leading potentially to bending of the nanotube. The long and thin CNTs are much more compliant in bending than to axial deformation.

All of IM PC-MWCNT 2205 except for that compounded at $270 \text{ }^\circ\text{C}$ recorded a lower hardness in comparison to CM PC 2205. One explanation for the difference is the orientation of the polymer chains in the IM samples. We cannot discount the possibility that the CNTs were well dispersed after compounding and pelletising, but our findings suggests that the secondary processes plays a greater role in determining the surface hardness of percolated PC-CNT systems than the compounding stage.

8.4 Tensile testing

Tensile testing is a method of measuring the material's elastic Young's modulus (E) and the ultimate tensile strength (UTS) in response to uniaxial tensile forces. E is determined from the gradient of the stress-strain relationship within the linear region. UTS is determined as the maximum nominal stress the specimen can withstand prior to failure.

The dog-bone specimen shape has two shoulders separated by a gauge length with a reduced and parallel width, providing a uniform cross sectional area. Dog-bone specimens were used to investigate tensile properties because the geometry promotes failure to occur at the gauge section.

8.4.1 Method

Gripping of the specimen during the test must be sufficient to prevent to slippage or breaking of the specimen in or close to the grip section. Mechanical wedge action jaws were used to provide increasing gripping pressure with cross head displacement, obtaining a firm grip during testing. The serrated grip faces helps to avoid slippage.

Each specimen was mounted at the top jaw first and aligned to the longitudinal axis of the tensile machine by visual inspection prior to gripping the bottom of the specimen. Alignment of the specimen to the testing machine prevents bending moments or side loading on the specimen.

Strain was measured at the specimen gauge section using a static axial clip-on extensometer. It was positioned to align with the centre line of specimen. The extensometer has a low operating-force arm to maintain the knife-edge position on the specimen in order to decrease the likelihood of the extensometer slipping during testing.

Tensile testing was performed with an Instron 5968. A load cell of 5 kN was used for all tests. Tests were performed at a strain rate of $5.56 \times 10^{-4} \text{ s}^{-1}$, corresponding to a cross-head speed of 1 mm min^{-1} and 2 mm min^{-1} , for CM and IM dog-bone specimens respectively. A 25 mm and 50 mm gauge length extensometer was used to measure strain of CM and IM dog-bone specimens. Five specimens for each forming method and for each compounding temperature across range of 230 to 290 °C were tested. All tensile measurements were performed at ambient temperature.

E of filled PC were determined between 0.1 and 0.45% strain. As IM bars of unfilled PC were not available, only E of CM PC 2205 was determined between 0.1 and 1.0% strain, for five specimens. The strain range of the filled and unfilled PC differs because the linear region of the stress-strain relationship for CM PC 2205 is greater than that of PC-MWCNT. Error bars and \pm represent two standard errors unless specified otherwise.

8.4.2 Results and discussion

8.4.2.1 Young's modulus

The effect of compounding temperature on E of CM PC-MWCNT 2205 is presented in Fig. 8.3. There is no significant change in modulus across the temperature range investigated. The Young's moduli measured are between 2420 and 2459 MPa, corresponding to a difference of 5% between the minimum and the maximum measured values. E of unfilled CM PC 2205 was measured as 2236 ± 2 MPa. The addition of CNTs (3 wt%) into PC increased E by up to $\sim 10\%$.

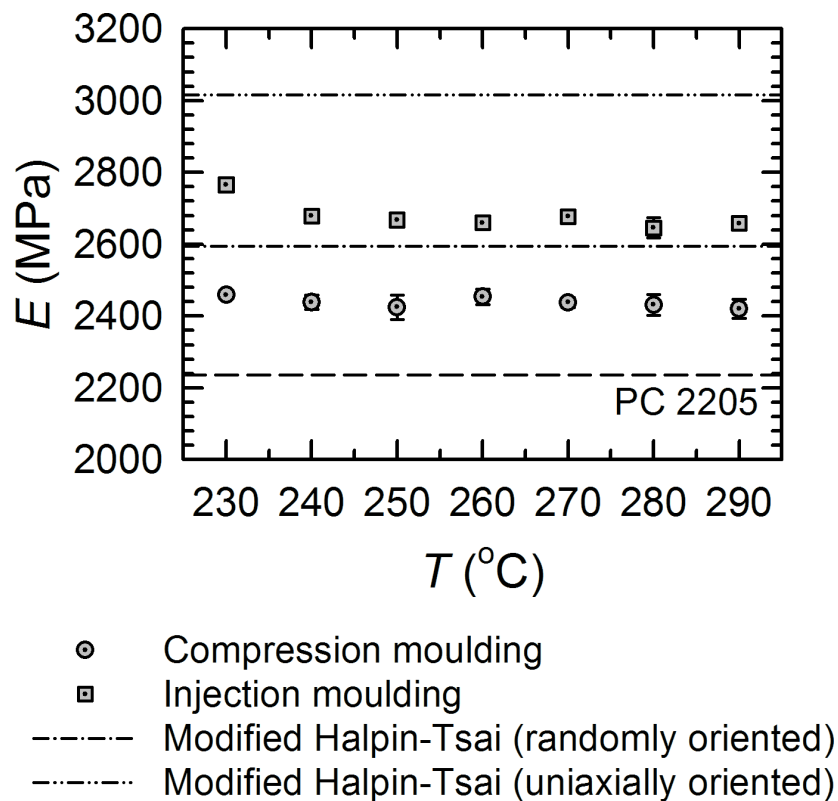


FIGURE 8.3: Young's moduli of compression moulded and injection moulded PC-MWCNTs 2205 compounded between 230 °C and 290 °C. The dashed lines represent the unfilled compression moulded PC 2205. The dashed-dot line represents the modified Halpin-Tsai equation for randomly oriented CNTs whereas the dashed-dot-dot line represents the modified Halpin-Tsai equation for highly oriented CNTs

Fig. 8.3 presents E of IM PC-MWCNT 2205 as a function of compounding temperature. The Young's moduli were measured to be in the range of 2645 to 2765 MPa. The data exhibits a slight decrease of 3% in E as the compounding temperature increases from 230 to 240 °C. Above 240 °C, there is no significant change in E as the compounding temperature increases.

There is a reduction of 4% between the minimum and maximum modulus, occurring at 230 °C and 280 °C respectively.

Fig. 8.3 shows that the moduli of IM PC-MWCNT are consistently higher than those of CM PC-MWCNT for the range of compounding temperature investigated. This can be explained by the CNT's orientation, parallel to the direction of the applied uniaxial force, providing a degree of reinforcement. The effects of molecular orientation of the PC in IM PC are small (Engels et al., 2009). Therefore, the change in modulus of PC-MWCNT relative to the unfilled is attributed to the presence of rigid oriented nanotubes and to the CNT network structure formed within the matrix during melt processing.

The moduli for both CM and IM samples were found to change by up to 5% between the minimum and maximum modulus across the extrusion temperature. The optical micrographs in Section 6.2.1.3 shows that the percolated PC-MWCNT system and the absence of CNT surface modification results in the agglomeration of CNTs in the matrix. The CNT agglomerates reduce the surface area of CNTs in contact with the polymer matrix, thus decreasing the stress transfer efficiency between matrix and CNT. In addition, Section 6.2.2 shows suspected voids in IM specimens that promotes the mechanical failure, resulting in a lower moduli. Even though there may be differences in the level of CNT dispersion between the compounding temperatures prior to forming, our findings reveal that the long times at moulding temperature for CM and the pressure driven quenching for IM, could result in similar agglomeration for the specific forming process, resulting in the similar moduli found for percolated PC-MWCNT systems across the compounding temperature range.

Therefore, we can observe two effects that influences E of percolated PC-MWCNT systems: (1) orientation of CNTs in the PC matrix and (2) the slow or fast cooling that determines the CNT network structure.

8.4.2.2 Ultimate tensile strength

All PC-MWCNT (3 wt%) samples, regardless of compounding temperature or forming method, failed by brittle fracture. There is no evidence of strain hardening in the filled PC, as observed in unfilled CM PC 2205. Since PC-MWCNT is brittle, the UTS coincides with the fracture point. However, for the unfilled PC, UTS relates to the maximum nominal stress in the plastic deformation region.

The effects of compounding temperature on the UTS of CM PC-MWCNT are presented in Fig. 8.4. UTS was observed to be more sensitive to extrusion temperatures than E . UTS for filled PC mixed at 230 °C decreased at 240 °C, before increasing up to a maximum at 270 °C. The minimum UTS is recorded for 280 °C before rising again at 290 °C. There is a significant (22%) change between the lowest UTS of 31.2 ± 3.0 MPa and highest UTS of 39.4 ± 1.2 MPa. The UTS recorded for unfilled CM PC 2205 is 53.0 ± 5.8 MPa, and failed by ductile fracture. The presence of 3 wt% CNTs in PC reduces the UTS of the matrix by up to 26% and transits the fracture behaviour of PC from ductile to brittle.

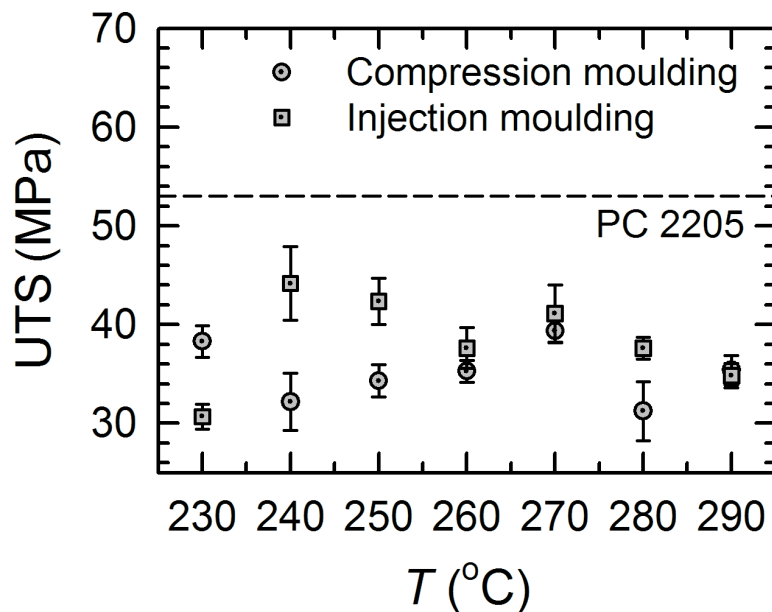


FIGURE 8.4: Ultimate tensile strength of compression moulded and injection moulded PC-MWCNT 2205 compounded between 230 °C and 290 °C. The dashed lines represent the unfilled compression moulded PC 2205

The influence of compounding temperatures on IM processed samples on UTS is presented in Fig. 8.4. UTS for filled PC increases substantially from 230 °C to the maximum value within the range, at 240 °C and, after this, decreases with increasing compounding temperature, with a slight exception at 270 °C. There is an increase of 34% between the minimum and the maximum UTS recorded for varying compounding temperatures.

UTS of CM and IM samples are comparable, with an overall average of 35.6 ± 4.3 MPa (CM) and 38.3 ± 6.4 MPa (IM), where \pm represent the standard deviation. UTS measured for IM PC-MWCNT compounded at 230 °C and 290 °C were lower than those of CM PC-MWCNT, implying that these particular IM samples are more brittle. This may have been

caused by minor defects and voids within the solid specimens, observed in Section 6.2.2, that contributed to the decrease in tensile strength.

8.4.2.3 Orientating the nanocomposites

In an attempt to produce oriented PC-MWCNT specimens, a limited number of specimens were stretched by uniaxial melt drawing. CM PC-MWCNT 2205 (extrusion temperature of 280 °C) bars, 60 mm × 5 mm × 0.9 mm, were pneumatically gripped in an Instron 5985 fitted with an environmental chamber. The draw temperatures, measured using a thermocouple positioned close to the grip section, ranged between 150 and 165 °C, in 5 °C increments. For all tests, the grip separation was 50 mm and a gauge length of 20 mm was marked on each specimen with a silver marker pen before stretching to confirm the draw ratio after stretching. All the specimens were drawn at a nominal strain rate of 0.02 s⁻¹, to a fixed draw ratio, λ of 2. A freezer spray was used to quench the material at the end of stretching prior to releasing from the grips (De Focatiis et al., 2010). Selected specimens are shown in Fig. 8.5.

Uniform oriented unfilled PC specimens were produced from CM bars, through stable necking, at a temperature of ~150 °C, with a nominal strain rate of 0.02 s⁻¹ and for $\lambda = 2$ and 3. In contrast to the unfilled PC, stretching the of PC-MWCNT was challenging as shear bands formed on all specimens for the range of temperature explored. The localisation of strain shows that the specimens could not be uniformly oriented for subsequent tensile testing. Therefore, the formation of shear bands during the production of oriented PC-MWCNT may be attributed to the rigid nanotubes, resulting in inhomogeneous deformation of the material.

8.4.3 Models for the prediction of Young's modulus of PC-MWCNT

A common approach to predict E of reinforced materials is to use micromechanical modelling, extensively employed in traditional fiber composite systems. Several studies have approached nanocomposites in a similar manner. One widely used method of predicting the elastic modulus of nanocomposites is the Halpin-Tsai equation, described in Section 2.5.3.3. The Halpin-Tsai is a two-phase model that takes into account the geometry and volume fraction of the filler phase. The former is an important factor as the high surface to volume ratio of CNTs

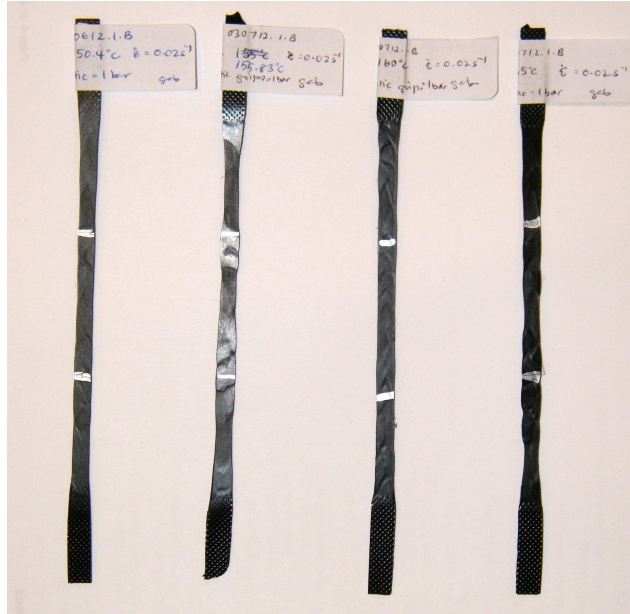


FIGURE 8.5: Uniaxial melt drawn CM PC-MWCNT 2205 (from left to right) at 150 °C, 156 °C, 160 °C and 165 °C with a nominal strain rate of 0.02 s⁻¹ and a $\lambda = 2$

provides greater interaction between CNT and matrix, thereby increasing the effectiveness of reinforcing the matrix. The Halpin-Tsai equation assumes strong interfacial bonding between the filler and matrix, as well as a homogenous distribution of the filler in the matrix.

The Halpin-Tsai equation was developed for the prediction of elastic properties of traditional fiber composites, and has been applied to both random and highly oriented CNT nanocomposites. In the case of fiber composites, the filler particles (fiber) can be thought of as solid cylinders or rods in the model. However, MWCNTs are hollow structures. As such, Thostenson and Chou (2003) modified the Halpin-Tsai equation to account for the nanotube structure by assuming that the outer nanotube wall alone acts as a solid fiber, supporting the loads applied.

8.4.3.1 Uniaxially oriented CNT nanocomposite

The Halpin-Tsai equation for filled systems with fillers perfectly oriented in the loading direction is

$$E = E_{\text{matrix}} \frac{1 + \zeta \eta V_{\text{fiber}}}{1 - \eta V_{\text{fiber}}} \quad (8.3)$$

in which

$$\eta = \frac{\frac{E_{\text{fiber}}}{E_{\text{matrix}}} - 1}{\frac{E_{\text{fiber}}}{E_{\text{matrix}}} + \zeta} \quad (8.4)$$

where ζ is a filler geometry parameter, E is the elastic modulus and V is the volume fraction. For low volume fractions, ζ is expressed as

$$\zeta = 2 \frac{l_{\text{fiber}}}{d_{\text{fiber}}} \quad (8.5)$$

where d_{fiber} is the diameter of the fiber and l_{fiber} is the length of the fiber.

The effective elastic modulus of the fiber, E_{fiber} can be related to the nanotube modulus, E_{CNT} through their cross sectional areas, A , under constant strain conditions, as the same external force is applied, giving (Thostenson and Chou, 2003).

$$E_{\text{fiber}} = \frac{A_{\text{CNT}}}{A_{\text{fiber}}} E_{\text{CNT}} \quad (8.6)$$

Considering the diameter of the CNT, d_{CNT} and the thickness of a CNT outer wall, t , Eq. 8.6 can be expressed as

$$E_{\text{fiber}} = \frac{4t}{d_{\text{CNT}}} E_{\text{CNT}} \quad (8.7)$$

Substituting Eqs. 8.5 and 8.7 (determined with d_{CNT} and CNT length, l_{CNT}) into Eq. 8.3, the modified Halpin-Tsai for highly aligned nanocomposites is

$$E = E_{\text{matrix}} \left(\frac{1 + \frac{2l_{\text{CNT}}}{d_{\text{CNT}}} \left(\frac{\frac{E_{\text{CNT}}}{E_{\text{matrix}}} - \frac{d_{\text{CNT}}}{4t}}{\frac{E_{\text{CNT}}}{E_{\text{matrix}}} + \frac{l_{\text{CNT}}}{2t}} \right) V_{\text{CNT}}}{1 - \left(\frac{\frac{E_{\text{CNT}}}{E_{\text{matrix}}} - \frac{d_{\text{CNT}}}{4t}}{\frac{E_{\text{CNT}}}{E_{\text{matrix}}} + \frac{l_{\text{CNT}}}{2t}} \right) V_{\text{CNT}}} \right) \quad (8.8)$$

Thostenson and Chou showed that Eq. 8.8 is in agreement with experimental measurements of E in stretched PS-MWCNT films at 5 wt% and 10 wt% loading, and that the elastic modulus is particularly sensitive to CNT diameter. Other systems have been compared the modified Halpin-Tsai (injection moulded PP-MWCNT for a greater range of filler loadings between 0.5 up to 5 wt%) and found the model to either agree with or to overestimate the modulus (Bhuiyan et al., 2013). The overestimation of E by the Eq. 8.8 for Bhuiyan's work is expected as IM produces a range of CNT alignment, with highest degree of aligned CNTs is found primarily at and close to the surfaces of the specimens (see Fig. 2.3). Therefore, we can assume that our IM samples also have a wide range of CNT alignment.

The modified Halpin-Tsai for highly oriented fillers is applied to PC-MWCNT to determine the upper bound of E that can be achieved through IM. The constants used are $E_{\text{matrix}} = 2236$ MPa (measured from CM PC 2205), $E_{\text{CNT}} = 450$ GPa¹ (Pan et al., 1999), $l_{\text{CNT}} = 418$ nm and $d_{\text{CNT}} = 10$ nm (Krause et al., 2011); and $V_{\text{CNT}} = 0.017$ (calculated using $\rho = 2.09$ g cm⁻³ as determined in Chapter 3). Using these values in Eq. 8.8 yields $E = 3017$ MPa. The average modulus for IM PC-MWCNT, over the range of compounding temperatures tested, is 2679 ± 50 MPa (\pm representing standard deviation). The model estimates the upper bound to be $\sim 13\%$ higher than the average measured E of IM PC-MWCNT.

Eq. 8.8 was also employed to see if the change in CNT length could be attributed to the change in modulus arising from the CNTs in our measurements. The constants used are $V_{\text{CNT}} = 0.017$, $E_{\text{matrix}} = 2236$ MPa (measured from CM PC 2205), $E_{\text{CNT}} = 450$ GPa, and measured $E_{\text{PC-MWCNT}} = 2412$ MPa and 2679 MPa for CM and IM bars, respectively. For the measured average IM PC-MWCNT modulus, l_{CNT} is obtain to be 94.4 nm. The calculated l_{CNT} represents a decreases by 77% relative to the original length value reported in Krause et al. (2011), that were measured after extrusion. Therefore, one possibility is that an even greater reduction of CNT length has taken place in our materials to shearing during IM. The change in aspect ratio and the fact that MWCNTs are worm-like structures rather than straight rods could also contribute to the overestimation of $E_{\text{PC-MWCNT}}$. Furthermore, the interfacial strength between PC and MWCNTs in this work is weak as no CNT surface modification was employed and the model assumes strong adhesion. In the case that the CNTs length did not reduce significantly after IM as predicted, then the calculated l_{CNT} represents the effective length for E measured for PC-MWCNT 2205. As the nanocomposite system is percolated, it is likely that the agglomerated CNTs, evident from OM micrographs in Section 6.2, acted as stress concentrators and reduced the CNTs effective length.

The calculations suggest that the Thostenson and Chou's approach may be used to provide an upper bound for the elastic modulus of IM PC-MWCNT (3 wt%).

¹It is noted that E_{CNT} for catalytic produced nanotubes, similar to this work, varies significantly in literature: from 27 GPa (Salvetat et al., 1999) up to 450 GPa (Pan et al., 1999). The latter reference was chosen for calculations as the MWCNT modulus was measured with well separated and parallel nanotubes whereas in the former reference MWCNTs were structurally disordered.

8.4.3.2 Randomly oriented CNT nanocomposite

Gojny and co-workers (2004) adapted Thostenson and Chou's approach to the Halpin-Tsai equation for randomly oriented short fibers. They reported good agreement between predicted and experimentally measured modulus for epoxy-CNT nanocomposite (0.1 wt%), whereas increasing the filler content to 1 wt% led to an overestimation of the modulus. They estimated E using (Gojny et al., 2004)

$$E = E_{\text{matrix}} \left(\frac{3}{8} \left(\frac{1 + \frac{2l_{\text{CNT}}}{d_{\text{CNT}}} \eta_{\text{L}} V_{\text{CNT}}}{1 - \eta_{\text{L}} V_{\text{CNT}}} \right) + \frac{5}{8} \left(\frac{1 + 2\eta_{\text{T}} V_{\text{CNT}}}{1 - \eta_{\text{T}} V_{\text{CNT}}} \right) \right) \quad (8.9)$$

where η_{L} is as in Eq. 8.4, and η_{T} is given by

$$\eta_{\text{T}} = \frac{\left(\frac{E_{\text{CNT}}}{E_{\text{matrix}}} - \frac{d_{\text{CNT}}}{4t} \right)}{\left(\frac{E_{\text{CNT}}}{E_{\text{matrix}}} + \frac{d_{\text{CNT}}}{2t} \right)} \quad (8.10)$$

Using the same constants as in Section 8.4.3.1, E for CM PC-MWCNT 2205 is calculated with Eq. 8.9 and yields a value of 2595 MPa, that is approximately 7% higher than experimentally determined overall average modulus of 2412 ± 71 MPa (\pm representing standard deviation). This could be explained by Halpin-Tsai's underlying assumptions of uniformly dispersed fillers and strong filler-matrix interaction. Contrary to the assumptions, there was CNT agglomeration in the PC-MWCNT systems of this work. Moreover, the theoretical CNT length that corresponds with the measured CM PC-MWCNT modulus is 66.2 nm, a value much lower than the reference length. Although Gojny's approach obtains an overestimate, the magnitude of the difference between the measured and calculated modulus is not significant, hence the predicted modulus can again be viewed as an upper bound for CM PC-MWCNT (3 wt%).

Villmow and co-workers (see Fig. 2.3) showed that the core region of IM PC-MWCNT specimens have relatively less oriented CNTs in comparison to the regions close to the specimen surfaces. We can assume the similar morphology for the IM specimens of this work, meaning that the specimens have both randomly oriented and aligned CNTs embedded in the matrix. Hence, Gojny's approach may be employed as the lower bound for the elastic modulus of

IM PC-MWCNT (3 wt%). The modulus range for IM PC-MWCNT estimated by the models are between 2595 and 3017 MPa. The measured average modulus of IM PC-MWCNT is within the predicted range. The close proximity of the measured modulus to the lower boundary suggests that the region of randomly oriented CNTs in IM PC-MWCNT is greater than that of the aligned CNTs.

8.5 Correlation between mechanical and electrical properties

Since the forming processes were observed to significantly influence the electrical resistivity and mechanical properties of PC-MWCNT, the correlation between these two properties of PC-MWCNT formed by both CM and IM processes were examined. The correlation coefficient, R was determined to investigate the relationship between the mechanical and electrical properties for the PC-MWCNT compounded at 230 - 290 °C. The variables were $\log \rho$ (from the electrical resistivity measured in Chapter 7), HV, E and UTS.

Table 8.2 presents the correlation coefficients for the relationship between mechanical properties and electrical resistivity for CM specimens. The most significant correlation is found between HV and $\log \rho$ of -0.40. Other variables were found to have less significant correlations.

TABLE 8.2: Correlation coefficients of the relationship between the final properties (electrical resistivity, ρ , hardness, HV, Young's modulus, E and ultimate tensile strength, UTS) for compression moulding

	$\log \rho$	HV	E	UTS
$\log \rho$				
HV	-0.40			
E	-0.10	0.06		
UTS	0.10	-0.26	0.05	

During CM, the long moulding times promote the formation of CNT agglomerates. One could speculate that the correlation between HV and ρ as shown in Fig. 8.6 arises from the distribution of these agglomerates. A high distribution of the CNT agglomerates may yield a higher HV and lower resistivity in comparison to a low distribution of the agglomerates. This is because a low distribution of the agglomerates gives rise to matrix rich regions that reduces CNT-CNT interactions between the individual tubes and the agglomerates. This view also provides a plausible explanation for the observed decrease in stiffness with increasing electrical resistivity, although the correlation between E and ρ is weak ($R = -0.10$).

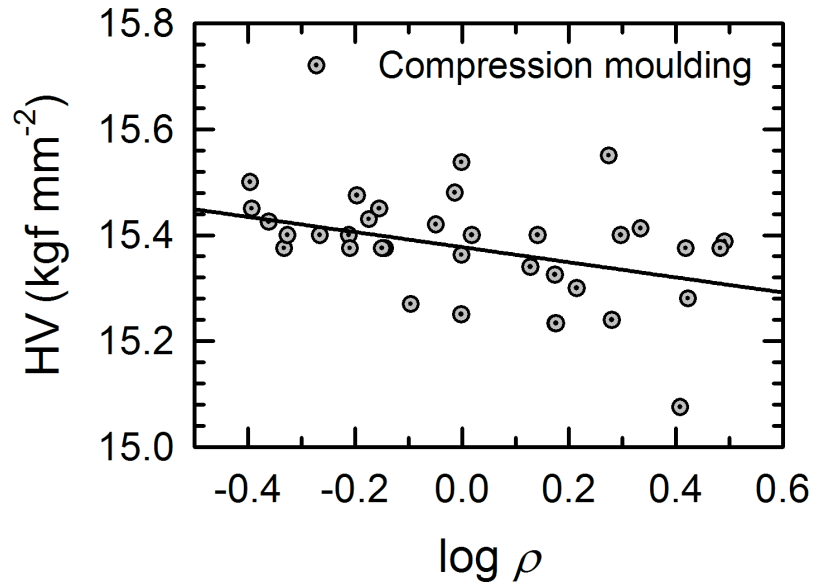


FIGURE 8.6: Relationship between hardness as a function of electrical resistivity for compression moulded specimens with linear regression, giving correlation coefficient, $R = -0.40$

It is postulated that as melt compounding temperature increases, viscosity of the matrix decreases, allowing the matrix to infiltrate into the primary agglomerates. However, the low viscosity matrix is unlikely to significantly disperse the primary agglomerates further to give smaller agglomerates in comparison to higher viscosity matrix that is favoured to breakup primary agglomerates through both erosion and rupture processes. This provides a possible explanation for the observed trend in Fig. 7.17 that showed the increase of ρ of CM samples as compounding temperature increases up to 270 °C. This suggests that the electrical conductive pathway may be disrupted by the presence of matrix rich regions; the decrease in ρ at 280 °C (see Fig. 7.17) is currently not fully understood. As the CNT network is shear history dependent (see Section 5.6.3), the observed trend in Fig. 7.17 suggests that compounding temperatures could have a slight influence on the initial level of CNT agglomerate distribution prior to CM, that affected the distribution of the secondary agglomerates formed during CM.

Table 8.3 presents the correlation coefficients for the relationship between mechanical properties and electrical resistivity for IM specimens. The most significant correlation is between E and HV with $R = 0.52$. All other variables yield weak correlations (≤ 0.3).

HV is a measure of the residual plastic deformation after indentation whereas E is a measure of the elastic stiffness. A nanocomposite system with a greater degree of CNT alignment would produce a higher stiffness in the flow direction, but in response to indentation, CNTs would appear more compliant, since they would then be subjected to bending perpendicular

TABLE 8.3: Correlation coefficients of the relationship between the final properties (electrical resistivity, ρ , hardness, HV, Young's modulus, E and tensile strength, UTS) for injection moulding

	$\log \rho$	HV	E	UTS
$\log \rho$				
HV	0.24			
E	0.22	0.52		
UTS	0.16	-0.31	-0.30	

to the tube axes. However, Fig. 8.7 shows a positive correlation between E and HV. Since HV records only the plastic deformation, a smaller hardness is a sign of a greater elastic recovery for a given maximum indenter position. Thus, it is possible to consider that bending nanotubes produces lower stress concentrations than axial stresses along the nanotube axes, and that therefore more orientation in the flow direction produces both a stiffer axial modulus and a greater hardness in the perpendicular direction.

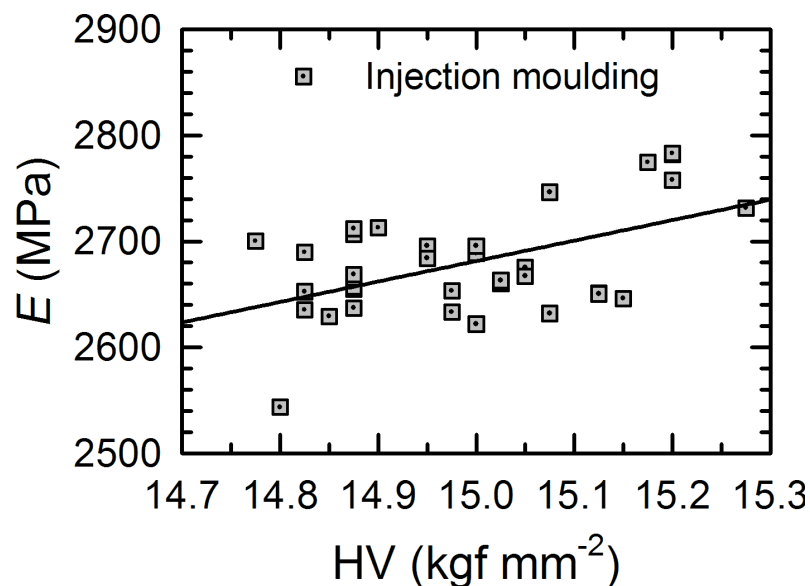


FIGURE 8.7: Relationship between Young's modulus as a function of hardness for injection moulded specimens with linear regression, giving correlation coefficient, $R = 0.52$

8.6 Conclusions

This chapter has presented measurements of mechanical properties of PC-MWCNT 2205 (3 wt%) produced at various extrusion temperatures and subsequently formed by CM and IM. The influence of extrusion temperature and the secondary melt processes (with different shearing and cooling rates) on the mechanical properties were investigated.

Section 8.3 discussed hardness of CM and IM PC-MWCNT, with an overall average HV of 15.41 ± 0.17 kgf mm² and 14.99 ± 1.43 kgf mm² respectively. The reduced HV of IM systems is attributed to the long and thin nanotubes that are much more compliant in bending relative to axial deformation. Both CM and IM specimens produced low variations of HV with compounding temperature, indicating that surface hardness is not significantly dependent on compounding temperature.

The tensile properties of CM and IM PC-MWCNT were measured in Section 8.4. Young's moduli of IM PC-MWCNT were consistently higher than CM samples. The average E of CM and IM is 2412 ± 71 MPa and 2679 ± 50 MPa correspondingly. No significant changes in Young's moduli was observed for both secondary melt process across the compounding temperature range studied. This was attributed to CNT agglomeration that reduces the stress transfer efficiency between the matrix and the nanotubes. Our findings reveal that the long times at moulding temperature for CM and the rapid cooling for IM of percolated CNT nanocomposite systems, could result in similar CNT agglomeration, and thus similar moduli regardless of extrusion temperature.

The prediction of E using the modified Halpin-Tsai equation, proposed by Thostenson and Chou to account for the tube structure, was explored in Section 8.4.3. Using reference values of CNT modulus and dimensions, a model for perfectly aligned CNTs provided an upper bound for the modulus of IM PC-MWCNT. In the case of CM PC-MWCNT, Gojny's approach, assuming randomly oriented nanotubes, was employed to predict E of randomly distributed CNTs. This can also be used as a lower bound for IM PC-MWCNT. The measured modulus of IM PC-MWCNT is within the bounds predicted by Thostenson's and Gojny's approaches. In the case of CM PC-MWCNT, Gojny's approach provided an upper bound of $\sim 7\%$ higher than the measured modulus of PC-MWCNT.

The theoretical CNT length corresponding to the measured modulus is determined as 94.4 nm (IM) and 66.2 nm (CM), much lower than the reference value of 418 nm. Several factors contribute to the difference between the calculated and referenced CNT lengths. For IM, the shorter estimated CNT length may be due to further shearing during IM, and the underlying assumptions of the Halpin-Tsai equation. In the case of CM, the estimated CNT lengths is postulated to be an indication of the effective length to achieve the measured modulus, therefore the reduction of CNT length from the reference is attributed to the agglomeration of CNTs and the assumptions of the model.

All filled systems in this work failed by brittle fracture. Section 8.4.2.2 shows that UTS were more sensitive to the compounding temperatures. CM and IM PC-MWCNT measured a change of 22% and 34% between the minimum and maximum UTS values correspondingly. The UTS of CM and IM PC-MWCNT were comparable, with an average of 35.6 ± 4.3 MPa and 38.3 ± 6.4 MPa respectively. Comparing both CM and IM PC-MWCNT to that of unfilled CM PC, that showed ductile fracture, the UTS values for PC-MWCNTs reduced by 33% (CM) and 28% (IM). This fracture behaviour must be considered when designing applications with percolated MWCNT systems.

The correlations between the electrical resistivity (from Chapter 7) and mechanical properties for CM and IM PC-MWCNT are examined and discussed in Section 8.5. The most significant correlation for CM PC-MWCNT is between HV and $\log \rho$ ($R = -0.40$). It is possible that the correlation arise from the state of distribution of the CNT agglomerates. A low distribution of CNT agglomerates leads to matrix rich regions that reduces the surface hardness and increases ρ of CM PC-MWCNT.

For IM PC-MWCNT, the highest correlation was obtained for the relationship between E and HV ($R = 0.52$). It is speculated that the bending of the nanotubes leads to lower stress concentrations than axial stresses along the CNT axes, and hence, orientation in the flow direction may yield a stiffer axial modulus and higher hardness in the perpendicular direction. The moderate to low R values of the correlation study for CM and IM show that the compounding temperature does not significantly affect the investigated PC-MWCNT properties as much as the secondary processes.

In conclusion, our findings suggests that the secondary processes play a crucial role in tailoring or controlling the final mechanical properties and electrical resistivity of percolated PC-MWCNT systems. This highlights the challenges in producing conductive nanocomposites with enhanced mechanical properties via conventional moulding methods that involve fast cooling.

Chapter 9

Conclusions

This thesis has investigated the solid and melt behaviour of PC filled with 3 wt% loading of MWCNTs. An emphasis has been placed on the role of the matrix in these materials. To date, much of the existing literature has been devoted to studying the influence of nanotube filler parameters, such as filler concentration and CNT structure, and the influence of processing parameters of small batch mixing (laboratory scale) on CNT nanocomposite behaviour. In order to commercialise such materials, there is a need to understand the effects of traditional polymer processing methods on the microstructure of the resulting polymeric system, since this determines the final properties of CNT filled thermoplastics.

9.1 Major conclusions

The main findings of this work are as follows:

Thermal analysis

- The addition CNTs in PC increases the onset of thermal degradation and decreases thermal stability in an inert atmosphere. However, thermo-oxidative tests exhibited a marginal increase in thermal stability for PC-MWCNT. Studies in both atmospheres show that CNTs are not an effective barrier to hinder degradation of PC in these systems.
- It was observed that while the degradation (weight loss) rate of PC was reduced in air compared to nitrogen atmosphere, PC-MWCNT recorded similar degradation rates in

both atmospheres. This indicates that CNTs hindered the formation of char in air and promoted degradation of the matrix, after the temporary CNT barrier broke down.

Melt rheology

- The decrease of the linear viscoelastic limit for PC-MWCNT compared to unfilled PC is attributed to the disruption of the CNT network with increasing strain amplitude rather than strain amplification
- Relaxation timescales of both unfilled and filled materials, obtained with the inverse of the cross-over frequency for unfilled PC and the peak in of the loss tangent for filled PC, were found to scale molar mass in the same way. This together with the fact that horizontal shift factors were independent of molar mass and, of CNT presence, supports the view that relaxation of the polymer network is the dominant relaxation mechanism in PC-MWCNT.
- Comparing the moduli obtained by the amplitude and frequency sweeps in the non-linear viscoelastic region, for the same reduced frequency and strain amplitude, show that the strain and temperature history affects the magnitude of the viscoelastic response of PC-MWCNT.

Solid state properties (electrical resistivity and mechanical behaviour)

- The order of magnitude difference in electrical resistivity between the secondary processes is attributed to re-agglomeration of CNTs, and to time-dependent build up of the CNT network during CM. No significant dependence on the compounding temperatures was observed, attributed to the presence of multiple conductive pathways in percolated PC-MWCNT systems.
- The hardness of IM samples were lower than of CM samples due orientation of CNTs in the flow direction. The long and thin tubes are more compliant in bending when the indentation force is perpendicular to the tube axes. There was no significant effect of compounding temperature on hardness of CM and IM PC-MWCNT.
- Young's moduli of IM PC-MWCNT were greater than those of CM samples. Both secondary processes recorded no significant change to the modulus as the compounding temperature increased suggesting that long CM moulding times and the rapid cooling

for IM of percolated systems may result in a similar degree of CNT agglomeration for each secondary process.

- Modified Halpin-Tsai equation for random oriented CNTs provided estimates of an upper and lower bound on Young's modulus for CM and IM PC-MWCNT respectively. The modified Halpin-Tsai equation for highly oriented CNTs predicted the upper bound on the modulus of IM PC-MWCNT. The measured moduli of IM PC-MWCNT were found to be within the predicted range. The difference between the measured values and the model predictions, for both CM and IM, suggests that the percolated system has weak matrix-filler interfacial strength and CNT agglomerates. The model also indicated that significant shortening of CNTs could be occurring due to shearing during melt processing.

9.2 Summary of relevant findings

There are several conclusions of reduced significance that could be drawn from this work. In an effort to establish the effect of the presence of CNTs and melt compounding parameters on the matrix, the molar mass of PC 2205 was compared to that of PC-MWCNT 2205 (compounded at 280 °C) and of PC 2205 1-pass (compounded with identical parameters to PC-MWCNT without the filler). No significant degradative effects on the PC matrix were found in either test. It was shown that the Soxhlet extraction technique is an effective method of separating the filler from PC-MWCNT to recover the base PC matrix.

In order to independently determine the filler concentration two techniques, the Soxhlet extraction and density measurements were employed. The filler content was found to be in agreement with that reported by the manufacturer.

Glass transition temperatures of filled and unfilled PC of all grades were measured to be between 146 °C and 148 °C, and only slightly sensitive to matrix molar mass. But since the decrease in T_g does not correspond with matrix degradation (as confirmed from GPC measurements), it is likely that a lack of matrix wetting on the CNT surface is giving rise to additional free volume.

The thermal conductivity of filled and unfilled PC was measured as $0.3068 \pm 0.0004 \text{ W m}^{-1} \text{ K}^{-1}$ and $0.2616 \pm 0.0012 \text{ W m}^{-1} \text{ K}^{-1}$ correspondingly. Simple two-phase models provide the lower

and upper bounds on $\kappa_{\text{PC-MWCNT}}$ as $0.27 \text{ W m}^{-1} \text{ K}^{-1}$ and $0.68 \text{ W m}^{-1} \text{ K}^{-1}$ respectively. The relatively low increment of $\kappa_{\text{PC-MWCNT}}$ is attributed to CNT agglomeration that interrupts phonon transport. Nevertheless, the test demonstrates that MWCNTs increases the thermal transport properties of the base matrix.

Rheological experiments were performed on all four grades of filled and unfilled PC, with varying matrix molar mass. The flocculation experiment provided evidence for structural build-up within PC-MWCNT. The addition of CNTs was found to reduce the viscoelastic limit due to strain amplification as evidenced by the strain amplification factor parameter for Song and Zheng's model and reduction of T_g with the presence of CNTs.

Time-temperature superposition was applied to the frequency dependence of the viscoelastic moduli. Both vertical and horizontal shifting were necessary. Vertical shifting of unfilled PC was performed by employing a density correction to the moduli, whereas for filled PC it was performed by superposition using van Gorp-Palmen plots. Horizontal shifting in the frequency domain was performed using an in-house optimiser. The filled PC mastercurves exhibit two distinct differences from those of unfilled PC. The first is a second plateau at low reduced frequency with a modulus of $\sim 10^5 \text{ Pa}$, associated with a percolated CNT network. Secondly, the loss tangent is less than unity across the extended frequency range.

Non-linear isothermal frequency sweeps were carried out at varying strain amplitudes between 0.05% and 50%, and mastercurves were produced with vertical and horizontal shifting. The different levels of disruption of the CNT network affected the vertical shifting significantly. However, the horizontal shifting was only marginally affected by strain amplitude.

Image analysis of optical micrographs of PC-MWCNT was challenging and complicated by knife defects on microtomed sections. Heat treatment of the sections to produce planar sections formed striations. Digital image processing applied to the sections (of lesser defects) obtained with a glass knife was unable to remove the artifacts, thus impeding quantitative evaluation of the CNT dispersion in PC-MWCNT. Grinding and polishing of CM and IM PC-MWCNT specimens showed features that are suspected to be voids with diameters of up to $\sim 70 \mu\text{m}$.

SEM on cryofractured surfaces of PC-MWCNT revealed enlarged CNT diameters and cracked appearance of the Pt coating layer, suggesting that the layer was too thick, and rendering any quantification of the state of CNT dispersion difficult. A focused ion beam was used

to mill the specimen while SEM captured images. However, these images exhibited a lack of contrast between PC and CNTs, even with backscattered electron detection. This was attributed to the comparable densities and atomic components of these materials.

A two-terminal fixture with surface contacts consisting of conductive elastomers was developed and constructed for measuring volume resistivities of CM and IM PC-MWCNT bars. The in-house fixture was evaluated to identify other resistance sources (i.e. thermoelectric effect, specimen heating), and calibrated with known resistances. Contact resistivity between the surface probes and the PC-MWCNT specimens was determined using a hybrid of methods, a combination of the extrapolation method and the transfer length method.

Resistivity measurements of PC-MWCNT, compounded between 230 °C and 290 °C followed by CM and IM, yielded an overall average resistivity of $1.29 \pm 0.80 \text{ } \Omega \text{ m}$ and $12.34 \pm 4.58 \text{ } \Omega \text{ m}$ respectively. The difference between the secondary processes is explained by the CNT re-agglomeration and CNT network build up during CM, most likely driven by polymer mobility. Varying the compounding temperatures did not significantly affect the resistivity of percolated PC-MWCNT systems. These findings revealed that tailoring the electrical behaviour of these filled systems requires more attention on the secondary process parameters compared to the compounding conditions.

Finally, characterisation of mechanical properties of PC-MWCNT were subsequently performed on the same specimens as for the electrical measurements. The average Vickers hardness of CM and IM PC-MWCNT, across the compounding temperatures, was measured as $15.41 \pm 0.17 \text{ kgf mm}^2$ and $14.99 \pm 1.43 \text{ kgf mm}^2$ respectively. On the other hand, IM PC-MWCNT recorded a higher Young's moduli of $\sim 200 \text{ MPa}$ than CM bars. All filled PC-MWCNT grades were found to be brittle, which must be accounted when designing for applications. Similarly to the findings for the electrical study, the secondary processing parameters rather than the compounding parameters play the crucial role in determining final mechanical properties of percolated PC-MWCNT systems.

Since electrical and mechanical properties of PC-MWCNT were studied on the same specimens, this provided the opportunity to relate the two properties together. In the case of CM, the most significant relationship is between HV and $\log \rho$ ($R = -0.40$). We can speculate that the correlation is due to the distribution of the CNT agglomerates within the matrix. This suggests that the compounding temperature may have influenced the CNT

agglomerates distribution prior to the CM process. For IM PC-MWCNT, the highest correlation was obtained between E and HV ($R = 0.52$). The CNTs would be appear more compliant to indentation, and subject to bending. It is possible that bending the nanotubes produces lower stress concentrations than the axial stresses along the CNT axes, and hence, orientation in the flow direction produces stiffer axial modulus and greater hardness in the perpendicular direction. The moderate to low correlations found for both CM and IM shows that compounding temperature has no significant effect on the electrical and mechanical properties of PC-MWCNTs. In comparison to CM, IM yields higher electrical resistivity, reduced hardness and greater stiffness. This is in line with the high shear and fast cooling rates that produces oriented CNT nanocomposites.

9.3 Recommendations for future work

There are several questions raised from this work that remain to be addressed. Quantification of the state of CNT dispersion of PC-MWCNTs was hindered by challenges with the specimen preparation. In order to obtain microscopy sections with less defects, a histo diamond knife may be used as a cutting tool. If a glass knife is the only option, attempts should be made to obtain thicker sections (of the order of $20 \mu\text{m}$) followed by a heat treatment. This may yield planar sections that are appropriate for OM analysis.

The significant changes in electrical properties for CM processed PC-MWCNT in comparison to IM PC-MWCNT were attributed to the longer moulding times resulting in CNT re-agglomeration. It would be interesting to carry out an annealing study of IM specimens, at temperatures close to T_g , to verify if this promotes the re-arrangement of the CNT network and hence, of the conductive pathways.

The two-terminal method developed to measure the electrical resistivity is not ideal due to difficulties in limiting contact resistance. In order to minimise this error, modifications to the four-terminal and van der Pauw fixtures are recommended. For the four-terminal method, surface probes with carbon-filled silicone sandwiched between the electrode probes and the PC-MWCNT specimen may be able to provide good contact between the rigid probes and specimen. Surface probes should be coated with gold in order to avoid oxidation of the probes. As an alternatively, the sharp tip probes could be replaced with surface contacts or wire contacts.

Finally, Castillo et al. (2011) have shown that MWCNTs from different manufacturers can influence nanocomposite properties due to variations in nanotube dimensions. In this work, only a single MWCNT supplier (Nanocyl S.A.) was used for all investigations. By studying nanocomposites made from different CNT sources, it may be possible to understand how nanotube characteristics influence properties, and hence the scope for applications.

Appendix A

Procedure for determining outliers in samples

A.1 Normality test

The Anderson-Darling test is a method to determine the specific distribution of the sample data (Stephens, 1974). This test calculates the empirical cumulative distribution function of the sample data and compares it with the expected distribution. The test determines the specific distribution using critical values that depend on the specific distribution tested, which for this work, is the normal distribution.

The test verifies a hypothesis that the data follows a normal distribution. The test is applied to the logarithmic values of the measured R obtained from the two-terminal method in Chapter 7. The hypothesis is rejected if the probability value is lower than or equal to the selected significance level.

In order to assess if the R values follow a normal distribution, 19 IM PC-MWCNT 2205 bars, compounded at 230 °C, are measured using the two-terminal method. The chosen significance level was 0.1 (10%). The Minitab software was used to calculate the probability for the Anderson-Darling test. The computed critical value for the Anderson-Darling test is 0.252, with a probability of 0.7. Since the probability value is higher than the significance level, the hypothesis cannot be rejected. Hence, it is reasonable to assume that the logarithmic R data follows a normal distribution.

A.2 Tietjen-Moore test

A.2.1 Introduction

The Tietjen-Moore test is a Grubbs' type test for examining suspected values that are lower or higher than the bulk of the univariate data (Tietjen and Moore, 1972). The Grubbs' test evaluates if the minimum or maximum value in the data set is an outlier by comparing the value to the sample mean. The Grubbs' test for a single outlier is not sufficient for the data set in this work as the procedure is insensitive when several values are close to one another relative to the bulk of the data. This is known as the masking effect.

In order to extend the Grubbs' test, Tietjen and Moore suggested the computation of the absolute residuals, r , for the data set, by subtracting the data with the sample mean, for the number of n data. The test statistic, E_k is calculated as the ratio of the summation of the squared deviation from the mean with the number of suspected outliers, k removed from the data set over the summation of the squared deviation from the mean of the full data set. The procedure is repeated after removing k lowest or highest points. The test statistic is then compared to critical values, determined through Monte Carlo simulation, that is dependent on the sample size (n) and k . These critical values are tabulated in Tietjen and Moore (1972).

The test defines two hypotheses: either (1) the data has no outliers, or (2) the data has k outliers. If the test statistic is lower than the critical value, based on the significance level, then hypothesis (1) is rejected.

It must be noted that k has to be exactly specified for each test statistic.

A.2.2 Procedure

A typical Tietjen-Moore test to identify any outliers for R measurements, as reported in Chapter 7, is presented for CM PC-MWCNT 2205, compounded at 230 °C. Table A.1 presents the R measured for five specimens ($n = 5$). The absolute residual for each specimen is calculated as (Tietjen and Moore, 1972)

$$r_i = |R_i - \bar{R}| \quad (\text{A.1})$$

where R_i represents the i th data value and \bar{R} is the mean of the data set.

TABLE A.1: Resistance measurements of five CM PC-MWCNT 2205 specimens compounded at 230 °C and the absolute residuals calculated from Eq. A.1

i	$\log R$	Residual, r_i
1	3.15	0.27
2	3.34	0.08
3	3.39	0.03
4	3.40	0.02
5	3.82	0.40
$\bar{R} = 3.419$		

The R is relabelled as z as r is arranged in an increasing order. E_k is calculated as (Tietjen and Moore, 1972)

$$E_k = \frac{\sum_{i=1}^{n-k} (z_i - \bar{z}_k)^2}{\sum_{i=1}^n (z_i - \bar{z})^2} \quad (\text{A.2})$$

The total sum of the squares of the deviations ($\sum_{i=1}^5 (z_i - \bar{z})^2$) is 0.2404. The specimens $n = 1$ and 5 in Table A.1 are suspected to be outliers. The sum of the squares of the deviations, excluding $\log R = 3.15$ and 3.82 ($\sum_{i=1}^3 (z_i - \bar{z}_2)^2$), is 0.0022. Using Eq. A.2, E_2 is 0.0093. The critical value for 5% significance level is 0.01 which is higher than E_2 , thus, the R measurement for specimens 1 and 5 are identified as outliers.

As the specific number of outliers must be known prior to the test, we performed the Tietjen-Moore test for the maximum number of possible outliers ($k = 2$) for a sample size of five, in order to be unbiased to the data. If a single outlier is found, the data point is removed from the sample and the test is repeated for the remaining four specimens to identify further outliers.

Bibliography

- Abbasi, S., Carreau, P. J. and Derdouri, A. (2009), ‘Flow induced orientation of multiwalled carbon nanotubes in polycarbonate nanocomposites: Rheology, conductivity and mechanical properties’, *Polymer* **51**(4), 922–935.
- Abdel-Goad, M. and Pötschke, P. (2005), ‘Rheological characterization of melt processed polycarbonate-multiwalled carbon nanotube composites’, *Journal of Non-Newtonian Fluid Mechanics* **128**(1), 2–6.
- Ajayan, P. M. (1999), ‘Nanotubes from carbon’, *Chemical Reviews* **99**, 1787–1799.
- Aklonis, J. J. and Macknight, W. J. (1983), *Introduction to Polymer Viscosity*, 2 edn, Wiley-Interscience Publication, United States of America.
- Alig, I., Skipa, T., Engel, M., Lellinger, D., Pegel, S. and Pötschke, P. (2007), ‘Electrical conductivity recovery in carbon nanotubepolymer composites after transient shear’, *Physica Status Solidi (b)* **244**(11), 4223–4226.
- Alig, I., Lellinger, D., Engel, M., Skipa, T. and Pötschke, P. (2008a), ‘Destruction and formation of a conductive carbon nanotube network in polymer melts: In-line experiments’, *Polymer* **49**(7), 1902–1909.
- Alig, I., Skipa, T., Lellinger, D. and Pötschke, P. (2008b), ‘Destruction and formation of a carbon nanotube network in polymer melts: Rheology and conductivity spectroscopy’, *Polymer* **49**(16), 3524–3532.
- Alig, I., Skipa, T., Lellinger, D., Bierdel, M. and Meyer, H. (2008), ‘Dynamic percolation of carbon nanotube agglomerates in a polymer matrix: comparison of different model approaches’, *Physica status solidi (b)* **245**(10), 2264–2267.

- Alig, I., Pötschke, P., Lellinger, D., Skipa, T., Pegel, S., Kasaliwal, G. and Villmow, T. (2012), 'Establishment, morphology and properties of carbon nanotube networks in polymer melts', *Polymer* **53**(1), 4–28.
- Aljaafari, A. A., Ibrahim, S. S. and El-Brolossy, T. A. (2011), 'Thermophysical and electrical characterization of PVC-SWNT nanocomposites', *Composites Part A: Applied Science and Manufacturing* **42**(4), 394–399.
- Baccaro, L. E. and Keenan, P. (2000), 'Current applications of polycarbonates'. In: Legrand, G. D. and Bendler, J. T. (Ed.) *Handbook of polycarbonate science and technology*, New York, Marcel Dekker Inc., pp. 341–351.
- Bai, J. B. and Allaoui, A. (2003), 'Effect of the length and the aggregate size of mwnts on the improvement efficiency of the mechanical and electrical properties of nanocomposites-experimental investigation', *Composites Part A: Applied Science and Manufacturing* **34**(8), 689–694.
- Barber, A. H., Cohen, S. R. and Wagner, H. D. (2003), 'Measurement of carbon nanotube–polymer interfacial strength', *Applied Physics Letters* **82**(23), 4140–4142.
- Barus, S., Zanetti, M., Bracco, P., Musso, S., Chiodoni, A. and Tagliaferro, A. (2010), 'Influence of mwcnt morphology on dispersion and thermal properties of polyethylene nanocomposites', *Polymer Degradation and Stability* **95**(5), 756–762.
- Bauhofer, W. and Kovacs, J. Z. (2009), 'A review and analysis of electrical percolation in carbon nanotube polymer composites', *Composites Science and Technology* **69**(10), 1486–1498.
- Berber, S., Kwon, Y. and Tománek, D. (2000), 'Unusually high thermal conductivity of carbon nanotubes', *Physical Review Letters* **84**(20), 4613.
- Berger, H. H. (1972), 'Contact resistance and contact resistivity', *Journal of The Electrochemical Society* **119**(4), 507–514.
- Bhuiyan, M. A., Pucha, R. V., Karevan, M. and Kalaitzidou, K. (2011), 'Tensile modulus of carbon nanotube/polypropylene composites a computational study based on experimental characterization', *Computational Materials Science* **50**(8), 2347–2353.

- Bhuiyan, M. A., Pucha, R. V., Worthy, J., Karevan, M. and Kalaitzidou, K. (2013), 'Defining the lower and upper limit of the effective modulus of cnt/polypropylene composites through integration of modeling and experiments', *Composite Structures* **95**(0), 80–87.
- Blythe, A. R. (1984), 'Electrical resistivity measurements of polymer materials', *Polymer Testing* **4**(24), 195–209.
- Blythe, T. and Bloor, D. (2005), *Electrical properties of polymers*, 2 edn, Cambridge University Press, New York.
- Bom, D., Andrews, R., Jacques, D., Anthony, J., Chen, B., Meier, M. S. and Selegue, J. P. (2002), 'Thermogravimetric analysis of the oxidation of multiwalled carbon nanotubes: Evidence for the role of defect sites in carbon nanotube chemistry', *Nano Letters* **2**(6), 615–619.
- Bradley, J. (2009), *Business watch*, [online] Nature news. [accessed 2 November 2013]. Available from: <http://www.nature.com/news/2009/091007/full/461702a.html>.
- British Standard (1999), 'BS EN ISO 3915:1999', *Plastics: Measurement of resistivity of conductive plastics*, British Standards Institution, London.
- British Standard (2012), 'BS EN ISO 527-2:2012', *Plastics: Determination of tensile properties*, British Standards Institution, London.
- Broughton, W. R., Koukoulas, T., Woolliams, P., Williams, J., and Rahatekar, S. S. (2013), 'Assessment of nanoparticle loading and dispersion in polymeric materials using optical coherence tomography', *Polymer Testing* **32**(7), 1290–1298.
- Brown, M. E. (2001), *Introduction to Thermal Analysis : Techniques and Applications (2nd Edition)*, Kluwer Academic Publishers, Secaucus, NJ, USA.
- Bushby, A. J., P'Ng, K. M. Y., Young, R. D., Pinali, C., Knupp, C. and Quantock, A. J. (2011), 'Imaging three-dimensional tissue architectures by focused ion beam scanning electron microscopy', *Nature Protocols* **6**(6), 845–858.
- Cadek, M., Coleman, J. N., Barron, V., Hedicke, K. and Blau, W. J. (2002), 'Morphological and mechanical properties of carbon-nanotube-reinforced semicrystalline and amorphous polymer composites', *Applied Physics Letters* **81**(27), 5123–5125.

- Cadek, M., Coleman, J. N., Ryan, K. P., Nicolosi, V., Bister, G., Fonseca, A., Nagy, J. B., Szostak, K., Bguin, F. and Blau, W. J. (2004), 'Reinforcement of polymers with carbon nanotubes: The role of nanotube surface area', *Nano Letters* **4**(2), 353–356.
- Castillo, F. Y., Socher, R., Krause, B., Headrick, R., Grady, B. P., Prada-Silvy, R. and Pöschke, P. (2011), 'Electrical, mechanical, and glass transition behavior of polycarbonate-based nanocomposites with different multi-walled carbon nanotubes', *Polymer* **52**(17), 3835–3845.
- Chandra, A., Kramschuster, A. J., Hu, X. and Turng, L.-S. (2007), 'Effect of injection molding parameters on the electrical conductivity of polycarbonate/carbon nanotube nanocomposites'.
- Chatterjee, T. and Krishnamoorti, R. (2008), 'Steady shear response of carbon nanotube networks dispersed in poly(ethylene oxide)', *Macromolecules* **41**(14), 5333–5338.
- Chiu, H. Y., Deshpande, V. V., Postma, H. W. C., Lau, C. N., Mikó, C., Forró, L. and Bockrath, M. (2005), 'Ballistic phonon thermal transport in multiwalled carbon nanotubes', *Physical Review Letters* **95**(22), 226101.
- Chiu, J. (1968), 'Polymer characterization by coupled thermogravimetry-gas chromatography', *Analytical Chemistry* **40**(10), 1516–1520.
- Choi, Y. K., Sugimoto, K. I., Song, S. M. and Endo, M. (2005), 'Mechanical and thermal properties of vapor-grown carbon nanofiber and polycarbonate composite sheets', *Materials Letters* **59**(27), 3514–3520.
- Choong, G. Y. H., Focatiis, D. S. A. and Hassell, D. G. (2013), 'Viscoelastic melt rheology and timetemperature superposition of polycarbonatemulti-walled carbon nanotube nanocomposites', *Rheologica Acta* **52**(8-9), 801–814.
- Coleman, J. N., Khan, U., Blau, W. J. and Gunko, Y. K. (2006), 'Small but strong: A review of the mechanical properties of carbon nanotubepolymer composites', *Carbon* **44**(9), 1624–1652.
- Coleman, J. N., Khan, U. and Gun'ko, Y. K. (2006), 'Mechanical reinforcement of polymers using carbon nanotubes', *Advanced Materials* **18**(6), 689–706.
- Colomer, J. F., Stephan, C., Lefrant, S., Van Tendeloo, G., Willems, I., Kónya, Z., Fonseca, A., Laurent, C. and Nagy, J. (2000), 'Large-scale synthesis of single-wall carbon nanotubes

- by catalytic chemical vapor deposition (CCVD) method', *Chemical Physics Letters* **317**(1-2), 83–89.
- Costa, F., Saphiannikova, M., Wagenknecht, U. and Heinrich, G. (2008), 'Layered double hydroxide based polymer nanocomposites', *Advances in Polymer Science* **210**, 101 – 168.
- Costache, M. C., Heidecker, M. J., Manias, E., Camino, G., Frache, A., Beyer, G., Gupta, R. K. and Wilkie, C. A. (2007), 'The influence of carbon nanotubes, organically modified montmorillonites and layered double hydroxides on the thermal degradation and fire retardancy of polyethylene, ethylenevinyl acetate copolymer and polystyrene', *Polymer* **48**(22), 6532–6545.
- Das, A., Stöckelhuber, K. W., Jurk, R., Saphiannikova, M., Fritzsche, J., Lorenz, H., Klüppel, M. and Heinrich, G. (2008), 'Modified and unmodified multiwalled carbon nanotubes in high performance solution-styrene butadiene and butadiene rubber blends', *Polymer* **49**(24), 5276–5283.
- De Focatiis, D. S. A., Embery, J. and Buckley, C. P. (2010), 'Large Deformations in Oriented Polymer Glasses: Experimental Study and a New Glass-Melt Constitutive Model', *Journal of Polymer Science: Part B: Polymer Physics* **48**(13), 1449–1463.
- De Focatiis, D. S. A. (2012), 'Tooling for near net-shape compression moulding of polymer specimens', *Polymer Testing* **31**(4), 550–556.
- Dealy, J. and Plazek, D. (2009), 'Time-temperature superposition - a users guide', *Rheology Bulletin* **78**(2), 32.
- Delaware Diamond Knives (2013), *Light microscopy: Effective knives for all of your cutting applications*. [accessed 2 November 2013]. Available from: <http://www.ddk.com/light-microscopy.php>.
- DeRudder, J. L. (2000), 'Commercial applications of polycarbonates'. In: Legrand, G. D. and Bendler, J. T. (Ed.) *Handbook of polycarbonate science and technology*, New York, Marcel Dekker Inc., pp. 303–315.
- Ding, W., Calabri, L., Kohlhaas, K., Chen, X., Dikin, D. and Ruoff, R. (2007), 'Modulus, fracture strength, and brittle vs. plastic response of the outer shell of arc-grown multi-walled carbon nanotubes', *Experimental Mechanics* **47**(1), 25–36.

- Dobkowski, Z. (1982), 'Influence of polydispersity and long chain branching on the melt viscosity of polycarbonate', *European Polymer Journal* **18**(12), 1051–1059.
- Dresselhaus, M. S., Dresselhaus, G., Charlier, J. C. and Hernández, E. (2004), 'Electronic, thermal and mechanical properties of carbon nanotubes', *Philosophical Transactions of the Royal Society of London. Series A: Mathematical, Physical and Engineering Sciences* **362**(1823), 2065–2098.
- Du, F., Scogna, R. C., Zhou, W., Brand, S., Fischer, J. E. and Winey, K. I. (2004), 'Nanotube networks in polymer nanocomposites: Rheology and electrical conductivity', *Macromolecules* **37**(24), 9048–9055.
- Ebbesen, T. W. and Ajayan, P. M. (1992), 'Large-scale synthesis of carbon nanotubes', *Nature* **358**(6383), 220–222.
- Ebbesen, T. W., Lezec, H. J., Hiura, H., Bennett, J. W., Ghaemi, H. F. and Thio, T. (1996), 'Electrical conductivity of individual carbon nanotubes', *Nature* **382**(6586), 54–56.
- Eitan, A., Fisher, F. T., Andrews, R., Brinson, L. C. and Schadler, L. S. (2006), 'Reinforcement mechanisms in mwcnt-filled polycarbonate', *Composites Science and Technology* **66**(9), 1162–1173.
- Ellison, C. J. and Torkelson, J. M. (2003), 'The distribution of glass-transition temperatures in nanoscopically confined glass formers', *Nature Materials* **2**(10), 6.
- Endo, M., Srano, M. S. and Ajayan, P. M. (2008), *Potential Applications of Carbon Nanotubes*, Vol. 111 of *Topics Applied Physics*, Springer, pp. 13–61.
- Engels, T. A. P., Govaert, L. E. and Meijer, H. E. H. (2009), 'The influence of molecular orientation on the yield and post-yield response of injection-molded polycarbonate', *Macromolecular Materials and Engineering* **294**(12), 821–828.
- Feng, J., Hao, J., Du, J. and Yang, R. (2010), 'Flame retardancy and thermal properties of solid bisphenol a bis(diphenyl phosphate) combined with montmorillonite in polycarbonate', *Polymer Degradation and Stability* **95**(10), 2041–2048.
- Fischer, J. E., Dai, H., Thess, A., Lee, R., Hanjani, N. M., Dehaas, D. L. and Smalley, R. E. (1997), 'Metallic resistivity in crystalline ropes of single-wall carbon nanotubes', *Physical Review B* **55**(8), R4921.

- Fisher, F. T., Bradshaw, R. D. and Brinson, L. C. (2002), 'Effects of nanotube waviness on the modulus of nanotube-reinforced polymers', *Applied Physics Letters* **80**(24), 4647–4649.
- Fornes, T. D., Baur, J. W., Sabba, Y. and Thomas, E. L. (2006), 'Morphology and properties of melt-spun polycarbonate fibers containing single- and multi-wall carbon nanotubes', *Polymer* **47**(5), 1704–1714.
- Fornes, T. D., Yoon, P. J., Keskkula, H. and Paul, D. R. (2001), 'Nylon 6 nanocomposites: the effect of matrix molecular weight', *Polymer* **42**(25), 09929–09940.
- Gay, D., Hoa, S. V. and Tsai, S. W. (2002), *Composite materials Design and Applications*, 4th edn, CRC press.
- Gedler, G., Antunes, M., Realinho, V. and Velasco, J. I. (2012), 'Thermal stability of polycarbonate-graphene nanocomposite foams', *Polymer Degradation and Stability* **97**(8), 1297–1304.
- Gergesova, M., Zupani, B., Saprunov, I. and Emri, I. (2010), 'The closed form t-t-p shifting (cfs) algorithm', *Journal of Rheology* **55**(1), 1–16.
- Giant Manufacturing Ltd. (2013), *Advanced SL composite technology*. [accessed 2 November 2013]. Available from: http://www.giant-bicycles.com/en-gb/technology/composite_technology/55/.
- Gojny, F. H., Wichmann, M. H. G., Fiedler, B., Kinloch, I. A., Bauhofer, W., Windle, A. H. and Schulte, K. (2006), 'Evaluation and identification of electrical and thermal conduction mechanisms in carbon nanotube/epoxy composites', *Polymer* **47**(6), 2036–2045.
- Gojny, F. H., Wichmann, M. H. G., Kpke, U., Fiedler, B. and Schulte, K. (2004), 'Carbon nanotube-reinforced epoxy-composites: enhanced stiffness and fracture toughness at low nanotube content', *Composites Science and Technology* **64**(15), 2363–2371.
- Grady, B. P. (2012), 'Effects of carbon nanotubes on polymer physics', *Journal of Polymer Science Part B: Polymer Physics* **50**(9), 591–623.
- Green, M. J. (2010), 'Analysis and measurement of carbon nanotube dispersions: nanodispersion versus macrodispersion', *Polymer International* **59**(10), 1319–1322.
- Groves, I., Lever, T. and Hawkings, N. (1993), 'Determination of carbon black pigment in nylon 66 by TGA', *Thermal Analysis application brief*, NumberTA - 122

- Gupta, R. K., Kennel, E. and Kim, K. J. (2010), *Polymer Nanocomposites Handbook*, 1 edn, CRC Press Taylor Francis Group.
- Gustafsson, S. E. (1991), 'Transient plane source techniques for thermal conductivity and thermal diffusivity measurements of solid materials', *Review of Scientific Instruments* **62**(3), 797–804.
- Han, M. S., Lee, Y. K., Yun, C. H., Lee, H. S., Lee, C. J. and Kim, W. N. (2011), 'Bent-shape effects of multi-walled carbon nanotube on the electrical conductivity and rheological properties of polycarbonate/multi-walled carbon nanotube nanocomposites', *Synthetic Metals* **161**(15-16), 1629–1634.
- Handge, U. and Pötschke, P. (2007), 'Deformation and orientation during shear and elongation of a polycarbonate/carbon nanotubes composite in the melt', *Rheologica Acta* **46**(6), 889–898.
- Handge, U., Zeiler, R., Dijkstra, D., Meyer, H. and Altstädt, V. (2011), 'On the determination of elastic properties of composites of polycarbonate and multi-wall carbon nanotubes in the melt', *Rheologica Acta* **50**(5), 503–518.
- Harris, P. J. F. (2004), 'Carbon nanotube composites', *International Materials Reviews* **49**(1), 31–43.
- Haslam, M. D. and Raeymaekers, B. (2013), 'A composite index to quantify dispersion of carbon nanotubes in polymer-based composite materials', *Composites Part B: Engineering* **55**(0), 16–21.
- Hatakeyama, T. and Quinn, F. (1999), *Thermal analysis: fundamental and applications to polymer*, John Wiley Sons Ltd.
- Heinrich, G., Klüppel, M. and Vilgis, T. A. (2002), 'Reinforcement of elastomers', *Current Opinion in Solid State and Materials Science* **6**(3), 195–203.
- Herrmann, K. (2011), *Hardness Testing: Principles and Applications*, ASM International.
- Hone, J., Whitney, M., Piskoti, C. and Zettl, A. (1999), 'Thermal conductivity of single-walled carbon nanotubes', *Physical Review B* **59**(4), R2514.
- Huang, Q., Gao, L., Liu, Y. and Sun, J. (2005), 'Sintering and thermal properties of multi-walled carbon nanotube-batio₃ composites', *Journal of Materials Chemistry* **15**(20), 1995–2001.

- Hyun, K., Wilhelm, M., Klein, C. O., Cho, K., Nam, J. G., Ahn, K. H., Lee, S. J., Ewoldt, R. H. and McKinley, G. H. (2011), 'A review of nonlinear oscillatory shear tests: Analysis and application of large amplitude oscillatory shear (laos)', *Progress in Polymer Science* **36**(12), 1697–1753.
- Iijima, S. (1991), 'Helical microtubules of graphitic carbon', *Nature* **354**(6348), 56–58.
- Jang, B. N. and Wilkie, C. A. (2004), 'A tga/ftir and mass spectral study on the thermal degradation of bisphenol a polycarbonate', *Polymer Degradation and Stability* **86**(3), 419–430.
- Jang, B. N. and Wilkie, C. A. (2005), 'The thermal degradation of bisphenol a polycarbonate in air', *Thermochimica Acta* **426**(1-2), 73–84.
- Jiang, W., Molian, P. and Ferkel, H. (2005), 'Rapid production of carbon nanotubes by high-power laser ablation', *Journal of Manufacturing Science and Engineering* **127**(3), 703–707.
- Jordan, T. C. and Richards, W. D. (2000), 'Polycarbonate Melt Rheology'. In: Legrand, G. D. and Bendler, J. T. (Ed.) *Handbook of polycarbonate science and technology*, New York, Marcel Dekker Inc., pp. 179–224.
- Kanagaraj, S., Varanda, F. R., Zhil'tsova, T. V., Oliveira, M. S. A. and Simões, J. A. O. (2007), 'Mechanical properties of high density polyethylene/carbon nanotube composites', *Composites Science and Technology* **67**(15-16), 3071–3077.
- Kasaliwal, G., Göldel, A. and Pötschke, P. (2009), 'Influence of processing conditions in small-scale melt mixing and compression molding on the resistivity and morphology of polycarbonate-mwnt composites', *Journal of Applied Polymer Science* **112**(6), 3494–3509.
- Kasaliwal, G., Göldel, A., Pötschke, P. and Heinrich, G. (2011), 'Influences of polymer matrix melt viscosity and molecular weight on mwnt agglomerate dispersion', *Polymer* **52**(4), 1027–1036.
- Kasaliwal, G. R. (2011), Analysis of multiwalled carbon nanotube agglomerate dispersion in polymer melts, PhD thesis, Technischen Universität Dresden.
- Kasaliwal, G. R., Pegel, S., Göldel, A., Pötschke, P. and Heinrich, G. (2010), 'Analysis of agglomerate dispersion mechanisms of multiwalled carbon nanotubes during melt mixing in polycarbonate', *Polymer* **51**(12), 2708–2720.

- Kasaliwal, G. R., Villmow, T., Pegel, S. and Pötschke, P. (2011), 'Influence of material and processing parameters on carbon nanotube dispersion in polymer melts'. In: McNally, T. and Pötschke, P. (Ed.) *Polymer-carbon nanotube composites: Preparation, properties and applications*, Cambridge, Woolhead publishings, pp. 92–132.
- Kashiwagi, T. (1994), Polymer combustion and flammability role of the condensed phase, in T. C. Institute, ed., '25th Symposium (International) on Combustion', The Combustion Institute, pp. 1423–1437.
- Kashiwagi, T., Grulke, E., Hilding, J., Groth, K., Harris, R., Butler, K., Shields, J., Kharchenko, S. and Douglas, J. (2004), 'Thermal and flammability properties of polypropylene/carbon nanotube nanocomposites', *Polymer* **45**(12), 4227–4239.
- Kashiwagi, T., Grulke, E., Hilding, J., Harris, R., Awad, W. and Douglas, J. (2002), 'Thermal degradation and flammability properties of poly(propylene)/carbon nanotube composites', *Macromolecular Rapid Communications* **23**(13), 761–765.
- Keithley Instruments (2004), *Low level measurements handbook: Precision DC current, voltage, and resistance measurements*, 6 edn.
- Keithley Instruments (2009), *Model 6517B Reference Manual*, 6517b-901-01 rev. b edn.
- Kharchenko, S. B., Douglas, J. F., Obrzut, J., Grulke, E. A. and Migler, K. B. (2004), 'Flow-induced properties of nanotube-filled polymer materials', *Nature Materials* **3**(8), 564–568.
- King, J. A., (2000), 'Synthesis of polycarbonates'. In: Legrand, G. D. and Bendler, J. T. (Ed.) *Handbook of polycarbonate science and technology*, New York, Marcel Dekker Inc., pp. 7–26.
- King, J. A., Via, M. D., Mills, O. P., Alpers, D. S., Sutherland, J. W. and Bogucki, G. R. (2012), 'Effects of multiple carbon fillers on the electrical and thermal conductivity and tensile and flexural modulus of polycarbonate-based resins', *Journal of Composite Materials* **46**(3), 331–350.
- Kochetov, R. (2012), Thermal and electrical properties of nanocomposites, including material processing, PhD thesis, Delft University of Technology.
- Koon, D. W. (1989), 'Effect of contact size and placement, and of resistive inhomogeneities on van der pauw measurements', *Review of Scientific Instruments* **60**(2), 271–274.

- Krause, B., Boldt, R. and Pötschke, P. (2011), 'A method for determination of length distributions of multiwalled carbon nanotubes before and after melt processing', *Carbon* **49**(4), 1243–1247.
- Krause, B., Mende, M., Pötschke, P. and Petzold, G. (2010), 'Dispersability and particle size distribution of cnts in an aqueous surfactant dispersion as a function of ultrasonic treatment time', *Carbon* **48**(10), 2746–2754.
- Krause, B., Pötschke, P. and Häuler, L. (2009), 'Influence of small scale melt mixing conditions on electrical resistivity of carbon nanotube-polyamide composites', *Composites Science and Technology* **69**(10), 1505–1515.
- Krishnan, A., Ebbesen, T. W., Dujardin, E., Yianilos, P. N. and Treacy, M. M. J. (1998), 'Young's modulus of single-walled nanotubes', *Physical Review B* **58**(20), 14013–14019.
- Kuriger, R. J., Alam, M. K., Anderson, D. P. and Jacobsen, R. L. (2002), 'Processing and characterization of aligned vapor grown carbon fiber reinforced polypropylene', *Composites Part A: Applied Science and Manufacturing* **33**(1), 53–62.
- Langford, R. M. (2006), 'Focused ion beams techniques for nanomaterials characterization', *Microscopy Research and Technique* **69**(7), 538–549.
- Lellinger, D., Xu, D., Ohneiser, A., Skipa, T. and Alig, I. (2008), 'Influence of the injection moulding conditions on the in-line measured electrical conductivity of polymer-carbon nanotube composites', *Physica Status Solidi (b)* **245**(10), 2268–2271.
- Lew, C. Y., Xia, H., McNally, T., Fei, G., Vargas, J., Millar, B., Douglas, P., Claes, M. and Luizi, F. (2009), 'A unified strategy to incorporating nanotube in twinscrew extrusion processing', Polymer Processing Society Europe/ Africa Regional Meeting.
- Lew, C. Y., Dewaghe, C. and Claes, M. (2011), 'Injection moulding of polymer-carbon nanotubes'. In: McNally, T. and Pötschke, P. (Ed.) *Polymer-carbon nanotube composites: Preparation, properties and applications*, Cambridge, Woolhead publishings, pp. 155–192.
- Li, J., Tong, L., Fang, Z., Gu, A. and Xu, Z. (2006), 'Thermal degradation behavior of multi-walled carbon nanotubes/polyamide 6 composites', *Polymer Degradation and Stability* **91**(9), 2046–2052.

- Lim, G. O., Min, K. T. and Kim, G. H. (2010), 'Effect of cooling rate on the surface resistivity of polymer/multi-walled carbon nanotube nanocomposites', *Polymer Engineering Science* **50**(2), 290–294.
- Liu, S. P., Hwang, S., Yeh, J. M. and Pan, K. W. (2010), 'Enhancement of surface and bulk mechanical properties of polycarbonate through the incorporation of raw mwnts – using the twin-screw extruder mixed technique', *International Communications in Heat and Mass Transfer* **37**(7), 809–814.
- Liu, T., Phang, I. Y., Shen, L., Chow, S. Y. and Zhang, W. D. (2004), 'Morphology and mechanical properties of multiwalled carbon nanotubes reinforced nylon-6 composites', *Macromolecules* **37**(19), 7214–7222.
- Logakis, E., Pandis, C., Peoglos, V., Pissis, P., Stergiou, C., Pionteck, J., Pötschke, P., Mičušík, M. and Omastová, M. (2009), 'Structure-property relationships in polyamide 6/multi-walled carbon nanotubes nanocomposites', *Journal of Polymer Science Part B: Polymer Physics* **47**(8), 764–774.
- Lourie, O., Cox, D. M. and Wagner, H. D. (1998), 'Buckling and collapse of embedded carbon nanotubes', *Physical Review Letters* **81**(8), 1638–1641.
- Lourie, O. and Wagner, H. D. (1999), 'Evidence of stress transfer and formation of fracture clusters in carbon nanotube-based composites', *Composites Science and Technology* **59**(6), 975–977.
- Lu, Q., Keskar, G., Ciocan, R., Rao, R., Mathur, R. B., Rao, A. M. and Larcom, L. L. (2006), 'Determination of carbon nanotube density by gradient sedimentation', *The Journal of Physical Chemistry B* **110**(48), 24371–24376.
- Mack, C., Sathyanarayana, S., Weiss, P., Mikonsaari, I., Hübner, C., Henning, F. and Elsner, P. (2012), 'Twin-screw extrusion of multi walled carbon nanotubes reinforced polycarbonate composites: Investigation of electrical and mechanical properties', *IOP Conference Series: Materials Science and Engineering* **40**(1), 012020.
- Mahmoodi, M., Arjmand, M., Sundararaj, U. and Park, S. (2012), 'The electrical conductivity and electromagnetic interference shielding of injection molded multi-walled carbon nanotube/polystyrene composites', *Carbon* **50**(4), 1455–1464.

- Makrolon 2205 technical datasheet* (2012), Technical report, Bayer MaterialScience AG, Leverkusen, Germany.
- Marosfői, B. B., Szab, A., Marosi, G., Tabuani, D., Camino, G. and Pagliari, S. (2006), ‘Thermal and spectroscopic characterization of polypropylene-carbon nanotube composites’, *Journal of Thermal Analysis and Calorimetry* **86**(3), 669–673.
- McCrum, N., Buckley, C. and Bucknall, C. (1997), *Principles of Polymer Engineering*, 2 edn, Oxford Science Publications.
- Meincke, O., Kaempfer, D., Weickmann, H., Friedrich, C., Vathauer, M. and Warth, H. (2004), ‘Mechanical properties and electrical conductivity of carbon-nanotube filled polyamide-6 and its blends with acrylonitrile/butadiene/styrene’, *Polymer* **45**(3), 739–748.
- Meyer-Plath, A., Orts-Gil, G., Petrov, S., Oleszak, F., Maneck, H. E., Dörfel, I., Haase, O., Richter, S. and Mach, R. (2012), ‘Plasma-thermal purification and annealing of carbon nanotubes’, *Carbon* **50**(10), 3934–3942.
- Mezger, T. G. (2011), *The rheology handbook: For users of rotational and oscillatory rheometers*, 3 edn, Vincentz Network, Hannover.
- Nanocyl S.A. (2009a), *Nanocyl NC7000 series Product Datasheet - Thin Multi-Wall Carbon Nanotube*.
- Nanocyl S.A. (2013), *Products and Solutions, Sector: Electronics*. [accessed 2 November 2013]. Available from: <http://www.nanocyl.com/en/Products-Solutions/Sectors/Electronics>.
- Nobile, M. R. (2011), ‘Rheology of polymer-carbon nanotube composites melts’. In: McNally, T. and Pötschke, P. (Ed.) *Polymer-carbon nanotube composites: Preparation, properties and applications*, Cambridge, Woolhead publishings, pp. 428–481.
- Nobile, M. R., Simon, G. P., Valentino, O. and Morcom, M. (2007), ‘Rheological and structure investigation of melt mixed multi-walled carbon nanotube/pe composites’, *Macromolecular Symposia* **247**(1), 78–87.
- Pan, Z. W., Xie, S. S., Lu, L., Chang, B. H., Sun, L. F., Zhou, W. Y., Wang, G. and Zhang, D. L. (1999), ‘Tensile tests of ropes of very long aligned multiwall carbon nanotubes’, *Applied Physics Letters* **74**(21), 3152–3154.

- Pang, L. S. K., Saxby, J. D. and Chatfield, S. P. (1993), 'Thermogravimetric analysis of carbon nanotubes and nanoparticles', *The Journal of Physical Chemistry* **97**(27), 6941–6942.
- Paul, D. R. and Robeson, L. M. (2008), 'Polymer nanotechnology: Nanocomposites', *Polymer* **49**(15), 3187–3204.
- Pegel, S., Pötschke, P., Petzold, G., Alig, I., Dudkin, S. M. and Lellinger, D. (2008), 'Dispersion, agglomeration, and network formation of multiwalled carbon nanotubes in polycarbonate melts', *Polymer* **49**(4), 974–984.
- Pegel, S., Pötschke, P., Villmow, T., Stoyan, D. and Heinrich, G. (2009), 'Spatial statistics of carbon nanotube polymer composites', *Polymer* **50**(9), 2123–2132.
- Pegel, S., Villmow, T. and Pötschke, P. (2011), 'Quantification of dispersion and distribution of carbon nanotubes in polymer composites using microscopy techniques'. In: McNally, T. and Pötschke, P. (Ed.) *Polymer-carbon nanotube composites: Preparation, properties and applications*, Cambridge, Woolhead publishings, pp. 265–294.
- Peng, B., Locascio, M., Zapol, P., Li, S., Mielke, S. L., Schatz, G. C. and Espinosa, H. D. (2008), 'Measurements of near-ultimate strength for multiwalled carbon nanotubes and irradiation-induced crosslinking improvements', *Nature Nanotechnology* **3**(10), 575–631.
- Pötschke, P., Bhattacharyya, A. R. and Janke, A. (2004), 'Melt mixing of polycarbonate with multiwalled carbon nanotubes: microscopic studies on the state of dispersion', *European Polymer Journal* **40**(1), 137–148.
- Pötschke, P., Bhattacharyya, A. R., Janke, A., Pegel, S., Leonhardt, A., Täschner, C., Ritschel, M., Roth, S., Hornbostel, B. and Cech, J. (2005), 'Melt mixing as method to disperse carbon nanotubes into thermoplastic polymers', *Fullerenes, Nanotubes and Carbon Nanostructures* **13**, 211–224.
- Pötschke, P., Bránig, H., Janke, A., Fischer, D. and Jehnichen, D. (2005), 'Orientation of multiwalled carbon nanotubes in composites with polycarbonate by melt spinning', *Polymer* **46**(23), 10355–10363.
- Pötschke, P., Dudkin, S. M. and Alig, I. (2003), 'Dielectric spectroscopy on melt processed polycarbonate–multiwalled carbon nanotube composites', *Polymer* **44**(17), 5023–5030.

- Pötschke, P., Fornes, T. D. and Paul, D. R. (2002), 'Rheological behavior of multiwalled carbon nanotube/polycarbonate composites', *Polymer* **43**(11), 3247–3255.
- Prashantha, K., Soulestin, J., Lacrampe, M. F., Claes, M., Dupin, G. and Krawczak, P. (2008), 'Multi-walled carbon nanotube filled polypropylene nanocomposites based on masterbatch route: Improvement of dispersion and mechanical properties through pp-g-ma addition', *Express Polymer Letters* **2**(10), 735–745.
- Pratap, A. and Sharma, K. (2012), 'Applications of some thermo-analytical techniques to glasses and polymers', *Journal of Thermal Analysis and Calorimetry* **107**(1), 171–182.
- Prewitt, J. M. S. and Mendelsohn, M. L. (1966), 'The analysis of cell images', *Annals of the New York Academy of Sciences* **128**(3), 1035–1053.
- Qian, D., Dickey, E. C., Andrews, R. and Rantell, T. (2000), 'Load transfer and deformation mechanisms in carbon nanotube-polystyrene composites', *Applied Physics Letters* **76**(20), 2868–2870.
- Rasband, W. (1997), *Image processing and analysis in Java (ImageJ)*, National Institute of Mental Health, Bethesda, Maryland, USA. Available from: <http://rsbweb.nih.gov/ij/index.html>.
- Ray, S. S. (2010), 'A new possibility for microstructural investigation of clay-based polymer nanocomposite by focused ion beam tomography', *Polymer* **51**(17), 3966–3970.
- Reichert, P., Hoffmann, B., Bock, T. and Thomann, R. and Málhaupt, R. F. C. (2001), 'Morphological stability of poly(propylene) nanocomposites', *Macromolecular Rapid Communications* **22**(7), 519–523.
- Richter, S., Saphiannikova, M., Jehnichen, D., Bierdel, M. and Heinrich, G. (2009), 'Experimental and theoretical studies of agglomeration effects in multi-walled carbon nanotube-polycarbonate melts', *Express Polymer Letters* **3**(12), 753 – 768.
- Rios, P. F., Ophir, A., Kenig, S., Efrati, R., Zonder, L. and Popovitz-Biro, R. (2011), 'Impact of injection-molding processing parameters on the electrical, mechanical, and thermal properties of thermoplastic/carbon nanotube nanocomposites', *Journal of Applied Polymer Science* **120**(1), 70–78.
- Rubinstein, M. and Colby, R. H. (2003), *Polymer Physics*, Vol. 1, Oxford University Press.

- Saito, R., Fujita, M., Dresselhaus, G. and Dresselhaus, M. S. (1992), 'Electronic structure of chiral graphene tubules', *Applied Physics Letters* **60**(18), 2204–2206.
- Salazar, A. (2003), 'On thermal diffusivity', *European Journal of Physics* **24**(4), 351.
- Salvetat, J., Briggs, G. A. D., Bonard, J., Bacsá, R. R. and Kulik, A. J. (1999), 'Elastic and shear moduli of single-walled carbon nanotube ropes', *Physical Review Letters* **82**(5), 944–947.
- Samuel, J., Dikshit, A., DeVor, R. E., Kapoor, S. G. and Hsia, K. J. (2009), 'Effect of carbon nanotube (cnt) loading on the thermomechanical properties and the machinability of cnt-reinforced polymer composites', *Journal of Manufacturing Science and Engineering* **131**(3), 031008–9.
- Satapathy, B. K., Weidisch, R., Pötschke, P. and Janke, A. (2007), 'Tough-to-brittle transition in multiwalled carbon nanotube (mwnt)/polycarbonate nanocomposites', *Composites Science and Technology* **67**(5), 867–879.
- Sawyer, L. C., Grubb, D. T. and Meyers, G. F. (2008), *Polymer microscopy*, 3 edn, Springer.
- Schartel, B., Braun, U., Knoll, U., Bartholmai, M., Goering, H., Neubert, D. and Pötschke, P. (2008), 'Mechanical, thermal, and fire behavior of bisphenol a polycarbonate/multiwall carbon nanotube nanocomposites', *Polymer Engineering Science* **48**(1), 149–158.
- Schartel, B., Pötschke, P., Knoll, U. and Abdel-Goad, M. (2005), 'Fire behaviour of polyamide 6/multiwall carbon nanotube nanocomposites', *European Polymer Journal* **41**(5), 1061–1070.
- Schrand, A. (2005), 'Polymer sample preparation for electron microscopy', *Microscopy and Microanalysis* **11**(SupplementS02), 702–703.
- Schroder, D. K. (2006), *Semiconductor material and device characterization*, 3 edn, Wiley-IEEE Press.
- Sennett, M., Welsh, E., Wright, J. B., Li, W. Z., Wen, J. G. and Ren, Z. F. (2003), 'Dispersion and alignment of carbon nanotubes in polycarbonate', *Applied Physics A: Materials Science & Processing* **76**(1), 111–113.
- Shaffer, M. S. P. and Sandler, J. K. W. (2007), *Carbon Nanotube/Nanofiber Polymer Composites*, World Scientific Publishing Co. Pte. Ltd, Singapore, chapter 1, pp. 1–59.

- Shaffer, M. S. P. and Windle, A. H. (1999), 'Fabrication and characterization of carbon nanotube/poly(vinyl alcohol) composites', *Advanced Materials* **11**(11), 937–941.
- Skipa, T., Lellinger, D., Böhm, W., Saphiannikova, M. and Alig, I. (2010), 'Influence of shear deformation on carbon nanotube networks in polycarbonate melts: Interplay between build-up and destruction of agglomerates', *Polymer* **51**(1), 201–210.
- Small, J. P., Shi, L. and Kim, P. (2003), 'Mesoscopic thermal and thermoelectric measurements of individual carbon nanotubes', *Solid State Communications* **127**, 181–186.
- Socher, R., Krause, B., Boldt, R., Hermasch, S., Wursche, R. and Pötschke, P. (2011), 'Melt mixed nano composites of pa12 with mwnts: Influence of mwnt and matrix properties on macrodispersion and electrical properties', *Composites Science and Technology* **71**(3), 306–314.
- Socher, R., Krause, B. and Müller, M. T., Boldt, R. and Pötschke, P. (2012), 'The influence of matrix viscosity on mwnt dispersion and electrical properties in different thermoplastic nanocomposites', *Polymer* **53**(2), 495–504.
- Solomon, M. J., Almusallam, A. S., Seefeldt, K. F., Somwangthanaroj, A. and Varadan, P. (2001), 'Rheology of polypropylene/clay hybrid materials', *Macromolecules* **34**(6), 1864–1872.
- Song, Y. and Zheng, Q. (2010), 'Linear viscoelasticity of polymer melts filled with nano-sized fillers', *Polymer* **51**(14), 3262–3268.
- Spikowski, J. M. and Kunzelman, J. (2012), 'Comparison of common electrical testing methods for the measurement of injection molded pc/cnt composites'.
- Spitalsky, Z., Tasis, D., Papagelis, K. and Galiotis, C. (2010), 'Carbon nanotube-polymer composites: Chemistry, processing, mechanical and electrical properties', *Progress in Polymer Science* **35**(3), 357–401.
- Stephens, M. A. (1974), 'EDF statistics for goodness of fit and some comparisons', *Journal of the American Statistical Association* **69**(347), 730–737.
- Stöckelhuber, K. W., Svistkov, A. S., Pelevin, A. G. and Heinrich, G. (2011), 'Impact of filler surface modification on large scale mechanics of styrene butadiene/silica rubber composites', *Macromolecules* **44**(11), 4366–4381.

- Su, S., Xu, Y. and Wilkie, C. A. (2011), 'Thermal degradation of polymer-carbon nanotube nanocomposites'. In: McNally, T. and Pötschke, P. (Ed.) *Polymer-carbon nanotube composites: Preparation, properties and applications*, Cambridge, Woolhead publishings, pp. 482–510.
- Sung, Y. T., Han, M. S., Song, K. H., Jung, J. W., Lee, H. S., Kum, C. K., Joo, J. and Kim, W. N. (2006), 'Rheological and electrical properties of polycarbonate/multi-walled carbon nanotube composites', *Polymer* **47**(12), 4434–4439.
- TBA Electro Conductive Products Ltd. (2013), *Polymer and Coatings: Applications*. [accessed 2 November 2013]. Available from: <http://www.tbaecp.co.uk/carbon-nanotube-conductive-polymers.html>.
- Thostenson, E. and Chou, T. W. (2002), 'Aligned multi-walled carbon nanotube-reinforced composites: processing and mechanical characterization', *Journal of Physics D: Applied Physics* **35**(16), L77.
- Thostenson, E. and Chou, T. W. (2003), 'On the elastic properties of carbon nanotube-based composites: modelling and characterization', *Journal of Physics D: Applied Physics* **36**(5), 573.
- Tietjen, G. L. and Moore, R. H. (1972), 'Some Grubbs-type statistics for the detection of several outliers', *Technometrics* **14**(3), 16.
- Tiusanen, J., Vlasveld, D. and Vuorinen, J. (2012), 'Review on the effects of injection moulding parameters on the electrical resistivity of carbon nanotube filled polymer parts', *Composites Science and Technology* **72**(14), 1741–1752.
- Treacy, M. M. J., Ebbesen, T. W. and Gibson, J. M. (1996), 'Exceptionally high young's modulus observed for individual carbon nanotubes', *Nature* **381**, 678–680.
- Valentino, O., Sarno, M., Rainone, N. G., Nobile, M. R., Ciambelli, P., Neitzert, H. C. and Simon, G. P. (2008), 'Influence of the polymer structure and nanotube concentration on the conductivity and rheological properties of polyethylene/cnt composites', *Physica E: Low-dimensional Systems and Nanostructures* **40**(7), 2440–2445.
- van der Pauw, L. (1958), 'A method of measuring the resistivity and hall coefficient on lamellae of arbitrary shape', *Philips Technical Review* **20**(8), 220 – 224.

- van Gorp, M. and Palmen, J. (1998), 'Time-temperature superposition for polymeric blends', *Rheology Bulletin* **67**, 5.
- Venugopal, A., Colombo, L. and Vogel, E. M. (2010), 'Contact resistance in few and multi-layer graphene devices', *Applied Physics Letters* **96**(1), 013512–3.
- Via, M. D., King, J. A., Keith, J. M., Miskioglu, I., Cieslinski, M. J., Anderson, J. J. and Bogucki, G. R. (2012), 'Tensile modulus modeling of carbon black/polycarbonate, carbon nanotube/polycarbonate, and exfoliated graphite nanoplatelet/polycarbonate composites', *Journal of Applied Polymer Science* **124**(3), 2269–2277.
- Vilgis, T. A. (2005), 'Time scales in the reinforcement of elastomers', *Polymer* **46**(12), 4223–4229.
- Villmow, T., Pegel, S., Pötschke, P. and Wagenknecht, U. (2008a), 'Influence of injection molding parameters on the electrical resistivity of polycarbonate filled with multi-walled carbon nanotubes', *Composites Science and Technology* **68**(34), 777–789.
- Villmow, T., Pötschke, P., Pegel, S., Häussler, L. and Kretzschmar, B. (2008b), 'Influence of twin-screw extrusion conditions on the dispersion of multi-walled carbon nanotubes in a poly(lactic acid) matrix', *Polymer* **49**(16), 3500–3509.
- Wagner, H. D. (2011), 'Raman spectroscopy of polymer-carbon nanotube composites'. In: McNally, T. and Pötschke, P. (Ed.) *Polymer-carbon nanotube composites: Preparation, properties and applications*, Cambridge, Woolhead publishings, pp. 400–427.
- Wan, T., Clifford, M. J., Gao, F., Bailey, A. S., Gregory, D. H. and Somsunan, R. (2005), 'Strain amplitude response and the microstructure of pa/clay nanocomposites', *Polymer* **46**(17), 6429–6436.
- Wildöer, J. W. G., Venema, L. C., Rinzler, A. G., Smalley, R. E. and Dekker, C. (1998), 'Electronic structure of atomically resolved carbon nanotubes', *Nature* **391**(6662), 59–62.
- Wu, Q., Merchant, F. and Kenneth, C. (2008), *Microscope Image Processing*, Academic Press.
- Wu, D., Wu, L., Sun, Y. and Zhang, M. (2007a), 'Rheological properties and crystallization behavior of multi-walled carbon nanotube/poly(-caprolactone) composites', *Journal of Polymer Science Part B: Polymer Physics* **45**(23), 3137–3147.

- Wu, D., Wu, L. and Zhang, M. (2007b), 'Rheology of multi-walled carbon nanotube/poly(butylene terephthalate) composites', *Journal of Polymer Science Part B: Polymer Physics* **45**(16), 2239–2251.
- Wu, D., Wu, L., Zhang, M. and Zhao, Y. (2008), 'Viscoelasticity and thermal stability of polylactide composites with various functionalized carbon nanotubes', *Polymer Degradation and Stability* **93**(8), 1577–1584.
- Yang, D. J., Zhang, Q., Chen, G., Yoon, S. F., Ahn, J., Wang, S. G., Zhou, Q., Wang, Q. and Li, J. Q. (2002), 'Thermal conductivity of multiwalled carbon nanotubes', *Physical Review B* **66**(16), 165440.
- Yi, W., Lu, L., Dian-lin, Z., Pan, Z. W. and Xie, S. S. (1999), 'Linear specific heat of carbon nanotubes', *Physical Review B* **59**(14), R9015.
- Yonex (2013), *Series Technology Nanoray range*. [accessed 2 November 2013]. Available from: <http://www.yonex.com/nanoray/#spec>.
- Yu, M., Oleg, L., Dyer, M., Moloni, K., Kelly, T. and Ruoff, R. (2000), 'Strength and breaking mechanism of multiwalled carbon nanotubes under tensile load', *Science* **287**, 637–640.
- Zeiler, R., Handge, U. A., Dijkstra, D. J., Meyer, H. and Altstädt, V. (2010), 'Influence of molar mass and temperature on the dynamics of network formation in polycarbonate/carbon nanotubes composites in oscillatory shear flows', *Polymer* **52**(2), 430–442.
- Zhou, W., Qi, S., Li, H. and Shao, S. (2007), 'Study on insulating thermal conductive bn/hdpe composites', *Thermochimica Acta* **452**(1), 36–42.
- Zoller, P. (1982), 'A study of the pressure-volume-temperature relationships of four related amorphous polymers: polycarbonate, polyarylate, phenoxy and polysulfone', *Journal of Polymer Science: Polymer Physics Edition* **20**, 1453 – 1464.